Table of Contents

List of Tables

List of Figures

Chapter 1 Introduction

1.1 Background

Nowadays, the growing demand for high performance and lightweight structural components at elevated temperatures (250 to 350℃) is a challenge for weight-sensitive automotive and aerospace industry. The traditional precipitation-strengthened aluminum alloys such as 2xxx, 6xxx and 7xxx can hardly meet the requirement of elevated-temperature mechanical properties, because of the rapid coarsening of nano-scale precipitates at elevated temperature (overaging effect) [1, 2]. In recent years, the dispersoid strengthening in AA3xxx aluminum alloys has been discovered, and the mechanical properties at both room and elevated temperatures could be greatly improved [3-7]. Moreover, α-Al(MnFe)Si dispersoids as the main strengthening phase in AA3xxx alloys have been proved to be thermally stable at elevated temperature [5, 6]. In addition, AA3xxx alloys possess good formability, excellent corrosion resistance and weldability [8, 9]. The combination of those properties makes AA3xxx alloys especially attractive for elevated temperature applications.

Until now, limited open literatures are available on the effect of chemical composition on microstructure and elevated-temperature mechanical properties in AA 3xxx alloys. Muggerud et al [4] studied the effect of Mn and Si on the evolution of dispersoids in AA3003 alloy. It is found that the addition of Mn and Si can promote the precipitation of α-Al(MnFe)Si dispersoids and thus improve room-temperature mechanical properties. The effect of Fe on the dispersoid precipitation and elevated-temperature properties in AA3004 alloy was investigated by Kun et al [6]. With an optimum Fe content, a higher volume fraction of α-Al(MnFe)Si dispersoids and hence a better mechanical properties and creep resistance at elevated temperature can be achieved.

In the present study, the research focused on the effect of Mg, Si, Cu, Sc and Zr elements on the microstructure and elevated-temperature mechanical properties of AA3xxx alloys.

1.2 Objectives

The general objective of this project is to develop a new wrought alloy which can be used for elevated-temperature applications (250℃-350℃). In the present study, Al-Mn-Mg 3xxx alloy were chosen to be the base alloy. In order to improve the elevated-temperature mechanical properties, the compositions of materials need to be optimized. The research was divided into following four parts with specific objectives.

1. The effect of Mg and Si on microstructure and properties at ambient and elevated temperatures

The amounts of Mg and Si are optimized to improve the mechanical properties at ambient and elevated temperatures.

2. The nucleation mechanisms of dispersoids

The study involves the relationship between metastable Mg_2Si and α-Al(Mn,Fe)Si dispersoids and the effect of deformation on the nucleation of the dispersoids. The goal is to clarify the nucleation mechanisms of α-Al(Mn,Fe)Si dispersoids under the influences of metastable Mg_2Si and pre-deformation.

3. The effect of Sc and Zr on microstructure and properties at ambient and elevated temperatures

In order to study the combined action of Al_3(Sc, Zr) precipitates and α-Al(Mn,Fe)Si dispersoids on the mechanical properties at elevated temperature, Sc and Zr elements will be added to AA3xxx alloys.

4. The effect of Cu on microstructure and properties at ambient and elevated temperature

With the addition of Cu, the effect of Cu on the precipitation behavior of dispersoids and elevated-temperature mechanical properties is investigated.

References

1. I. J. Polmear, M. J. Couper, Design and development of an experimental wrought aluminum alloy for use at elevated temperatures, Metallurgical Transactions A. 19 (1988) 1027-1035. Doi: http://dx.doi.org/10.1007/BF02628387.
2. Y. Zhou, Z. Liu, S. Bai, P. Ying, L. Lin, Effect of Ag additions on the lengthening rate of Ω plates and formation of σ phase in Al-Cu-Mg alloys during thermal exposure, Materials Characterization. 123 (2017) 1-8. Doi: http://dx.doi.org/10.1016/j.matchar.2016.11.008.
3. Y. J. Li, A. M. F. Muggerud, A. Olsen, T. Furu, Precipitation of partially coherent α-Al(Mn,Fe)Si dispersoids and their strengthening effect in AA 3003 alloy, Acta Materialia. 60 (2012) 1004-1014. Doi: http://dx.doi.org/10.1016/j.actamat.2011.11.003.
4. A. M. F. Muggerud, E. A. Mørtsell, Y. Li, R. Holmestad, Dispersoid strengthening in AA3xxx alloys with varying Mn and Si content during annealing at low temperatures, Materials Science and Engineering: A. 567 (2013) 21-28. Doi: http://dx.doi.org/10.1016/j.msea.2013.01.004.
5. K. Liu, X. G. Chen, Development of Al–Mn–Mg 3004 alloy for applications at elevated temperature via dispersoid strengthening, Materials & Design. 84 (2015) 340-350. Doi: http://dx.doi.org/10.1016/j.matdes.2015.06.140.
6. K. Liu, X.-G. Chen, Evolution of Intermetallics, Dispersoids, and Elevated Temperature Properties at Various Fe Contents in Al-Mn-Mg 3004 Alloys, Metallurgical and Materials Transactions B. 47 (2016) 3291-3300. Doi: http://dx.doi.org/10.1007/s11663-015-0564-y.
7. K. Liu, H. Ma, X. G. Chen, Enhanced elevated-temperature properties via Mo addition in Al-Mn-Mg 3004 alloy, Journal of Alloys and Compounds. 694 (2017) 354-365. Doi: http://dx.doi.org/10.1016/j.jallcom.2016.10.005.

8. H.-W. Huang, B.-L. Ou, Evolution of precipitation during different homogenization treatments in a 3003 aluminum alloy, Materials & Design. 30 (2009) 2685-2692. Doi: http://dx.doi.org/10.1016/j.matdes.2008.10.012.

9. A. R. Yazdzad, T. Shahrabi, M. G. Hosseini, Inhibition of 3003 aluminum alloy corrosion by propargyl alcohol and tartrate ion and their synergistic effects in 0.5% NaCl solution, Materials Chemistry and Physics. 109 (2008) 199-205. Doi: http://dx.doi.org/10.1016/j.matchemphys.2007.11.012.

Chapter 2 Literature review

2.1 Introduction of AA3xxx alloys

Due to their relatively low cost, workability, and excellent corrosion resistance [1, 2], traditional AA3xxx series aluminum alloys are widely used in the industrial production, such as architecture, packaging and automobile.

However, the good elevated-temperature properties of AA3xxx alloys are often ignored. Nowadays, the growing demand for high performance and lightweight structural components at elevated temperatures (250 to 350℃) is a challenge for weight-sensitive automotive and aerospace industries. The traditional precipitation-strengthened aluminum alloys such as 2xxx, 6xxx and 7xxx can hardly meet the requirement of elevated-temperature mechanical properties, because of the rapid coarsening of nano-scale precipitates at elevated temperature (over-aging effect) [3, 4]. In recent years, the dispersoid strengthening in 3xxx aluminum alloys that can improve the mechanical properties at both room and elevated temperatures has been discovered [5-9]. Although Al-Mn-Mg 3xxx alloys are traditionally classified as non-heat-treatable alloys, the precipitation of thermally stable α-Al(MnFe)Si dispersoids during heat treatment and hence the improvement of high temperature properties in 3004 alloy have been recently reported [7, 8]. The combination of those properties makes 3xxx alloys especially attractive for elevated-temperature applications. Therefore, in the present study, the development of the new alloys was on the basis of AA3004 alloy. The composition of AA3004 alloy is shown in Table 2.1.

Table 2.1 Composition of AA3004 alloys[10]

	Mn	Si	Fe	Cu	Mg	Al
Wt%	1.0-1.5	Max0.30	Max0.70	Max0.25	0.8-1.3	Bal

2.2 Microstructure of AA3xxx alloys

2.2.1 Intermetallic particles

Serval studies have been conducted on the microstructure evolution during different heat treatments in 3xxx alloys, mainly focusing on 3003 and 3004 alloys [1, 5-8, 11-20] . The as-cast microstructure of 3003 and 3004 alloys consist of mainly Al_6(Mn,Fe), α-Al(Mn,Fe)Si and Mg_2Si intermetallic phases [12, 17, 18, 21-23]. During solidification, constituent particles Al_6(Mn,Fe) and α-Al(Mn,Fe)Si formed in interdendritic arm spaces or along grain boundaries. The constituent particles are originally eutectic particles that distributed in the interdendritic regions during solidification. Upon the homogenization treatment, morphology of those constituent particles changes with a possible phase transformation of Al_6(Mn,Fe) phase to α-Al(Mn,Fe)Si as shown in Fig. 2.1[17].

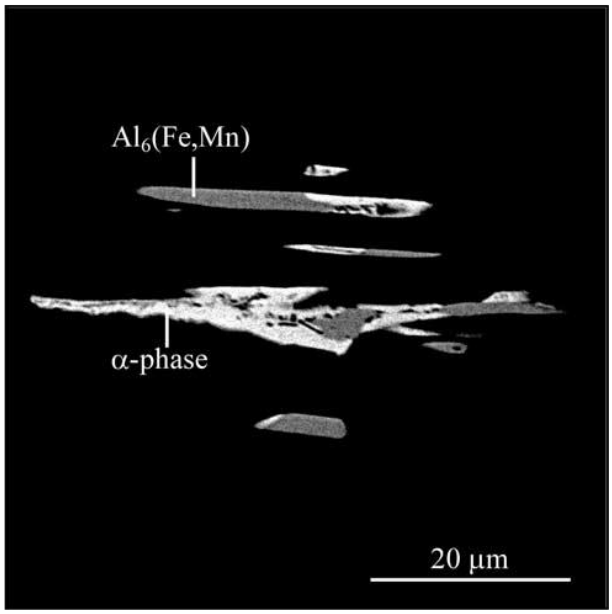

Fig. 2.1 Backscattered SEM image of Al_6(Mn,Fe) and α-Al(Mn,Fe)Si intermetallic particles

The solidification microstructure of 3xxx alloys is shown in Fig. 2.2, a large amount of rod like, plate like and eutectic intermetallic particles are distributed in the interdendritic

regions and grain boundaries. Most of the intermetallic particles have been determined to be Al_6(Mn, Fe) and only a small fraction of primary particles are determined to be α-Al(Mn,Fe)Si.

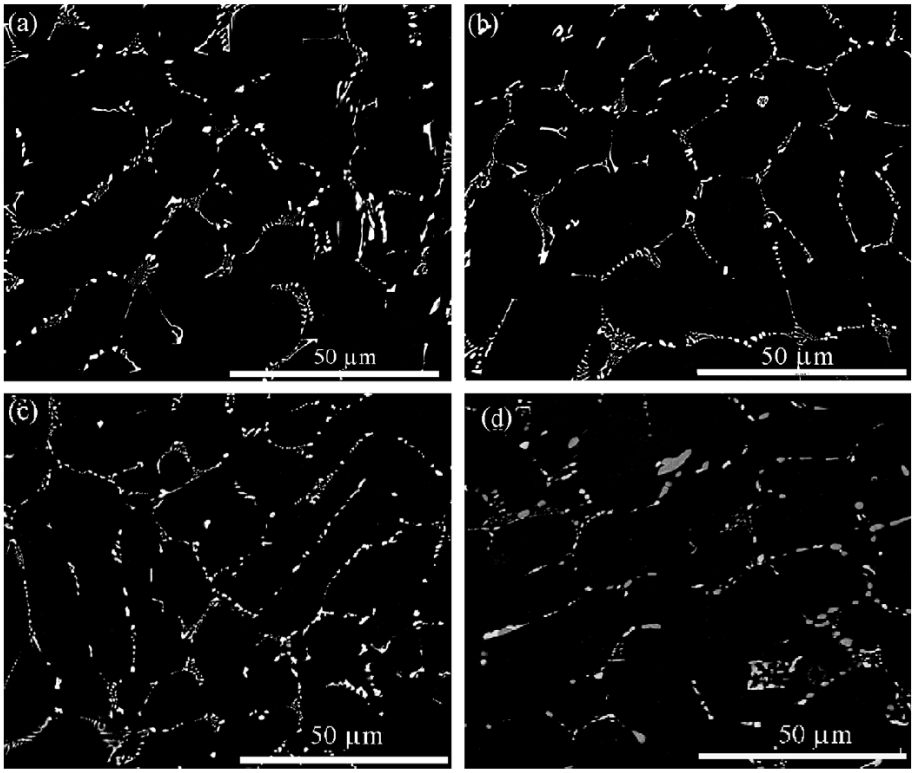

Fig. 2.2 Backscattered SEM images of intermetallic particles (a) in the as-cast state and quenched from (b) 400 ℃, (c) 560 ℃ and (d) 630 ℃ during heating

In the previous work [12], the evolution of the size and number density of intermetallic particles was studied, as shown in Fig. 2.3 [12]. as the temperature went up, the number density of intermetallic particles increased, in the other word, the eutectic networks of intermetallic particles breaked up which can be seen in Fig. 2.2 (a)-(c). However, if the temperature was over 550 ℃, the number density would drop sharply and the diameter increased which indicated that coarsening was the main mechanism to control the evolution of primary, as is shown in Fig. 2.2 (d).

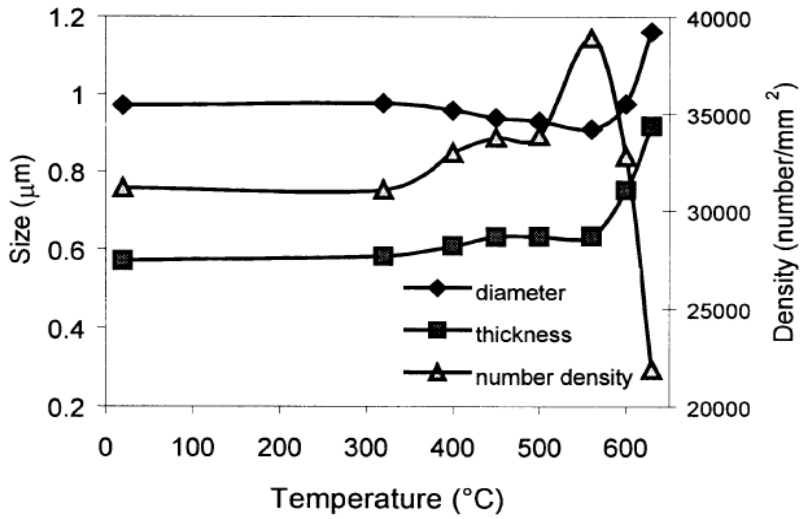

Fig. 2.3 Size and number evolution of intermetallic particles

As is shown in Fig. 2.4 [12], when temperature increased, intermetallic particles Al_6(Mn, Fe) started to transform into α-Al(Mn,Fe)Si, the fraction of α-Al(Mn,Fe)Si increased shapely with temperature. The transformation process from Al_6(Mn,Fe) to α-Al(Mn,Fe)Si is identified as a eutectoid process in which the Al_6(Mn,Fe) phase decomposes to a mixture of α-Al(Mn,Fe)Si and aluminum solid solution. The decomposition preserves the local volume and content of iron and manganese (which diffuse slowly) [22], but requires intake of silicon. The silicon appears to diffuse from the matrix.

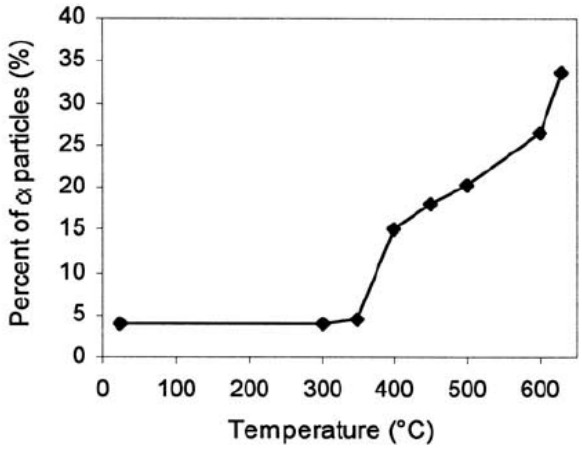

Fig. 2.4 Fraction of α-Al(Mn,Fe)Si in total amount of intermetallic particles

2.2.2 Dispersoid particles

During heat treatment, a considerable number of α-Al(Mn,Fe)Si dispersoids precipitate and the size and amount of dispersoids are dependent on the alloy chemistry and heat treatment condition [5-7, 11, 19]. The dispersoids mainly distribute in the corns of dendrite arms. The area with a large number density of dsipersoids can be defined as the dispersoid zone. On the other hand, very few dispersoids precipitated in the grain boundaries and the interdendritic areas. These locations are defined as the dispersoid free zone (DFZ). All the dispersoid free zones locate in the Mn depleted areas formed during solidification[13], so the cause of dispersoid free zone is the segregation of Mn elements. Due to the large scale of dispersoid zone and dispersoid free zone, TEM cannot be used for observation. The dispersoid zone and dispersoid free zone can be observed using optical microscope and SEM with etched samples. The morphology is shown in Fig. 2.5 [17].

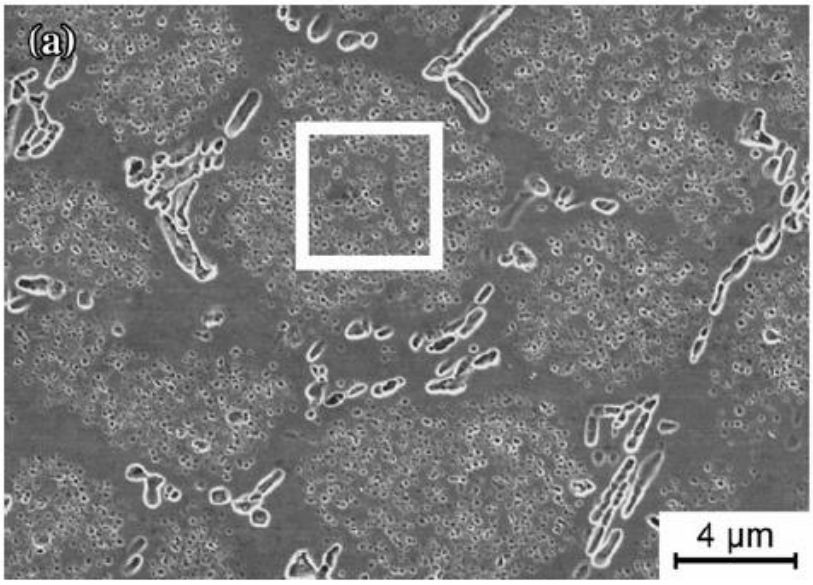

Fig. 2.5 SEM images which show the location of dispersoids

The α-Al(Mn,Fe)Si dispersoids are partially coherent with the matrix [5, 24] and has a cubic crystal structure [11]. The diffraction pattern of dispersoids is shown in Fig. 2.6 [11]. The precipitation of α-Al(Mn,Fe)Si dispersoids starts from approximately 340 ℃ [7]. After a

proper heat treatment, the maximum volume fraction can reach as high as ~3% and the dispersoids are proved to be thermally stable at 300 ℃, resulting in excellent mechanical properties and creep resistance at 300 ℃ [7]. During heating, α-Al(Mn,Fe)Si dispersoids precipitate from the matrix. Two dispersoid morphologies were observed: spherical shape and rodlike shape as shown in Fig. 2.7 [11]. The size of most dispersoids is in the range of 50-200 nm.

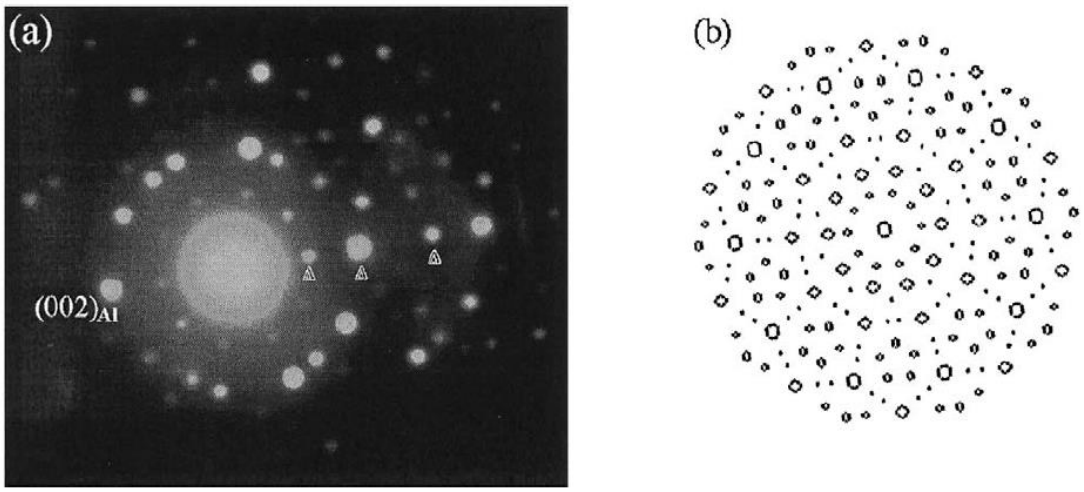

Fig. 2.6 (a) Selected area diffraction pattern of dispersoids precipitated after 96 h of homogenization at 300 °C and (b) computer simulated diffraction pattern of an icosahedral quasicrystal phase showing five-fold symmetry

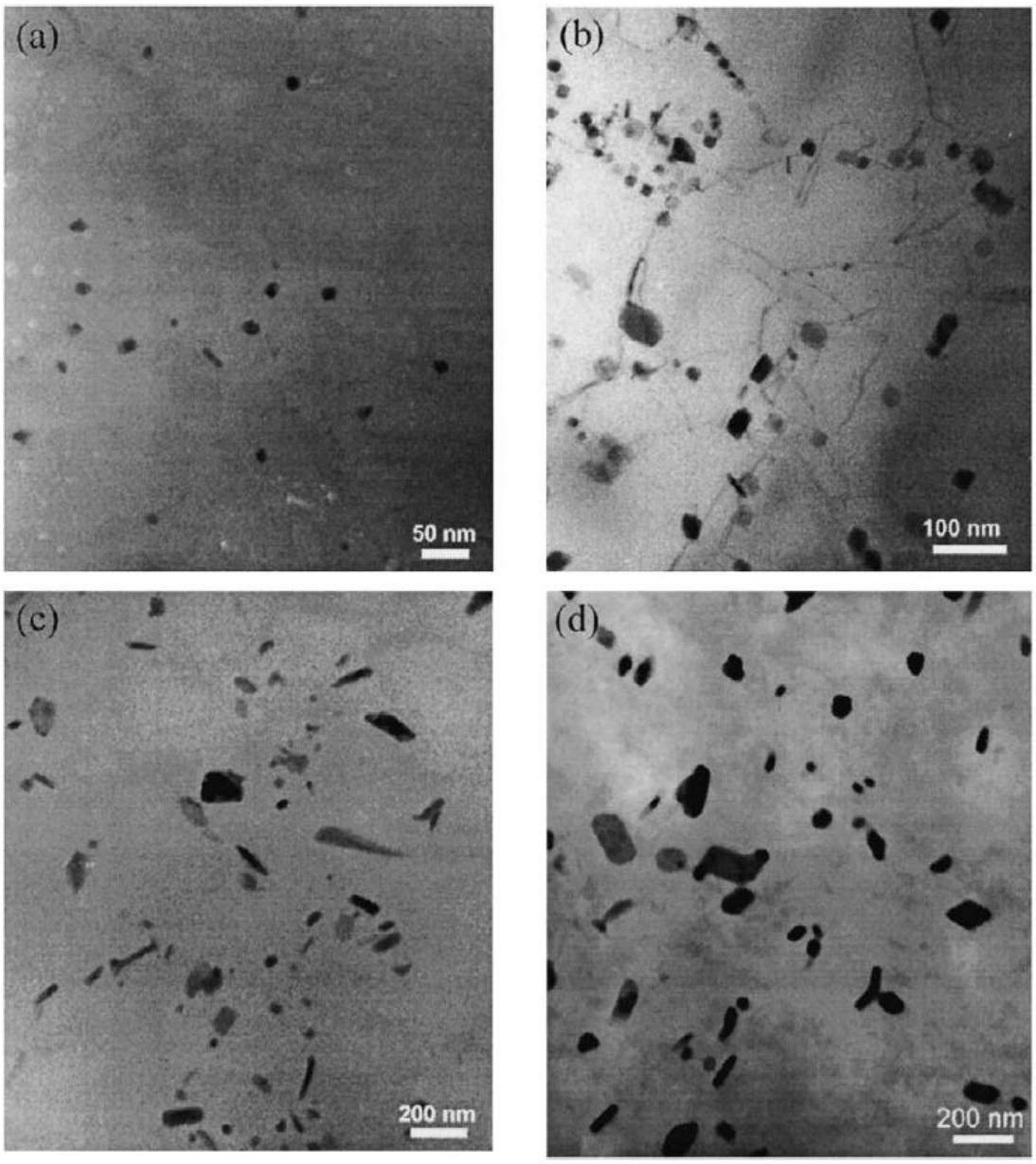

Fig. 2.7 TEM images showing the morphology of dispersoids precipitated during heating, (a) 350 °C, (b) 400 °C, (c) 500 °C and (d) 580 °C

As the annealing temperature increases, the number density of dispersoids first increases and then decreases. For 3003 alloys, at 400 ℃ the number density reaches the maximum point and most of the dispersoids dissolve in the matrix at 600 ℃, however, for other 3xxx alloys, the temperature and heating time are affected greatly by the chemical composition of alloys. The size of despersoids increases with heating temperature and heating time. Fig. 2.8 [11]

shows the evolution of size and number density of dispersoids as a function of heat treatment temperature..

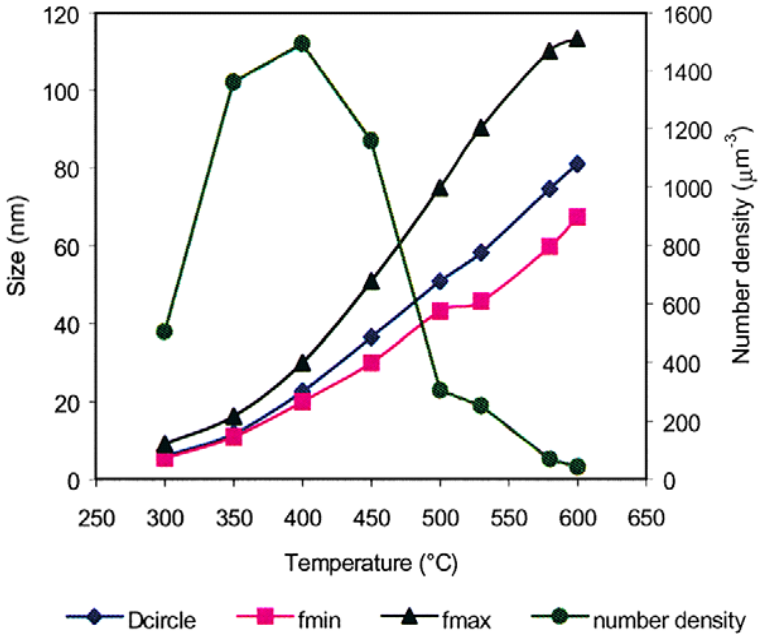

Fig. 2.8 The evolution of the size and number density of dispersoids

Determination of the volume fraction of dispersoids is experimentally challenging, as the size of dispersoids is too small for optical or SEM microscopes. Transmission electron microscope must be used for the observation of dispersoids in details. However, due to the non-uniform distribution of dispersoids, many micro-scale dispersoid free zones presented in the microstructure. Because of the large scale, the observation and quantification of the dispersoid free zone are not possible for TEM.

Previous work by Li [11] and Dehmas [17] presented two methods to determine the volume fraction of dispersoids by TEM. Both of them use optical microscope to quantity the volume fraction of the dispersoid free zone by analyzing the etched sample. For quantitatively study of the morphology and size of dispersoids, TEM images are recorded.

In the work of Dehmas [17], the volume fraction of the dispersoids in the dispersoid zone is calculated by assuming a disc-shape morphology, with a mean diameter equal to d and a

thickness equal to d/2, where d is the equivalent diameter. So the volume fraction of the dispersoids in the dispersoid zone can be then expressed as:

$$V_{int}(pct) = \pi/8 \cdot d^3 \cdot N_{int} \cdot 100 \qquad \text{Eq. 2.1}$$

Where $N_{int}(pct)$ is the volume number density of the dispersoids in dispersoid zone, and d is the mean diameter calculated by TEM images.

When the volume fraction of the dispersoid free zone is taken into account, the volume number density in the alloy is calculated as:

$$N_v(pct) = N_{int}(1-P) \qquad \text{Eq. 2.2}$$

Where P is the volume fraction of the dispersoid free zone including intermetallic particles.

The dispersoid volume fraction in the alloy can thus be expressed as:

$$V_{int}(pct) = \pi/8 \cdot d^3 \cdot N_v \cdot 100 \qquad \text{Eq. 2.3}$$

The other method is presented in the study of Li [11]. The dispersoids are assumed as rectangular parallelepipedic particles with length a, width b and height c, randomly distribute in the thin foil without overlapping, the average projected area of these particles in the film is:

$$A = 1/2(ab + bc + ac) \qquad \text{Eq. 2.4}$$

The average equivalent diameter of dispersoids projected on the film, D, can be calculated by the following equation:

$$D^2 = \frac{2a^2}{\pi}(k_1 + k_2 + k_1k_2) \qquad \text{Eq. 2.5}$$

Where, $k_1=b/a$, $k_2=c/a$, $0< k_1<1$, $0< k_2<1$.

The shape factor K can be calculated as:

$$K=\frac{V}{AD}=\frac{\sqrt{2\pi}k1k2}{(k1+k2+k1k2)^{3/2}} \quad \text{Eq. 2.6}$$

Then the volume fraction can be calculated as:

$$V_V=\sum_{i=1}^{n} A_A^i D_i K_i/t \quad \text{Eq. 2.7}$$

Where A_A^i, D_i and K_i are projected area fraction, average equivalent diameter, and shape factor of dispersoids respectively, and t is the thickness of TEM foil. The influences of overlapping and truncation by foil surface is not considered. Since the thickness of the TEM foil for AA3xxx alloys is usually small enough, the overlapping effect of dispersoids can be neglected. The effect of truncation must be considered. A correction equation is given as following:

$$V_V= \sum_{i=1}^{n} A_A^i \frac{D_i K_i}{D_i K_i+t} \quad \text{Eq. 2.8}$$

Due to the difficulty to get the shape factor, an average shape factor is used. Also the dispersoid free zone must be taken into consideration, thus, the volume fraction can be calculated by:

$$V_V=A_A \frac{KD}{KD+t}(1-A_{PFZ}) \quad \text{Eq. 2.9}$$

Where, A_{PFZ} is the volume fraction of dispersoid free zone.

2.3 Effect of chemical composition on AA3xxx alloys

2.3.1 Mn

Mn element is a major alloying element of AA3xxx alloys, as much as 1.82 wt.% are soluble in aluminum matrix. The phase diagram of Al-Mn alloys of the Al-rich part is shown in Fig. 2.9 [25]. However, in commercial AA3xxx alloys, the content of Mn is often less than 1.25%. Because Fe decreases the solubility of Mn, and therefore increases the probability of forming large primary intermetallic particles of $Al_6(Mn,Fe)$, which can have a negative effect of ductility. During solidification, large amount of Mn is retained in solution in aluminum matrix, the reminder is present as $Al_6(Mn,Fe)$ constituent particles. During homogenization, α-Al(Mn,Fe)Si dispersoids precipitate from the supersaturated matrix. Adding Mn element could enhance the precipitation of α-Al(Mn,Fe)Si dispersoids and improve the yield strength [6], as long as the concentration of Mn was under the solid solution limit.

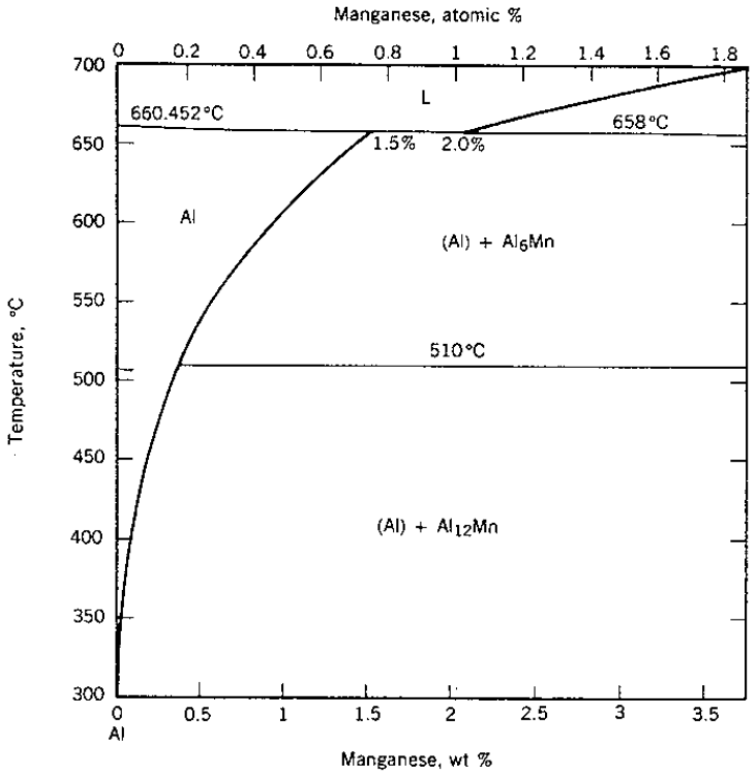

Fig. 2.9 The phase diagram of Al-Mn alloys of the Al-rich part

2.3.2 Fe

The addition of Fe into AA3xxx alloys decreases the solubility of Mn which leads to the precipitation of constituent particles Al_6(Mn,Fe) and α-Al(Mn,Fe)Si. On the other hand, Fe and Mn can substitute each other freely in α-Al(Mn,Fe)Si dispersoids.

According to previous literature [8], the content of Fe significantly affects the intermetallic particles, dispersoids and mechanical properties at both room and elevated temperatures. Results show that while the content of Fe is 0.1%, the dominant intermetallic particles are α-Al(Mn,Fe)Si, However, the concentration of Fe increases to 0.3%~0.6%, the dominant intermetallic particles change from α-Al(Mn,Fe)Si to Al_6(Mn,Fe). The alloys with 0.3% Fe possess the finest and highest volume fraction of dispersoids A significant improvement on the yield strength and creep resistance at elevated temperature (Fig. 2.10 and Fig. 2.11) are achieved by 0.3% Fe addition [8].

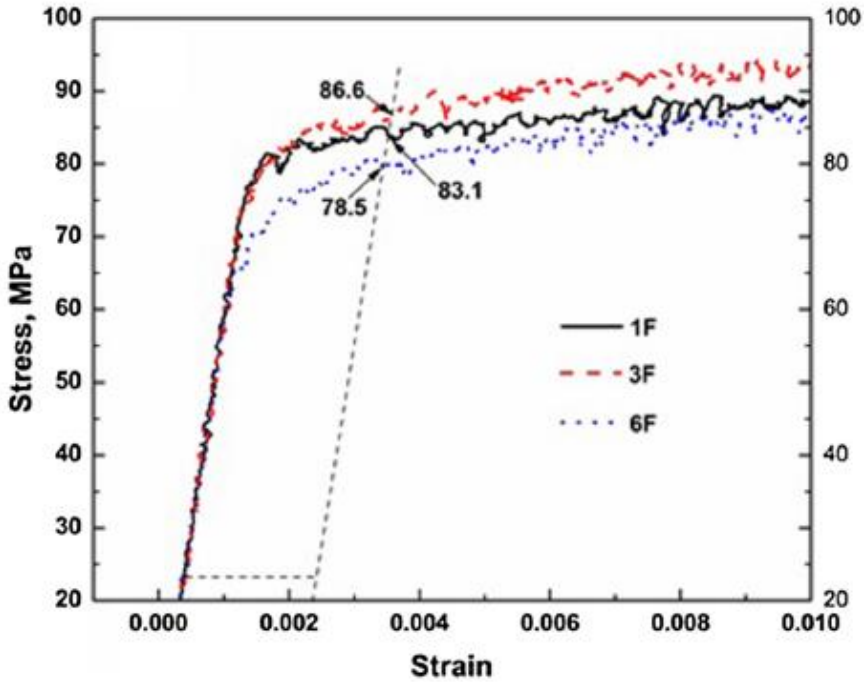

Fig. 2.10 The yield strength at 300 °C of AA3xxx alloys with 0.1%Fe, 0.3% and 0.6%Fe

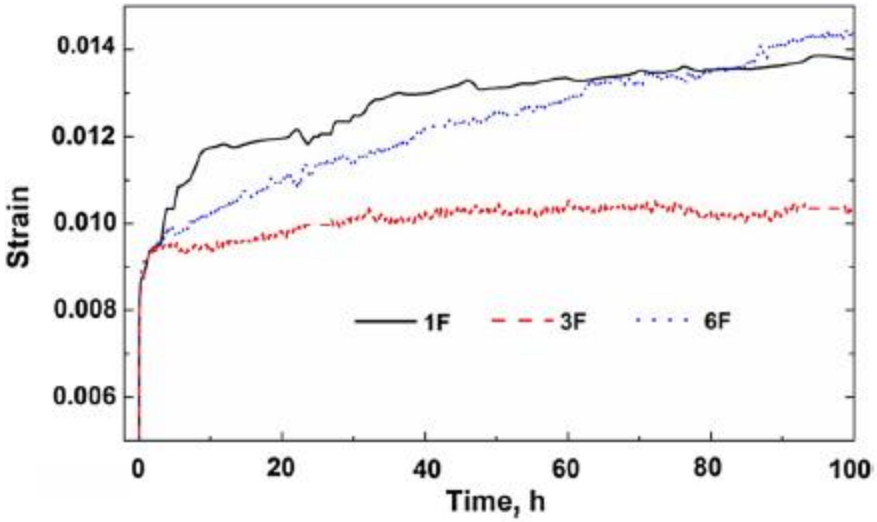

Fig. 2.11 The creep strain curve measured at 300 °C of AA3xxx alloys with 0.1%Fe, 0.3% and 0.6%Fe

2.3.3 Mg

Mg has a very high solid solubility in aluminum (up to 14.9% at 450 ℃), its solubility decrease to 1.7wt% at room temperature, as is shown in Fig. 2.12 [26], and the rate of decomposition of the supersaturated solid solution in very low, therefore solid solution hardening is easily achieved. The strengthening contribution of Mg solid solution at room temperature could be calculated according to the equation below [27, 28]:

$$\sigma_{SS} = HC^{\alpha} \qquad \text{Eq. 2.10}$$

Where C was concentration of solute atoms, H_{Mg}=13.8MPa/wt.% [27], $\alpha_{Mg} = 1$ [27].

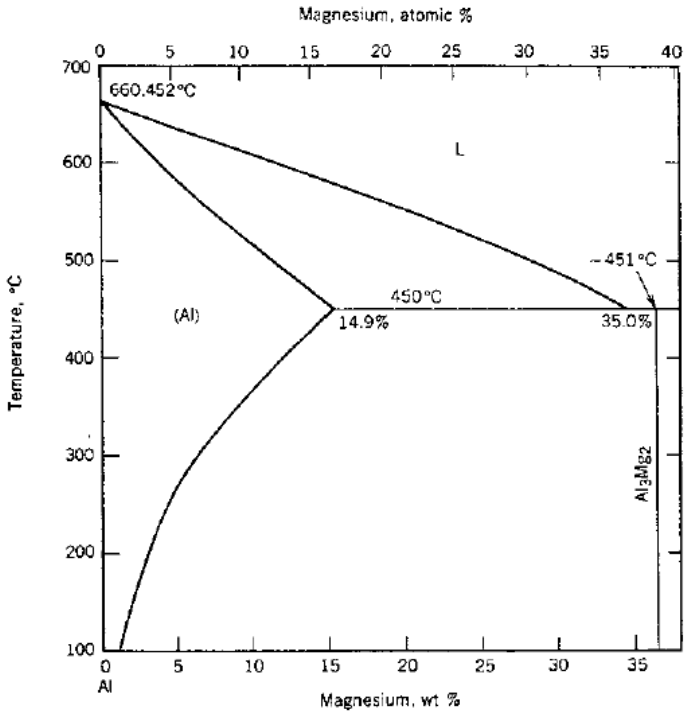

Fig. 2.12 Phase diagram of Al-Mg Alloys

When Mg is added to AA3xxx aluminum alloys, due to the presence of silicon, Mg_2Si particles precipitate from matrix during heat-treatment. The precipitation sequence of Mg_2Si is reported as: Mg and Si cluster→needle-like β″ →lath-like or rod-like β′→plate-like equilibrium β [29-34]. The peek-aging mechanical strength of the Al–Mg–Si alloys originates mainly from the β″. The typical size of needle β″ is around 4 * 4 *50 nm^3[31]. Further over-aging transforms the needle β″ into thick rods β′. The β′ phase forms as rods of ~10 * 10 * 500 nm^3 [32]. The β equilibrium phase has been found to be as plates with dimensions of several micrometers with composition Mg_2Si[29, 35, 36]. According to the previous study [37, 38], metastable Mg_2Si precipitates have positive effect on the nucleation of dispersoids. α-Al(Mn,Fe,Cr) Si dispersoids and α-AlMnSi dispersoids heterogeneously nuclear on β′-Mg_2Si in 6xxx alloys. An intermediate phase u-phase nucleated on the β′-Mg_2Si. With continued annealing, α -Al(Mn,Fe,Cr) Si dispersoids nucleated heterogeneously on the ‘u-phase’ precipitates before these precipitates dissolved [38] as shown in Fig. 2.13.

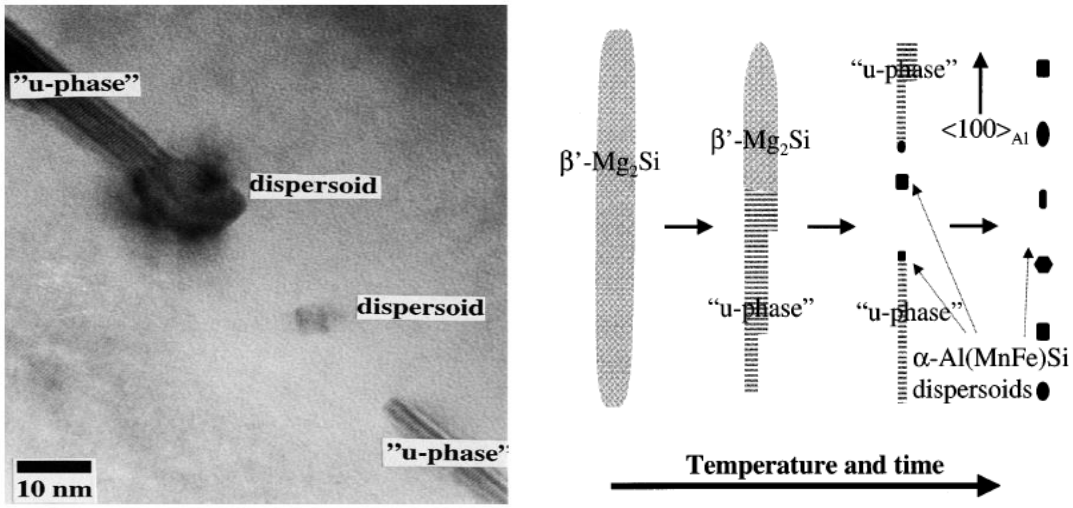

Fig. 2.13 (a) TEM image of dispersoid nucleated on the surface of u-phase (b) a model of the precipitation of the dispersoids

To sum up, Mg has the positive effect on AA3xxx alloys on two aspects: First, solid solution hardening is easily achieved by solute Mg atoms. Mg provided solid solution strength for AA3xxx alloys [18]. Second, Mg element would affect the nucleation process of α-Al(Mn,Fe)Si dispersoids by forming metastable Mg_2Si [37, 38] which promoted the precipitation of α-Al(Mn,Fe)Si dispersoids.

2.3.4 Si

Silicon also has a major influence on the constituent particles transformation from $Al_6(Mn,Fe)$ to α-Al(Mn,Fe)Si. The morphology of these two phases are shown in Fig. 2.14 [17]. The transformation process is a eutectoid process in which the $Al_6(Fe,Mn)$ phase decomposes to a mixture of α-Al(Mn,Fe)Si and aluminum solid solution as following [22]:

$$3Al_6(Mn, Fe)+Si \rightarrow \alpha\text{-}Al_{12}(Mn,Fe)_3Si+6Al \qquad \text{Eq. 2.11}$$

Previous work stated that it was the only element required for transformation from aluminum matrix. The decomposition preserves the local volume and contents of iron and

manganese (which are comparatively slow diffusers), but requires intake of silicon. Rising the level of silicon in the alloys increases the proportion of α-Al(Mn,Fe)Si constituent particles and the transformation rate.

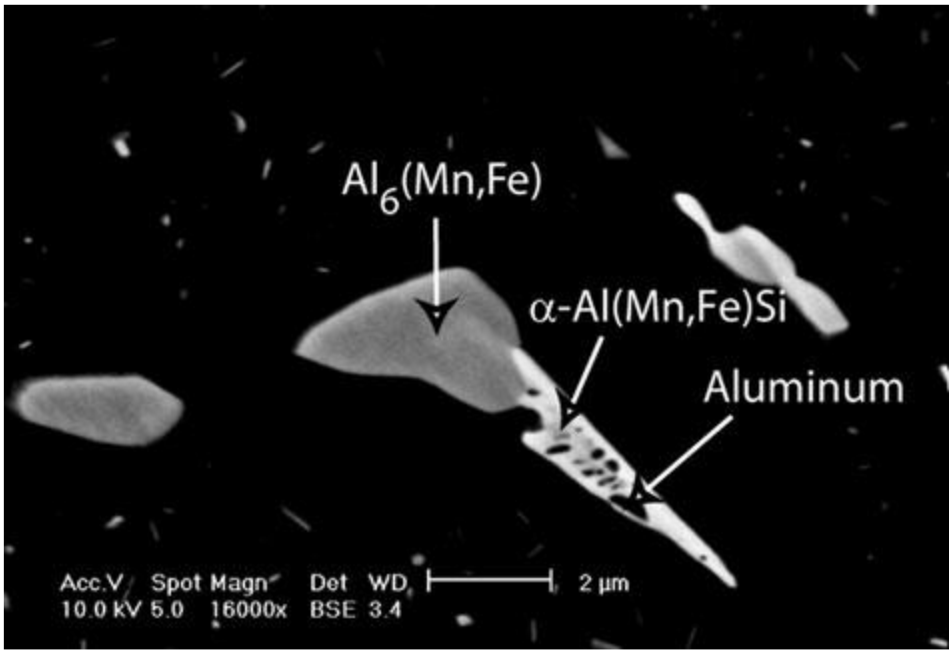

Fig. 2.14 Backscattered SEM image after 1 h at 500 °C with 20°C/s heating rate revealing the eutectoid transformation of Al_6(Mn, Fe) into α-Al(Mn,Fe)Si.

Si element also significantly influences the nano-scale microstructure of AA3xxx alloys. As discussed in the last chapter, metastable Mg_2Si precipitates affect the precipitation of dispersoids by providing nucleation sites. Moreover, Si element favors the precipitation of dispersoids α-Al(Mn,Fe)Si and increases the volume fraction of α-Al(Mn,Fe)Si dispersoids [6].

2.3.5 Cu

Cu element is a main alloying element of AA2xxx alloys (Al-Cu) and important alloying element of AA7xxx alloys (Al-Zn-Mg-Cu) and AA6xxx alloys (Al-Mg-Si-Cu). By applying aging heat treatment at 100°C~200°C, nano-scale metastable Al_2Cu [39], $Mg(Zn,Al,Cu)_2$ [40] and AlCuMgSi (Q phase) [36, 41] precipitated. Metastable $Mg(Zn,Al,Cu)_2$ and AlCuMgSi (Q

phase) possessed lower coarsening rate than metastable $MgZn_2$ and Mg_2Si[40, 42, 43]. It could be contributed to the addition of Cu into the alloys. The influence of Cu on the precipitation and coarsening behaviour of α-Al(Mn,Fe)Si dispersoids had never reported before. In the previous study, no literature reported that Cu would improve the thermal stability of α-Al(Mn,Fe)Si dispersoids, however, a few studies [42-44] confirmed that Cu would enhanced the thermal stability of AA6xxx alloys. This was due to the better thermal coarsening resistance of metastable Q phases compared with metastable Mg_2Si [42]. Similar phenomenon was also found in AA7xxx alloys, the addition of Cu decreased the coarsening rate of $MgZn_2$ [40]. According to previous investigations, Cu element tended to segregate at the interface of metastable Q phases and aluminum matrix as shown in Fig. 2.15 [45-47]. Cu segregation limited the diffusion growth of metastable Q phase and hence produced a finer microstructure [45]. The segregation of Cu elements at the interfaces between secondary precipitation phases and aluminum matrix was also found in AA2xxx alloys, the extra Cu atoms were detected at the interfaces of metastable Al_2Cu [39]. It seemed that Cu atoms had a tendency to segregate at the interfaces of secondary precipitation phases. Similar phenomenon may happen to α-Al(Mn,Fe,Cu) Si dispersoids as well.

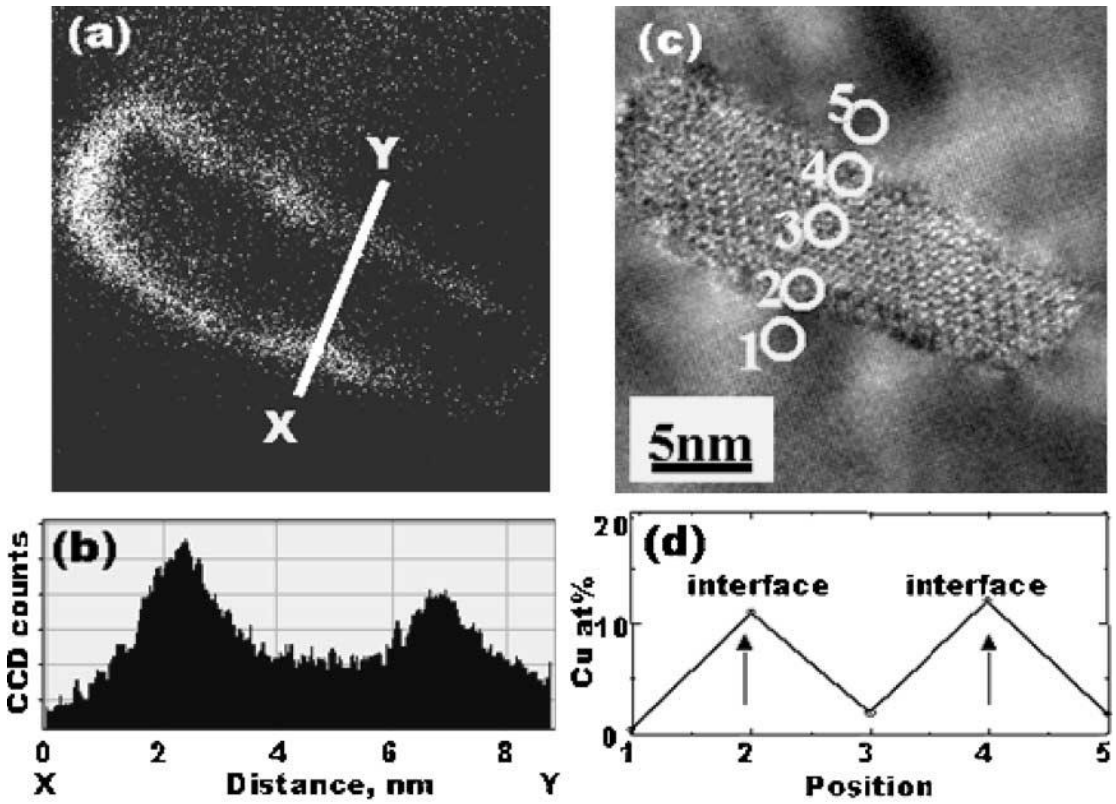

Fig. 2.15 Comparison of chemical composition between an elemental map and EDS for the same precipitate (a) Cu-L map, (b) estimated chemical compositions from elemental maps, (c) a zero-loss image, and (d) EDS data obtained for a precipitate of (c).

2.3.6 Sc and Zr

A number of previous literature about the effect of Sc and Zr were reported [48-55]. Due to the addition of Sc, a large number of nano-scale Al_3Sc could precipitate and its lattice structure was reported to be of $L1_2$ type. The structure can be described as ordered FCC. The Al_3Sc precipitates are spherical shape. These Al_3Sc were coherent with matrix and thermally stable at 350 °C [49]. Zr element was often added together with Sc. Zr could substitute Sc in Al_3Sc to form $Al_3(Sc,Zr)$ precipitates as shown in Fig. 2.16 [52]. $Al_3(Sc,Zr)$ precipitates exhibited a better thermal coarsening resistance than Al_3Sc precipitates[52-54]. This was due to the segregation of Zr element around Al_3Sc cores as shown in Fig. 2.17 [56]. Zr element possessed a slower diffusion rate which slowed down the coarsening rate of $Al_3(Sc,Zr)$ precipitates. Because of the excellent thermal coarsening resistance of $Al_3(Sc,Zr)$ precipitates, $Al_3(Sc,Zr)$ precipitates may be a great choice to be introduced into AA3xxx alloys for further enhancing the elevated temperature properties. In the previous studies, none of the study is found about the effect of Sc and Zr on AA3xxx alloys.

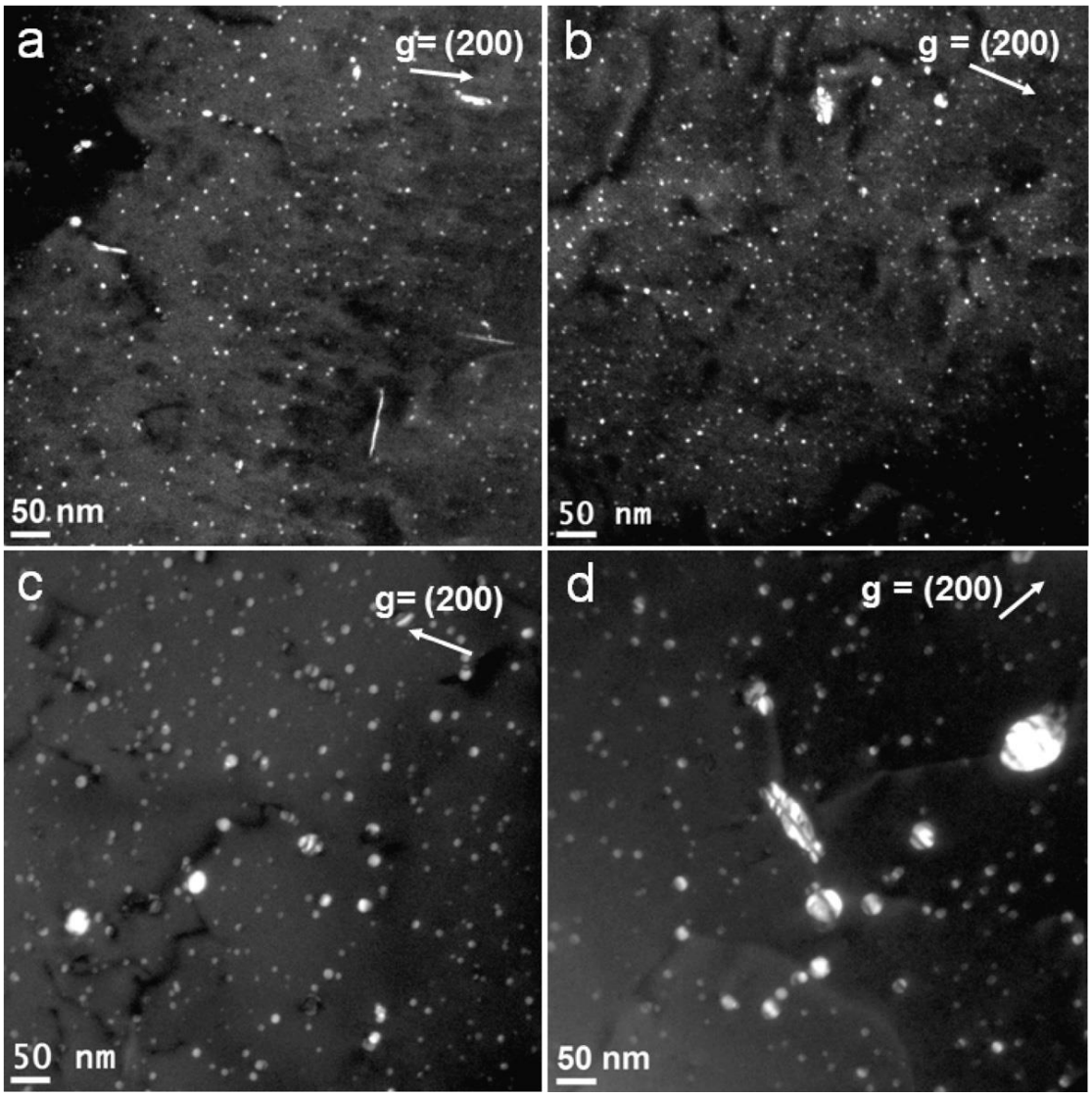

Fig. 2.16 TEM dark-field images showing the $Al_3(Sc,Zr)$ precipitates in an Al-B_4C composite: (a) initial peak aging (350 ◦C/10 h), (b) 2000 h annealing at 300 ◦C, (c) 1000 h annealing at 350 ◦C and (d) 2000 h annealing at 350 ◦C.

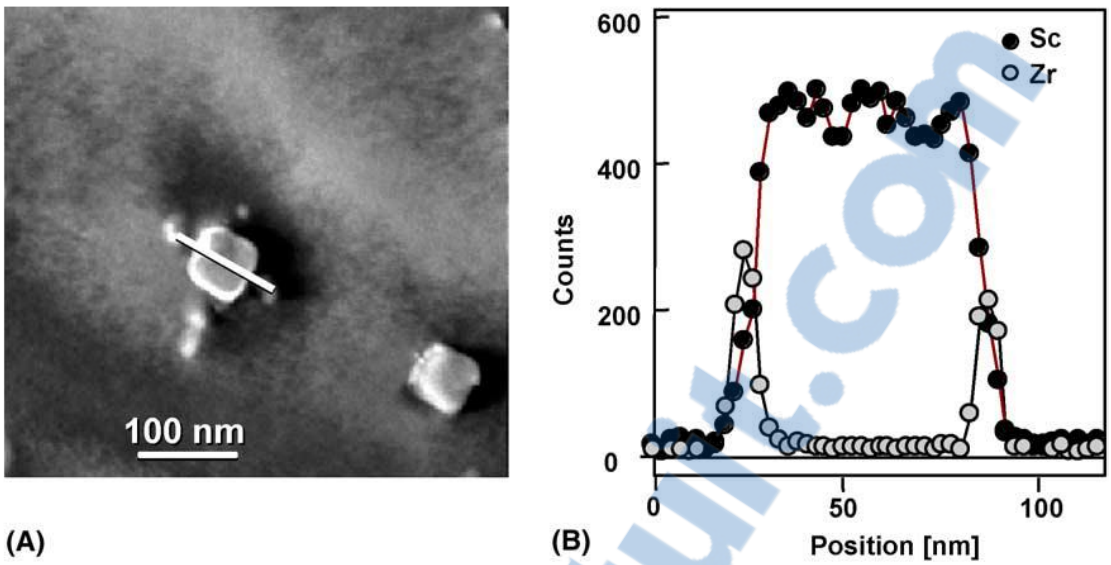

Fig. 2. 17 (a) Dark field image of a precipitate in ternary Al–Sc–Zr. The image was obtained close to the 001 zone axis. (b) Composition profile along the line indicated in (A) showing the number of EDS counts under the Sc Kα and Zr Kα peaks as a function of position

2.4 Mechanical properties at elevated temperature

2.4.1 Strengthening mechanisms for yield strength at elevated temperature

The yield strength of materials measured at elevated temperature is a very important property to evaluate the performance of materials for elevated-temperature applications. The yield strength contribution at elevated temperature could be divided into following three parts: aluminum matrix contribution, secondary precipitation particles strengthening contribution and solid solution strengthening contribution. According to previous literature, the yield strength of commercial pure aluminum alloys AA1100-O at 315°C is 14 MPa [57]. The precipitation of secondary strengthening phases can effectively slow down the movement of dislocations even at elevated temperature. However, the strengthening mechanism depends on the size of strengthening phases. According to literature[58], while the size of strengthening phase is less than ~8nm, the strengthening mechanism is dislocation climbing mechanism at 300 °C. On the other hand, Orowan bypass strengthening mechanism is the dominant strengthening

mechanism when the size is larger than 8nm. The theoretical calculation of yield stresses based on the model of dislocation climb and Orowan mechanisms is shown in Fig. 2.18.

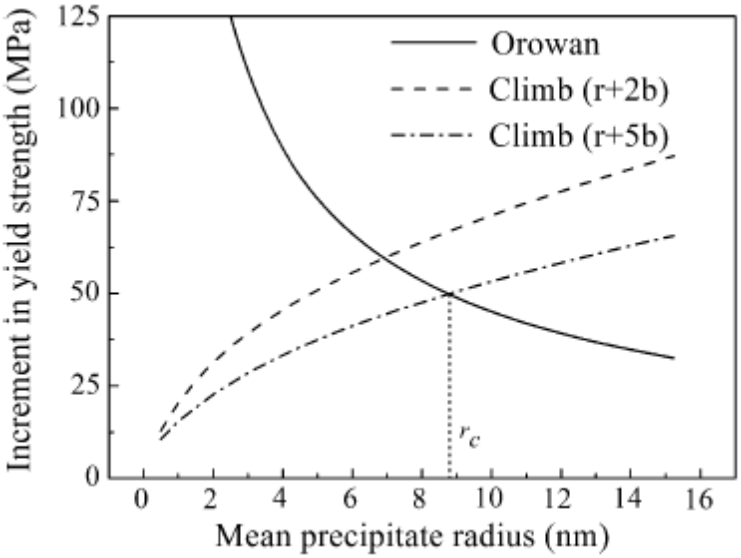

Fig. 2.18 Theoretical calculation of yield stresses based on the models of dislocation climb and Orowan mechanisms for an Al-B_4C composite with 0.24 vol.% Al_3Sc at 300°C as a function of precipitate radius.

2.4.1.1 Orowan strengthening mechanism

For the large size strengthening phases, Orowan proposed a mechanism illustrated in Fig. 2.19 [59]. The yield stress is determined by the shear stress required to bow a dislocation line between two particles separated by a distance L. Stage (a) shows a straight dislocation line approaching two particles. Stage (b) the line is beginning to bend. At stage (c), since the segments of dislocation that meet on the other side of the particles are of opposite sign, they can annihilate each other, leaving a dislocation loop around each particles [60]. Finally, at stage (e), the dislocations are free to move on.

The yield strength contribution of large size particles could be calculated according the following equation [61]:

$$\Delta\sigma_{Orowan} = \frac{0.4MG_m b\ln(\frac{2r}{b})}{\pi\sqrt{1-v_m}\lambda} \quad \text{Eq. 2.12}$$

$$\lambda = [(\frac{3\pi}{4f})^{\frac{1}{2}}\text{-}1.64]r \quad \text{Eq. 2.13}$$

Where M was Talor factor; G_m was shear modulus of Al matrix; b was Burgers vector, v was Poison ratio; λ was interspacing of dispersoids; r was average radius of dispersoids; f was volume fraction of dispersoids.

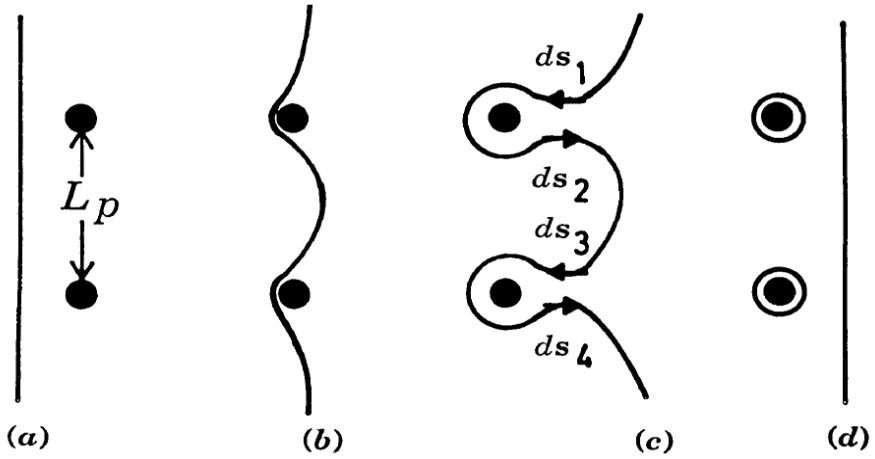

Fig. 2.19 A dislocation bypasses impenetrable particles, shown schematically. The external stress increases from left to right

2.4.1.2 Climb strengthening mechanism

According to Fig. 2.18, while the size of strengthening phases is smaller than 8 nm, at elevated temperature dislocations overcome obstacles by climbing mechanism [58]. For dislocation climb to occur, the diffusion of vacancies is very important. When a vacancy arrives at the place where the dislocation is stuck, it can help the dislocation climb out of its glide plane as shown in Fig. 2.20 [62]. Due to importance of diffusion rate for climbing, climbing is highly dependent on the temperature. At higher temperatures dislocations are more easily to move around obstacles. For this reason, many hardened materials become exponentially weaker at higher temperatures. The repulse stress for dislocation climbing is caused by the elastic

interaction between the dislocations and the precipitates [63]. The components of the elastic reaction are due to lattice mismatch and modulus mismatch [62]. Therefore, the dislocation climbing mechanism (σ_{Climb}) consisted two parts: modulus mismatch strengthening (σ_{MMC}) and lattice mismatch strengthening (σ_{LMC}). The equations were as following:

$$\Delta\sigma_{Climb} = \Delta\sigma_{MMC}+\Delta\sigma_{LMC} \quad \text{Eq. 2.14}$$

$$\Delta\sigma_{MMC} = \frac{MF^{\frac{3}{2}}}{\left(\frac{G_m b^2 2\pi}{3f}\right)^{\frac{1}{2}} br} \quad \text{Eq. 2.15}$$

$$\Delta\sigma_{LMC} = \chi M(\varepsilon G_m)^{\frac{3}{2}}\sqrt{\frac{2fbr}{G_m b^2}} \quad \text{Eq. 2.16}$$

Where, χ=2.6 [58, 64] was a constant, ε [58, 65]was the constrained strain, G_m=21.1GPa [58] was shear modulus of Al matrix, M=3.06 [58] was mean matrix orientation factor, b=0.288nm [58] was Burgers vector, r was average radius of precipitates, f was volume fraction of precipitates, F [58] was force on the dislocations.

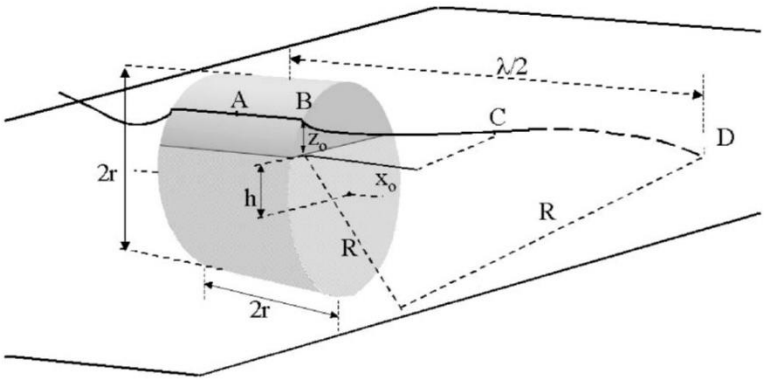

Fig. 2.20 Geometry of general climb model, showing an edge dislocation with segment CD in the glide plane and segment AC climbing over a particle

2.4.1.3 Solid solution strengthening mechanism

When solute atoms are introduced, local stress fields are formed that interact with those of the dislocations, slow their motion and causing an increase in the yield stress of the material, which means an increase in strength of the material. This is the solid solution strengthening [66]. There are two types of solid solutions as shown in Fig. 2.21. If the solute and solvent atoms are roughly similar in size, the solute atoms will occupy lattice points in the crystal lattice of the solvent atoms. This is called substitutional solid solution. If the solute atoms are much smaller than the solvent atoms, they occupy interstitial positions in the solvent lattice. This is called interstitial solid solution [67]. The strengthening contribution of the solid solution of solute elements could be calculated according to the equation below [27, 28]:

$$\sigma_{SS} = HC^{\alpha} \qquad \text{Eq. 2.17}$$

Where C was concentration of solute atoms, H and α are constant.

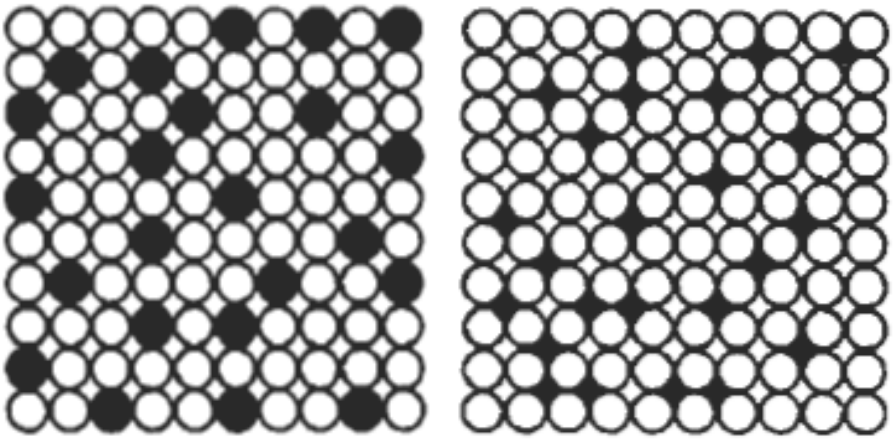

Fig. 2.21 Schematic models of solid solutions: substitutional solid solution and interstitial solid solution [68]

2.4.2 Creep phenomenon and mechanisms at elevated temperature

2.4.2.1 Creep phenomenon

Creep is a permanent deformation of materials under constant load and at constant temperature. It can occur as a result of long-term exposure to high levels of stress that are still below the yield strength of the material [69].

Generally, there are three different regions of tensile creep as shown in Fig. 2.22. The strain rate of the primary creep region is very high due to the material elastically and plastically responds to the applied load. While the deformation keeps increasing, the material is strengthened by work hardening, which leads to the decrease of the creep rate. As the deformation continues, primary creep stage gradually transits into the secondary creep stage. This stage is also called the steady-state creep. The creep rate almost does not change with time under a constant load. This is a result of the balance between recovery and hardening. The secondary creep region dominates most of the time of the test. Therefore, the secondary creep rate is one of the most important design parameters derived from the creep curve for the design of components. As creep continuing, the secondary creep changes into the third stage (tertiary creep).Tertiary creep only occurs in tensile creep test. Continuous deformation produces voids or internal cracks which decrease the cross-section and increase the stress. As a result, a neck occurs at tertiary stage of the creep, which ends up the fracture of the materials (Fig. 2.22). The tertiary stage creep possesses a much higher creep rate.

However, in compression creep curves, there is no such necking as occurred in tensile creep tests, due to the geometric effect that the sample cross-section will get larger with increased strain. Thus, the steady-state creep stage dominated during compression creep. As shown in Fig. 2.22 (dotted lines), the compressive creep curves can be generally divided into two different stages, and no tertiary creep can be observed.

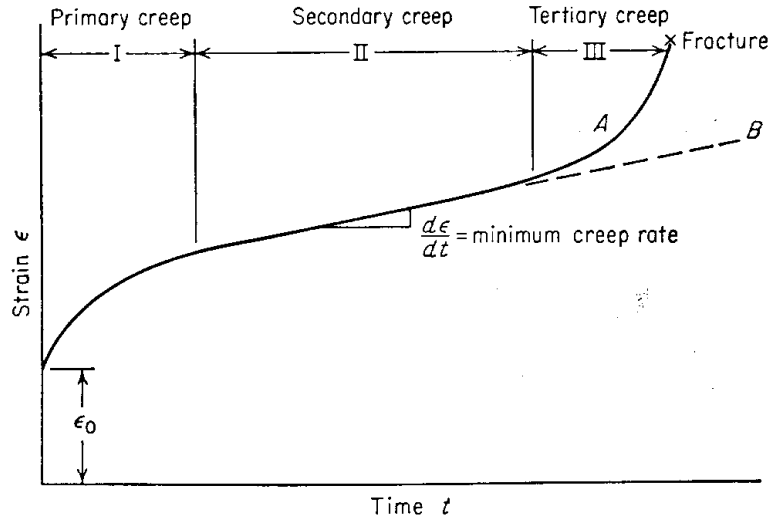

Fig. 2.22 Typical creep curve showing the three steps of creep [70]. The dotted line shown in the figure is for the compression creep curves

2.4.2.2 Creep mechanism

Creep mechanism is highly dependent on the applied temperature and stress. Weertman Ashby[71] plots creep deformation mechanism map according to the temperature and stress as shown in Fig. 2.23. The creep mechanism is categorized into four types: dislocation glide creep, dislocation creep, Coble creep, Nabarro-Herring creep.

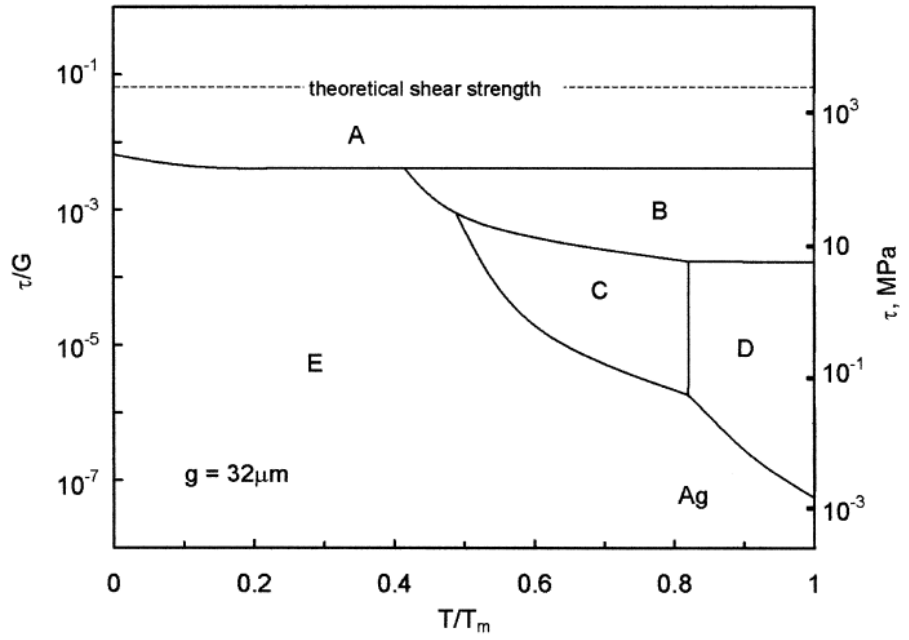

Fig. 2.23 Ashby deformation map of silver. A – Dislocation glide creep, B – Dislocation creep, C – Coble creep, D – Nabarro-Herring creep, E – Elastic deformation

(A) Dislocation glide creep

Creep resulting from a dislocation glide mechanism occurs at high stress levels [72]. Creep is controlled by the movement of dislocation. Dislocation glide creep has a strong dependence on the applied stress and the intrinsic activation energy, but no grain size dependence. The creep rate depends on the obstacles which slow down the movement of dislocations such as precipitates, dispersoids, solute atoms and other dislocations.

(B) Dislocation creep

Dislocation creep tends to occur by dislocation glide and climb aided by vacancy diffusion (when an obstacle is to be overcome); this is called dislocation creep [73]. This mechanism should not be confused with Harper-Dorn creep[74], which relies exclusively on dislocation climb. At elevated temperature, if a dislocation is stopped by obstacles, climb may permit it to pass the obstacles. Dislocation climb requires diffusion of vacancies to finish the climbing process. Therefore, the diffusion rate is very important for this creep mechanism.

(C) Nabarro–Herring creep

Nabarro–Herring creep is a form of diffusion creep [75]. It involves the diffusion of vacancies inside the grain. The vacancies move in such a way as to produce an increase in length of the grain along the direction of applied stress. Hence, the vacancies move from the top and bottom region to the lateral regions of the grain [76]. Nabarro-Herring creep dominates at high temperatures and low stresses. Nabarro–Herring creep has a weak stress dependence and a moderate grain size dependence. Nabarro–Herring creep is strongly temperature dependent.

(D) Coble creep

In 1963, Coble [77] proposed a mechanism by which creep was instead controlled by grain-boundary diffusion. He suggested that, at lower temperatures ($T<0.7\ Tm$), the contribution of grain-boundary diffusion is larger than that of self-diffusion through the grains.

Thus, diffusion of vacancies along grain boundaries controls creep. The strain-rate suggested by Coble creep is strongly size dependence [78].

2.4.2.3 Methods to improve creep resistance

The creep resistance of materials could be improved by the following methods:

1. Creep resistance is greater in a matrix of low stacking fault energy, because the dislocations are dissociated, and thus find it more difficult to cross-slip and to climb, in order to avoid obstacles. The stacking fault energy of a pure metal can be lowered by solute additions. For this purpose, solutes of high valence are best because they more readily increase the electron/atom ration, and thus decrease stacking fault energy[79].
2. Solid solution hardening is a useful contribution. This is best achieved by use of solutes differing markedly in atom size and valence from the parent metal [79].
3. Long range order in solid solutions provides a further contribution to the creep strength of solid solutions, because the super-lattice dislocations are paired to preserve order across the slip plane, and are thus similar to extend dislocations [79].
4. Precipitates are essential to increase further the creep strength of a solid solution, and a theory provides an estimate of the critical spacing if dispersion for optimum strength in terms of that just small enough to prevent dislocations bowing around the particles [79].
5. Use of precipitates in association with crystal defects. Some precipitates form more readily than others on dislocations, and thus are important source of strengthening, both at low and elevated temperatures. Precipitates which form during creep are particularly useful if they nucleate on dislocations. Nucleation in association with stacking fault is another form of strengthening. Precipitation at grain boundary is useful in reducing grain boundary sliding, but in many cases this leads to early cavity formation and premature intergranular cracking [79].
6. Dispersoids are effective for improving the creep resistance as well. Because they are usually thermally stable at elevated temperature. The coarsening rate is lower than precipitates particles.

7. The creep resistance at elevated and high temperature also benefit from larger grain size. For high temperature diffusion creep with low load, the creep resistance is strongly grain size dependent.

References

1. H.-W. Huang, B.-L. Ou, Evolution of precipitation during different homogenization treatments in a 3003 aluminum alloy, Materials & Design. 30 (2009) 2685-2692. Doi: http://dx.doi.org/10.1016/j.matdes.2008.10.012.
2. A. R. Yazdzad, T. Shahrabi, M. G. Hosseini, Inhibition of 3003 aluminum alloy corrosion by propargyl alcohol and tartrate ion and their synergistic effects in 0.5% NaCl solution, Materials Chemistry and Physics. 109 (2008) 199-205. Doi: http://dx.doi.org/10.1016/j.matchemphys.2007.11.012.
3. I. J. Polmear, M. J. Couper, Design and development of an experimental wrought aluminum alloy for use at elevated temperatures, Metallurgical Transactions A. 19 (1988) 1027-1035. Doi: http://dx.doi.org/10.1007/BF02628387.
4. Y. Zhou, Z. Liu, S. Bai, P. Ying, L. Lin, Effect of Ag additions on the lengthening rate of Ω plates and formation of σ phase in Al-Cu-Mg alloys during thermal exposure, Materials Characterization. 123 (2017) 1-8. Doi: http://dx.doi.org/10.1016/j.matchar.2016.11.008.
5. Y. J. Li, A. M. F. Muggerud, A. Olsen, T. Furu, Precipitation of partially coherent α-Al(Mn,Fe)Si dispersoids and their strengthening effect in AA 3003 alloy, Acta Materialia. 60 (2012) 1004-1014. Doi: http://dx.doi.org/10.1016/j.actamat.2011.11.003.
6. A. M. F. Muggerud, E. A. Mørtsell, Y. Li, R. Holmestad, Dispersoid strengthening in AA3xxx alloys with varying Mn and Si content during annealing at low temperatures, Materials Science and Engineering: A. 567 (2013) 21-28. Doi: http://dx.doi.org/10.1016/j.msea.2013.01.004.

7. K. Liu, X. G. Chen, Development of Al–Mn–Mg 3004 alloy for applications at elevated temperature via dispersoid strengthening, Materials & Design. 84 (2015) 340-350. Doi: http://dx.doi.org/10.1016/j.matdes.2015.06.140.

8. K. Liu, X.-G. Chen, Evolution of Intermetallics, Dispersoids, and Elevated Temperature Properties at Various Fe Contents in Al-Mn-Mg 3004 Alloys, Metallurgical and Materials Transactions B. 47 (2016) 3291-3300. Doi: http://dx.doi.org/10.1007/s11663-015-0564-y.

9. K. Liu, H. Ma, X. G. Chen, Enhanced elevated-temperature properties via Mo addition in Al-Mn-Mg 3004 alloy, Journal of Alloys and Compounds. 694 (2017) 354-365. Doi: http://dx.doi.org/10.1016/j.jallcom.2016.10.005.

10. R. Nunes, J. H. Adams, etc., ASM Handbook Volume 2: Properties and Selection: Nonferrous Alloys and Special-Purpose Materials. (ASM International, 1990), Vol. 2, pp. 330.

11. Y. J. Li, L. Arnberg, Quantitative study on the precipitation behavior of dispersoids in DC-cast AA3003 alloy during heating and homogenization, Acta Materialia. 51 (2003) 3415-3428. Doi: http://dx.doi.org/10.1016/S1359-6454(03)00160-5.

12. Y. J. Li, L. Arnberg, Evolution of eutectic intermetallic particles in DC-cast AA3003 alloy during heating and homogenization, Materials Science and Engineering: A. 347 (2003) 130-135. Doi: http://dx.doi.org/10.1016/S0921-5093(02)00555-5.

13. Q. Du, W. J. Poole, M. A. Wells, N. C. Parson, Microstructure evolution during homogenization of Al–Mn–Fe–Si alloys: Modeling and experimental results, Acta Materialia. 61 (2013) 4961-4973. Doi: http://dx.doi.org/10.1016/j.actamat.2013.04.050.

14. Q. Zhao, B. Holmedal, Y. Li, Influence of dispersoids on microstructure evolution and work hardening of aluminium alloys during tension and cold rolling, Philosophical Magazine. 93 (2013) 2995-3011. Doi: http://dx.doi.org/10.1080/14786435.2013.794315.

15. A. M. F. Muggerud, Y. Li, R. Holmestad, Composition and orientation relationships of constituent particles in 3xxx aluminum alloys, Philosophical Magazine. 94 (2014) 556-568. Doi: http://dx.doi.org/10.1080/14786435.2013.857796.

16. N. Sun, B. R. Patterson, J. P. Suni, E. A. Simielli, H. Weiland, L. F. Allard, Microstructural evolution in twin roll cast AA3105 during homogenization, Materials Science and Engineering: A. 416 (2006) 232-239. Doi: http://dx.doi.org/10.1016/j.msea.2005.10.018.

17. M. Dehmas, E. Aeby-Gautier, P. Archambault, M. Serrière, Interaction Between Eutectic Intermetallic Particles and Dispersoids in the 3003 Aluminum Alloy During Homogenization Treatments, Metallurgical and Materials Transactions A. 44 (2013) 1059-1073. Doi: http://dx.doi.org/10.1007/s11661-012-1473-1.

18. Z. Li, Z. Zhang, X. G. Chen, Effect of magnesium on dispersoid strengthening of Al—Mn—Mg—Si (3xxx) alloys, Transactions of Nonferrous Metals Society of China. 26 (2016) 2793-2799. Doi: http://dx.doi.org/10.1016/S1003-6326(16)64407-2.

19. S. P. Chen, N. C. W. Kuijpers, S. van der Zwaag, Effect of microsegregation and dislocations on the nucleation kinetics of precipitation in aluminium alloy AA3003, Materials Science and Engineering: A. 341 (2003) 296-306. Doi: http://dx.doi.org/10.1016/S0921-5093(02)00245-9.

20. M. Dehmas, P. Weisbecker, G. Geandier, P. Archambault, E. Aeby-Gautier, Experimental study of phase transformations in 3003 aluminium alloys during heating by in situ high energy X-ray synchrotron radiation, Journal of Alloys and Compounds. 400 (2005) 116-124. Doi: http://dx.doi.org/10.1016/j.jallcom.2005.03.062.

21. M. Warmuzek, G. Mrówka, J. Sieniawski, Influence of the heat treatment on the precipitation of the intermetallic phases in commercial AlMn1FeSi alloy, Journal of Materials Processing Technology. 157–158 (2004) 624-632. Doi: http://dx.doi.org/10.1016/j.jmatprotec.2004.07.125.

22. D. T. L. Alexander, A. L. Greer, Solid-state intermetallic phase tranformations in 3XXX aluminium alloys, Acta Materialia. 50 (2002) 2571-2583. Doi: http://dx.doi.org/10.1016/S1359-6454(02)00085-X.

23. H. D. Merchant, J. G. Morris, D. S. Hodgson, Characterization of intermetallics in aluminum alloy 3004, Materials Characterization. 25 (1990) 339-373. Doi: http://dx.doi.org/10.1016/1044-5803(90)90062-O.

24. A. M. F. Muggerud, J. C. Walmsley, R. Holmestad, Y. Li, Combining HAADF STEM tomography and electron diffraction for studies of α-Al(Fe,Mn)Si dispersoids in 3xxx aluminium alloys, Philosophical Magazine. 95 (2015) 744-758. Doi: http://dx.doi.org/10.1080/14786435.2015.1006294.

25. George E. Totten, D. S. MacKenzie, Handbook of Aluminum Volume 1: Physical Metallurgy and Processes. (Marcel Dekker, New York, 2003), Vol. 1, pp. 159.

26. George E. Totten, D. S. MacKenzie, Handbook of Aluminum Volume 1: Physical Metallurgy and Processes. (Marcel Dekker, New York, 2003), Vol. 1, pp. 164.

27. E. L. Huskins, B. Cao, K. T. Ramesh, Strengthening mechanisms in an Al–Mg alloy, Materials Science and Engineering: A. 527 (2010) 1292-1298. Doi: http://dx.doi.org/10.1016/j.msea.2009.11.056.

28. Ø. Ryen, B. Holmedal, O. Nijs, E. Nes, E. Sjölander, H.-E. Ekström, Strengthening mechanisms in solid solution aluminum alloys, Metallurgical and Materials Transactions A. 37 (2006) 1999-2006. Doi: http://dx.doi.org/10.1007/s11661-006-0142-7.

29. G. A. Edwards, K. Stiller, G. L. Dunlop, M. J. Couper, The precipitation sequence in Al–Mg–Si alloys, Acta Materialia. 46 (1998) 3893-3904. Doi: http://dx.doi.org/10.1016/S1359-6454(98)00059-7.

30. C. D. Marioara, S. J. Andersen, H. W. Zandbergen, R. Holmestad, The influence of alloy composition on precipitates of the Al-Mg-Si system, Metallurgical and Materials Transactions A. 36 (2005) 691-702. Doi: http://dx.doi.org/10.1007/s11661-005-0185-1.

31. S. J. Andersen, H. W. Zandbergen, J. Jansen, C. TrÆholt, U. Tundal, O. Reiso, The crystal structure of the β″ phase in Al–Mg–Si alloys, Acta Materialia. 46 (1998) 3283-3298. Doi: http://dx.doi.org/10.1016/S1359-6454(97)00493-X.

32. R. Vissers, M. A. van Huis, J. Jansen, H. W. Zandbergen, C. D. Marioara, S. J. Andersen, The crystal structure of the β′ phase in Al–Mg–Si alloys, Acta Materialia. 55 (2007) 3815-3823. Doi: http://dx.doi.org/10.1016/j.actamat.2007.02.032.

33. M. Murayama, K. Hono, Pre-precipitate clusters and precipitation processes in Al–Mg–Si alloys, Acta Materialia. 47 (1999) 1537-1548. Doi: http://doi.org/10.1016/S1359-6454(99)00033-6.

34. C. S. Tsao, C. Y. Chen, U. S. Jeng, T. Y. Kuo, Precipitation kinetics and transformation of metastable phases in Al–Mg–Si alloys, Acta Materialia. 54 (2006) 4621-4631. Doi: http://doi.org/10.1016/j.actamat.2006.06.005.

35. M. H. Jacobs, The structure of the metastable precipitates formed during ageing of an Al-Mg-Si alloy, Philosophical Magazine. 26 (1972) 1-13. Doi: http://dx.doi.org/10.1080/14786437208221015.

36. X. Wang, S. Esmaeili, D. J. Lloyd, The sequence of precipitation in the Al-Mg-Si-Cu alloy AA6111, Metallurgical and Materials Transactions A. 37 (2006) 2691-2699. Doi: http://dx.doi.org/10.1007/BF02586103.

37. H. Hirasawa, Precipitation process of Al-Mn and Al-Cr supersaturated solid solution in presence of age hardening phases, Scripta Metallurgica. 9 (1975) 955-958. Doi: http://dx.doi.org/10.1016/0036-9748(75)90551-7.

38. L. Lodgaard, N. Ryum, Precipitation of dispersoids containing Mn and/or Cr in Al–Mg–Si alloys, Materials Science and Engineering: A. 283 (2000) 144-152. Doi: http://dx.doi.org/10.1016/S0921-5093(00)00734-6.

39. L. Bourgeois, C. Dwyer, M. Weyland, J.-F. Nie, B. C. Muddle, Structure and energetics of the coherent interface between the θ′ precipitate phase and aluminium in Al–Cu, Acta Materialia. 59 (2011) 7043-7050. Doi: http://doi.org/10.1016/j.actamat.2011.07.059.

40. T. Marlaud, A. Deschamps, F. Bley, W. Lefebvre, B. Baroux, Influence of alloy composition and heat treatment on precipitate composition in Al–Zn–Mg–Cu alloys, Acta Materialia. 58 (2010) 248-260. Doi: http://dx.doi.org/10.1016/j.actamat.2009.09.003.

41. C. Marioara, S. Andersen, T. Stene, H. Hasting, J. Walmsley, A. Van Helvoort, R. Holmestad, The effect of Cu on precipitation in Al–Mg–Si alloys, Philosophical Magazine. 87 (2007) 3385-3413. Doi: http://dx.doi.org/10.1080/14786430701287377.

42. C. D. Marioara, S. J. Andersen, J. Røyset, O. Reiso, S. Gulbrandsen-Dahl, T.-E. Nicolaisen, I.-E. Opheim, J. F. Helgaker, R. Holmestad, Improving Thermal Stability in Cu-Containing Al-Mg-Si Alloys by Precipitate Optimization, Metallurgical and Materials Transactions A. 45 (2014) 2938-2949. Doi: http://dx.doi.org/10.1007/s11661-014-2250-0.

43. J. Man, L. Jing, S. G. Jie, The effects of Cu addition on the microstructure and thermal stability of an Al–Mg–Si alloy, Journal of Alloys and Compounds. 437 (2007) 146-150. Doi: http://doi.org/10.1016/j.jallcom.2006.07.113.

44. Y.-g. Liao, X.-q. Han, M.-x. Zeng, M. Jin, Influence of Cu on microstructure and tensile properties of 7XXX series aluminum alloy, Materials & Design. 66 (2015) 581-586. Doi: http://dx.doi.org/10.1016/j.matdes.2014.05.003.

45. K. Matsuda, D. Teguri, Y. Uetani, T. Sato, S. Ikeno, Cu-segregation at the Q′/α-Al interface in Al–Mg–Si–Cu alloy, Scripta Materialia. 47 (2002) 833-837. Doi: http://doi.org/10.1016/S1359-6462(02)00325-1.

46. M. Fiawoo, X. Gao, L. Bourgeois, N. Parson, X. Q. Zhang, M. Couper, J. F. Nie, Formation of multiple orientation relationships of Q precipitates in Al–Mg–Si–Cu alloys, Scripta Materialia. 88 (2014) 53-56. Doi: http://doi.org/10.1016/j.scriptamat.2014.05.013.

47. K. Matsuda, D. Teguri, T. Sato, Y. Uetani, S. Ikeno, Cu Segregation around Metastable Phase in Al-Mg-Si Alloy with Cu, MATERIALS TRANSACTIONS. 48 (2007) 967-974. Doi: http://doi.org/10.2320/matertrans.48.967.

48. E. A. Marquis, D. N. Seidman, Coarsening kinetics of nanoscale Al3Sc precipitates in an Al–Mg–Sc alloy, Acta Materialia. 53 (2005) 4259-4268. Doi: https://doi.org/10.1016/j.actamat.2005.05.025.

49. E. A. Marquis, D. N. Seidman, Nanoscale structural evolution of Al3Sc precipitates in Al(Sc) alloys, Acta Materialia. 49 (2001) 1909-1919. Doi: https://doi.org/10.1016/S1359-6454(01)00116-1.

50. G. M. Novotny, A. J. Ardell, Precipitation of Al3Sc in binary Al–Sc alloys, Materials Science and Engineering: A. 318 (2001) 144-154. Doi: https://doi.org/10.1016/S0921-5093(01)01326-0.

51. Y. Deng, Z. Yin, K. Zhao, J. Duan, Z. He, Effects of Sc and Zr microalloying additions on the microstructure and mechanical properties of new Al–Zn–Mg alloys, Journal of Alloys and Compounds. 530 (2012) 71-80. Doi: https://doi.org/10.1016/j.jallcom.2012.03.108.

52. C. Fuller, J. Murray, D. Seidman, Temporal evolution of the nanostructure of Al(Sc,Zr) alloys: Part I – Chemical compositions of Al(ScZr) precipitates, Acta Materialia. 53 (2005) 5401-5413. Doi: https://doi.org/10.1016/j.actamat.2005.08.016

53. C. Fuller, D. Seidman, Temporal evolution of the nanostructure of Al(Sc,Zr) alloys: Part II-coarsening of Al(ScZr) precipitates, Acta Materialia. 53 (2005) 5415-5428. Doi: https://doi.org/10.1016/j.actamat.2005.08.015

54. J. Lai, Z. Zhang, X. G. Chen, The thermal stability of mechanical properties of Al–B4C composites alloyed with Sc and Zr at elevated temperatures, Materials Science and Engineering: A. 532 (2012) 462-470. Doi: https://doi.org/10.1016/j.msea.2011.11.013.

55. J. Lai, Z. Zhang, X. G. Chen, Precipitation strengthening of Al–B4C metal matrix composites alloyed with Sc and Zr, Journal of Alloys and Compounds. 552 (2013) 227-235. Doi: http://doi.org/10.1016/j.jallcom.2012.10.096.

56. A. Tolley, V. Radmilovic, U. Dahmen, Segregation in Al3(Sc,Zr) precipitates in Al–Sc–Zr alloys, Scripta Materialia. 52 (2005) 621-625. Doi: https://doi.org/10.1016/j.scriptamat.2004.11.021.

57. J. G. Kaufman, Properties of Aluminum Alloys: Tensile, Creep, and Fatigue Data at High and Low Temperatures. (ASM international, 1999), pp. 9.

58. J. Qin, Z. Zhang, X.-G. Chen, Mechanical Properties and Strengthening Mechanisms of Al-15 Pct B4C Composites with Sc and Zr at Elevated Temperatures, Metallurgical and Materials Transactions A. 47 (2016) 4694-4708. Doi: http://dx.doi.org/10.1007/s11661-016-3606-4.

59. E. Nembach, Particle strengthening of metals and alloys. (John Wiley&Sons, 1996), pp. 236.

60. G. E. Dieter, Mechanical metallurgy. (McGraw Hill, 1986), pp. 218.

61. C. B. Fuller, D. N. Seidman, D. C. Dunand, Mechanical properties of Al(Sc,Zr) alloys at ambient and elevated temperatures, Acta Materialia. 51 (2003) 4803-4814. Doi: https://doi.org/10.1016/S1359-6454(03)00320-3.

62. E. A. Marquis, D. C. Dunand, Model for creep threshold stress in precipitation-strengthened alloys with coherent particles, Scripta Materialia. 47 (2002) 503-508. Doi: https://doi.org/10.1016/S1359-6462(02)00165-3.

63. R. A. Karnesky, L. Meng, D. C. Dunand, Strengthening mechanisms in aluminum containing coherent Al3Sc precipitates and incoherent Al2O3 dispersoids, Acta Materialia. 55 (2007) 1299-1308. Doi: http://dx.doi.org/10.1016/j.actamat.2006.10.004.

64. A. J. Ardell, Precipitation hardening, Metallurgical Transactions A. 16 (1985) 2131-2165. Doi: http://dx.doi.org/10.1007/BF02670416.

65. D. N. Seidman, E. A. Marquis, D. C. Dunand, Precipitation strengthening at ambient and elevated temperatures of heat-treatable Al(Sc) alloys, Acta Materialia. 50 (2002) 4021-4035. Doi: http://dx.doi.org/10.1016/S1359-6454(02)00201-X.

66. George E. Totten, D. S. MacKenzie, Handbook of Aluminum Volume 1: Physical Metallurgy and Processes. (Marcel Dekker, New York, 2003), Vol. 1, pp. 90.

67. G. E. Dieter, Mechanical metallurgy. (McGraw Hill, 1986), pp. 203.

68. R. W.Cahn, P. Haasen, Phyical metallurgy. (North-Holland, 1996), Vol. 1, pp. 140.

69. M. Kassner, Fundamentals of creep in metals and alloys. (Elsevier Science 2008), pp. 3.

70. G. E. Dieter, Mechanical metallurgy. (McGraw Hill, 1986), pp. 439.

71. M. F. Ashby, A first report on deformation-mechanism maps, Acta Metallurgica. 20 (1972) 887-897. Doi: http://dx.doi.org/10.1016/0001-6160(72)90082-X.

72. G. E. Dieter, Mechanical metallurgy. (McGraw Hill, 1986), pp. 446.

73. Mac Meyes, K. Chawla, Mechanilca behavior of materials. (Combridege University Press, 2008), pp. 670.

74. J. Harper, J. E. Dorn, Viscous creep of aluminum near its melting temperature, Acta Metallurgica. 5 (1957) 654-665. Doi: http://dx.doi.org/10.1016/0001-6160(57)90112-8.

75. C. Herring, Diffusional Viscosity of a Polycrystalline Solid, Journal of Applied Physics. 21 (1950) 437-445. Doi: http://aip.scitation.org/doi/abs/10.1063/1.1699681.

76. Mac Meyes, K. Chawla, Mechanilca behavior of materials. (Combridege University Press, 2008), pp. 667.

77. R. L. Coble, A Model for Boundary Diffusion Controlled Creep in Polycrystalline Materials, Journal of Applied Physics. 34 (1963) 1679-1682. Doi: http://aip.scitation.org/doi/abs/10.1063/1.1702656.

78. M. Kassner, Fundamentals of creep in metals and alloys. (Elsevier Science 2008), pp. 92.

79. R.W.K.Honeycombe, The plastic deforamtion of metals. (EDWARD ARNOLD, 1984), pp. 392.

Chapter 3 Experimental

3.1 Alloys preparation and compositions

The alloys used for each part of the study was separated designed. These alloys were prepared with pure Al (99.7wt.%), pure Mg (99.9wt.%), Al-25wt.%Mn, Al-25wt.%Fe, Al-50wt.%Si, Al-50wt.%Cu, Al-2%wt.Sc and Al-15wt.%Zr master alloys. For each batch, about 3kg materials were melted by electrical resistance furnace. The melt was kept at 750 ℃ for 30 mins, degassed for 15 mins and poured into a preheated (250 ℃) permanent steel mold. The dimensions of the cast ingots were 30mm*40mm*80 mm.

3.1.1 The effect of Mg and Si

The following ten compositions are designed for this part of the study, as shown in Table 3.1. In order to separately investigate the effect of Mg and Si on the mechanical properties and microstructure of 3xxx alloys, these ten alloys were divided into two groups: DM series and DS series. All the DM series alloys contained 1.2%Mn, 0.6%Fe and 0.25%Si, the content of Mg changed from 0% to 2.0%. All the DS series alloys contained 1.2%Mn, 0.6%Fe and 1.0%Mg, the content of Si changed from 0% to 1.0%.

Table 3.1 Chemical compositions of DM and DS series alloys

Alloy	Si	Fe	Mn	Mg	Al
DM0	0.25	0.60	1.20	**0**	Bal.
DM50	0.25	0.56	1.24	**0.47**	Bal.
DM100	0.25	0.60	1.24	**1.00**	Bal.
DM150	0.26	0.60	1.24	**1.50**	Bal.
DM200	0.27	0.60	1.24	**2.02**	Bal.
DS0	**0.03**	0.56	1.25	1.02	Bal.
DS25	**0.23**	0.53	1.25	1.05	Bal.

DS45	**0.42**	0.57	1.26	1.07	Bal.
DS70	**0.70**	0.54	1.25	1.01	Bal.
DS100	**0.97**	0.56	1.28	1.00	Bal.

3.1.2 The effect of metastable Mg_2Si and dislocations

Two experimental alloys were used in this part of the study, as shown in Table 3.2. They all contained 1.2%Mn, 0.6%Fe and 0.25%Si. The only difference was the content of Mg. The base alloy contained 0%Mg while M1 alloy contained 1.0%Mg.

Table 3.2 Chemical composition of the experimental alloys

Alloy	Si	Fe	Mn	Mg	Al
Base	0.25	0.60	1.25	**0**	Bal.
M1	0.25	0.60	1.24	**1.00**	Bal.

3.1.3 The effect of Sc and Zr

The following three alloys were designed to study the effect of Sc and Zr, as shown in Table 3.3. All the SZ series alloys contained 1.2%Mn, 0.6%Fe, 0.25%Si and 1.0%Mg. The content of Sc and Zr were changed from to investigate the effect on microstructure and mechanical properties. SZ0 alloy contained 0%Sc and 0%Zr, SZ15 alloy contained 0.18%Sc and 0.18%Zr and SZ30 alloy contained 0.29%Sc and 0.17%Zr.

Table 3.3 Composition of SZ series alloys

Alloy	Zr	Sc	Si	Fe	Mn	Mg	Al
SZ0	**0**	**0**	0.60	0.60	1.20	1.00	Bal
SZ15	**0.18**	**0.18**	0.25	0.59	1.18	1.04	Bal
SZ30	**0.17**	**0.29**	0.25	0.57	1.19	1.01	Bal

3.1.4 The effect of Cu

The following four alloys were designed to study the effect of Cu, as shown in Table 3.4. All the DU series alloys contained 1.2%Mn, 0.6%Fe, 0.25%Si and 1.0%Mg. And the content of Cu changed from 0% to 1.2%.

Table 3.4 Composition of DU series alloys

Alloy	Cu	Si	Fe	Mn	Mg	Al
DU0	**0**	0.25	0.60	1.20	1.00	Bal
DU35	**0.37**	0.27	0.60	1.24	1.03	Bal
DU75	**0.72**	0.26	0.60	1.24	0.99	Bal
DU120	**1.23**	0.25	0.60	1.24	1.04	Bal

3.2 Heat-treatment conditions

3.2.1 The effect of Mg and Si

The samples were heated from room temperature to 375 °C with a heating rate 5 °C per minute. The samples were holding at 375 °C for 2 h, 6 h, 12 h, 24 h and 48 h respectively, followed by water quench to room temperature.

Table 3.5 Heat-treatment conditions

Temperature	Holding time				
375℃	**2**	**6**	12	24	48

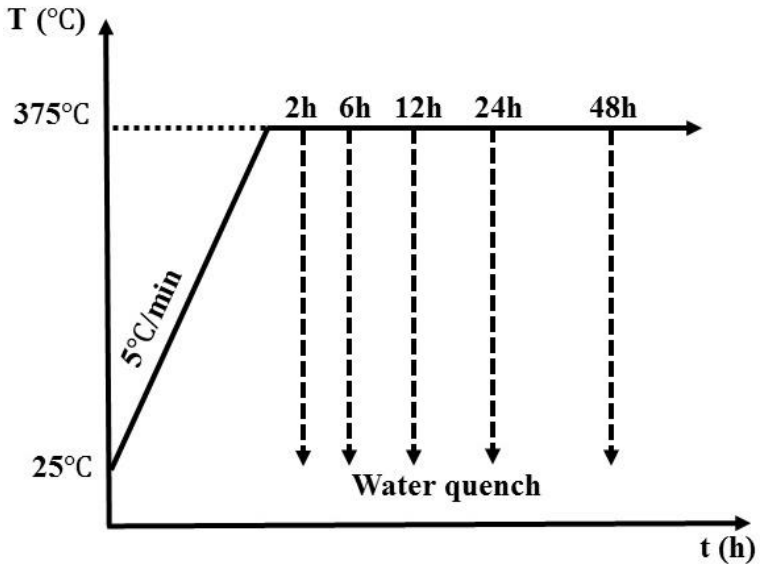

Fig. 3.1 The schematic diagram of heat treatment condition for DM series and DS series alloys

3.2.2 The effect of metastable Mg_2Si and dislocations

To examine the influence of metastable Mg_2Si and dislocation on dispersoid nucleation, the as-cast or deformed samples were heat-treated under different heat treatment programs. In the program A, the samples were heated with a heating rate of 5 ℃/min in an electrical resistant furnace from room temperature to various temperatures. When the sample temperature arrived at 275 °C, or 375 °C, samples were immediately taken out from the furnace, followed by water quench to room temperature. In the program B, the samples were heated with a rate of 5 ℃/min to 375 °C, and then the samples are held at 375 °C for various holding times, followed by water quench to room temperature. A schematic diagram of the heat treatment program A and B is shown in Fig. 3.2(a). The heat treatment program C is a two-step program. In this program, the samples were, at first, directly put in the furnace at 175 ºC or 250 ºC and then holding for 5 hours at 175 ºC or holding for 12 hours at 250 ºC, respectively, followed by water quench to room temperature. As the second step, the samples were directly put into a furnace at 375 ℃ holding for 24 hours followed by water quench to room temperature (see Fig. 3.2(b)).

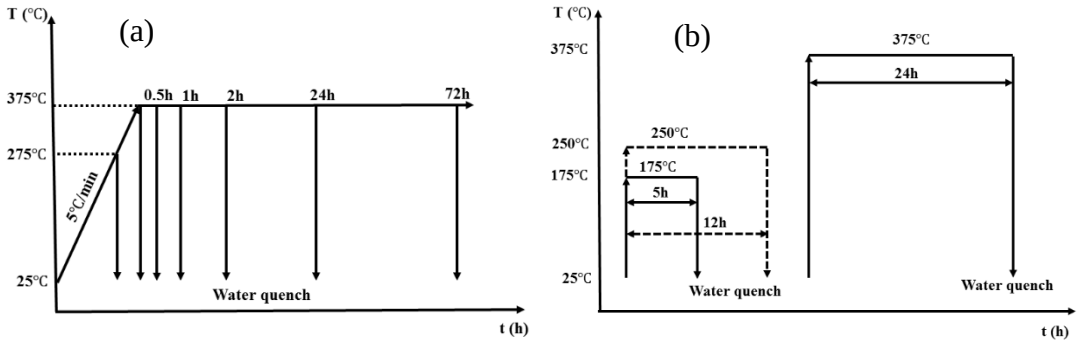

Fig. 3.2 the schematic diagram of the various heat treatment conditions: (a) program A and B, (b) program C.

3.2.3 The effect of Sc and Zr

The heat-treatment were conducted at 300 ℃ and 375 ℃ with a heating rate 5 ℃/min. The holding time was from 2h to 48h. After the heat-treatment, the samples were quenched into water of room temperature. The heat treatment conditions were shown in Table. 3.6 and Fig. 3.3.

Table 3.6 Heat-treatment conditions for DSZ series alloys

Temperature	**Holding hours**				
300℃	2	6	12	24	48
375℃	2	6	12	24	48

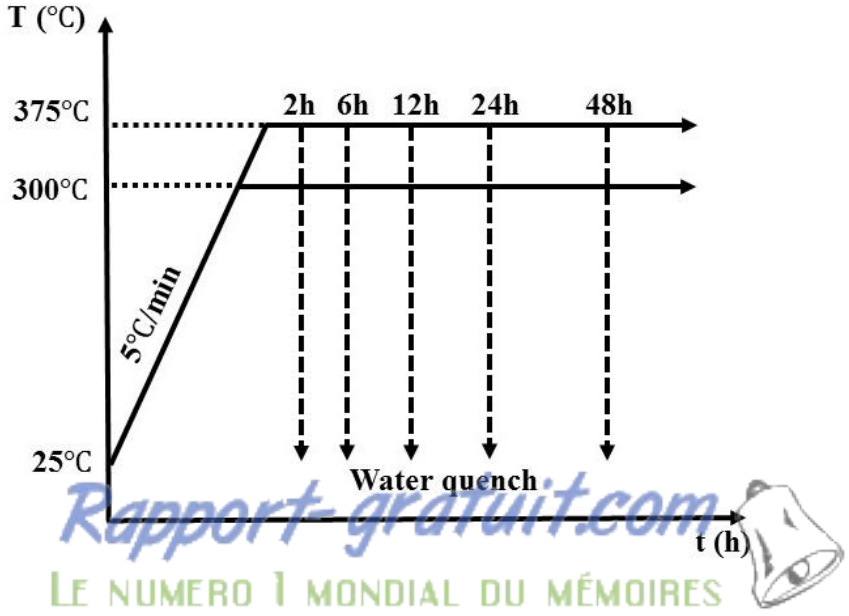

Fig. 3.3 The schematic diagram of heat treatment condition for SZ series alloys

3.2.4 The effect of Cu

Heat treatment were conducted at 375 ℃, 425 ℃ and 475 ℃ with a heating rate 5℃/min, and then held at this temperature for different holding time from 2 h to 48 h as shown in Table 3.6 and Fig. 3.3(a). After heat-treatment, the samples were quenched by water to room temperature. In order to study dispersoids nucleation process, another heat treatment as shown in Fig. 3.3(b) was conducted. The samples were heated from room temperature to 425 ℃ with 5℃/min heating rate. While the temperature reached 330 ℃ and 425 ℃, the samples were quenched directly into water to freeze the microstructure.

Table 3.7 Heat-treatment conditions for DU series alloys

Temperature	**Holding time**				
375℃	**2**	**6**	12	24	48
425℃	**2**	**6**	12	24	48
475℃	**2**	**6**	12	24	48

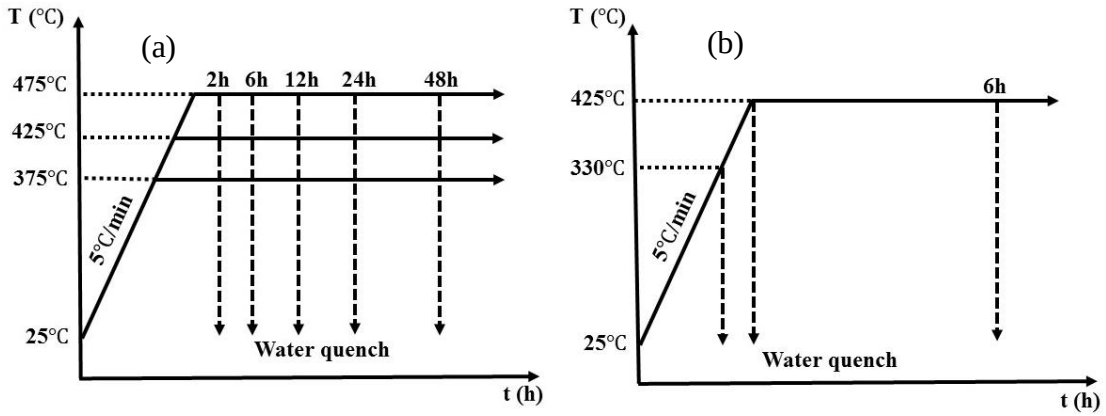

Fig. 3.4 The schematic diagram of the various heat treatment conditions: (a) heat treatment at 375 ℃, 425 ℃ and 475 ℃, (b) heat treatment for the study of dispersoids precipitation process

3.3 Mechanical properties

3.3.1 Microhardness

Vicker hardness was measured to evaluate the room-temperature properties. The tests were conducted by NG-1000 CCD micro-hardness test machine with a 200 g load and a 20 s dwelling time. A total of 10 measurements were performed to calculate the average hardness value for each sample. Polished samples were used for the test.

3.3.2 Electrical conductivity

Electrical conductivity was measured by Sigmascope SMP10 electrical conductivity test device at room temperature, at least 5 measurements was recorded for each sample using a unit MS/m.

3.3.3 Yield strength

Compression yield strength tests were conducted at room temperature (25 ℃) and elevated temperature (300 ℃) by Gleeble 3800 thermomechanical testing unit; strain rate was set to 0.001 s^{-1}. The samples were machined into cylinder with a 15mm length and 10mm diameter. The results were obtained from the average value of three repeated samples.

3.3.4 Creep

Creep tests were performed at 300 °C for 96 hours in compression condition with a load of 44 MPa, 52 MPa, 58 MPa and 66.5 MPa, each samples was repeated three times. The samples size was the same with Gleeble test samples.

3.4 Microstructure observation

Optical microscope was used to observe intermetallic particles and the distribution of dispersoids. Scanning electron microscope (SEM, JSM-6480LV) equipped with an energy-dispersive X-ray spectrometer (EDS) was used to identify the composition of intermetallic phases. In order to make the dispersoid free zone (DFZ) visible under optical microscope, the samples were etched by 0.5% HF for 25 seconds. Image analysis software (Clemex PE 4.0) were used to characterize the volume fraction of the dispersoid zone and DFZ from the etched samples. TEM foils were prepared by twin-jet machine at -25℃; foil were observed by a transmission electron microscope (TEM, JEM-2100) operated at 200kV to observe the morphology and size of dispersoids. Electron energy loss spectroscopy (EELS) which is attached to TEM was used to measure the thickness of the samples. The size, number density and volume fraction dispersoids were quantified by the image analysis on TEM images. The volume fraction calculation of α-Al(Mn,Fe)Si dispersoids was according to literature [1]. The equation was as following:

$$V_v = A_A \frac{K\bar{D}}{K\bar{D} + t}(1 - A_{DFZ}) \qquad \text{Eq. 3.1}$$

Where A_A is the volume fraction of dispersoids in dispersoid zone; A_{DFZ} is the volume fraction of DFZ; $\bar{D}$ is the average equivalent diameter of dispersoids; t is the TEM foil thickness; and K is the average shape factor of dispersoids.

Reference

1. Y. J. Li, L. Arnberg, Quantitative study on the precipitation behavior of dispersoids in DC-cast AA3003 alloy during heating and homogenization, Acta Materialia. 51 (2003) 3415-3428. Doi: http://dx.doi.org/10.1016/S1359-6454(03)00160-5.

Chapter 4 Microstructure, elevated-temperature mechanical properties and creep resistance of dispersoid-strengthened Al-Mn-Mg 3xxx alloys with varying Mg and Si contents

4.1 Introduction

At present, the growing demand for high performance and lightweight structural components at elevated temperatures (250 to 350 ℃) is a challenge for the weight-sensitive automotive and aerospace industries. The traditional precipitation-strengthened aluminum alloys such as 2xxx, 6xxx and 7xxx can hardly meet the requirements of elevated-temperature mechanical properties, because of the rapid coarsening of nano-scale precipitates at elevated temperatures (overaging effect) [1, 2]. In recent years, the dispersoid strengthening in 3xxx aluminum alloys that can improve the mechanical properties at both room and elevated temperatures has been discovered [3-7]. Although Al-Mn-Mg 3xxx alloys are traditionally classified as non-heat-treatable alloys, thermally stable α-Al(MnFe)Si dispersoids form during heat treatment and hence the improvement of high temperature properties in the 3004 alloy have recently been reported [5, 6]. In addition, Al-Mn-Mg 3xxx alloys possess good formability, excellent corrosion resistance and weldability [8, 9]. The combination of those properties makes 3xxx alloys especially attractive for elevated temperature applications.

Several studies have been conducted on the evolution of microstructure during different heat treatments in 3xxx alloys, focusing mainly on 3003 and 3004 alloys [3-6, 8, 10-19]. The as-cast microstructure of 3003 and 3004 alloys consists mainly of Al_6(MnFe), α-Al(MnFe)Si and Mg_2Si intermetallic phases [11, 16, 17, 20-22]. During heat treatment, a considerable number of α-Al(Mn,Fe)Si dispersoids precipitate, and the size and amount of dispersoids are dependent on the alloy chemistry and heat treatment conditions [3-5, 10, 18]. The α-Al(MnFe)Si dispersoids are partially coherent with the matrix [3, 23] and have a cubic crystal

structure [10]. The precipitation of α-Al(MnFe)Si dispersoids starts at approximately 340 °C [5]. After a proper heat treatment, the maximum volume fraction can reach as high as ~3% and the dispersoids are proven to be thermally stable at 300 ℃, resulting in excellent mechanical properties and creep resistance at 300 ℃ [5].

To date, limited open literature is available concerning the effect of chemical composition on microstructure and elevated-temperature mechanical properties in Al-Mn-Mg 3xxx alloys. Muggerud et al [4] studied the effect of Mn and Si on the evolution of dispersoids in the 3003 alloy, and found that the addition of Mn and Si can promote the precipitation of α-Al(MnFe)Si dispersoids and thus improve room temperature mechanical properties. The effect of Fe on the dispersoid precipitation and elevated-temperature properties in 3004 alloy was investigated by Kun et al [6]. With an optimum Fe content, a high volume fraction of α-Al(MnFe)Si dispersoids form in the alloy and hence good mechanical properties and creep resistance at elevated temperature can be achieved.

In the present study, the effects of two main alloying elements in 3xxx alloys, Mg and Si, on the microstructure and elevated-temperature mechanical properties were investigated systematically. The microstructure evolution during heat treatment has been quantitatively evaluated by optical and electron microscopy. In addition, the creep properties at 300 ℃ as a function of Mg and Si content have been evaluated.

4.2 Experimental

Two series of experimental alloys with different Mg and Si contents were designed at the present work. In the first series (referred to as “DM” alloys), the Mg content changes from 0 to 2% while the Si content is fixed at 0.25%. In the second series (referred to as “DS” alloys), the Si content varies from 0 to 1% while the Mg content remains constant at 1%. In all of the experimental alloys, Mn and Fe were controlled at the same levels, approximately 1.25% and 0.6%, respectively. The chemical compositions as analyzed with the optical emission

spectrometer are given in Table 4.1. All of the alloy compositions here are in wt% unless otherwise indicated.

Table 4.1 Chemical compositions of the experimental alloys investigated (wt%)

Alloy ID	Mg	Si	Fe	Mn	Al
DM0	**0**	0.25	0.60	1.20	Bal.
DM50	**0.47**	0.25	0.56	1.24	Bal.
DM100 *	**1.00**	0.25	0.60	1.24	Bal.
DM150	**1.50**	0.26	0.60	1.24	Bal.
DM200	**2.02**	0.27	0.60	1.24	Bal.
DS0	1.02	**0.03**	0.56	1.25	Bal.
DS25 *	1.05	**0.23**	0.53	1.25	Bal.
DS45	1.07	**0.42**	0.57	1.26	Bal.
DS70	1.01	**0.70**	0.54	1.25	Bal.
DS100	1.00	**0.97**	0.56	1.28	Bal.

* With cross change of Mg and Si content in both DM and DS series, the chemical compositions of the DM100 alloy and the DS25 alloy are similar.

The experimental alloys were prepared in an electric resistance furnace. The temperature of the melt was maintained at 750 ℃ for 30 min and then degassed for 15 min. The melt was poured and solidified in a steel permanent mold preheated at 250 ℃. The dimension of the cast ingots was 30mm×40mm×80mm. To promote the precipitation of dispersoids, cast ingots were heat-treated at 375 ℃ with a heating rate of 5 ℃/min and then held for 24 hours, followed by water quench to room temperature. The heat treatment of 375℃/24h was used as the peak precipitation treatment in the previous work [6].

The compressive yield strength tests were conducted at 300 ℃ by a Gleeble 3800 thermomechanical simulator unit. The total strain of the deformed samples was 0.2 and the strain rate was 0.001 s^{-1}. The samples were machined in a cylinderical form with a 15 mm

length and 10 mm diameter. The results were obtained from the average value of three tests. Creep tests were performed at 300 °C for 90 hours under the compression condition with a constant load of 45 MPa. Each condition was repeated three times. The sample size is the same as the Gleeble sample. Microhardness was evaluated by an NG-1000 CCD microhardness test machine with a load of 200 g and a 20-second holding time. The tests were performed on polished samples for at least 10 measurements. The samples for hardness tests and microstructure observation were prepared using conventionally metallographic polishing. The final polish step was completed with 1 μm diamond paste followed by 60 nm colloidal silica. Electrical conductivity was measured on the samples with machined surface by a Sigmascope SMP10 at room temperature, and at least 5 measurements were performed for each sample.

Optical microscopy was used to observe the distribution of the dispersoid zone and the dispersoid free zone (DFZ). To reveal the dispersoids, the samples were etched by 0.5% HF for 20 seconds. The image analysis with the software (Clemex PE 4.0) was used to quantify the amount of the intermetallics, the dispersoids zone and DFZ by color contrast. The volume fractions of the intermetallics, the dispersoids zone and DFZ were converted from the area fractions of the intermetallics, the dispersoids zone and DFZ measured by the image analysis from optical microscope images according to the Delesse's principle [24]. For each image analysis data, 100 graphs with x500 magnification were analyzed. A transmission electron microscope (TEM, JEM-2100) operated at 200kV was used to observe the morphology and the size of the dispersoids. An electron energy loss spectroscope (EELS) attached to the TEM was used to measure the thickness of the samples. The size and number density of the dispersoids were quantified by the image analysis on the TEM images. The volume fraction of dispersoids was calculated using the method introduced in [10] shown in Eq. 4.1:

$$V_v = A_A \frac{K\bar{D}}{K\bar{D} + t}(1 - A_{DFZ}) \qquad \text{Eq. 4.1}$$

Where A_A is the volume fraction of dispersoids in TEM image, A_{DFZ} is the volume percentage of the DFZ, $\bar{D}$ is the average equivalent diameter of the dispersoids, t is the TEM foil thickness, and K is the average shape factor of dispersoids, which was taken to equal 0.45 in the present study.

4.3 Results

4.3.1 As-cast Microstructure

Fig. 4.1 shows the typical as-cast microstructure of the experimental alloys. The as-cast microstructure was generally composed of aluminum dendrite cells and a number of intermetallic phases, which distributed in the aluminum dendrite boundaries. In DM0 and DS0 alloys, there were only Mn-containing intermetallic particles (Al_6(MnFe)) in the interdendrite regions (Fig. 4.1a). With additions of Mg in the DM series and Si in the DS series, primary Mg_2Si appeared in the as-cast microstructure. Under the optical microscope (Fig. 4.1), the primary Mg_2Si particles are in dark color while Al_6(MnFe) intermetallics appear in grey color. As the content of Si increased, a small number of α-Al(MnFe)Si intermetallic particles are also observed but they are not specifically distinguished due to their similarity with Al_6(MnFe) intermetallics. Two different intermetallic phases co-existed in aluminum dendrite boundaries: Mn-containing intermetallic particles as a major phase and primary Mg_2Si particles as a minor phase (Fig. 4.1b). The microstructural features of Mg-containing DM series (DM50, 100, 150, 200 alloys) and Si-containing DS series (DS25, 45, 70, 100 alloys) are very similar, but the amounts of intermetallic phases change with alloying element content. The volume fractions of both intermetallic phases in DM and DS series alloys were quantified by image analysis, as shown in Fig. 4.2 (a) and (b). With increasing Mg and Si contents, the volume fraction of Mn-containing intermetallic particles increases moderately while the amount of primary Mg_2Si particles increases rapidly.

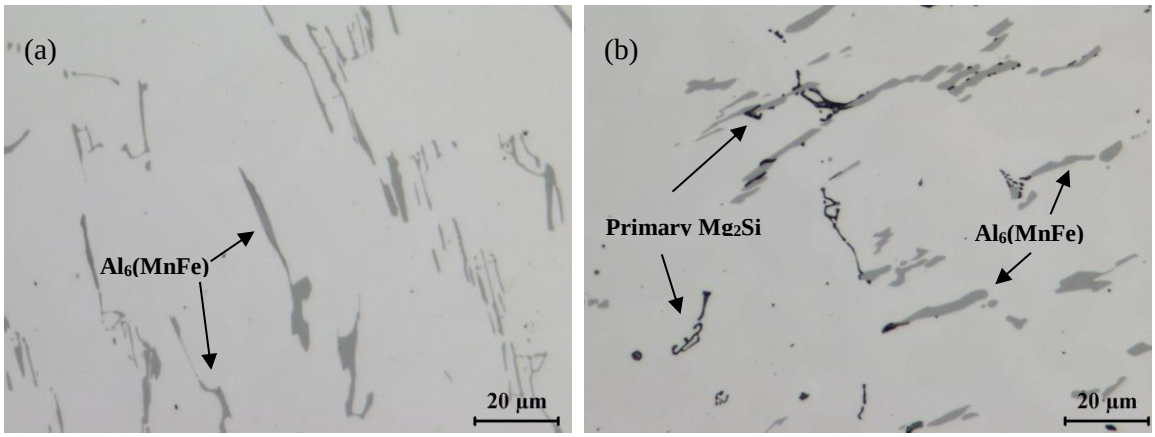

Fig. 4.1 As-cast microstructure of (a) DM0 alloys (0% Mg) and (b) DM100 alloys (1.0% Mg).

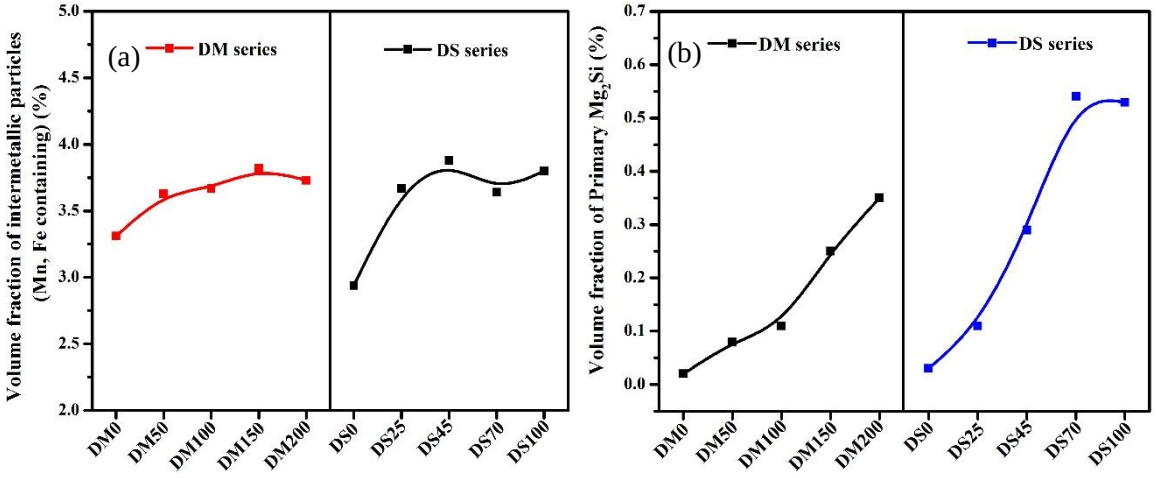

Fig. 4.2 Volume fraction of Mn-, Fe-containing intermetallic particles (a) and primary Mg_2Si particles (b) of the as-cast samples.

4.3.2 Microstructure after heat treatment

4.3.2.1 Dispersoid and dispersoid free zones

After heat-treatment at 375℃/24h, a number of α-Al(MnFe)Si dispersoids precipitated in the aluminum matrix of both DM and DS series. By etching with 0.5% HF, the precipitated dispersoids can be clearly revealed. In optical images, the dispersoid zone and dispersoid free

zone (DFZ) are visible as shown in Fig. 4.3 and Fig. 4.4. The dispersoid zone is an area with a high number density of α-Al(MnFe)Si dispersoids, while the DFZ is the area with very few α-Al(Mn,Fe)Si dispersoids present. The volume fractions of the dispersoid zone and DFZ were analyzed by the image analysis, and the results are shown in Fig. 4.5. For the DM0 alloy (0%Mg), only a few of dispersoids appeared around intermetallic particles, which left an extensive DFZ in the microstructure, as shown in Fig. 4.3a. The percentage of the dispersoid zone was only approximately 20%. With increasing Mg to 0.5% Mg (DM50 alloy), a larger number of dispersoids appeared (Fig. 4.3b) and the dispersoid zone increased to ~45% (Fig. 4.5). When 1.0% Mg was added (DM100 alloy), the precipitated dispersoids continued to increase (Fig. 4.3c), and the percentage of the dispersoid zone reached the maximum value of ~70%. With Mg content increasing further in DM150 and DM200 alloys, the percentage of the dispersoid zone decreased slightly while the DFZ increased moderately, and both values remained more or less stable (Figs. 4.3d and 4.5).

In the DS series, the precipitation of dispersoids depends largely on Si content. In the base alloy (DS0 alloy with 0% Si), very few dispersoids can be observed and no clear dispersoid zone can be defined in the microstructure (Fig. 4.4a). Without Si addition, the dispersoids can hardly form during heat treatment. With 0.23% Si addition (DS25 alloy), a large number of dispersoids appear (Fig. 4.4b) and the volume fraction of the dispersoid zone reaches to ~70% (Fig. 4.5). By increasing the Si to 0.42% (DS45 alloy), a dense distribution of dispersoids remains in the microstructure (Fig. 4.4c), and the volume fraction of the dispersoid zone decreases slightly to ~50%. By increasing the Si further to 0.7% and more (DS70 and DS100 alloys), in addition to the dispersoid precipitation, a number of coarse β-Mg_2Si particles (black needle phase in the optical microstructure) appear, accompanied by large DFZs (Fig. 4.4d). Apparently, the high levels of Si and Mg in DS70 and DS100 alloys induced the precipitation of coarse β-Mg_2Si particles, which consumed a large amount of the Si solutes in the matrix, and those Si atoms were no longer available for the formation of dispersoids. Consequently, the volume fraction of the dispersoid zone in DS70 and DS100 samples decreases while the volume fraction of DFZ continues to increase (Fig. 4.5).

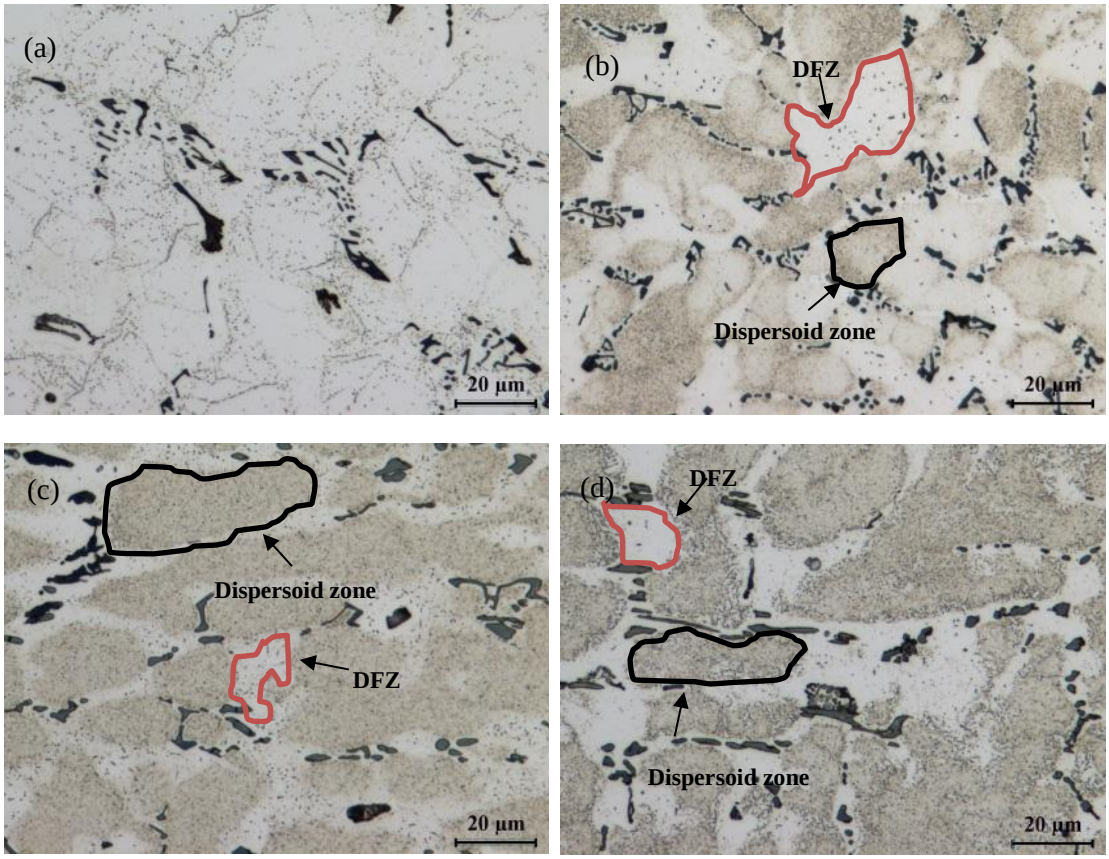

Fig. 4.3 Distribution of the dispersoid zone and DFZ in the DM series (a) DM0 alloy (0% Mg), (b) DM50 alloy (0.47%% Mg), (c) DM100 alloy (1.00% Mg) and (d) DM200 alloy (2.02% Mg).

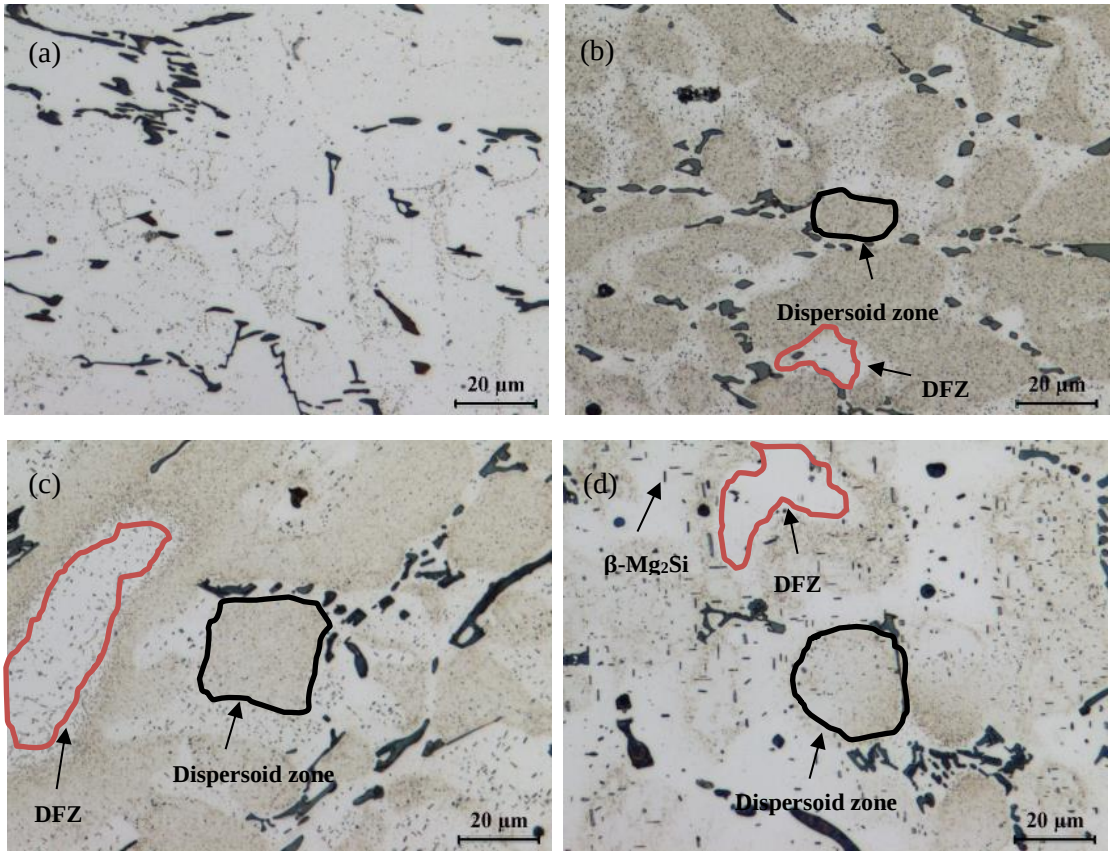

Fig. 4.4 Distribution of the dispersoid zone and DFZ in the DS series (a) DS0 alloy (0% Si), (b) DS25 alloy (0.23% Si), (c) DS45 alloy (0.42%Si) and (d) DS100 alloy (0.97% Si).

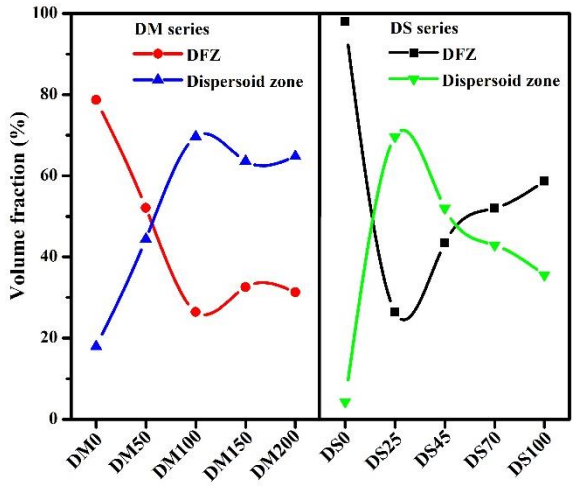

Fig. 4.5 Volume fraction of the dispersoid zone and DFZ in the DM and DS alloy series.

4.3.2.2 Precipitation of dispersoids in aluminum matrix

Due to the submicron size of the dispersoids, the precipitation of dispersoids in the dispersoid zone was closely observed by TEM. Typical TEM images in the DM and DS series are shown in Figs. 4.6 and 4.7. All of the TEM images were taken along the <001> axis direction of Al. The size and number density of dispersoids were quantified by the image analysis on TEM images, and the results are shown in Fig. 4.8. In general, the dispersoids have two morphologies: cubic-shaped and plate-shaped, as shown in Fig. 4.6a. Using TEM-EDS, no significant difference in the composition was found between these two morphologies. All dispersoids have a composition close to $Al_{12\text{-}20}(MnFe)_3Si$, which is referred to as α-Al(MnFe)Si dispersoids in the present work, according to the literature [5, 10].

In the DM0 alloy without Mg, the dispersoids distributes sparsely after heat-treatment at 375℃/24h (Fig. 4.6a). The size of the dispersoids is quite large (in the range of 100 nm) and the number density is very low (Fig. 4.8). With Mg addition, the precipitation of dispersoids is largely promoted (Figs. 4.6b and c). The size of the dispersoids in the DM50 alloy decreases to ~45 nm, and the number density increases greatly to 1500/μm^3, which reaches the peak value in the DM series. With further increasing Mg content, the size of the dispersoids increases slightly and remains nearly constant at the value of ~50 nm, while the number density of the dispersoids decreases moderately with an increase in Mg content (Fig. 4.8).

In the DS0 alloy without Si, very few dispersoids can be observed in the aluminum matrix and most of them have precipitated along dislocations (Fig. 4.7a). With the addition Si at 0.23 – 0.7% in DS25, DS45 and DS70 alloys, a great number of dispersoids were present in the aluminum matrix (Fig. 4.7b). The size of the dispersoids ranges from 40 to 50 nm and the number density lies in the range of 1500/μm^3 (Fig. 4.8). The alloy with the highest Si (DS100) has the smallest dispersoids and the densest dispersoids in the dispersoid zone as shown in Fig.4.7 (c), although it exhibits a high percentage of DFZ (Fig. 4.5).

The volume fractions of dispersoids in all of the alloys were calculated according to Eq. 4.1, and the results are presented in Fig. 4.9. The tendency of volume fraction with alloying element content is similar in two series of alloys. In both base alloys (DM0 and DS0), the

volume fractions of dispersoids are very low because of lack of Mg or Si. In the DM series when the Mg content increases to 1% (DM100), the volume fraction of dispersoids reaches its peak value, while the maximum volume fraction of dispersoids is obtained in the DS25 alloy with 0.23% Si in the DS series. Since the DM 100 and DS25 alloys have a similar chemical composition, the results from both the DM and DS series indicate that the alloy with 1.0% Mg and 0.25% Si has the maximum volume fraction of dispersoids (~2.75 vol.%) and the minimum DFZ. As the Mg content is over 1% in the DM series and the Si content is above 0.23% in the DS series, the volume fractions of dispersoids decrease with increasing alloying elements, primarily due to the increase of DFZs in the microstructure (Fig. 4.5).

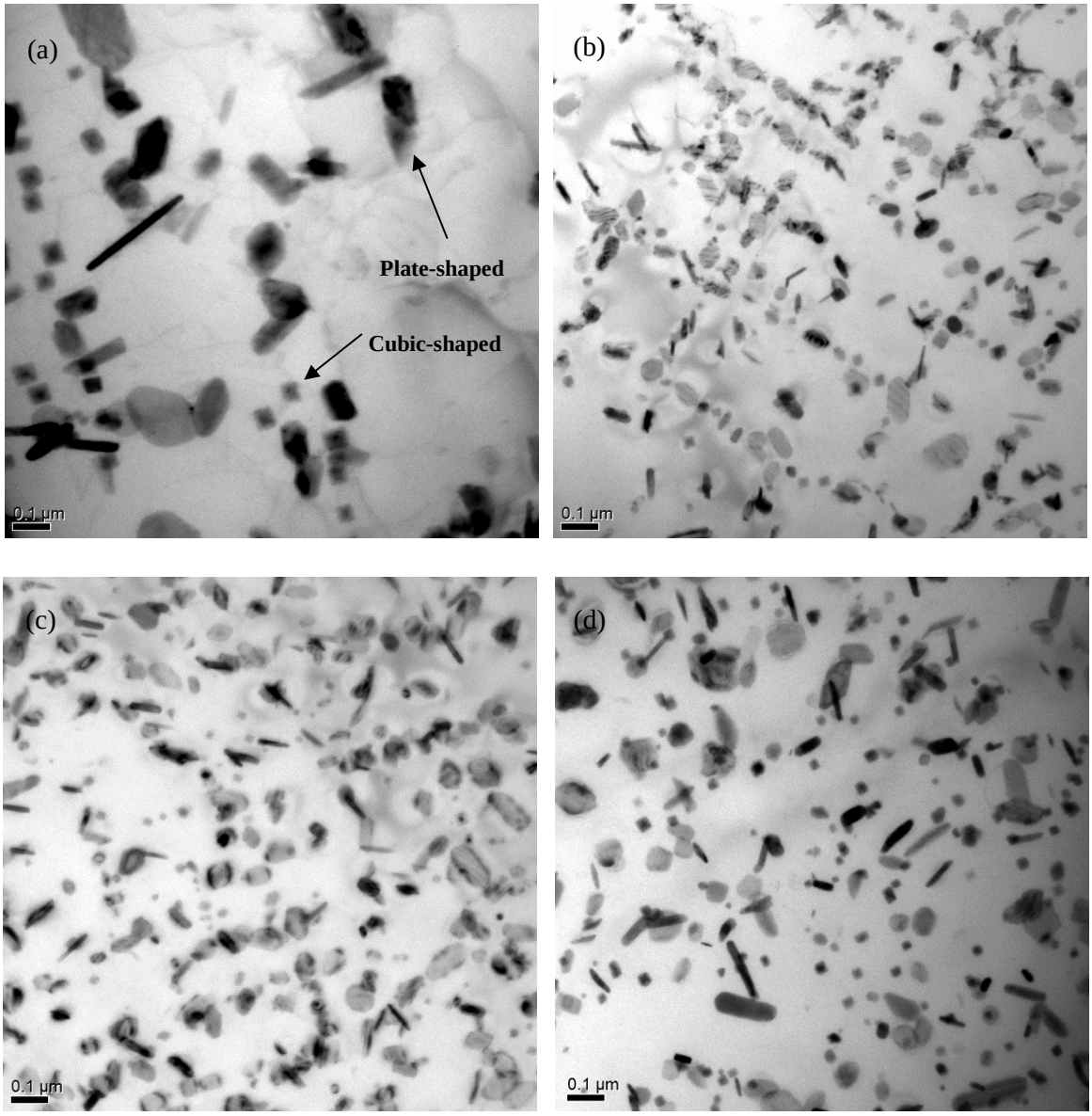

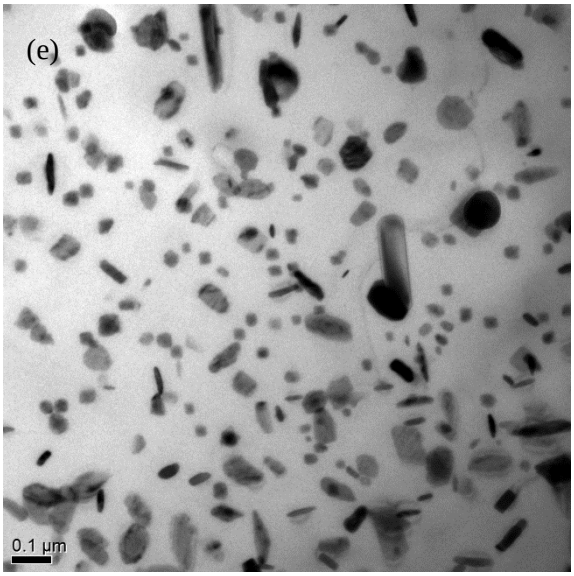

Fig. 4.6 TEM images of dispersoid distribution in the DM series: (a) DM0 (0% Mg), (b) DM50 (0.47%% Mg), (c) DM100 (1.00% Mg), (d) DM150 (1.50% Mg) and (e) DM200 (2.02% Mg).

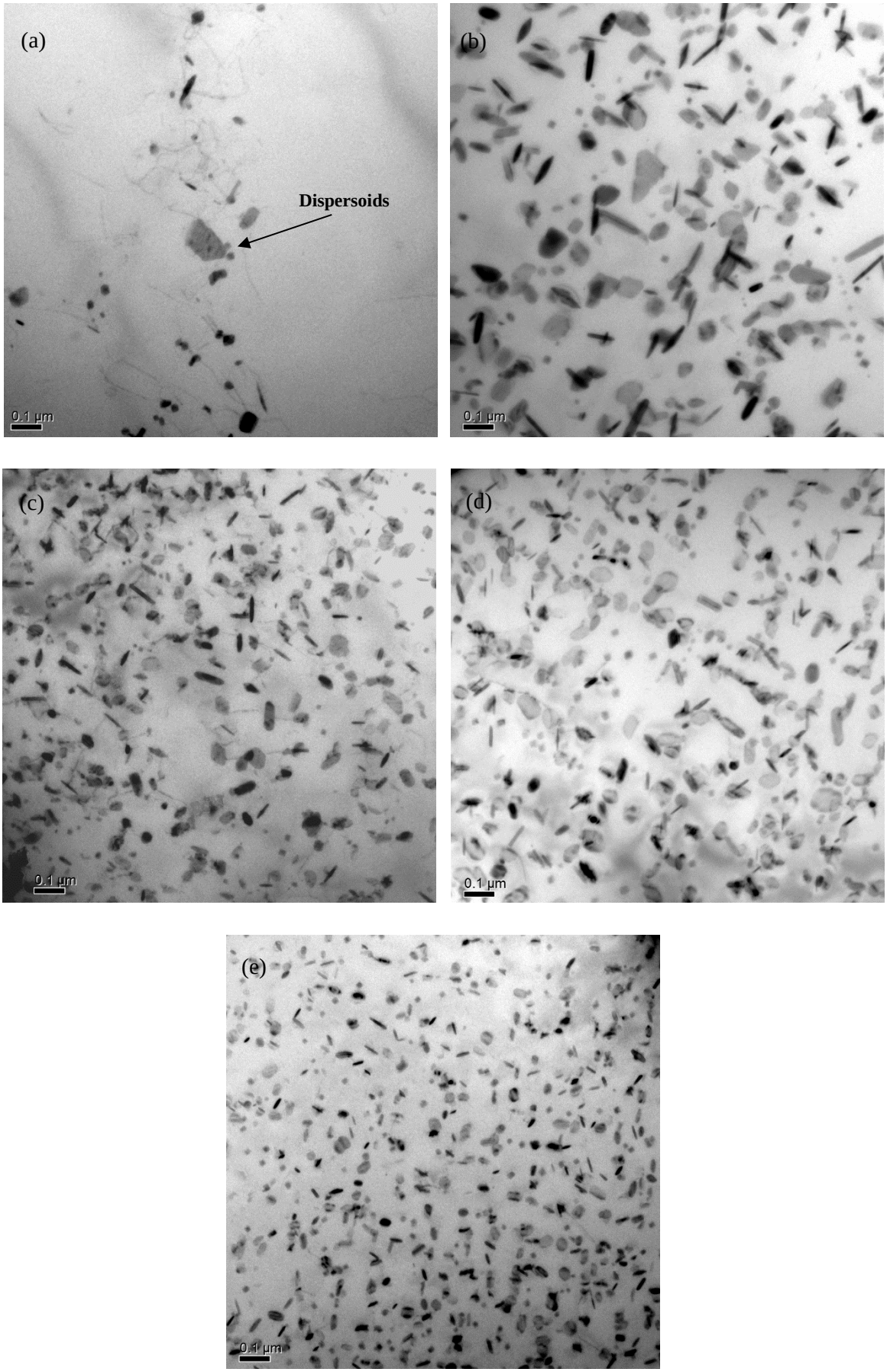
(a)
Dispersoids
0.1 µm
(b)
0.1 µm
(c)
0.1 µm
(d)
0.1 µm
(e)
0.1 µm

Fig. 4.7 TEM images of dispersoid distribution in the DS series: (a) DS0 (0% Si), (b) DS25 alloy (0.23% Si), (c) DS45 (0.42% Si), (d) DS70 (0.70%) and (e) DS100 (0.97%Si).

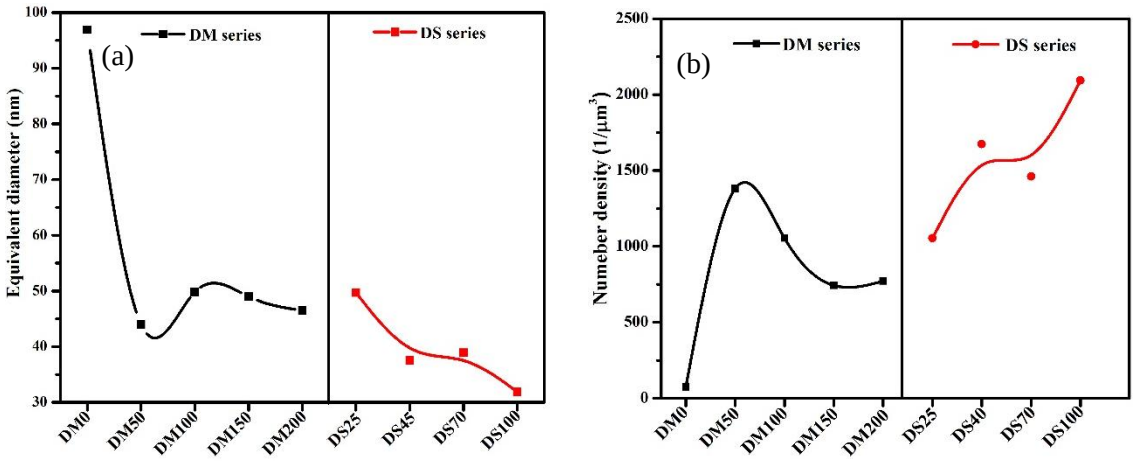

Fig. 4.8 Equivalent diameter (a) and number density (b) of disperoids in the DM and DS series.

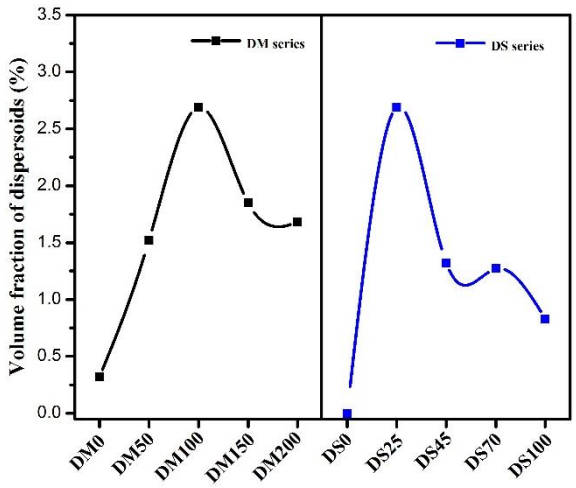

Fig. 4.9 Volume fraction of dispersoids in the DM and DS series.

4.3.3 Electrical conductivity and microhardness

To study the precipitation behavior of dispersoids, the evolution of electrical conductivity (EC) and microhardness as a function of holding time at 375 ℃ was determined experimentally. The results of EC and microhardness in the DM series are shown in Fig. 4.10. The EC in all of the alloy samples increases rapidly in the first several hours and then gradually rises to reach a

plateau after 24 h. For the DM0 alloy, the increase of EC is mainly due to the decrease in the supersaturated Mn level in the aluminum matrix, which results from the precipitation of a limited number of α-Al(MnFe)Si dispersoids (Fig. 4.3a) and a slight increase in the amount of intermetallic particles during heat treatment [11]. For all other Mg-containing alloys, the increase of EC with time is caused by the continuous decomposition of the supersaturated solid solution (Mn and Si) and the precipitation of a large amount of α-Al(MnFe)Si dispersoids (Fig. 4.3b-d).

Except the DM0 alloy, the microhardness of four other alloys increases with increasing holding time (Fig. 4.10b), indicating the strengthening effect of dispersoids that is confirmed by the microstructure observation (Fig. 4.3b-d). The values of microhardness reach the maximum level after 24 h holding time and become quite stable up to 48 h holding time, indicating that the full precipitation of dispersoids was achieved mostly after 24 h holding. For the base alloy without Mg (DM0), the microhardness drops slightly with the increase in the holding time, because a limited precipitation of dispersoids has little strengthening effect and the reduction of the Mn solute level with holding time leads to a weak matrix.

At any given holding time, the EC decreases and the microharness increases with increasing Mg content in the DM series, suggesting that in addition to the dispersoid precipitation, the alloying element in the solid solution also plays an important role in EC and microhardness. During the heat treatment of four Mg-containing alloys, the most Mn and Si were consumed due to the precipitation process of α-Al(MnFe)Si dispersoids. However, almost no Mg-containing phases formed during heat treatment. Therefore, it is reasonable to assume that except for the Mg bonded in primary Mg_2Si particles, all rest Mg solutes remained in aluminum matrix. The estimated Mg and Si concentrations in the solid solution after heat treatment can be calculated, as shown in Table 4.2. Evidently, a considerable amount of Mg remained in the solid solution of four Mg-containing alloys, and the Mg solute level increased with increasing Mg addition, which causes the reduced EC and increased microhardness in the DM series.

Table 4.2 Estimated Mg and Si contents in the solid solution after heat-treatment at 375℃/24h

ID	Original content (wt%)		Volume fraction of primary Mg_2Si (%)	Bonded in primary Mg_2Si (wt%)		Upper bound content in solid solution (wt%)	
	Mg	Si		Mg	Si	Mg	Si
DM0	0	0.25	0	0	0	0	0.25
DM50	0.47	0.25	0.10	0.05	0.03	0.42	0
DM100	1.00	0.25	0.24	0.11	0.06	0.89	0
DM150	1.50	0.26	0.30	0.14	0.08	1.36	0
DM200	2.02	0.27	0.30	0.14	0.08	1.88	0

The EC and microhardness as a function of holding time in the DS series are shown in Fig. 4.11. In the base alloy (DS0), the EC increases only slightly with holding time, indicating an insignificant precipitation of dispersoids (Fig. 4.4a). In all other Si-containing alloys, the values of EC increase remarkably with holding time, suggesting a strong dispersoid precipitation during heat treatment. Because of lack of a strengthening phase, the microhardness of the DS0 alloy remains almost unchanged during holding time, and its values are generally lower than the microhardness values of other Si-containing alloys. With precipitation of α-Al(MnFe)Si dispersoids (Fig. 4.4b), the microhardness of the DS25 and DS45 alloys increases with holding time and reaches a plateau after 24 h holding. In the case of high Si alloys (DS70 and DS100), the values of microhardness after 24 h holding are lower than those of DS25 and DS45 alloys, which is attributed to the reduced dispersoid precipitation and the presence of coarse β-Mg_2Si precipitates (Fig. 4.4c-d).

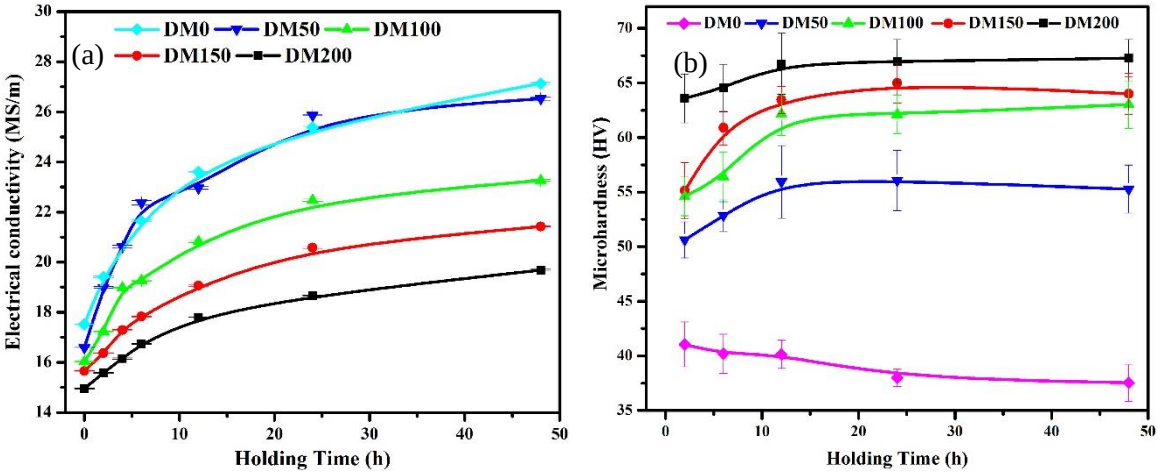

Fig. 4.10 Electrical conductivity (a) and microharness (b) as a function of holding time at 375 ℃ in the DM series.

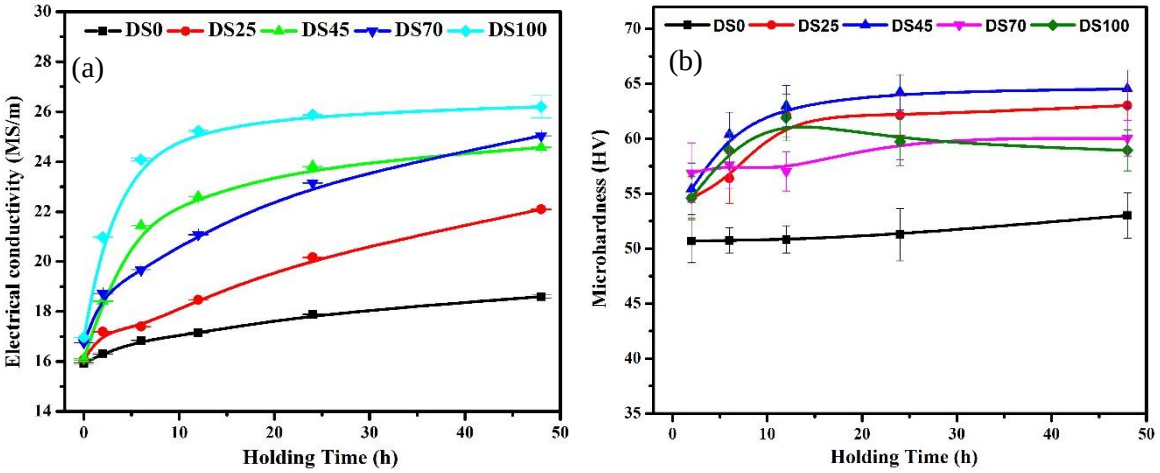

Fig. 4.11 Electrical conductivity (a) and microharness (b) as a function of holding time at 375 ℃ in the DS series.

4.3.4 Yield strength at 300℃

The elevated-temperature yield strengths of the DM and DS series are shown in Fig. 4.12. In the DM series, the DM0 alloy with 0% Mg possesses the lowest yield strength (43 MPa at 300 ℃). With 0.47% Mg in the DM50 alloy, the yield strength increases sharply to 75 MPa. With increasing Mg content to 1% (DM100), the yield strength continues to increase and

reaches 80 MPa. A further increase of Mg up to 2% does not bring additional benefit and the yield strength remains at a similar level.

The large increase of yield strength up to 1% Mg can be attributed mainly to the increase in the dispersoid volume fraction. The volume fraction of dispersoids increases from 0.3% in the DM0 alloy to 1.6% in the DM50 alloy and further to 2.75% in the DM100 alloy (Fig. 4.9). When Mg increases from 1% to 2%, the volume fraction of dispersoids decreases from its maximum level of 2.75% in the DM100 alloy to 1.6-1.8% in the DM150 and DM200 alloys, which could result in a reduction of yield strength. However, the Mg solute level increases from 0.89% (DM100) to 1.36% (DM150) and further to 1.88% (DM200), as shown in Table 4.2. It is most likely that the increased solid solution strengthening of Mg could compensate for the reduced dispersoid strengthening in the DM150 and DM200 alloys. Therefore, the yield strength in three alloys (DM100, DM150 and DM200) remains at a similar level.

In the DS series, the DS0 alloy with 0% Si has a relatively low value for the yield strength (60 MPa at 300 ℃). With 0.23% Si addition in the DS25 alloy, the yield strength increases remarkably to 80 MPa. With further increase of the Si up to 1%, the yield strength decreases moderately and remains at a similar level of 72-75 MPa for the DS45, DS70 and DS100 alloys.

Compared to the DM0 alloy, the DS0 alloy has considerably higher yield strength (Fig. 4.12). Both base alloys have an insufficient dispersoid precipitation, leading to a negligible dispersoid strengthening. However, the DS0 alloy contains 1% Mg, which is almost in the solid solution and provides the Mg solid solution strengthening. However, all alloys in the DS series have the same Mg content and hence, the effect of the Mg solid solution on yield strength is more or less the same. Therefore, the yield strength in the DS series is closely related to the volume fraction of dispersoids. For instance, the yield strength of DS25 alloy is 20 MPa higher than that of the DS0 alloy, attributed to the α-Al(MnFe)Si dispersoid strengthening. The moderate decrease in yield strength for the high Si alloys (0.45 to 1%) is caused mainly by the reduced volume fraction of dispersoids (Fig. 4.9).

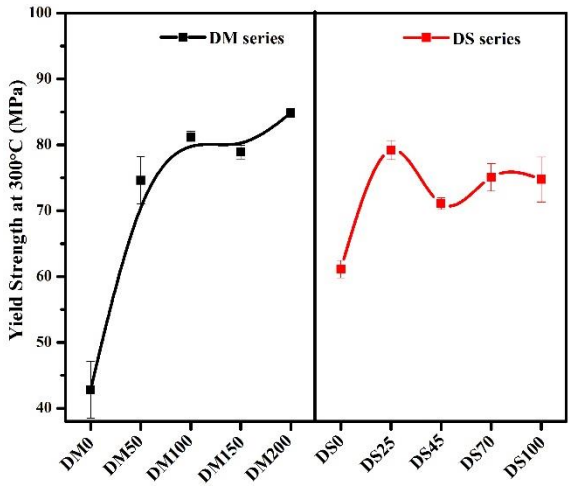

Fig. 4.12 Evolution of yield strength measured at 300 ℃ in the DM and DS series.

4.3.5 Creep resistance at 300℃

Creep properties are considered one of most important material properties for high temperature applications. The compressive creep tests were conducted at 300 ℃ under a constant load of 45 MPa. The typical creep curves are shown in Fig. 4.13. It is obvious that after the creep tests, both the DM0 and DS0 alloys have the highest creep deformation, followed by the DM200 and DM150 alloys, while the other alloys (DM50, DM100, DS25, DS45, DS70 and DS100 alloys) show very little creep deformation at 300 ℃. During compressive creep deformation, the creep strain increases rapidly in the first few hours. After this initial stage, the creep deformation turns to a quasi-steady state, in which the creep rate becomes more or less constant with the progress of the creep deformation. The minimum creep rate can be calculated as the average creep rate in the quasi-steady state. In the present work, the total creep strain and the minimum creep rate are used to characterize the creep properties. The smaller the total creep strain and minimum creep rate, the better the creep resistance is. The results of the total strain and minimum creep rate of all tested samples are shown in Fig. 4.14.

Two base alloys (DM0 and DS0) have the highest total strain and minimum creep rate, indicating the lowest creep resistance in the DM and DS series. Both alloys have an insufficient number of dispersoids, acting as barriers to the movement of dislocations and grain boundaries.

However, the DS0 alloy has higher creep resistance that the DM0 alloy due to 1% Mg solutes in the matrix, which can also impede dislocation movement and decrease the grain boundary mobility. In the DM series, the total strain and minimum creep rate decrease sharply to the lowest level in the DM50 and DM100 alloys, indicating a significant improvement in the creep resistance attributed mainly to the increased amount of dispersoids and partially to a higher Mg solute relative to the DM0 alloy. During creep deformation, a large number of dispersoids present act as strong barriers impeding the dislocation movement, which is confirmed by TEM examination after the creep test in DM100 alloy that contained the highest dispersoid volume fraction in DM series (Fig. 4.15). In the DS series, the total strain and minimum creep rate drop from the highest level in the DS0 alloy to the lowest level in the DS25 alloys, showing a great gain in the creep resistance. With a further increase in the Si content, the creep resistance of the DS45, DS70 and DS100 alloys remains almost unchanged.

The evolution of creep resistance in the DM series is somewhat different from the tendency of the yield strength, especially with high Mg-containing alloys (DM150 and DM200), suggesting that there is another factor affecting the creep resistance. The creep resistance at high temperatures is reported to be sensitive to the grain size of the materials [25, 26]. Creep deformation can occur by grain boundary sliding and vacancy diffusions through the grain boundary, especially at high temperatures. The finer the grain size and thus more grain boundary area, the more easily the creep deformation occurs. The grain sizes of experimental alloys have been examined and measured by the electron backscatter diffraction technique (EBSD). The results are listed in Table 4.3 and typical grain structures of two alloys, DM200 and DM50, are shown in Fig. 4.16. DM200 and DM50 alloys contain the maximum and minimum magnesium concentration respectively in the magnesium contained alloys. With the increase in Mg content, the average grain size in the DM series decreases. It would be contributed to the increase of the constitutional undercooling at the front of the solid/liquid interface during solidification by Mg addition [27]. The negative effect of grain size on the creep resistance in the DM50 and DM 100 alloys can be overlapped by the large amount of dispersoids. However, the grain size decreases significantly in the DM150 and DM200 alloys,

which is believed to be the main reason that the creep resistance deteriorates. In the DS series, the grain sizes of all alloys are almost the same, which is close to the grain sizes of the DM50 and DM100 alloys. In addition, the total strain and minimum strain rate of the DS25, DS45, DS70 and DS 100 alloys are very close to those of the DM50 and DM100 alloys. Therefore, the gain size is not an additional factor influencing the creep resistance in the DS series.

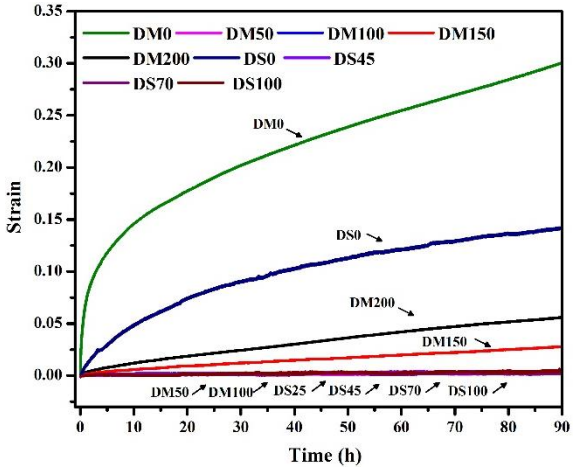

Fig. 4.13 Typical creep curves in the DM and DS series.

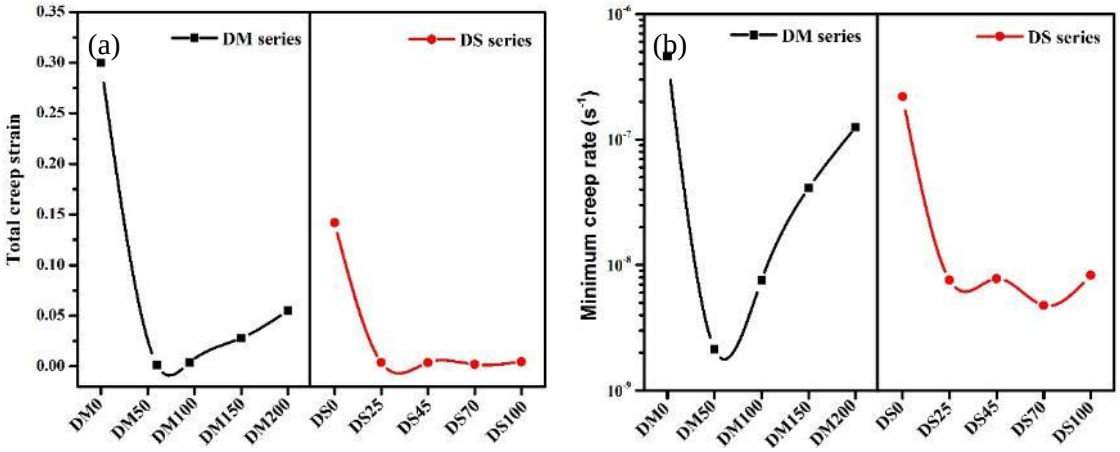

Fig. 4.14 Total creep strain (a) and the minimum creep rate (b) of different alloys in the DM and DS series.

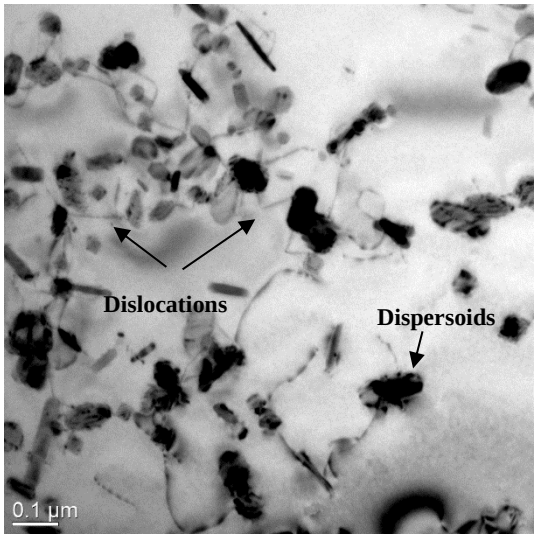

Fig. 4.15 TEM image of DM100 alloy after the creep test demonstrating the pinning effect of dispersoids on dislocations.

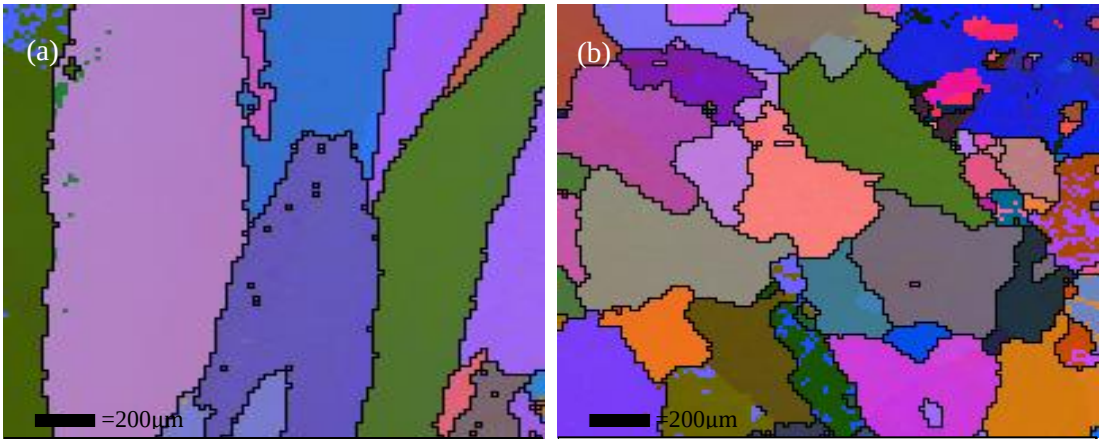

Fig. 4.16 EBSD images of grain structure (a) DM50 alloys (0.47%Mg) and (b) DM200 alloys (2.02%Mg) in as-cast condition.

Table 4.3 Grain size of different alloys in as-cast condition

	DM0	DM50	DM100	DM150	DM200	DS25	DS45	DS70	DS100
Equivalent grain diameter (μm)	775	539	556	342	302	512	495	459	523

4.4 Discussion

It is evident that Mg and Si contents in the 3xxx alloys have a strong influence on the microstructure and elevated-temperature mechanical properties. The results in the DM alloy series demonstrated that without Mg addition (DM0 alloy), the precipitation of dispersoids was so difficult that only an insufficient number of dispersoids came out. With Mg addition, a large number of α-Al(MnFe)Si dispersoids precipitated and the volume fraction of dispersoids increased significantly, indicating the important role of Mg in promoting the dispersoid precipitation. In Mn-containing Al-Mg-Si alloys [28, 29], the pre-existing β'-Mg_2Si is reported to be the prerequisite for a high density nucleation of α-Al(MnFe)Si dispersoids. In the present work, we observed that, during the heating process towards 375 ℃, a large number of β'-Mg_2Si precipitated at the temperature range of 200-300 ℃ and then slowly dissolved at higher temperatures of 300-375 ℃. Fig. 4.17a shows a TEM image of the water-quenched DM100 sample during heating at 275 ℃, in which lath-shaped β'-Mg_2Si precipitated and aligned along $<100>_{Al}$ in the matrix. When the temperature rose to 375℃ and during further holding, most of β'-Mg_2Si dissolved and α-Al(MnFe)Si preferentially nucleated and grew in the original area and orientation where pre-existing β'-Mg_2Si was (Fig. 4.17b). Due to the lack of Mg in the DM0 alloy, no pre-existing β'-Mg_2Si could be found during the heating process. Therefore, it is reasonable to believe that a proper Mg content provide an essential condition for precipitation of β'-Mg_2Si before the formation of α-Al(MnFe)Si dispersoids, which strongly promotes the nucleation of α-Al(MnFe)Si dispersoids during heat treatment.

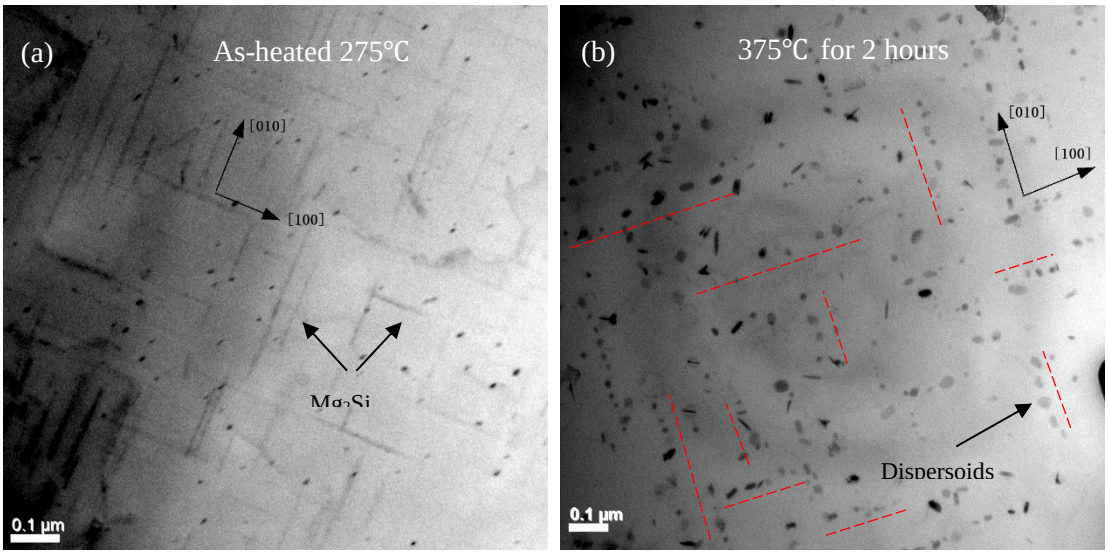

Fig. 4.17 TEM images of the water-quenched DM100 sample: (a) after heating to 275 ℃ and (b) after heat-treated at 375℃/2h. The red dash lines in (b) indicate the $<001>_{Al}$ direction.

Si is the essential element for α-Al(MnFe)Si dispersoids formation. Without Si (DS0 alloy), α-Al(MnFe)Si dispersoids can hardly form even after prolonged heat treatment because of lack of Si atoms in the matrix. With Si addition accompanied by 1%Mg in the DS series, a large number of dispersoids precipitated due to the same promoting effect of pre-existing β'-Mg_2Si on the nucleation of α-Al(MnFe)Si dispersoids, resulting in a significant improvement of YS and creep resistance at 300 ℃ in all Si-containing alloys in the DS series. With Si addition at 0.23% (DS25 alloy), it seems that an optimum combination of Mg and Si arrives, leading to the highest volume of dispersoids and hence the highest values of YS and creep resistance. In fact, the DM100 and the DS25 alloys have almost the same chemical composition (Table 4.1). The results from both the DM and DS series confirm that the alloy containing 1% Mg and 0.25% Si attains the best level of elevated-temperature strength and creep resistance.

It has been demonstrated that once precipitated, α-Al(MnFe)Si dispersoids are thermally stable at 300 ℃ [5], which is specially suitable as a strengthening phase in the aluminum matrix for high temperature applications. Compared to both base alloys (DM0 and DS0), all of the alloys containing Mg and Si in the DM and DS series show better precipitation of dispersoids and hence, remarkably higher YS and creep resistance at 300 ℃, confirming the important role

of dispersoid strengthening at elevated temperatures. Furthermore, the DM100 and DS25 alloys have the same Mg content as the DS0 alloy but achieves the highest YS and creep resistance at 300 ℃ with the maximum volume fraction of dispersoids, clearly indicating the strong dispersoid strengthening effect. On the other hand, because pre-existing β'-Mg_2Si dissolved back into the matrix and no further Mg-containing phases formed during the heat treatment, the solute Mg in the matrix can provide an additional strengthening effect on the elevated-temperature mechanical properties. When the Mg content is above 1%, the promotion effect on α-Al(MnFe)Si dispersoids seems to become weaker, and the volume fraction of dispersoids decreases moderately. However, the increase in the solute Mg level with the increasing Mg content in the alloys (Table 4.2) can compensate for the reduced dispersoid strengthening. Therefore, YS at 300 ℃ in the higher Mg-containing alloys can maintain a level similar to the DM100 alloy. It becomes evident that the increase in elevated-temperature strength and creep resistance in the experimental alloys studied is the synthetic effect of dispersoid strengthening and Mg solid solution strengthening, in which the precipitation of α-Al(MnFe)Si dispersoids plays the dominant role in the strengthening mechanism.

In addition to the best performance of the alloy containing 1% Mg and 0.25%Si, a significant improvement in overall elevated-temperature yield strength and creep resistance was achieved for the alloys with a wide range of Mg (0.5-1.5%) and Si (0.25-1.0%) (Figs. 4.12 and 4.14), providing great flexibility in the alloy design and selection for developing high-temperature resistant aluminum alloys.

4.5 Conclusions

1. Mg and Si have a significant influence on the distribution and volume fraction of dispersoids in Al-Mn-Mg 3xxx alloys. Without Mg or Si addition, α-Al(MnFe)Si dispersoids could hardly form during the precipitation heat treatment.
2. Mg and Si strongly promote the formation of α-Al(MnFe)Si dispersoids during precipitation heat treatment at 375 ℃. With 1% Mg and 0.25% Si, the alloy obtained the maximum volume fraction of dispersoids and the minimum volume fraction of the dispersoid free zone. Further increase of Mg and Si content resulted in a reduced volume fraction of dispersoids.
3. The base alloy free of Mg or Si possessed low yield strength and creep resistance at elevated temperature due to the lack of the strengthening phases. A significant improvement in yield strength and creep resistance at 300 ℃ was obtained over a wide range of Mg (0.5-1.5%) and Si (0.25-1.0%) contents studied, confirming the important strengthening effect of thermally stable dispersoids at elevated temperature.
4. The alloy containing 1.0% Mg and 0.25% Si demonstrated the best overall performance in terms of the distribution and volume fraction of dispersoids, elevated-temperature yield strength and creep resistance.

References

1. I. J. Polmear, M. J. Couper, Design and development of an experimental wrought aluminum alloy for use at elevated temperatures, Metallurgical Transactions A. 19 (1988) 1027-1035. Doi: http://dx.doi.org/10.1007/BF02628387.
2. Y. Zhou, Z. Liu, S. Bai, P. Ying, L. Lin, Effect of Ag additions on the lengthening rate of Ω plates and formation of σ phase in Al-Cu-Mg alloys during thermal exposure, Materials Characterization. 123 (2017) 1-8. Doi: http://dx.doi.org/10.1016/j.matchar.2016.11.008.

3. Y. J. Li, A. M. F. Muggerud, A. Olsen, T. Furu, Precipitation of partially coherent α-Al(Mn,Fe)Si dispersoids and their strengthening effect in AA 3003 alloy, Acta Materialia. 60 (2012) 1004-1014. Doi: http://dx.doi.org/10.1016/j.actamat.2011.11.003.

4. A. M. F. Muggerud, E. A. Mørtsell, Y. Li, R. Holmestad, Dispersoid strengthening in AA3xxx alloys with varying Mn and Si content during annealing at low temperatures, Materials Science and Engineering: A. 567 (2013) 21-28. Doi: http://dx.doi.org/10.1016/j.msea.2013.01.004.

5. K. Liu, X. G. Chen, Development of Al–Mn–Mg 3004 alloy for applications at elevated temperature via dispersoid strengthening, Materials & Design. 84 (2015) 340-350. Doi: http://dx.doi.org/10.1016/j.matdes.2015.06.140.

6. K. Liu, X.-G. Chen, Evolution of Intermetallics, Dispersoids, and Elevated Temperature Properties at Various Fe Contents in Al-Mn-Mg 3004 Alloys, Metallurgical and Materials Transactions B. 47 (2016) 3291-3300. Doi: http://dx.doi.org/10.1007/s11663-015-0564-y.

7. K. Liu, H. Ma, X. G. Chen, Enhanced elevated-temperature properties via Mo addition in Al-Mn-Mg 3004 alloy, Journal of Alloys and Compounds. 694 (2017) 354-365. Doi: http://dx.doi.org/10.1016/j.jallcom.2016.10.005.

8. H.-W. Huang, B.-L. Ou, Evolution of precipitation during different homogenization treatments in a 3003 aluminum alloy, Materials & Design. 30 (2009) 2685-2692. Doi: http://dx.doi.org/10.1016/j.matdes.2008.10.012.

9. A. R. Yazdzad, T. Shahrabi, M. G. Hosseini, Inhibition of 3003 aluminum alloy corrosion by propargyl alcohol and tartrate ion and their synergistic effects in 0.5% NaCl solution, Materials Chemistry and Physics. 109 (2008) 199-205. Doi: http://dx.doi.org/10.1016/j.matchemphys.2007.11.012.

10. Y. J. Li, L. Arnberg, Quantitative study on the precipitation behavior of dispersoids in DC-cast AA3003 alloy during heating and homogenization, Acta Materialia. 51 (2003) 3415-3428. Doi: http://dx.doi.org/10.1016/S1359-6454(03)00160-5.

11. Y. J. Li, L. Arnberg, Evolution of eutectic intermetallic particles in DC-cast AA3003 alloy during heating and homogenization, Materials Science and Engineering: A. 347 (2003) 130-135. Doi: http://dx.doi.org/10.1016/S0921-5093(02)00555-5.

12. Q. Du, W. J. Poole, M. A. Wells, N. C. Parson, Microstructure evolution during homogenization of Al–Mn–Fe–Si alloys: Modeling and experimental results, Acta Materialia. 61 (2013) 4961-4973. Doi: http://dx.doi.org/10.1016/j.actamat.2013.04.050.

13. Q. Zhao, B. Holmedal, Y. Li, Influence of dispersoids on microstructure evolution and work hardening of aluminium alloys during tension and cold rolling, Philosophical Magazine. 93 (2013) 2995-3011. Doi: http://dx.doi.org/10.1080/14786435.2013.794315.

14. A. M. F. Muggerud, Y. Li, R. Holmestad, Composition and orientation relationships of constituent particles in 3xxx aluminum alloys, Philosophical Magazine. 94 (2014) 556-568. Doi: http://dx.doi.org/10.1080/14786435.2013.857796.

15. N. Sun, B. R. Patterson, J. P. Suni, E. A. Simielli, H. Weiland, L. F. Allard, Microstructural evolution in twin roll cast AA3105 during homogenization, Materials Science and Engineering: A. 416 (2006) 232-239. Doi: http://dx.doi.org/10.1016/j.msea.2005.10.018.

16. M. Dehmas, E. Aeby-Gautier, P. Archambault, M. Serrière, Interaction Between Eutectic Intermetallic Particles and Dispersoids in the 3003 Aluminum Alloy During Homogenization Treatments, Metallurgical and Materials Transactions A. 44 (2013) 1059-1073. Doi: http://dx.doi.org/10.1007/s11661-012-1473-1.

17. Z. Li, Z. Zhang, X. G. Chen, Effect of magnesium on dispersoid strengthening of Al—Mn—Mg—Si (3xxx) alloys, Transactions of Nonferrous Metals Society of China. 26 (2016) 2793-2799. Doi: http://dx.doi.org/10.1016/S1003-6326(16)64407-2.

18. S. P. Chen, N. C. W. Kuijpers, S. van der Zwaag, Effect of microsegregation and dislocations on the nucleation kinetics of precipitation in aluminium alloy AA3003, Materials Science and Engineering: A. 341 (2003) 296-306. Doi: http://dx.doi.org/10.1016/S0921-5093(02)00245-9.

19. M. Dehmas, P. Weisbecker, G. Geandier, P. Archambault, E. Aeby-Gautier, Experimental study of phase transformations in 3003 aluminium alloys during heating by in situ high energy X-ray synchrotron radiation, Journal of Alloys and Compounds. 400 (2005) 116-124. Doi: http://dx.doi.org/10.1016/j.jallcom.2005.03.062.

20. M. Warmuzek, G. Mrówka, J. Sieniawski, Influence of the heat treatment on the precipitation of the intermetallic phases in commercial AlMn1FeSi alloy, Journal of Materials Processing Technology. 157–158 (2004) 624-632. Doi: http://dx.doi.org/10.1016/j.jmatprotec.2004.07.125.

21. D. T. L. Alexander, A. L. Greer, Solid-state intermetallic phase tranformations in 3XXX aluminium alloys, Acta Materialia. 50 (2002) 2571-2583. Doi: http://dx.doi.org/10.1016/S1359-6454(02)00085-X.

22. H. D. Merchant, J. G. Morris, D. S. Hodgson, Characterization of intermetallics in aluminum alloy 3004, Materials Characterization. 25 (1990) 339-373. Doi: http://dx.doi.org/10.1016/1044-5803(90)90062-O.

23. A. M. F. Muggerud, J. C. Walmsley, R. Holmestad, Y. Li, Combining HAADF STEM tomography and electron diffraction for studies of α-Al(Fe,Mn)Si dispersoids in 3xxx aluminium alloys, Philosophical Magazine. 95 (2015) 744-758. Doi: http://dx.doi.org/10.1080/14786435.2015.1006294.

24. G. F. V. Voort, ASM Handbook: Metallography and Microstructures. (ASM International, 2004), Vol. 9, pp. 429.

25. R. L. Coble, A Model for Boundary Diffusion Controlled Creep in Polycrystalline Materials, Journal of Applied Physics. 34 (1963) 1679-1682. Doi: http://aip.scitation.org/doi/abs/10.1063/1.1702656.

26. C. Herring, Diffusional Viscosity of a Polycrystalline Solid, Journal of Applied Physics. 21 (1950) 437-445. Doi: http://aip.scitation.org/doi/abs/10.1063/1.1699681.

27. Y. Birol, Effect of solute Mg on grain size of aluminium alloys, Materials Science and Technology. 28 (2012) 924-927. Doi: http://dx.doi.org/10.1179/1743284712Y.0000000024.

28. L. Lodgaard, N. Ryum, Precipitation of dispersoids containing Mn and/or Cr in Al–Mg–Si alloys, Materials Science and Engineering: A. 283 (2000) 144-152. Doi: http://dx.doi.org/10.1016/S0921-5093(00)00734-6.

29. H. Hirasawa, Precipitation process of Al-Mn and Al-Cr supersaturated solid solution in presence of age hardening phases, Scripta Metallurgica. 9 (1975) 955-958. Doi: http://dx.doi.org/10.1016/0036-9748(75)90551-7.

Chapter 5 Effect of metastable Mg_2Si and dislocations on α-Al(MnFe)Si dispersoid formation in Al-Mn-Mg 3xxx alloys

5.1 Introduction

Traditional Al-Mn-Mg 3xxx alloys are widely used for architecture, packaging and automobile applications due to their excellent corrosion resistance, formability and weldability. Though 3xxx alloys are normally classified as non-heat-treatable alloys, a strong dispersoid strengthening effect has been discovered in recent years by applying a suitable heat treatment [1-5]. Formed during heat treatment, α-Al(MnFe)Si dispersoids are the key strengthening phase in the aluminum matrix, which greatly improves the strength of 3xxx alloys, particularly at elevated temperature [6]. α-Al(MnFe)Si dispersoids have a partial coherence with the aluminum matrix [4, 7] and are thermally stable up to 300 ℃ [1, 3, 8], which leads 3xxx alloys to be promising candidates for elevated temperature applications .

During heating process of the heat-treatment, metastable Mg_2Si could precipitate in some Al-Mn-Mg-Si alloys because of the presence of Mg and Si. The precipitation sequence of Mg_2Si in Mg and Si containing aluminum alloys was generally described as follows: Mg and Si clusters → needle-like β''-Mg_2Si → lath-like or rod-like β'-Mg_2Si → plate-like equilibrium β-Mg_2Si [9-14]. The typical size of the needle-like β''-Mg_2Si precipitates is in the range of 4 x 4 x 50 nm [11]. The lath-like or rod-like β'-Mg_2Si precipitates have dimensions of approximately 10 x 10 x 500 nm [12]. The size of the plate-like equilibrium β-Mg_2Si phase can reach to several micrometers [9, 15, 16]. It was reported in previous studies [17, 18] that metastable Mg_2Si precipitates could have a positive effect on the nucleation of α-Al(MnFeCr)Si and α-AlMnSi dispersoids in 6xxx alloys. It was observed during the dispersoid formation [18] that there existed an intermediate phase, the u-phase, that first nucleated on the β'-Mg_2Si and that the α-Al(MnFeCr)Si dispersoids heterogeneously nucleated on these 'u-

phase' precipitates. However, the effect of metastable Mg_2Si on the nucleation of Mn-containing dispersoids has not been systematically investigated.

It is well known that some defects, such as vacancies and dislocations, may enhance the precipitation kinetics of the secondary precipitation phase due to the increasing number of nucleation sites and diffusivities of the alloying elements in the materials [19-24]. There were a few reports that documented the precipitation behavior of dispersoids in deformed 3xxx alloys [25, 26], in which the deformation had an impact on the number density and volume fraction of the dispersoids. It is worth mentioning that the above reported alloys did not contain Mg, and thus, no Mg_2Si existed. This suggests that the dislocations in the deformed samples could have an impact on dispersoid nucleation in addition to the possible Mg_2Si nucleation effect.

In our previous work [27], the effects of Mg and Si on α-Al(MnFe)Si dispersoid precipitation, elevated-temperature strength and creep resistance in 3xxx alloys were systematically studied, in which there was an evidence that pre-existing β'-Mg_2Si could promote the formation of α-Al(MnFe)Si dispersoids. The aim of the present work is to clarify the effects of metastable Mg_2Si and dislocations on the nucleation and growth of α-Al(MnFe)Si dispersoids in the Al-Mn-Mg 3xxx alloys. The influence of metastable Mg_2Si on the nucleation of the dispersoids was investigated by a close examination of the dispersoid precipitation process using the quench technique and TEM observation. The effect of different types of metastable Mg_2Si on the dispersoid formation was also evaluated using two-step heat treatments. Moreover, the effect of dislocations on the nucleation of dispersoids in the deformed samples was studied and compared to the non-deformed control sample.

5.2 Experimental procedures

Two experimental Al-Mn-Mg 3xxx alloys were used in this study. The base alloy, used as a control material, contains 1.25%Mn, 0.25%%Si and 0.6%Fe (all of the alloy compositions are in wt% unless indicated otherwise). The main alloy investigated contains additionally

1%Mg, while the concentrations of Mn, Si and Fe remain the same as in the base alloy. The two alloys were prepared from commercially pure Al (99.7%), and Mg (99.9%), and Al-25%Mn, Al-25%Fe and Al-50%Si master alloys. The chemical compositions of the experimental alloys were analyzed using an optical emission spectrometer and are listed in Table 5.1. In each test, approximately 3 kg of material was prepared in a clay-graphite crucible using an electric resistance furnace. The temperature of the alloy melt was maintained at 750 ℃ and then degassed for 15 minutes. The melt was then poured into a pre-heated permanent steel mold. The dimension of the cast ingot is 30 x 40 x 80 mm.

Table 5.1 Chemical composition of experimental alloys (wt%)

Alloy code	**Si**	**Fe**	**Mn**	**Mg**	**Al**
Base	0.23	0.56	1.23	**0.002**	Bal.
M1	0.26	0.57	1.25	**1.00**	Bal.

To examine the influence of metastable Mg_2Si and dislocations on the dispersoid nucleation, the as-cast or deformed samples were heat-treated under different heat treatment procedures. In procedure A, the samples were heated with a constant heating rate of 5 ºC/min in an electrical resistance furnace from room temperature to the desired temperature. Samples were heated to either 275 °C or 375 °C, or in some cases held at 375 °C for various holding times, followed by water quench to room temperature. A schematic diagram of the heat treatment is shown in Fig. 5.1a. Procedure B is the two-step heat treatment, in which the samples were directly put in the furnace at 175 ºC for 5 hours and 250 ºC for 12 hours respectively, followed by water quench to room temperature. Then, the samples were put into a furnace directly at 375 ℃ and held for 24 hours followed by water quench (see Fig. 5.1b).

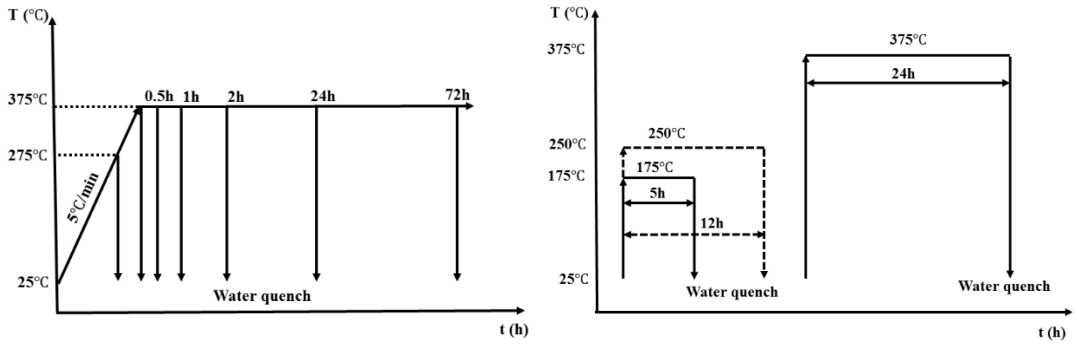

(a) (b)

Fig. 5.1 Schematic diagram of various heat treatments (a) procedure A and (b) procedure B (two-step heat treatment).

For the deformation test, the samples were machined to a cylindrical form with 15 mm in length and 10 mm. In the tests, the samples were cold-compressed to 0.2 strain at a strain rate of 10^{-3} s^{-1} on a Gleeble 3800 thermomechanical testing machine.

After heat treatment, the samples were prepared using the conventional metallographic method. The polished samples were etched by 0.5%HF for 20 seconds to reveal the dispersoids. An optical microscope equipped with an imaging analysis system (Clemex PE 4.0) was used to observe the distribution of the dispersoids and to quantify the dispersoid free zone (DFZ). Vicker hardness was measured by an NG-1000 CCD microhardness test machine with a load of 200 g and a dwell time of 20 s. A transmission electron microscope (TEM, JEM-2100) equipped with an energy dispersive X-ray spectroscopy (EDS) was used to observe the dispersoids in details. TEM foils were prepared in a twin jet electropolisher using a solution of 30% nitric acid in methanol at -20 ºC. To evaluate of the dispersoid volume fraction, the thicknesses of TEM foils were measured using the electron energy loss spectroscopy (EELS) equipped on the TEM. The size and number density of the dispersoids were measured by using imaging analysis (Clemex PE 4.0) on the TEM images. The volume fraction of dispersoids, Vv, was calculated using Eq. 5.1 [6].

$$V_v = A_A \frac{K\bar{D}}{K\bar{D}+t}(1 - A_{DFZ}) \qquad \text{Eq. 5.1}$$

where A_A is the volume percentage of dispersoids and $\bar{D}$ is the average equivalent diameter of dispersoids from the TEM images; t is the TEM foil thickness; A_{DFZ} is the volume percentage

of dispersoid free zone; and K is the shape factor of dispersoids, which is equal to 0.45 in this study.

5.3 Results and discussion

5.3.1 Precipitation of α-Al(MnFe)Si dispersoids in the base alloy

Fig. 5.2 shows the typical microstructure of the base alloy (Mg-free) after heat treatment at 375 °C for 24 h and at 375 °C for 72 h. The large needle-like and plate-like particles are Al_6(Mn,Fe) intermetallics, which originate from the as-cast microstructure and are distributed in interdendrite regions. The small black dots are α-Al(MnFe)Si dispersoids, which precipitated during the heat treatment and were revealed after etching with 0.5% HF. After heat-treatment at 375 ℃ for 24 h, only a few of the dispersoids appeared around intermetallic particles, which left an extensive dispersoid free zone (DFZ) in the microstructure, as shown in Fig. 5.2a. With a prolonged heat treatment up to 72 h (Fig. 5.2b), more dispersoids precipitated out of the matrix. However, the amount of dispersoids precipitated is still limited. The volume fraction of DFZ after 375 ºC for 24 h reached as high as 79%, while the volume fraction of DFZ after 375 ºC for 72 h still remained at 51.4%. Fig. 5.3 shows the TEM bright field images, which dispays the dispersoids in details. The α-Al(MnFe)Si dispersoids have cubic-like or rod-like morphologies with a composition close to $Al_{12\text{-}20}(MnFe)_3Si$. In the sample treated 375 ℃ for 24 h (Fig. 5.3a), the number density of the dispersoids was very low and the size was quite large (~97 nm in diameter). After a longer, 72 h treatment (Fig. 5.3b), the number density of the dispersoids moderately increased and the size slightly decreased to 80 nm. The volume fraction of dispersoids after 375 ºC for 24 h was only 0.32% and it increased to 0.82% after 375 ºC for 72 h. After solidification, there was a supersaturated solid solution of Mn and Si in the aluminum matrix, which tended to decompose for dispersoid precipitation during heat treatment. Results indicate that the precipitation of α-Al(MnFe)Si dispersoids in

the base alloy was very difficult. After 24 h at 375 ºC, only a small amount of dispersoids (0.32%) precipitated, and the amount was still limited even after a prolonged 72 h treatment.

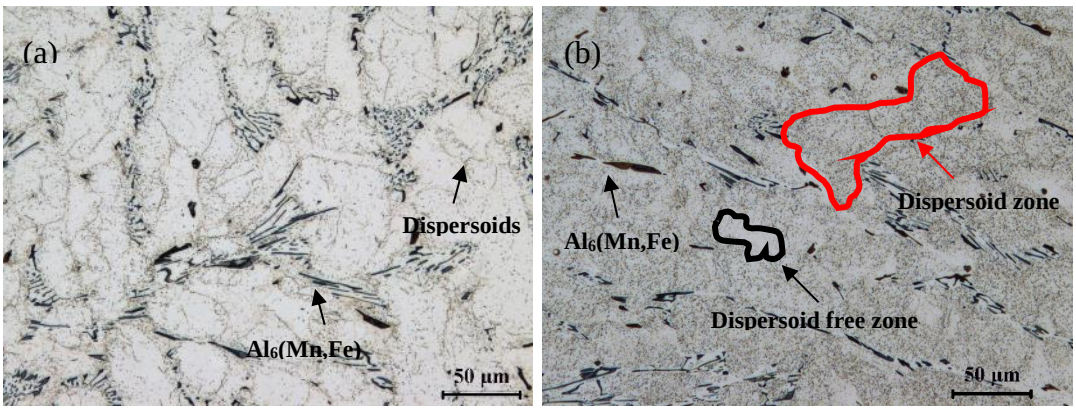

Fig. 5.2 Optical images showing the dispersoid distribution in the base alloy, (a) 375 ºC for 24 h and (b) 375 ºC for 72 h.

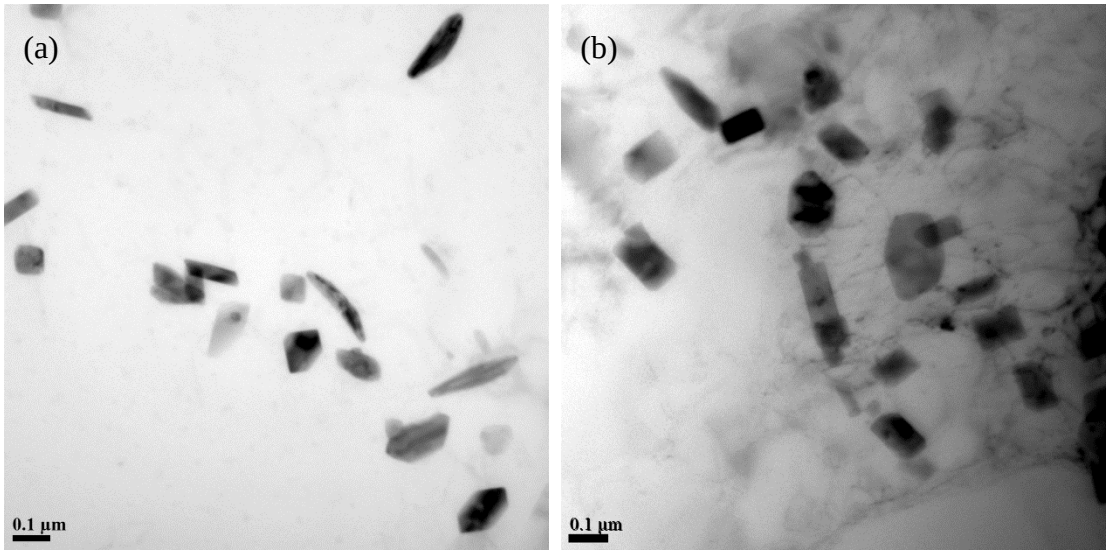

Fig. 5.3 TEM bright field images showing the dispersoids in the base alloy, (a) 375 ºC for 24 h and (b) 375 ºC for 72 h, recorded near $[001]_{Al}$ zone axis.

5.3.2 Precipitation of α-Al(MnFe)Si dispersoids in the M1 alloy

The precipitation of α-Al(MnFe)Si dispersoids in the Mg containing alloy (M1) after 375 ºC for 24 h is shown in Fig. 5.4a. The dispersoid zone and dispersoid free zone (DFZ) were

clearly distinguishable in the optical microstructure after etching, as shown in Fig. 5.4. The dispersoid zones were centered inside aluminum cells and grains, while the DFZs were located in the interdendrite regions close to the Mn-containing intermetallic particles. With the addition of 1% Mg, a large number of the dispersoids appeared in the heat-treated microstructure and the precipitation of dispersoids became much easier when compared to the Mg-free base alloy under the same heat treatment condition. The volume fraction of the DFZ decreased from 79% in the base alloy to 26.5% in the M1 alloy. TEM observations (Fig. 5.5a) confirmed that a large number of rod-like or plate-like dispersoids precipitated in the dispersoid zone. The number density and volume fraction of the dispersoids in the M1 alloy were much higher than in the base alloy. All measured results are shown in Table 5.2. For example, the volume fraction of dispersoids increased from 0.32% in the base alloy to 2.69% in the M1 alloy after 375 ºC for 24 h. It is evident that the presence of Mg greatly promoted the formation of dispersoids.

The typical microstructure of the M1 alloy after the two-step heat treatments (175ºC/5h + 375ºC/24h and 250ºC/12h + 375ºC/24h) are shown in Fig. 5.4b and c, respectively. Compared to the one step treatment (375ºC/24h), the sample that underwent the two-step 175ºC/5h + 375ºC/24h treatment showed a reduced amount of dispersoids and an increased DFZ. After the 250ºC/12h + 375ºC/24h treatment, the amount of dispersoids further increased, while the corresponding DFZ decreased. TEM images (Fig. 5.5b and c) clearly revealed that the number density of dispersoids in the 175ºC/5h + 375ºC/24h sample was smaller than the one step sample, and the number density of dispersoids in the 250ºC/12h + 375ºC/24h sample increased. The image analysis results (Table 5.2) show that the volume fraction of the DFZ increased from 26.4% after 375ºC/24h to 30% after 175ºC/5h + 375ºC/24h, and decreased to 23% after 250ºC/12h + 375ºC/24h. On the other hand, the volume fraction of dispersoids decreased from 2.69% after 375ºC/24h to 1.93% after 175ºC/5h + 375ºC/24h, and increased to 2.15% after 250ºC/12h + 375ºC/24h. It is apparent that the 175ºC/5h + 375ºC/24h treatment is less efficient at promoting the dispersoid precipitation. Reports suggest that metastable β"-Mg_2Si and β'-Mg_2Si could precipitate in alloys containing Mg and Si during the heat treatment at 175 ºC for

5h and 250 ºC for 12h, respectively [11, 12]. The effect of variants of the metastable Mg_2Si precipitates on the formation of dispersoids and their mechanisms will be discussed later.

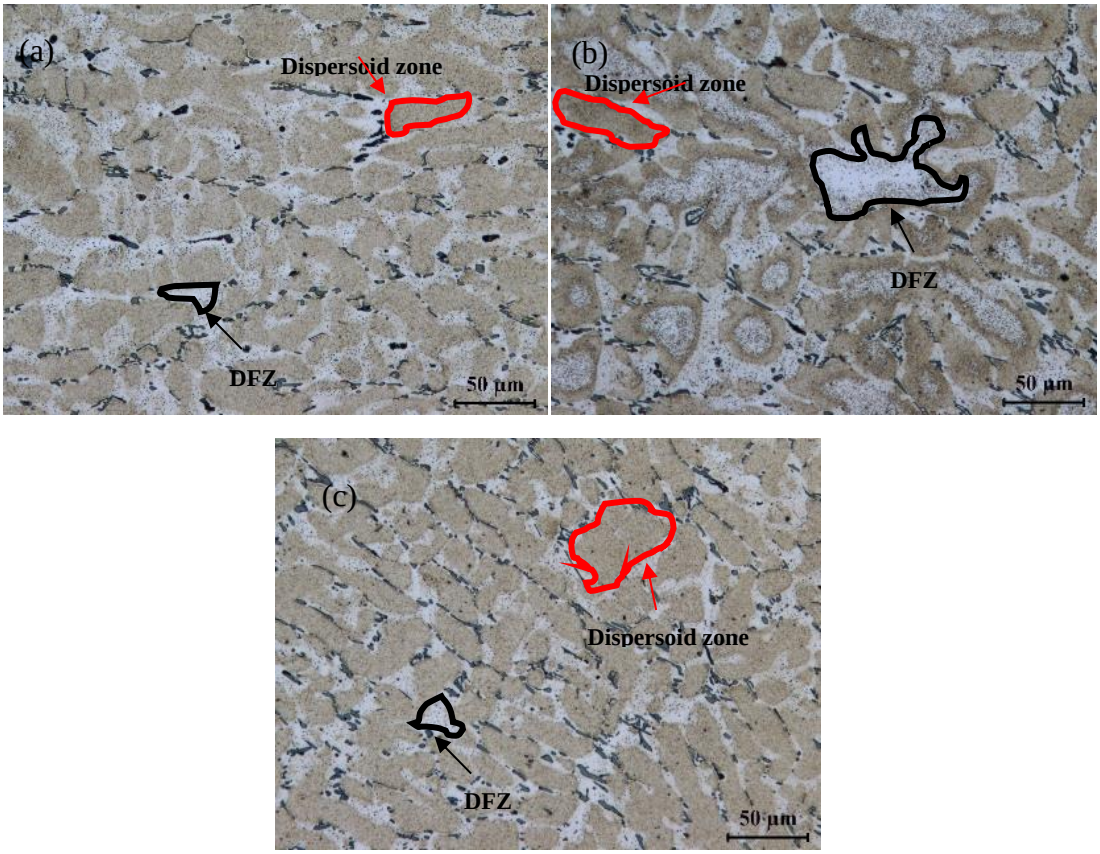

Fig. 5.4 Optical images showing the precipitation of dispersoids in the M1 alloy under different heat treatment conditions, (a) 375ºC/24h, (b) 175ºC/5h + 375/24h and (c) 250ºC/2h + 375 ºC/24h.

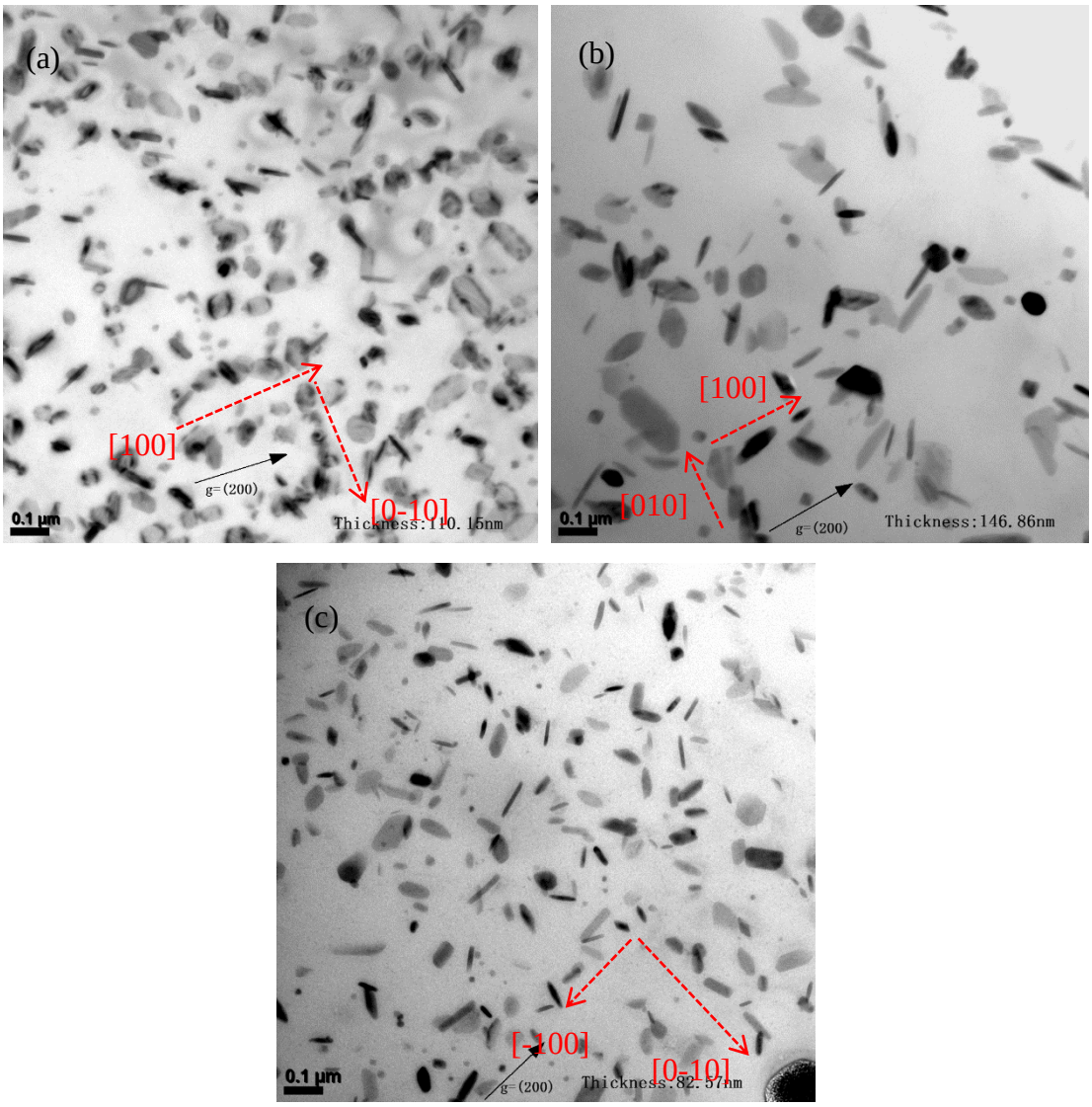

Fig. 5.5 TEM bright field images showing the dispersoids in the M1 alloy after different heat treatments, (a) 375ºC/24h, (b) 175ºC/5h + 375ºC/24h and (c) 250ºC/12h + 375ºC/24h, recorded near the $[001]_{Al}$ zone axis. The arrows indicate the $<100>_{Al}$ orientation.

Table 5.2 Dispersoid and DFZ parameters measured under different conditions

Alloy	Heat treatment	Volume Fraction of DFZ (%)	Equivalent diameter of dispersoids (nm)	Number density of dispersoids (μm^{-3})	Volume Fraction of dispersoids (%)
Base	375ºC/24h	79	97	72	0.32
Base	375ºC/72h	51.4	80	-	0.82
M1 Alloy	375ºC/24h	26.4	50	1055	2.69
M1 Alloy	175ºC/5h+375ºC/24h	30	56	563	1.93
M1 Alloy	250ºC/5h+375ºC/24h	23	42	1326	2.15
Deformed M1 Alloy	375ºC/24h	7	68	294	2.58

5.3.3 Precipitation of α-Al(MnFe)Si dispersoids in the deformed M1 alloy

The optical microstructure of the deformed M1 sample after the heat treatment at 375ºC/24h is shown in Fig. 5.6. At first glance, it appears that the dispersoids appeared almost everywhere, and their distribution was more uniform than that of the non-formed M1 alloy (Fig. 5.4a). Furthermore, hardly any DFZs were observed in the deformed samples. The image analysis results show that the volume fraction of DFZ in the deformed samples was only 7.0%, while it was 26.5% in the non-formed M1 alloy (Table 5.2). This implies that the deformation has a strong benefit on the uniformity of the dispersoid distribution, particularly in the interdendrite regions.

A close observation revealed that the density of the dispersoids was not even in the matrix, and some areas had a higher density than others. To better assess the number density and volume fraction of dispersoids in the deformed sample, the dispersoid zone was further

divided to the dense dispersoid zone and the less dense dispersoid zone, as shown in Fig. 5.6 The former is mostly in the core of the aluminum grain and the latter is found toward the interdendrite region and close to Mn-containing intermetallic particles. TEM observation confirmed the existence of the two different zones and Fig. 5.7 shows TEM images of the different densities of the α-Al(MnFe)Si dispersoids in these two zones. To quantify the number density and volume fraction of the dispersoids, the following equations were used in the image analysis on TEM images:

$$N_{av} = N_d \cdot V_d + N_l \cdot V_l \qquad \text{Eq. 5.2}$$

$$V_d = V_{dd} \cdot V_d + V_{dl} \cdot V_l \qquad \text{Eq. 5.3}$$

where N_{av} is the average number density, N_d is number density in the dense zone, V_d is the volume fraction in the dense zone, N_l is the number density in the less dense zone, V_l is the volume fraction in the less dense zone in the sample, V_d is the volume fraction of dispersoid in the sample, V_{dd} is the volume fraction in dense zone, and V_{dl} is the volume fraction in the less dense zone.

The results are listed in Table 5.2. It can be seen that the dispersoid size is larger and the number density is smaller than it is in the non-deformed sample under the same heat treatment condition. However, the dispersoid volume fraction in the deformed sample is almost the same as that in the non-deformed sample. It was reported that dislocations may enhance the precipitation kinetics of second phase precipitation [19-24]. The effect of deformation and thus the generated dislocations on the dispersoid precipitation will be discussed later.

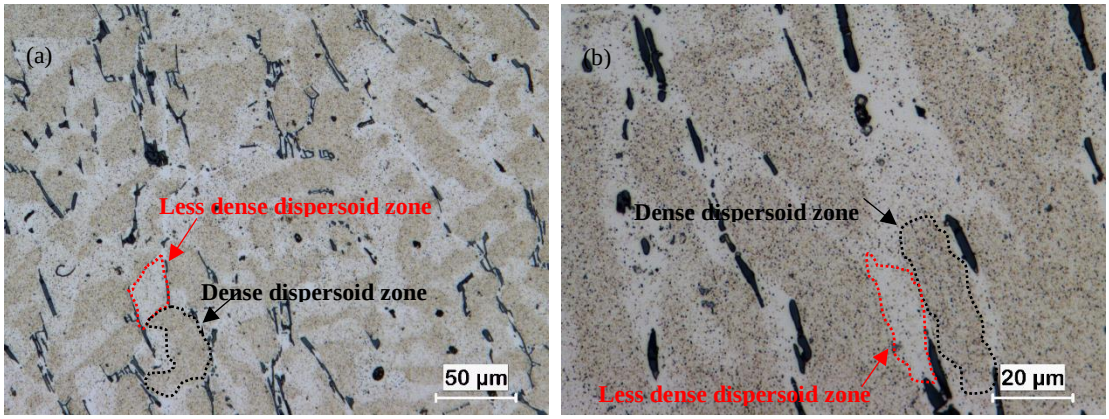

Fig. 5.6 Optical image showing the precipitation of dispersoids in the deformed M1 alloy after heat treatment at 375ºC/24h: (a) the dense dispersoid zone and the less dense dispersoid zone and (b) enlarged image of (a).

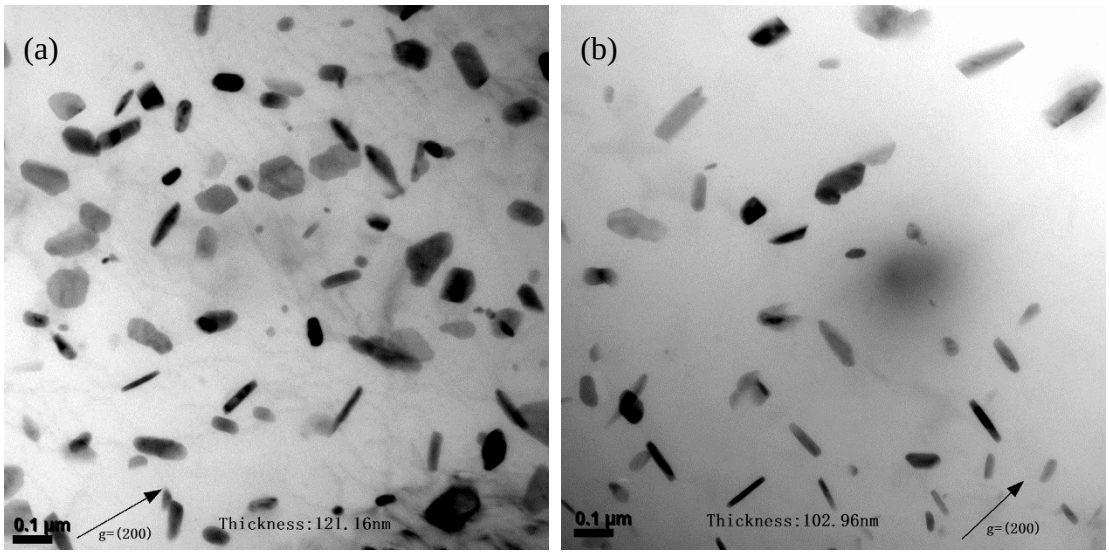

Fig. 5.7 TEM bright field images showing the dispersoids in the deformed M1 alloy (0.2 strain + 375ºC/24h), a) in the dense dispersoid zone and b) in the less dense dispersoid zone.

5.3.4 The effect of Mg and deformation on microhardness

To confirm the dispersiod precipitation and its strengthening effect, the Vicker microhardness of the base and M1 alloys under different conditions was measured. The results of hardness measurements for the base and M1 alloys are shown in Fig. 5.8 At the same heat treatment condition (375ºC/24h), the hardness of the Mg containing M1 alloy is much higher

than that of the base alloy. Moreover, all hardness values of the Mg containing M1 alloy under various heat treatment conditions are higher than that of the base alloy, indicating the strong dispersoid strengthening effect caused by adding Mg.

The hardness of the sample after the 250^{o}C/12h + 375 ^{o}C/24h two-step treatment is 65 HV while it is 58 HV for the sample that experienced the 175^{o}C/5h + 375 ^{o}C/24h two-step treatment, suggesting that the two-step treatment at 250^{o}C/5h + 375 ^{o}C/24h is more effective at enabling the dispersoid strengthening effect, which was confirmed by the optical and TEM observations (Figs. 5.4 and 5.5).

The hardness of the deformed sample (0.2 stain compression) is moderately higher than that of the non-deformed M1 sample under the same heat treatment condition. The deformed sample's hardness is similar to the sample after the 250^{o}C/5h + 375 ^{o}C/24h two-step treatment. Therefore, the best strengths of materials are achieved by the two-step 250^{o}C/5h + 375^{o}C/24h treatment and by the deformation.

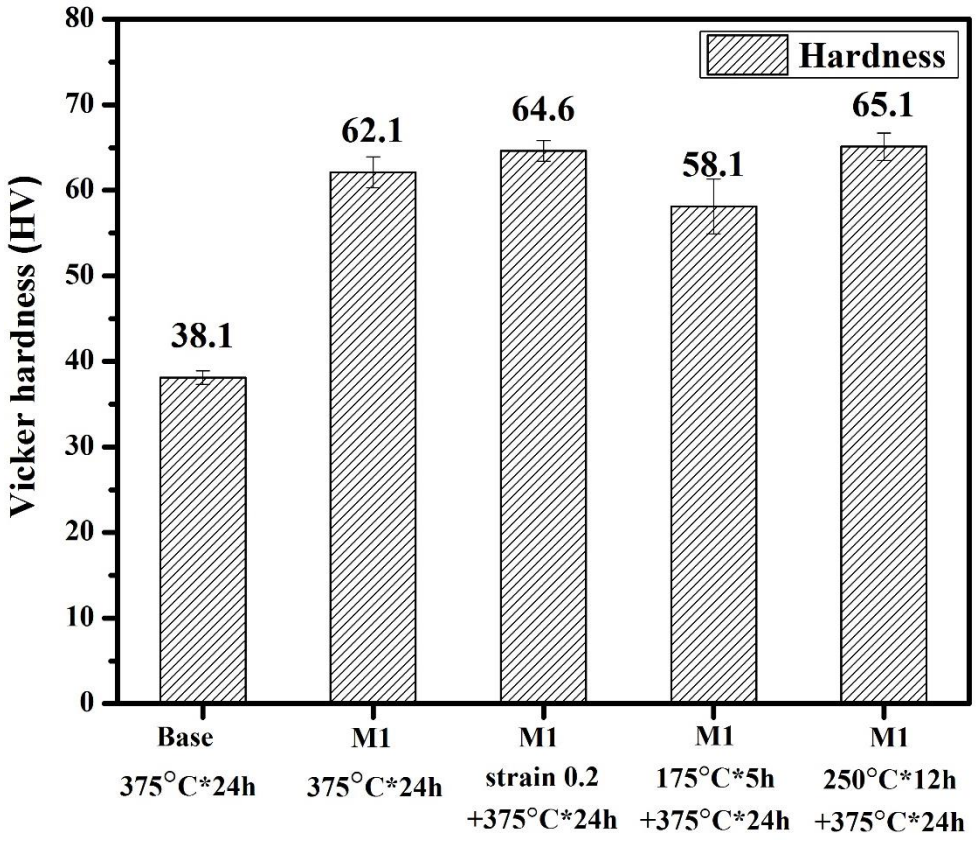

Fig. 5.8 Microhardness of the base alloy and M1 alloy under various experimental conditions.

5.3.5 Metastable Mg_2Si-based nucleation mechanism

According to above observation, the number density and the volume fraction of α-Al(MnFe)Si dispersoids in the M1 alloy (1%Mg) are much higher than those in the base alloy without Mg. It should be noted that α-Al(MnFe)Si dispersoids do not contain Mg, which means that Mg is not a necessary component of the α-Al(MnFe)Si phase. The only possible phase containing Mg in the M1 alloy is the metastable Mg_2Si precipitates that appeared during heating process. To explore how Mg and metastable Mg_2Si promote the dispersoid formation, the precipitation process in the M1 alloy during heat treatment was investigated using the quenching technique described in Fig. 5.1a and TEM analysis.

Fig. 5.9 shows TEM images of the precipitation of the metastable Mg_2Si precipitates and α-Al(MnFe)Si dispersoids during different stages of the heat treatment. When the samples were heated to 275 ^oC, a number of lath-like precipitates appeared (Fig. 5.9a), which were identified to be β'-Mg_2Si based on the morphology and orientation of the precipitates [9-12]. The small black dots are the cross sections of the lath-like precipitates. These lath-like precipitates growing along $<100>_{Al}$ are approximately 10 nm in width and 100-200 nm in length. It is evident that the supersaturated solid solution after solidification in the M1 alloy was decomposed during the heating to 275 ^oC and the β'-Mg_2Si precipitated. It should be mentioned that no α-Al(MnFe)Si dispersoids formed at this stage.

After the samples heated to 375 ^oC, all lath-like β'-Mg_2Si dissolved and left only a few of the cubic-like equilibrium Mg_2Si particles (Fig. 5.9b). No visible α-Al(MnFe)Si dispersoids were observed. During isothermal holding at 375℃, fine α-Al(MnFe)Si dispersoids appeared, and after 30 mins the size of dispersoids was approximately 10-20 nm (Fig. 5.9c). The dispersoids were distributed along $<001>_{Al}$ direction which is the preferred precipitation orientation of previous β'-Mg_2Si.

After holding for 1 and 2 hours at 375^oC, the dispersoids gradually grew, as shown in Figs. 5.9d and e. The precipitation direction of dispersoids along $<001>_{Al}$ is still clearly visible, which means that most dispersoids nucleated and grew on the previous β'-Mg_2Si sites, even though they dissolved. As the holding time prolonged towards 24 hours, Ostwald ripening

(coarsening) occurred and the size of dispersoids after 24 h reached 50 nm, as shown in Fig. 5.6a and Table 5.2. Due to a great number of dispersoids, the preferred precipitation direction of the dispersoids seems to be a little unclear. However, a majority of the dispersoids can still be seen distributed along $<001>_{Al}$ direction (see the marks in Fig. 5.6). Certainly, after the initial nucleation and growth, the dispersoids might have chances to nucleate and grow on other sites, such as at dislocations. After being heat-treated for 24 h, it is not necessary that all the dispersoids were along $<001>_{Al}$ direction. It is also worth mentioning that the nucleation of the dispersoids on equilibrium β-Mg_2Si was not observed.

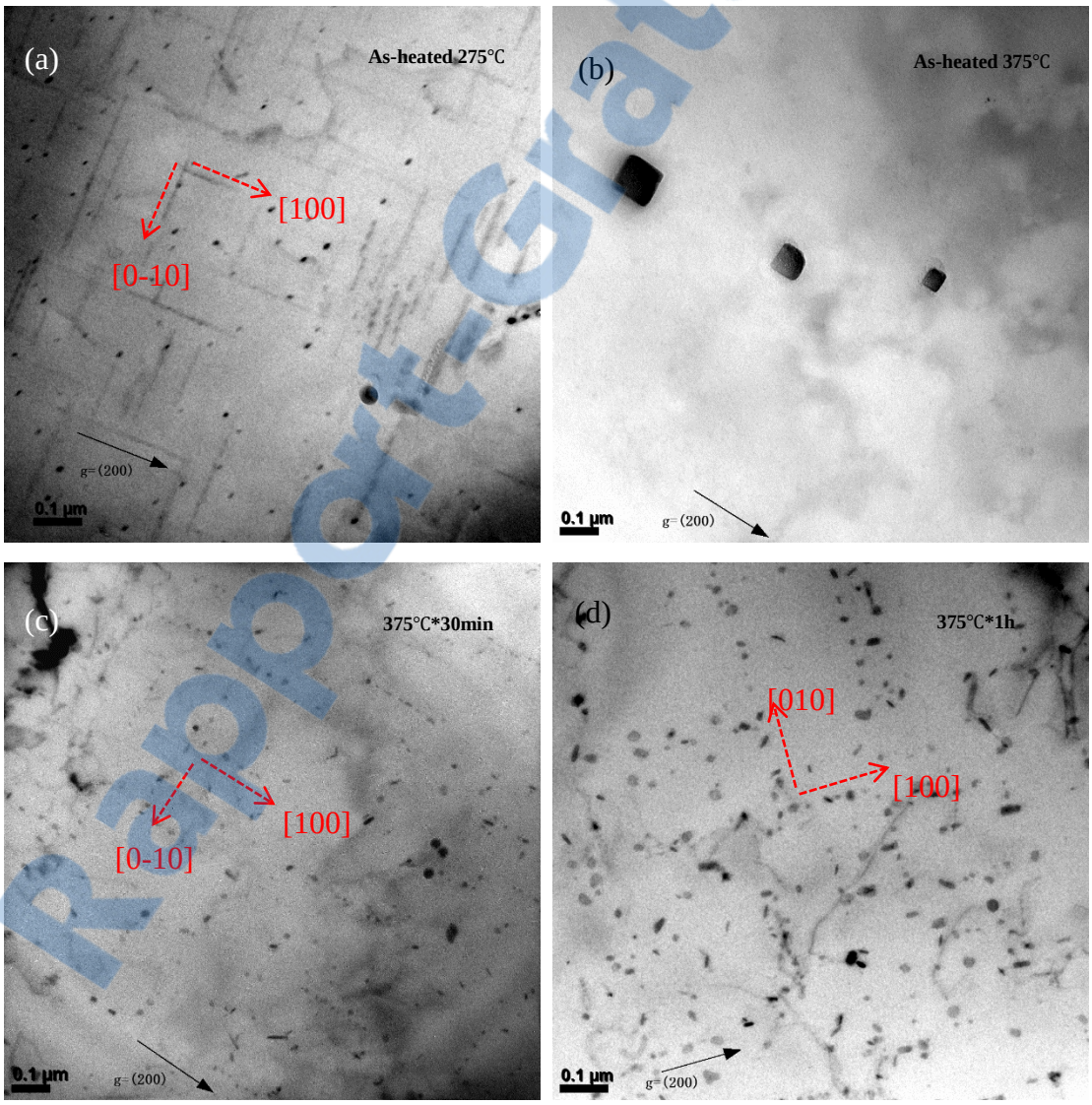

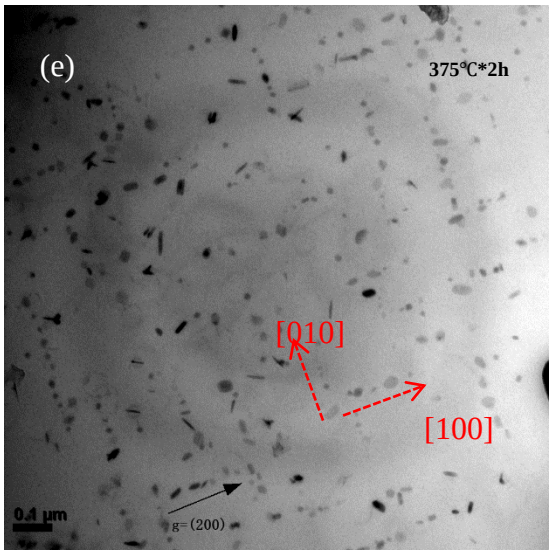

Fig. 5.9 The precipitation process in the M1 alloy (a) as-heated at 275 ºC, (b) as-heated at 375 ºC, (c) 375 ºC for 30 min, (d) 375 ºC for 1 h, (e) 375 ºC for 2 h.

The local chemical composition at the sites of dissolved β'-Mg_2Si was analyzed using TEM-EDS line scanning. The typical result of the Si distribution along the dissolved β'-Mg_2Si in the sample held for 15 minutes at 375 ºC are shown in Figure 5.10. It can be seen that a few small α-Al(MnFe)Si particles began to precipitate along $<001>_{Al}$ direction (see Fig. 5.10a), which was a previous site of β'-Mg_2Si. Across this site (the scan line A-C), the Si concentration at the location of the dissolved β'-Mg_2Si was higher than in the surrounding aluminum matrix (local Si enrichment), as shown in Fig. 5.10b. As mentioned above, Mg is not a necessary element but Si is the essential element for α-Al(MnFe)Si dispersoid formation. Without Si, α-Al(MnFe)Si dispersoids can hardly form in the matrix. It becomes evident that α-Al(MnFe)Si would preferentially nucleate on the sites of previous β'-Mg_2Si precipitates, which could provide more Si atoms than at other places in the aluminum matrix. It should be noted that the intermediate phase, the u-phase, that could promote the nucleation of α-Al(MnFe)Si reported in [18], has not been observed in the present study, which could be due to the different alloy compositions and heat treatment conditions.

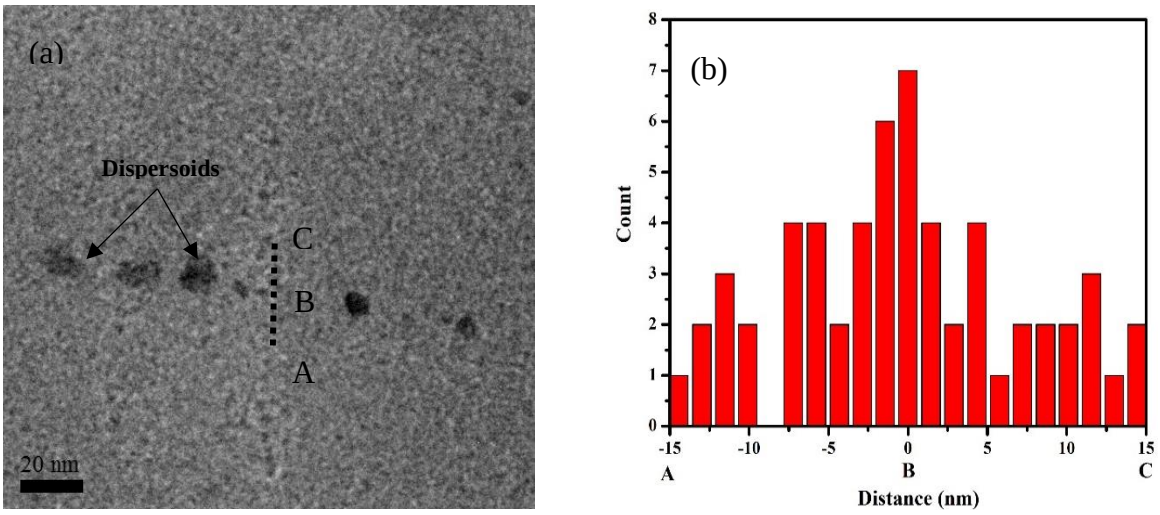

Fig. 5.10 TEM analysis of the M1 sample held at 375ºC for 15 minutes showing the local Si enrichment on the sites of previous β′-Mg_2Si precipitates, (a) TEM image on the site of a previous β′-Mg_2Si and the position of the line scanning (A-C) and (b) Si distribution along the line A-C.

In the section 5.3.2, the effect of two-step heat treatments, 175ºC/5h + 375ºC/24h and 250ºC/12h + 375ºC/24h, on the precipitation of α-Al(MnFe)Si dispersoids were described. The details of the precipitation process under these two conditions are shown in Fig. 5.11. For the sample treated at 175 ºC for 5 h, the only phase that appeared was the needle-like β"-Mg_2Si located along the $<001>_{Al}$ direction (Fig. 5.11a). The needle-like β"-Mg_2Si precipitates were approximately 3 nm in width and 20-100 nm in length. The corresponding SADP (Fig. 5.11e) was consistent with literature[27]. During further heating to 375 ºC, all needle-like β"-Mg_2Si dissolved in the aluminum matrix. For the sample treated at 250 ºC for 12 h, the precipitated phase was lath-like β'-Mg_2Si with a size of approximately 10 nm in width and 100-200 nm in length (Fig. 5.11b). The corresponding SADP was shown in Fig. 5.11f which the SADP of β'-Mg_2Si in previous literature[28]. β'-Mg_2Si also dissolved in aluminum matrix during further heating to 375 ºC. After holding for 1 h at 375 ºC in both 175ºC/5h and 250ºC/12h samples, all of the α-Al(MnFe)Si dispersoids lay along $<001>_{Al}$ direction (Figs. 5.11c and d), which indicates that the α-Al(MnFe)Si dispersoids nucleated and grew in the sites of previous β"-

Mg_2Si or β'-Mg_2Si precipitates. Although the β''-Mg_2Si precipitates in the 175ºC/5h sample are denser than the β'-Mg_2Si precipitates in the 250ºC/12h sample, the amount of α-Al(MnFe)Si dispersoids in the 175ºC/5h + 375 ºC/1h sample (Fig. 5.11c) is much lower than that in the 250ºC/12h + 375ºC/1h sample (Fig. 5.11d). Compared to the one step heat treatment sample (375ºC/1h, Fig. 5.9d), the amount of α-Al(MnFe)Si dispersoids in the 175ºC/5h + 375ºC/1h sample is also lower. In addition, the number density and volume fraction of the dispersoids in the final treated sample (175ºC/5h + 375ºC/24h) are lower than those in the one step (375ºC/24h) and two-step (250ºC/12h + 375ºC/2h) final samples (Table 5.2), which both contained the pre-existing β'-Mg_2Si. It is apparent that pre-existing β'-Mg_2Si precipitates are more effective at promoting dispersoid nucleation than pre-existing β''-Mg_2Si precipitates. It is most likely that the local Si enrichment of dissolved β'-Mg_2Si is larger than that of the β''-Mg_2Si precipitates, because of the large size of β'-Mg_2Si. This, in turn, creates a more favorable condition for α-Al(MnFe)Si dispersoid nucleation and growth.

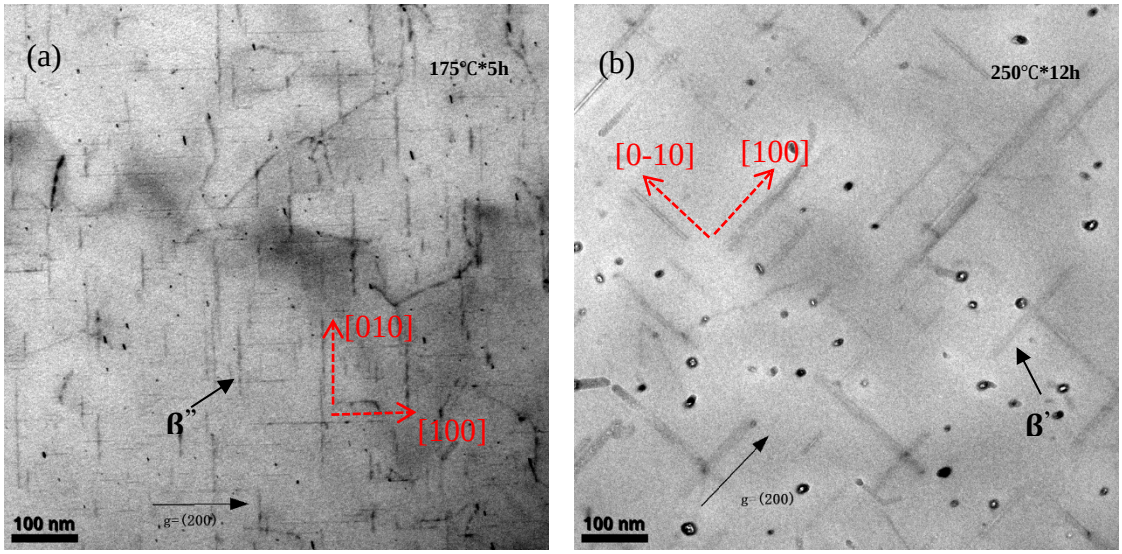

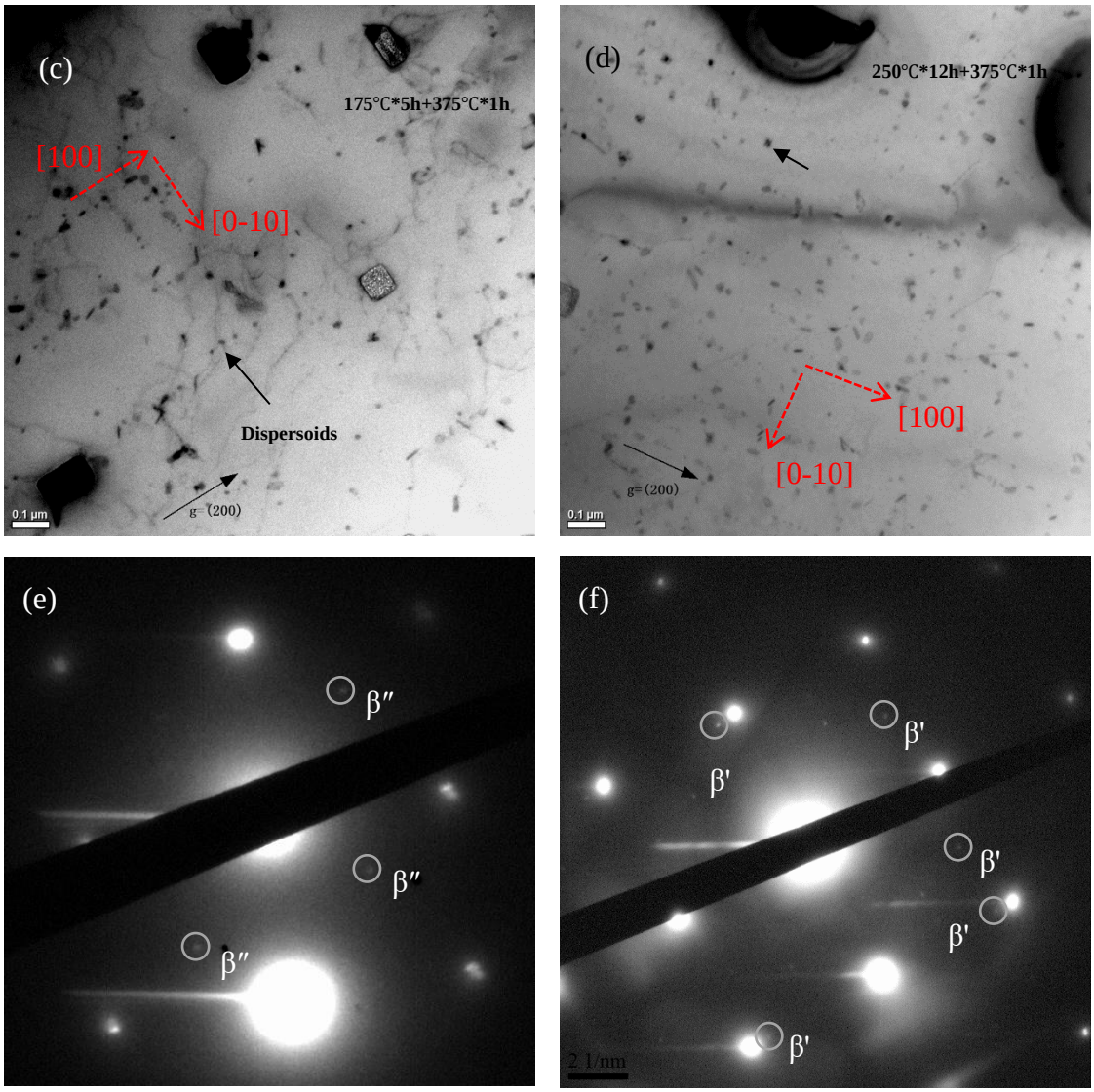

Fig. 5.11 TEM images of the M1 samples experienced (a) 175ºC for 5 h, (b) 250 ºC for 12 h, (c) 175ºC for 5 h + 375 ºC for 1 h, (d) 250ºC for 12 h + 375ºC for 1 h, (e) SADP corresponding to the samples after heat-treatment 175ºC for 5 h, (f) SADP corresponding to the samples after heat-treatment 250ºC for 12 h.

Based on the above results, the nucleation mechanism of the dispersoids based on the metastable Mg_2Si precipitates can be described as follows (Fig. 5.12). In the Mg containing M1 samples under various heat treatments (including both one step and two-step treatments), a large number of metastable Mg_2Si phase first precipitated during heating process at the temperature range of 150-275 ºC (Fig. 5.12a), and then gradually dissolved at higher temperatures of 300-375 ºC (Fig. 5.12b). The sites of the dissolved metastable Mg_2Si were still

Si-rich, which provided favorable sites for the nucleation of α-Al(MnFe)Si dispersoids. When the samples reach the formation temperature of α-Al(MnFe)Si, for example above 350-375 ºC, α-Al(MnFe)Si dispersoids started to nucleate and grow along the $<001>_{Al}$ direction in the Si-rich sites of the previously metastable Mg_2Si (Fig. 5.12c). During heating process, two possible metastable phases could be formed under different heating rates, namely, β"-Mg_2Si and β'-Mg_2Si. The results obtained in the present work indicated that pre-existing β'-Mg_2Si precipitates were more effective in the promotion of the dispersoid nucleation than pre-existing β"-Mg_2Si. This probably implies that the size of the lath-like β'-Mg_2Si precipitates was larger than that of needle-like β"-Mg_2Si, and thus the available Si on Si-rich sites of the former was higher than that of the latter, resulting in a more favorable condition for dispersoid nucleation and growth.

It is understandable that in the Mg-free base alloy, no pre-existing metastable Mg_2Si could be formed during the heating process. Thus, the precipitation of α-Al(MnFe)Si dispersoids was so difficult that only an insufficient number of dispersoids formed even after extensively prolonged heat treatment (375ºC/72h). In previous works [17, 18], the pre-existing β'-Mg_2Si was reported to be the prerequisite for a high density nucleation of α-Al(MnFe)Si dispersoids in Mn containing Al-Mg-Si alloys, which is confirmed by the present work in the Al-Mn-Mg 3xxx alloy.

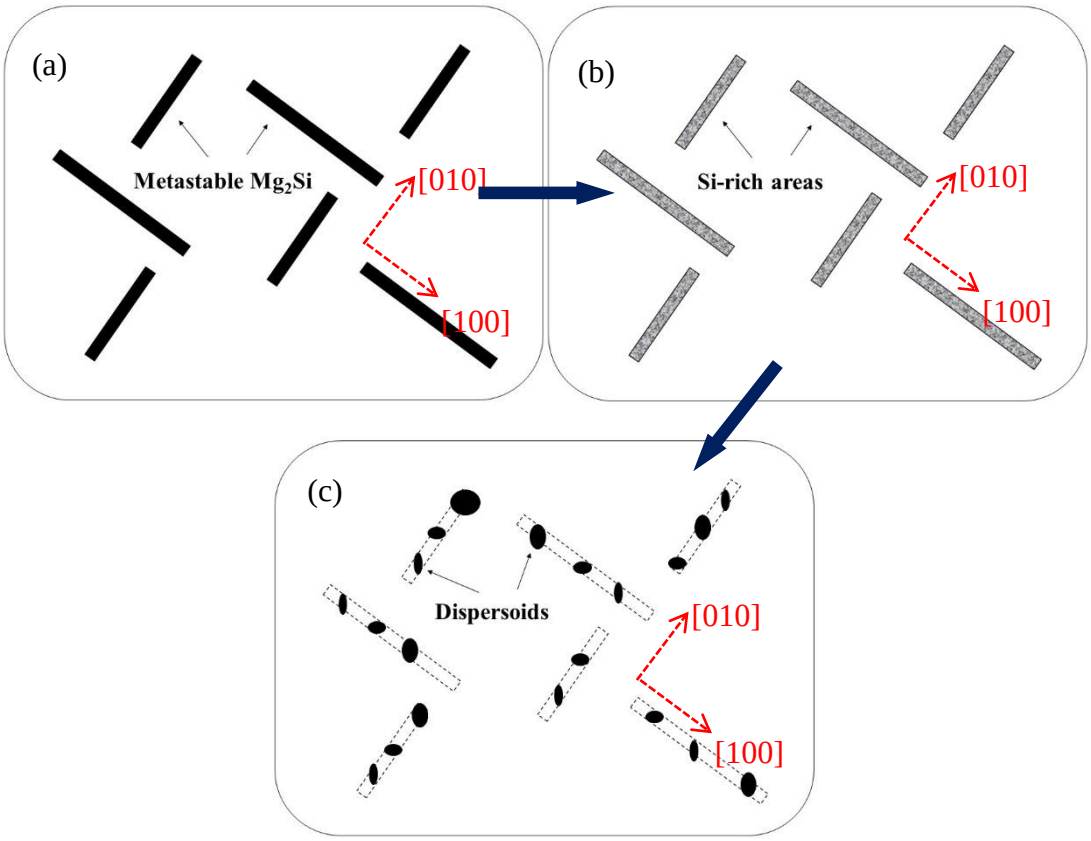

Fig. 5.12 Schematic diagram of the dispersoid formation based on metastable Mg_2Si nucleation mechanism, (a) metastable Mg_2Si precipitated, (b) Mg_2Si dissolved forming Si-rich areas and (c) α-Al(MnFe)Si disperspoid nucleation and growth in the Si-rich sites of previous metastable Mg_2Si along the $<001>_{Al}$ direction.

5.3.6 Dislocation-based nucleation mechanism

As described in Section 3.3, the cold deformation of the M1 sample that generated a great number of dislocations had an important influence on the dispersoid precipitation. {111} planes are the close-packed planes of aluminum and they are also the main dislocation slip planes. Hence, TEM bright field images were taken on the (-111) plane near the [011] zone axis to observe the dislocations and the precipitation process (see Fig. 5.13). After the deformed sample was heated to 275 ºC, both β'-Mg_2Si and dislocations can be observed as shown in Fig. 5.13a and b. When the deformed M1 sample held at 375 ºC for 1 h, dispersoids and dislocations

coexisted in aluminum matrix, but the β'-Mg_2Si disappeared and dissolved (Fig. 5.13c). Here, most of the dispersoids precipitated on dislocations, markedly different from the precipitation seen in the non-deformed sample (Fig. 5.9a).

To verify the orientation relationship between the α-Al(MnFe)Si dispersoids and the β'-Mg_2Si precipitates, the microstructure of the deformed samples was observed with the (200) crystal plane near the [001] direction. Growing along the $<001>_{Al}$ direction, lath-like β'-Mg_2Si precipitates were clearly seen without any interference from the dislocations in the sample heated to 275 ºC (Fig. 5.13b). The sample held at 375 ºC for 1 h showed that β'-Mg_2Si had already dissolved but that α-Al(MnFe)Si dispersoids did not lie along the $<001>_{Al}$ direction, but rather along the dislocations (Figs. 5.13c and d). This finding indicates that the sites of the previous β'-Mg_2Si precipitates were no longer the priority locations for dispersoids nucleation in the deformed sample. Due to the presence of a great number of dislocations, the fast diffusion of the alloying elements (including Si) would weaken the advantage of the local Si enrichment from the dissolved β'-Mg_2Si for α-Al(MnFe)Si dispersoid nucleation. Instead of the sites of previous β'-Mg_2Si, dislocations become the predominate sites for the dispersoid nucleation in the deformed sample.

When the deformed sample was held for 24 hours at 375 ºC, the dispersoids kept growing and became coarse (Fig. 5.13e). The size of dispersoids in the deformed sample after heating at 375 ºC for 24 h was larger than that in the non-deformed sample, whereas the number density of dispersoids in the former is less than that in the latter (Table 5.2). It is likely that the fast diffusion of alloying elements through the dislocations can benefit the Ostwald ripening of dispersoids (coarsening). However, the volume fraction of the dispersoids in the deformed sample remains at a level similar to that found in the non-deformed sample.

In the as-cast microstructure, there were Mn depletion zones close to the Al_6(Mn,Fe) intermetallic particles and to the aluminum grain boundaries [29], causing the DFZs during heat treatment because of the lack of the essential element Mn required for α-Al(MnFe)Si dipersoid formation (Fig. 5.4). In the deformed sample, a great number density of dislocation piled up around intermetallic particles and grain boundaries because the intermetallic particles

and grain boundaries were barriers to block dislocation migrations during deformation. During heat treatment, these dislocations acted not only as fast diffusion channels to transport Mn solutes to the Mn depletion zones but also as favorable nucleation sites, making the nucleation and growth of α-Al(MnFe)Si dipersoids possible in those zones. This is why, besides the dense dispersoid zones in the cores of the aluminum grains, there were the less dense despersoid zones close to the Al_6(Mn,Fe) intermetallic particles and grain boundaries in the deformed sample (Fig. 5.6), which was the DFZ where the precipitation of α-Al(MnFe)Si was impossible in the non-deformed sample. This resulted in a large reduction of DFZs and a more uniform dispersoid distribution when compared to the non-deformed sample.

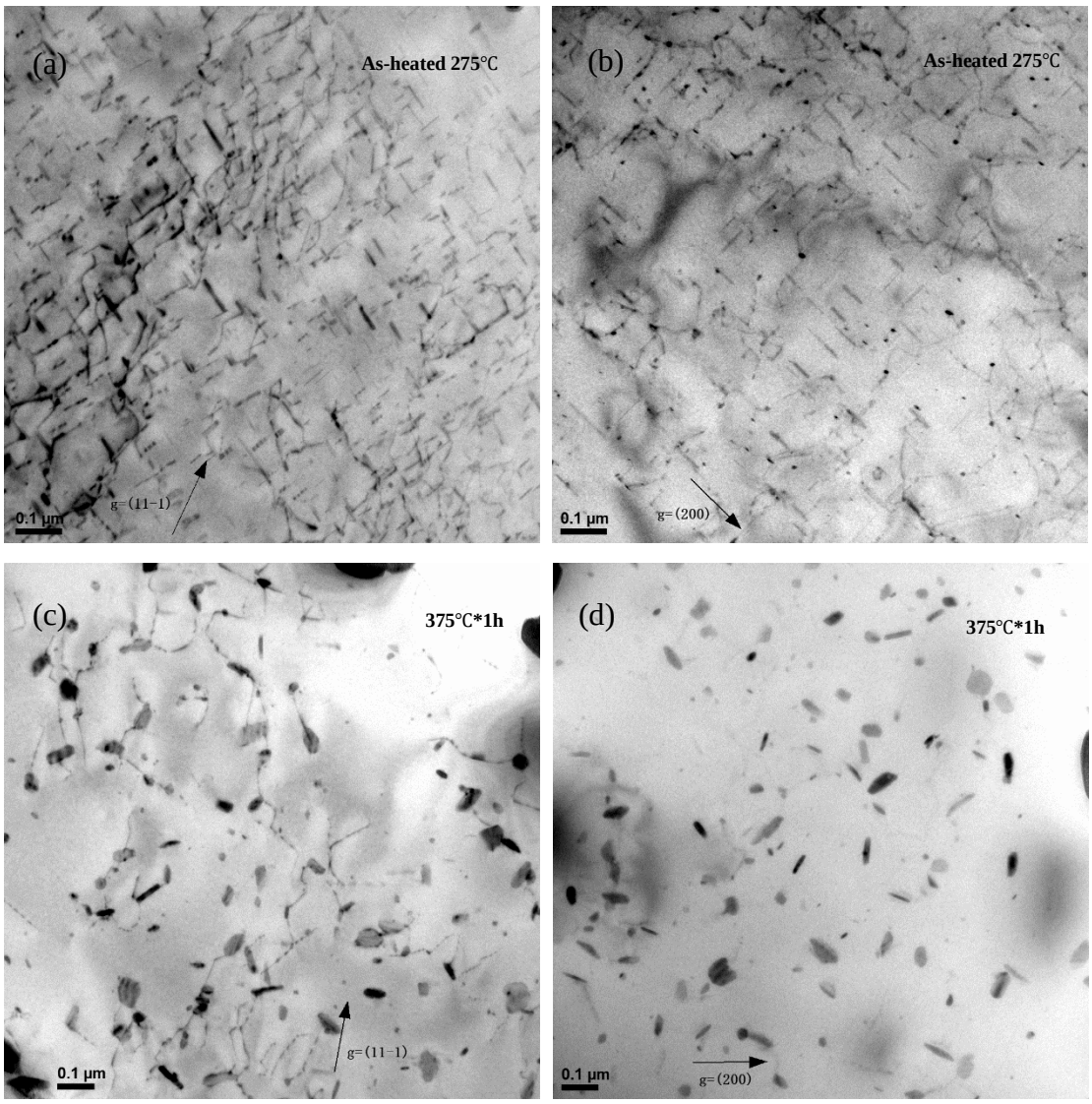

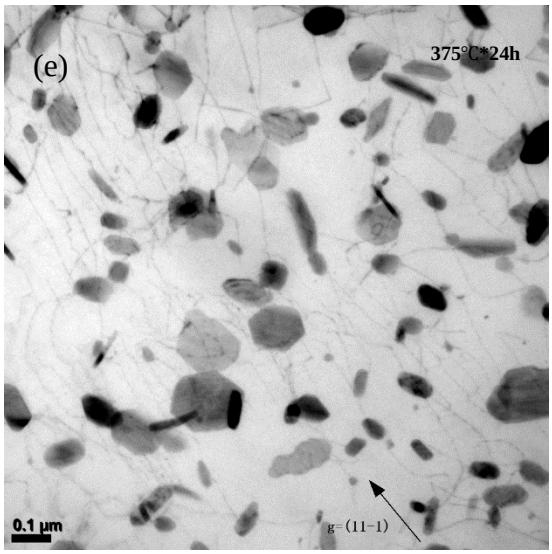

Fig. 5.13 The precipitation process in the deformed M1 samples (a) heated to 275 ºC showing dislocations, recorded near $[011]_{Al}$; (b) heated to 275 ºC showing β'-Mg_2Si, recorded near $[001]_{Al}$; (c) held at 375 ºC for 1 h, recorded near $[011]_{Al}$, (d) held at 375 ºC for 1 h, recorded near $[001]_{Al}$; (e) held at 375 ºC for 24 h, recorded near $[011]_{Al}$.

Based on the above results, the nucleation mechanism of the dispersoids based on dislocations in the deformed sample can be schematically expressed as follows (Fig. 5.14). During the heating process toward 275 ºC, metastable β'-Mg_2Si phase first precipitated out, and a great number of dislocations and β'-Mg_2Si co-existed in the microstructure (Fig. 5.14a). As the temperature continued to increase toward 375 ºC, β'-Mg_2Si precipitates dissolved before the precipitation of α-Al(MnFe)Si dispersoids, and many dislocations remained in the aluminum matrix (Fig. 5.14b). When the temperature rose above the precipitation temperature of the dispersoids (thermal holding at 375 ºC), α-Al(MnFe)Si dispersoids began to nucleate and grow on the dislocations (Fig. 5.14c). In the deformed sample, the dislocations acted as the preferable sites for the dispersoid nucleation. Due to the fast diffusion of the alloying elements and favorable nucleation conditions created by the presence of a great number of dislocations, α-Al(MnFe)Si dispersoids can also precipitate in the Mn depleted zone (formerly the DFZ) close to intermetallic particles and grain boundaries, resulting in an overall uniform dispersoid distribution by reducing the DFZs in the microstructure.

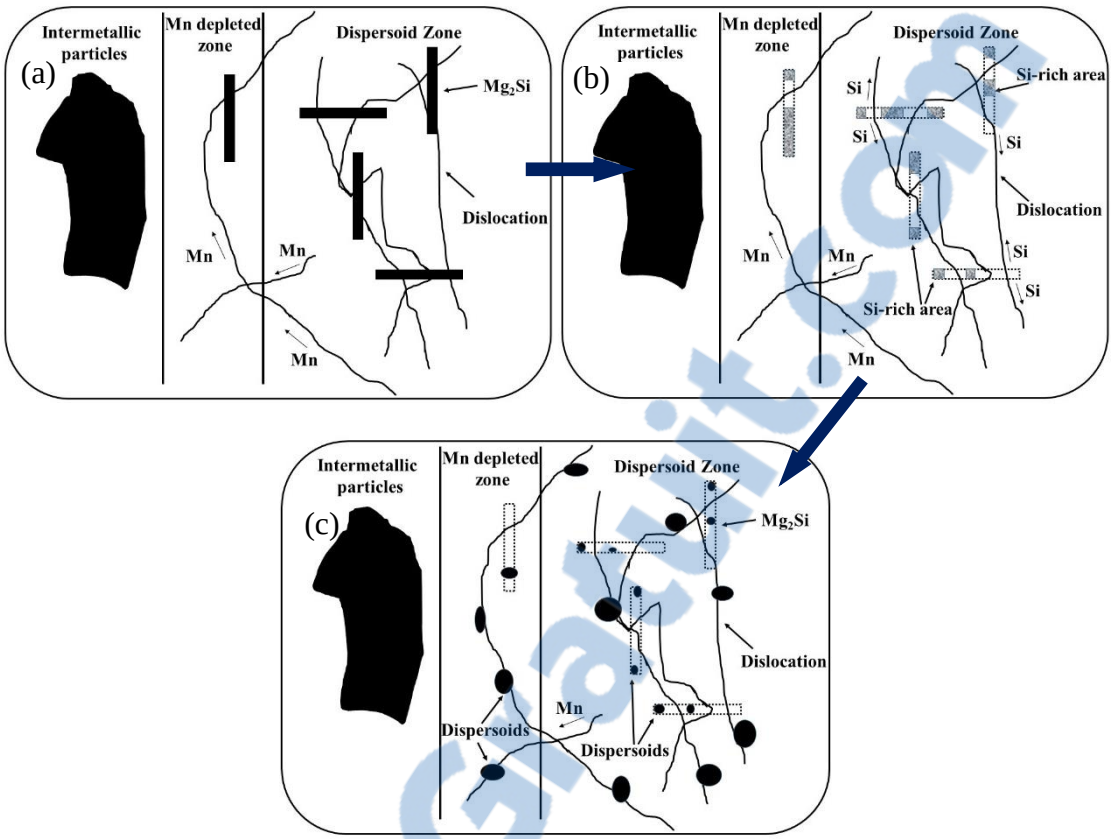

Fig. 5.14 Schematic diagram of the dislocation-based nucleation mechanism of α-Al(MnFe)Si dispersoids in the deformed sample, (a) metastable Mg_2Si precipitated and co-existed with dislocations; (b) metastable Mg_2Si dissolution and Si and Mn diffusion along dislocations and (c) α-Al(MnFe)Si dispersoid nucleation and growth on dislocations including in the Mn depleted zone (formerly the DFZ).

5.5 Conclusions

1) In Al-Mn-Mg 3xxx alloys, Mg plays an important role in promoting the formation of α-Al(MnFe)Si dispersoids. Without Mg addition, the precipitation of α-Al(MnFe)Si dispersoids was so difficult that only an insufficient number of dispersoids could be obtained. The number density and volume fraction of the dispersoids in the Mg containing alloy are much higher than that in the base alloy without Mg, resulting in a strong dispersoid strengthening effect.

2) During heating process of the heat treatment of the Mg containing alloy, metastable Mg_2Si precipitated and dissolved, leaving local Si-rich areas, which provided favorable nucleation sites for α-Al(MnFe)Si dispersoids. Both metastable β"-Mg_2Si and β'-Mg_2Si have a positive effect on increasing the number density and volume fraction of the dispersoids. However, equilibrium β-Mg_2Si precipitates do not have any effect on the dispersoid formation.
3) β'-Mg_2Si precipitates are more effective than β"-Mg_2Si in promoting dispersoid nucleation. It could be attributed to the fact that β'-Mg_2Si would provide more available Si in the Si-rich areas for α-Al(MnFe)Si nucleation and growth than β"-Mg_2Si.
4) In the deformed sample, the dislocations become the preferable sites for α-Al(MnFe)Si dispersoid nucleation. Due to the presence of a great number of dislocations, α-Al(MnFe)Si dispersoids can nucleate and grow in the Mn depleted zone (formerly the DFZ) close to intermetallic particles and grain boundaries, resulting in a more uniform dispersoid distribution compared to the non-deformed sample.
5) The dispersoid nucleation mechanisms based on both metastable Mg_2Si and dislocations are proposed and discussed.

References

1. K. Liu, X. G. Chen, Development of Al–Mn–Mg 3004 alloy for applications at elevated temperature via dispersoid strengthening, Materials & Design. 84 (2015) 340-350. Doi: http://dx.doi.org/10.1016/j.matdes.2015.06.140.
2. Z. Li, Z. Zhang, X. G. Chen, Effect of magnesium on dispersoid strengthening of Al—Mn—Mg—Si (3xxx) alloys, Transactions of Nonferrous Metals Society of China. 26 (2016) 2793-2799. Doi: http://dx.doi.org/10.1016/S1003-6326(16)64407-2.
3. K. Liu, X.-G. Chen, Evolution of Intermetallics, Dispersoids, and Elevated Temperature Properties at Various Fe Contents in Al-Mn-Mg 3004 Alloys, Metallurgical and Materials Transactions B. 47 (2016) 3291-3300. Doi: http://dx.doi.org/10.1007/s11663-015-0564-y.

4. Y. J. Li, A. M. F. Muggerud, A. Olsen, T. Furu, Precipitation of partially coherent α-Al(Mn,Fe)Si dispersoids and their strengthening effect in AA 3003 alloy, Acta Materialia. 60 (2012) 1004-1014. Doi: http://dx.doi.org/10.1016/j.actamat.2011.11.003.

5. A. M. F. Muggerud, E. A. Mørtsell, Y. Li, R. Holmestad, Dispersoid strengthening in AA3xxx alloys with varying Mn and Si content during annealing at low temperatures, Materials Science and Engineering: A. 567 (2013) 21-28. Doi: http://dx.doi.org/10.1016/j.msea.2013.01.004.

6. Y. J. Li, L. Arnberg, Quantitative study on the precipitation behavior of dispersoids in DC-cast AA3003 alloy during heating and homogenization, Acta Materialia. 51 (2003) 3415-3428. Doi: http://dx.doi.org/10.1016/S1359-6454(03)00160-5.

7. A. M. F. Muggerud, J. C. Walmsley, R. Holmestad, Y. Li, Combining HAADF STEM tomography and electron diffraction for studies of α-Al(Fe,Mn)Si dispersoids in 3xxx aluminium alloys, Philosophical Magazine. 95 (2015) 744-758. Doi: http://dx.doi.org/10.1080/14786435.2015.1006294.

8. K. Liu, H. Ma, X. G. Chen, Enhanced elevated-temperature properties via Mo addition in Al-Mn-Mg 3004 alloy, Journal of Alloys and Compounds. 694 (2017) 354-365. Doi: http://dx.doi.org/10.1016/j.jallcom.2016.10.005.

9. G. A. Edwards, K. Stiller, G. L. Dunlop, M. J. Couper, The precipitation sequence in Al–Mg–Si alloys, Acta Materialia. 46 (1998) 3893-3904. Doi: http://dx.doi.org/10.1016/S1359-6454(98)00059-7.

10. C. D. Marioara, S. J. Andersen, H. W. Zandbergen, R. Holmestad, The influence of alloy composition on precipitates of the Al-Mg-Si system, Metallurgical and Materials Transactions A. 36 (2005) 691-702. Doi: http://dx.doi.org/10.1007/s11661-005-0185-1.

11. S. J. Andersen, H. W. Zandbergen, J. Jansen, C. TrÆholt, U. Tundal, O. Reiso, The crystal structure of the β″ phase in Al–Mg–Si alloys, Acta Materialia. 46 (1998) 3283-3298. Doi: http://dx.doi.org/10.1016/S1359-6454(97)00493-X.

12. R. Vissers, M. A. van Huis, J. Jansen, H. W. Zandbergen, C. D. Marioara, S. J. Andersen, The crystal structure of the β′ phase in Al–Mg–Si alloys, Acta Materialia. 55 (2007) 3815-3823. Doi: http://dx.doi.org/10.1016/j.actamat.2007.02.032.

13. M. Murayama, K. Hono, Pre-precipitate clusters and precipitation processes in Al–Mg–Si alloys, Acta Materialia. 47 (1999) 1537-1548. Doi: http://doi.org/10.1016/S1359-6454(99)00033-6.

14. C. S. Tsao, C. Y. Chen, U. S. Jeng, T. Y. Kuo, Precipitation kinetics and transformation of metastable phases in Al–Mg–Si alloys, Acta Materialia. 54 (2006) 4621-4631. Doi: http://doi.org/10.1016/j.actamat.2006.06.005.

15. M. H. Jacobs, The structure of the metastable precipitates formed during ageing of an Al-Mg-Si alloy, Philosophical Magazine. 26 (1972) 1-13. Doi: http://dx.doi.org/10.1080/14786437208221015.

16. X. Wang, S. Esmaeili, D. J. Lloyd, The sequence of precipitation in the Al-Mg-Si-Cu alloy AA6111, Metallurgical and Materials Transactions A. 37 (2006) 2691-2699. Doi: http://dx.doi.org/10.1007/BF02586103.

17. H. Hirasawa, Precipitation process of Al-Mn and Al-Cr supersaturated solid solution in presence of age hardening phases, Scripta Metallurgica. 9 (1975) 955-958. Doi: http://dx.doi.org/10.1016/0036-9748(75)90551-7.

18. L. Lodgaard, N. Ryum, Precipitation of dispersoids containing Mn and/or Cr in Al–Mg–Si alloys, Materials Science and Engineering: A. 283 (2000) 144-152. Doi: http://dx.doi.org/10.1016/S0921-5093(00)00734-6.

19. C. Genevois, D. Fabrègue, A. Deschamps, W. J. Poole, On the coupling between precipitation and plastic deformation in relation with friction stir welding of AA2024 T3 aluminium alloy, Materials Science and Engineering: A. 441 (2006) 39-48. Doi: http://dx.doi.org/10.1016/j.msea.2006.07.151.

20. A. Deschamps, F. Livet, Y. Bréchet, Influence of predeformation on ageing in an Al–Zn–Mg alloy—I. Microstructure evolution and mechanical properties, Acta Materialia. 47 (1998) 281-292. Doi: http://dx.doi.org/10.1016/S1359-6454(98)00293-6.

21. A. Deschamps, Y. Brechet, Influence of predeformation and agEing of an Al–Zn–Mg alloy—II. Modeling of precipitation kinetics and yield stress, Acta Materialia. 47 (1998) 293-305. Doi: http://dx.doi.org/10.1016/S1359-6454(98)00296-1.

22. R. S. Yassar, D. P. Field, H. Weiland, The effect of predeformation on the β″ and β′ precipitates and the role of Q′ phase in an Al–Mg–Si alloy; AA6022, Scripta Materialia. 53 (2005) 299-303. Doi: http://doi.org/10.1016/j.scriptamat.2005.04.013.

23. D. Yin, Q. Xiao, Y. Chen, H. Liu, D. Yi, B. Wang, S. Pan, Effect of natural ageing and pre-straining on the hardening behaviour and microstructural response during artificial ageing of an Al–Mg–Si–Cu alloy, Materials & Design. 95 (2016) 329-339. Doi: http://doi.org/10.1016/j.matdes.2016.01.119.

24. T. Saito, S. Muraishi, C. D. Marioara, S. J. Andersen, J. Røyset, R. Holmestad, The Effects of Low Cu Additions and Predeformation on the Precipitation in a 6060 Al-Mg-Si Alloy, Metallurgical and Materials Transactions A. 44 (2013) 4124-4135. Doi: http://dx.doi.org/10.1007/s11661-013-1754-3.

25. S. P. Chen, N. C. W. Kuijpers, S. van der Zwaag, Effect of microsegregation and dislocations on the nucleation kinetics of precipitation in aluminium alloy AA3003, Materials Science and Engineering: A. 341 (2003) 296-306. Doi: http://dx.doi.org/10.1016/S0921-5093(02)00245-9.

26. J. D. Robson, T. Hill, N. Kamp, The Effect of Hot Deformation on Dispersoid Evolution in a Model 3xxx Alloy, Materials Science Forum. 794 (2014) 697-703. Doi: http://10.4028/www.scientific.net/MSF.794-796.697.

27. W. Yang, M. Wang, R. Zhang, Q. Zhang, X. Sheng, The diffraction patterns from β″ precipitates in 12 orientations in Al–Mg–Si alloy, Scripta Materialia. 62 (2010) 705-708. Doi: https://doi.org/10.1016/j.scriptamat.2010.01.039.

28. W. Yang, M. Wang, X. Sheng, Q. Zhang, L. Huang, Precipitate characteristics and selected area diffraction patterns of the β′ and Q′ precipitates in Al–Mg–Si–Cu alloys, Philosophical Magazine Letters. 91 (2011) 150-160. Doi: https://doi.org/10.1080/09500839.2010.541165.

29. Q. Du, W. J. Poole, M. A. Wells, N. C. Parson, Microstructure evolution during homogenization of Al–Mn–Fe–Si alloys: Modeling and experimental results, Acta Materialia. 61 (2013) 4961-4973. Doi: http://dx.doi.org/10.1016/j.actamat.2013.04.050.

Chapter 6 Improvement of mechanical properties and creep resistance in Al-Mn-Mg 3004 alloy with Sc and Zr addition

6.1 Introduction

Al-Mn-Mg 3004 alloys are widely used in architecture, packaging and automobile industries, because of their excellent corrosion resistance and great workability. To achieve adequate mechanical properties, the 3004 alloys are generally strengthened by work hardening. Recently, dispersion strengthening has been found to be an effective method to strength AA3xxx alloys, particularly at elevated temperature [1-5]; in this case, α-Al(Mn,Fe)Si dispersoids act as the key strengthening phase. By appropriate heat-treatment, a large number of α-Al(Mn,Fe)Si dispersoids can be precipitated in the aluminum matrix of 3004 alloys and their volume fractions can be as high as 3% when the particles are in the size range of 40-80 nm [3]. In addition, α-Al(Mn,Fe)Si dispersoids are partially coherent with the aluminum matrix [6] and thermally stable up to 300 °C [3]. Although the size of α-Al(Mn,Fe)Si dispersoids is larger than those of traditional strengthening precipitates, such as Mg_2Si and Al_2Cu, the α-Al(Mn,Fe)Si dispersoids can efficiently be used for strengthening 3004 alloys at elevated temperature due to their large volume fractions and high thermal stability [3, 5], which are very attractive features for elevated temperature applications.

In several studies [7-9], Sc was introduced into aluminum alloys to enhance their mechanical properties by forming high density nano-scale Al_3Sc precipitates. Al_3Sc precipitates were coherent with the aluminum matrix and thermally stable up to 300 °C with a low coarsening rate [8]. Zr has often been added along with Sc, and it was found that Zr could substitute Sc in Al_3Sc to form $Al_3(Sc,Zr)$ precipitates [10]. $Al_3(Sc,Zr)$ precipitates exhibited better thermal coarsening resistance than Al_3Sc precipitates [10-12]. Due to the low solubility of Sc and Zr in aluminum, the obtainable volume fractions of the $Al_3(Sc,Zr)$ precipitates are

usually low. However, the particle size of Al_3(Sc,Zr) precipitates was quite small (a few nanometers) and their distribution was very uniform. As a result, the Al_3(Sc,Zr) precipitates could improve the mechanical properties of aluminum alloys at both ambient and elevated temperatures. Therefore, Al-Sc-Zr matrices are considered promising candidates to develop materials to be used at elevated temperature.

In several other studies, Sc and Zr were introduced into conventional age-hardening aluminum alloys, such as AA2xxx, AA6xxx and AA7xxx alloys, to improve their mechanical properties [13-15]. The addition of Sc and Zr into AA2219 alloys was found to significantly improve their hardness levels [13]. It was also observed that the tensile strength and high cycle fatigue limit of AA6106 alloys increased by alloying with Sc and Zr [14]; similarly, alloying with Sc and Zr increased the yield strength ofAA7xxx alloys [15]. The strength increase in AA2xxx, AA6xxx and AA7xxx alloys can be attributed to the combined action of aging precipitation strengthening phases (Al_2Cu, Mg_2Si and $MgZn_2$) and Al_3(Sc,Zr) precipitates. Due to the rapid coarsening of Al_2Cu, Mg_2Si and $MgZn_2$ precipitates at elevated temperature (overage effect), most of the above cited studies focused on room-temperature mechanical properties. Hence, the advantages of alloying with Sc and Zr and precipitation of thermally stable Al_3(Sc,Zr) were not fully utilized. Very little literature can be found on improving high-temperature mechanical properties by the synergetic effect of the two different types of strengthening phases.

The goal of the present work was to improve both ambient and elevated-temperature mechanical properties of 3004 alloy by introducing two distinct populations of strengthening particles: a high volume fraction of submicron α-Al(Mn,Fe)Si dispersoids and a low volume fraction of nano-size Al_3(Sc,Zr) precipitates. The influence of Sc and Zr addition on the microstructure, mechanical properties and creep resistance at ambient and elevated temperatures was investigated. The combined effects of α-Al(Mn,Fe)Si dispersoids and Al_3(Sc,Zr) precipitates on the yield strengths at 25 °C and 300 °C were quantitatively analyzed based on the existing strengthening mechanisms and equations. The analytically predicted yield strengths were then compared with the experimental data.

6.2 Experimental procedure

Three experimental 3004 alloys with different Sc and Zr contents were prepared with commercially pure Al (99.7%), pure Mg (99.9%), Al-25%Mn, Al-25%Fe, Al-50%Si, Al-2%Sc, and Al-15%Zr master alloys. In addition to the base alloy, the SZ15 and SZ30 alloys contained 0.18%Sc and 0.18%Zr and 0.29%Sc and 0.17%Zr, respectively. The chemical compositions of the experimental alloys analyzed by an optical emission spectrometer are listed in Table 6.1 (all the alloy compositions are indicated in wt.% unless otherwise mentined). For each batch, approximately 3 kg of the materials were melted in an electrical resistance furnace; the melt was held at 750 °C for 30 min and degassed for 15min. It was then poured into a permanent steel mold preheated at 250 °C. The dimensions of the cast ingots was 30 mm x 40 mm x 80 mm.

Table 6.1 Chemical composition of experimental alloys (wt.%)

Code	Sc	Zr	Mn	Fe	Mg	Si	Al
SZ0 (base)	**0**	**0**	1.23	0.60	0.97	0.24	Bal
SZ15	**0.18**	**0.18**	1.18	0.59	1.04	0.25	Bal
SZ30	**0.29**	**0.17**	1.19	0.57	1.01	0.25	Bal

The three alloys were heat-treated with a heating rate 5 °C/min to 300 and 375 ℃ respectively, and then held at those temperatures for a time period varying between 2 h and 48 h, followed by water quenching. Heat treatment at 300 °C was used to evaluate the effect of Al_3(Sc,Zr) precipitates; at 300 °C only Al_3(Sc,Zr) can precipitate [16] because α-Al(Mn,Fe)Si dispersoids are not yet formed [3]. However, at 375 °C α-Al(Mn,Fe)Si dispersoids can fully precipitate in addition to the precipitation of Al_3(Sc,Zr).

After polishing the samples, their Vicker hardness values were measured with a 200g load at a 20s dwelling time. Ten measurements were conducted to calculate the average hardness value of each sample. Compression yield strength tests were conducted at room temperature

and elevated temperature (300 °C) using a Gleeble 3800 thermomechanical testing unit at a strain rate of 0.001 s^{-1}. The Gleeble samples were machined in a cylinder form of 15 mm high and 10 mm diameter. Average results were obtained from three repeated tests. Creep tests were performed at 300 °C for 96 h in a compression condition with different loads of 44 MPa, 52 MPa, 58 MPa and 66.5 MPa, respectively. Each creep test was repeated twice. The creep specimens were the same size as the Gleeble samples.

An optical microscope and a scanning electron microscope were used to observe the as-cast and heat-treated microstructures. To clearly observe α-Al(Mn,Fe)Si dispersoids and dispersoid free zone (DFZ), the polished samples were etched by 0.5% HF for 25 s. A transmission electron microscope (TEM) operating at 200 kV was used to observe the precipitation of Al_3(Sc,Zr) and α-Al(Mn,Fe)Si. TEM foils were prepared by a twin-jet machine using a solution of 30% nitric acid in methanol at -25 °C. For Al_3(Sc,Zr) observation, centered dark field images of the precipitates were formed using the {100}c superlattice reflections of precipitates along the <110> or <100> zone axis. For α-Al(Mn,Fe)Si observation, the <100> zone axis was used to observe dispersoid precipitation in the {200} plane. An electron energy loss spectroscopy (EELS) attached to the TEM was used to measure the thickness of the TEM specimens. The size, number density and volume fraction of the Al_3(Sc,Zr) precipitates and α-Al(Mn,Fe)Si dispersoids were quantified by image analysis (Clemex PE 4.0) of the TEM images. The volume fraction of the α-Al(Mn,Fe)Si dispersoids was calculated using the following equation [1]:

$$V_v = A_A \frac{K\bar{D}}{K\bar{D} + t}(1 - A_{DFZ}) \qquad \text{Eq. 6.1}$$

Where A_A is the volume fraction of dispersoids and $\bar{D}$ is the average equivalent diameter of dispersoids in TEM images; A_{DFZ} is the volume fraction of DFZ measured in optical images; t is the TEM foil thickness; and K is the average shape factor of dispersoids.

6.3 Results and discussion

6.3.1 Microstructures in as-cast and heat-treated conditions

Fig. 6.1 shows the typical as-cast microstructure of the three experimental alloys; it can be seen that the microstructures consist of aluminum dendrite cells and two intermetallic phases. The first type of intermetallics are grey color appeared under optical microscope; they are distributed in the aluminum dendrite boundaries. Most of them were identified as Al_6(Mn,Fe) and very few of them identified as Al(Mn,Fe)Si [3, 4, 17]. Due to their similarities and no influence on alloy properties, this kind of intermetallics are referred to as Mn-containing intermetallics in this study. The second type of intermetallics are black color under optical microscope; they correspond to a minor phase identified as primary Mg_2Si, which is often attached to Mn-containing intermetallics. The volume fractions of both the intermetallic phases were quantified by image analysis, as shown in Fig. 6.2. The volume fractions of Mn-containing intermetallics and primary Mg_2Si particles in the base alloy were the lowest. With increasing Sc and Zr content, the fractions of both Mn-containing intermetallics and primary Mg_2Si particles increased. It was reported that the addition of Sc and Zr could reduce the solubility of Mg and Mn in liquid aluminum [7, 18]. This is most likely the reason behind the remarkable increase in the amounts of Mn-containing intermetallics and primary Mg_2Si particles in the as-cast microstructure after Sc and Zr addition. Both SZ15 and SZ30 contain the same level of Zr but SZ30 exhibites a higher Sc level. This indicates that the Sc plays a major role in reducing the solubility of Mg and Mn and thus increase the amount of intermetallic particles in the as-cast microstructure.

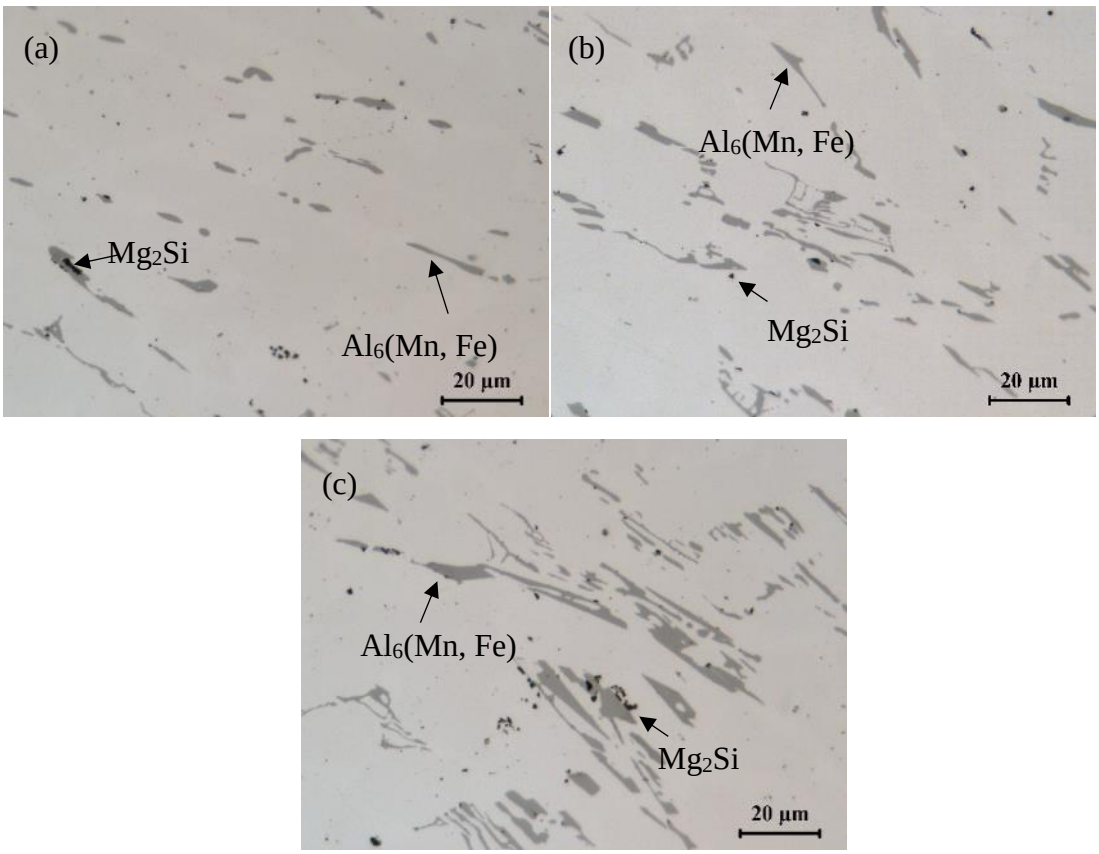

Fig. 6.1 As-cast microstructure of (a) SZ0, (b) SZ15 and (c) SZ30 alloys

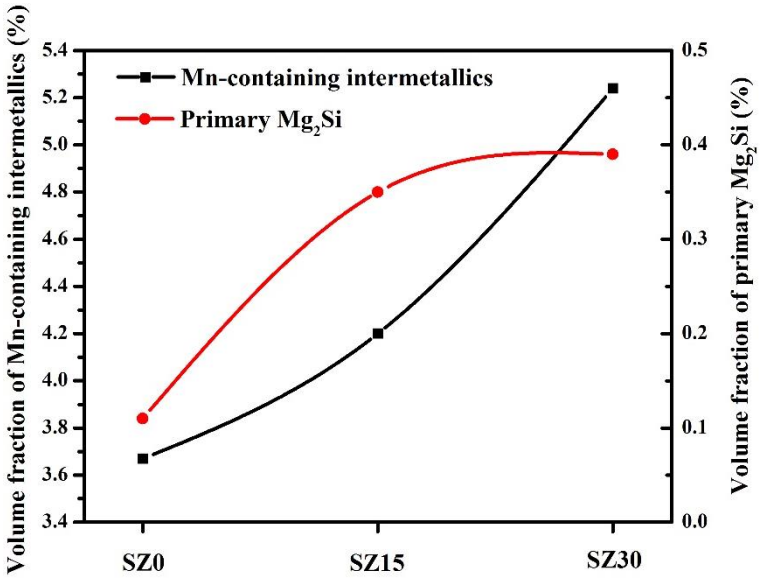

Fig. 6.2 Volume fraction of Mn-containing intermetallics and primary Mg_2Si particles of three alloys

In AA3004 alloys, a large amount of α-Al(MnFe)Si dispersoids can precipitate in the aluminum matrix when a suitable heat-treatment is applied, such as heat-treated at 375 ℃ for 24 h [3-5]. Fig. 6.3 depicts the microstructures of the three alloys after heat treatment at 375 °C for 24 h. The dark areas indicate the dispersoid zone in which a large number of α-Al(Mn,Fe)Si dispersoids appeare within dendrite cells and grains. The light areas correspond to the dispersoid free zone (DFZ) close to the intermetallic particles in the interdendritic regions. where only a few α-Al(Mn,Fe)Si dispersoids could be found. As shown in Fig. 6.3, with increasing Sc and Zr content, the dispersoid zones gradually decreased in size while the DFZs were enlarged. Quantitative results of both the dispersoid zone and DFZ, obtained by image analysis, are included in Fig. 6.4. It is evident that as the Sc and Zr content increases, the volume fraction of the dispersoid zone decreased while the volume fraction of the DFZ increased. For instance, the volume fraction of DFZ increased from 29 vol.% in the base alloy (SZ0) to 34 vol.% in the SZ15 alloy, and further to 38 vol.% in the SZ30 alloy.

It should be mentioned that the optical images of the microstructure obtained after etching can only be used to evaluate the distribution of α-Al(Mn,Fe)Si dispersoids, and it cannot reveal any information on the $Al_3(Sc,Zr)$ precipitates due to their small sizes (nanometric order).

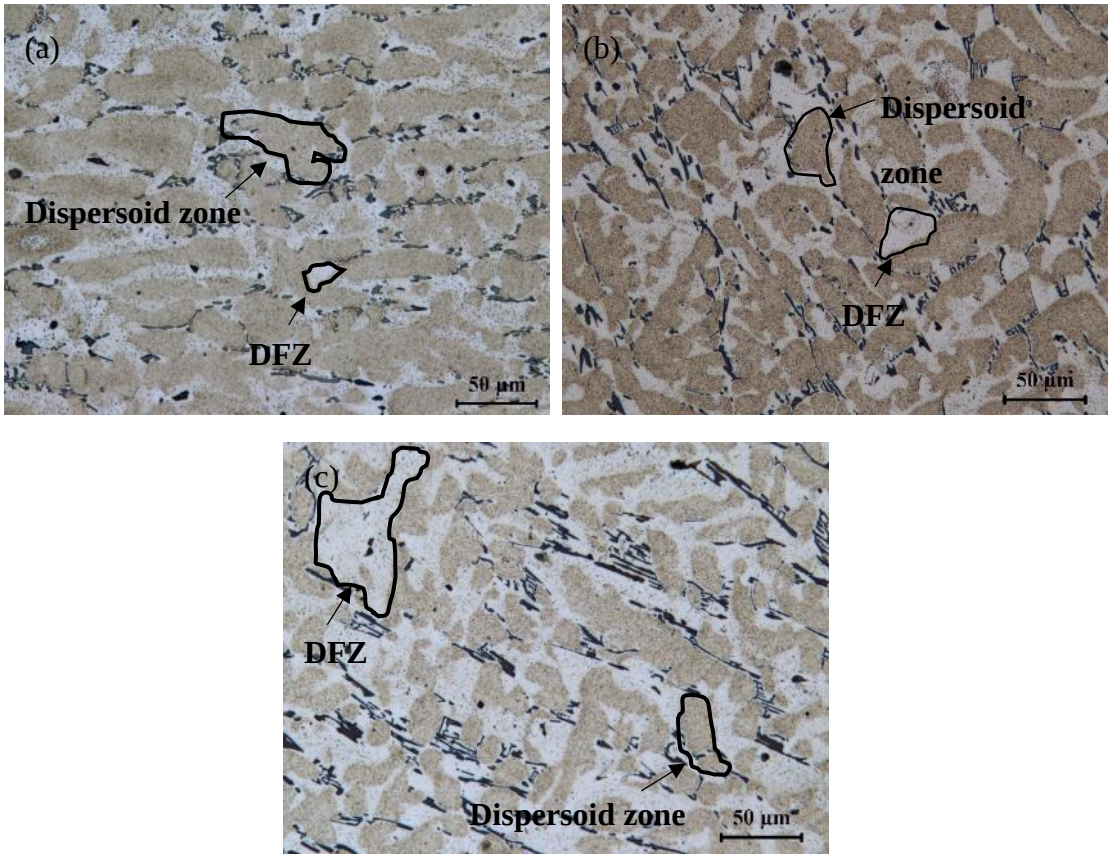

Fig. 6.3 Optical images after heat treatment at 375°C/24h (etched by 0.5% HF): (a) SZ0, (b) SZ15 and (c) SZ30 alloys

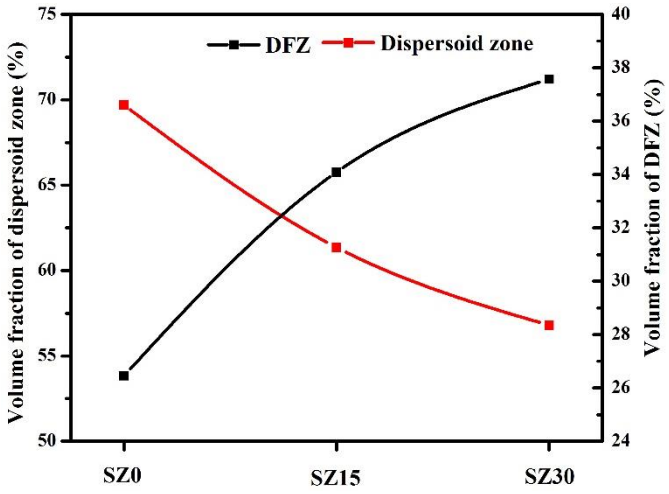

Fig. 6.4 Volume fraction of the dispersoid zone and DFZ of three alloys after heat treatment at 375°C/24h

6.3.2 Precipitation of α-Al(Mn,Fe)Si dispersoids and Al_3(Sc,Zr) precipitates

Due to the small size of the Al_3(Sc,Zr) precipitates and α-Al(Mn,Fe)Si dispersoids, TEM was used to investigate the precipitation of both Al_3(Sc,Zr) and α-Al(Mn,Fe)Si in aluminum matrices. After heat treatment at 375°C for 24 h, a number of α-Al(Mn,Fe)Si dispersoids precipitated within the aluminum cells and grains; typical TEM images are shown in Fig. 6.5. The size and number density of dispersoids were quantified by image analysis on TEM images, as shown in Fig. 6.6a. In the base alloy (SZ0 without Sc and Zr), the sizes of α-Al(Mn,Fe)Si dispersoids are quite small (in the range of 50 nm) and the number density is high (>1000 μm^{-3}). With increasing Sc and Zr content, the size of the α-Al(Mn,Fe)Si dispersoids increased while their number density decreased. For instance, the equivalent diameter of the dispersoids increased from 50 nm (SZ0 Alloy) to 66 nm (SZ15 alloy), and further to 70 nm in the SZ30 alloy. The volume fractions of their dispersoids in the three alloys were calculated according to Eq. 6.1 and the results are presented in Fig. 6.6b. The volume fraction of α-Al(Mn,Fe)Si dispersoids in the SZ0 Alloy is 2.69% and it reduced to 1.24% in the SZ15 Alloy and to 1.15% in the SZ30 alloy. It is evident that Sc and Zr addition greatly influences the precipitation of α-Al(Mn,Fe)Si dispersoids, although Sc and Zr do not seem to be the essential elements for the formation of α-Al(Mn,Fe)Si dispersoids. This could be attributed to the fact that the addition of Sc and Zr reduces the solubility of Mn and Si [7, 18] and results in a large amount of intermetallics and a low level of the supersaturated solid solution of Mn and Si after solidification, which are less available for the formation of α-Al(Mn,Fe)Si dispersoids during heat treatment, when compared to the base alloy (SZ0).

To observe Al_3(Sc,Zr) precipitates, centered dark field TEM images were recorded using {100} superlattice reflections of the precipitates along the <110> or <100> zone axis. Typical TEM images of the Al_3(Sc,Zr) precipitates in SZ15 and SZ30 alloys after heat-treatment at 300 °C and 375 °C are shown in Fig. 6.7. The precipitates can be observed as small bright particles in the TEM images; they are uniformly distributed in the aluminum matrix with high density. The sizes of the Al_3(Sc,Zr) precipitates depends on the heat treatment temperature. When the heat treatment temperature was 300 °C, the diameter of the Al_3(Sc,Zr) precipitates

of SZ15 and SZ30 alloys was ~6 nm. As the heat treatment temperature increased to 375 °C, the diameter of the Al_3(Sc, Zr) precipitates in SZ15 and SZ30 alloys slightly increased to ~8 nm (Fig. 6.8). According to image analysis, after heat treatment at 375 °C for 24 h, the SZ15 and SZ30 alloys contain approximately 0.24% and 0.30% Al_3(Sc,Zr) precipitates, respectively.

If the dark field TEM images were captured slightly off center of the {100} superlattice reflections of the precipitates, the populations of the two types of strengthening particles, namely α-Al(Mn,Fe)Si dispersoids and Al_3(Sc,Zr) precipitates, can be visualized at the same time. Fig. 6.9 shows the distribution of α-Al(Mn,Fe)Si dispersoids and Al_3(Sc,Zr) precipitates in the TEM images in the example of the SZ15 alloy. It can be seen that the inter-particle distance in the α-Al(Mn,Fe)Si dispersoids is quite large (in the range of 200 nm) in addition to their relatively large size (Fig. 6.9a). On the other hand, the Al_3(Sc,Zr) precipitates are much finer and denser in the aluminum matrix than the α-Al(Mn,Fe)Si dispersoids. They filled uo the spaces in between large dispersoids (Fig. 6.9b). Therefore, the inter-particle distances between strengthening particles are dramatically decreased due to the presence of fine Al_3(Sc,Zr) precipitates, resulting in more obstacles for dislocation movement in aluminum cells and grains.

The DFZ along the grain boundaries was also observed by TEM, as shown in Fig. 6.10. In the bright field image (Fig. 6.10a), a large DFZ of α-Al(Mn,Fe)Si dispersoids could be observed along the grain boundary. The half-width of the DFZ was calculated to be ~0.67 μm. At the same location, it can been seen in Fig. 6.10b that Al_3(Sc,Zr) not only appeared in the dispersoid zone but also precipitated in most of the DFZ. There is only a narrow particle free zone near the grain boundary. The half-width of the particle free zone reduced from 0.67 μm to 0.17 μm, which is 4 times lesser than that observed in the presence of α-Al(Mn,Fe)Si dispersoids only.

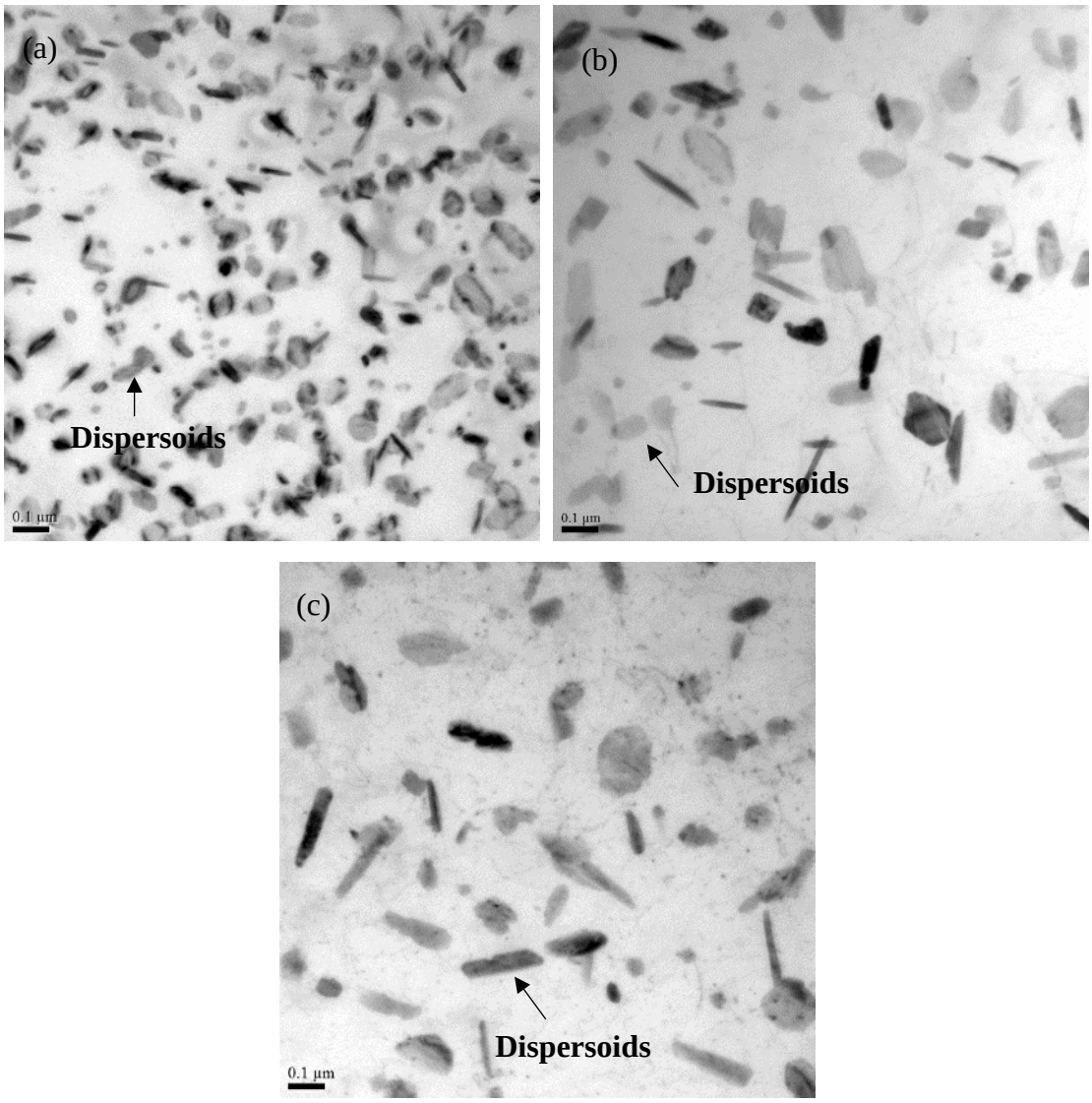

Fig. 6.5 TEM images of α-Al(Mn,Fe)Si dispersoids (a) SZ0, (b) SZ15 and SZ30 alloys

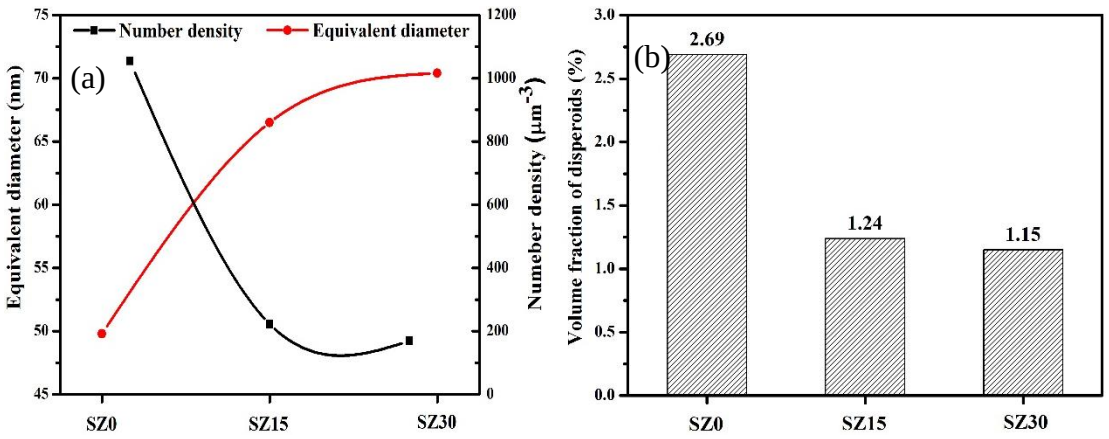

Fig. 6.6 (a) the equivalent diameter and number density of α-Al(Mn,Fe)Si dispersoids, (b) the volume fraction of α-Al(Mn,Fe)Si dispersoids of three alloys

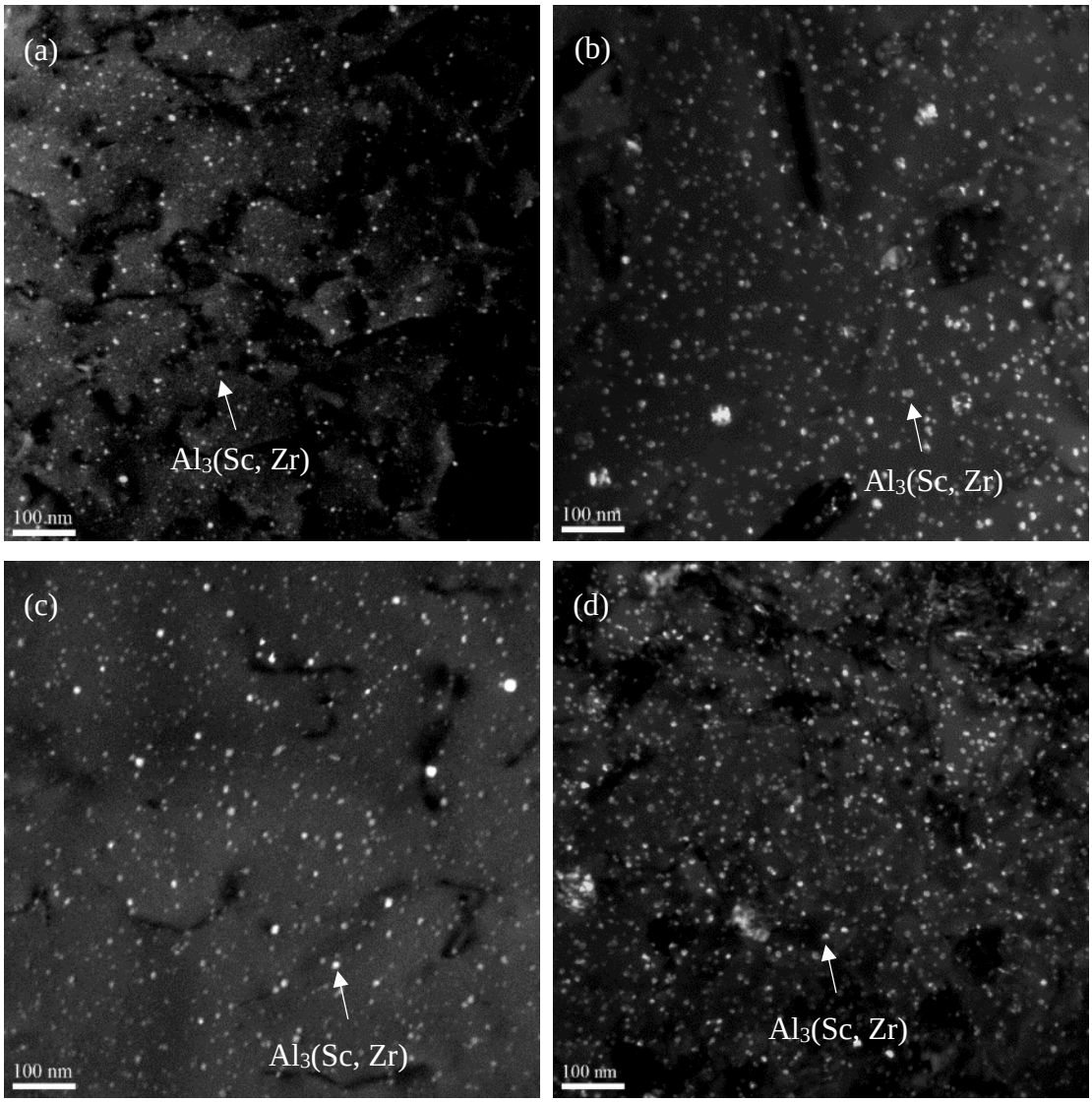

Fig. 6.7 Centered dark field TEM images of Al_3(Sc,Zr) precipitates (a) SZ15 alloy after 300°C/12h, (b) SZ15 alloy after 375°C/24h, (c) SZ30 alloy after 300°C°/12h, (d) SZ30 alloy after 375°C/24h

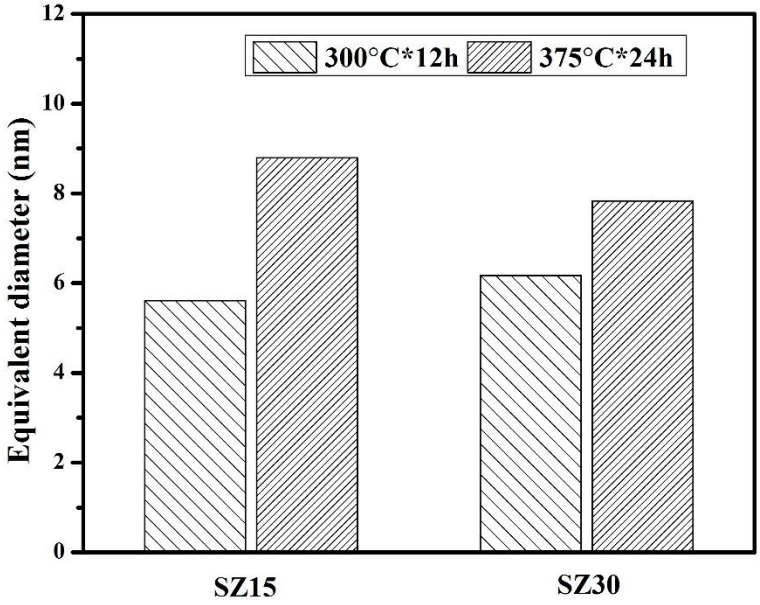

Fig. 6.8 The equivalent diameter of $Al_3(Sc,Zr)$ precipitates of two alloys at two heat treatment conditions

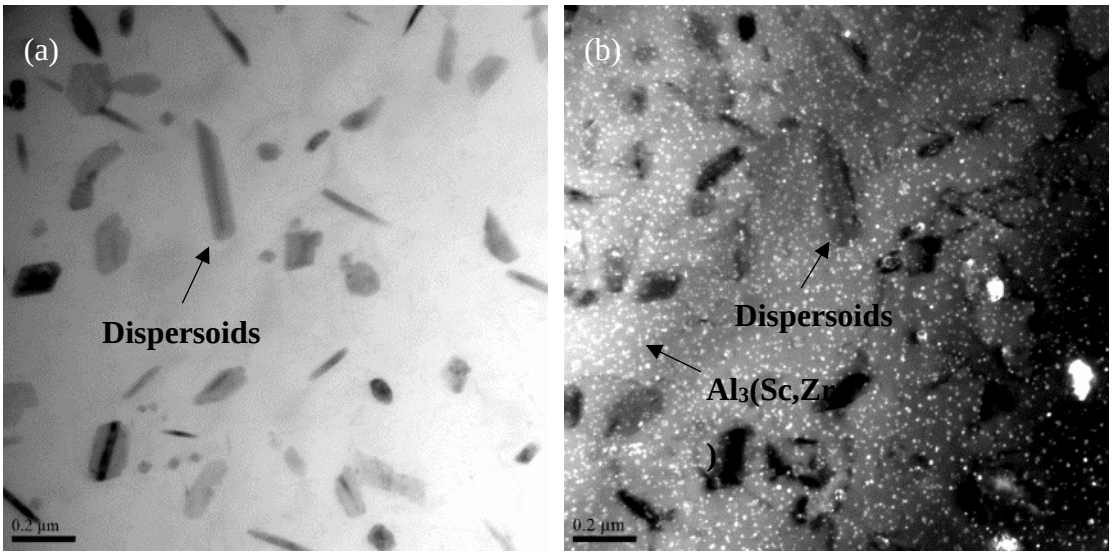

Fig. 6.9 TEM images showing both α-Al(Mn,Fe)Si dispersoids and $Al_3(Sc,Zr)$ in the aluminum matrix of SZ15 Alloy, (a) bright field TEM image and (b) dark field TEM image captured slightly off the center of {100} superlattice reflections of the $Al_3(Sc,Zr)$ precipitates.

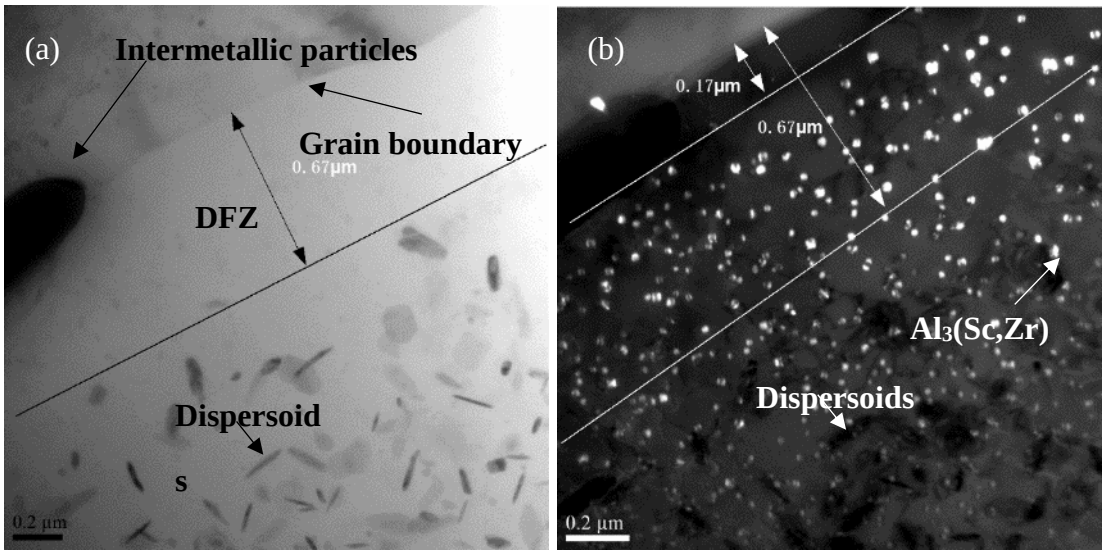

Fig. 6.10 TEM images of the particle free zone along the grain boundary in SZ15 alloy, (a) bright field TEM image and (b) dark field TEM image captured slightly off the center of {100} superlattice reflections of $Al_3(Sc,Zr)$ precipitates.

6.3.3 Mechanical properties at ambient and elevated temperatures

6.3.3.1 Microhardness

To evaluate the influence of Sc and Zr content on the mechanical properties at the ambient temperature, the evolution of microhardness was analyzed in the three alloys after heat treatment at 300 °C and 375 °C (Fig. 6.11). In the case of the alloys treated at 300 °C (Fig. 6.11a), the microhardness of the base alloy showed no remarkable change with holding time and remained at a relatively low level because no phase (α-Al(Mn,Fe)Si) precipitation occurred at this temperature. With the addition of Sc and Zr, the hardness of the SZ15 and SZ30 alloys increased with holding time and reached the peak value after 12 h, which indicates the precipitation of $Al_3(Sc,Zr)$, as conformed by the TEM images in Fig. 6.7. The peak hardness values of SZ0, SZ15 and SZ30 alloys after 300 °C for 12 h are 62, 75 and 81 HV, respectively. The peak hardness of Sc and Zr containing alloys increased by 21% (SZ15) and 31% (SZ30) as compared to the SZ0 base alloy. Because there is no α-Al(M,Fe)Si precipitation in the three

alloys, the increase in the hardness of SZ15 and SZ30 alloys is clearly attributed to the strengthening effect of the $Al_3(Sc,Zr)$ precipitates.

In the case of the alloys heat treated at 375 °C (Fig. 6.11b), the microhardness of the base alloy increased with holding time and reached the peak value after 24 h, indicating the precipitation of α-Al(Mn,Fe)Si dispersoids. For the Sc and Zr containing alloys, 375 °C is a compatible temperature at which both α-Al(Mn,Fe)Si dispersoids and $Al_3(Sc,Zr)$ preciptates can simultaneously precipitate. The hardness of the SZ15 and SZ30 alloys increased with holding time and reached the peak value after 24 h, indicating the combined precipitation of the two populations of strengthening phases, as conformed by TEM observations in Fig. 6.9. The peak hardness values of the SZ0, SZ15 and SZ30 alloys after 375 °C for 24 h are 63, 77 and 88 HV, respectively. Due to the addition of Sc and Zr, $Al_3(Sc,Zr)$ precipitates boost the peak hardness by 22% (SZ15) and 40% (SZ30) compared to the base alloy, thus contributing to a considerable fraction of the total hardness, despite a lower volume fraction of the α-Al(Mn,Fe)Si dispersoids in Sc and Zr containing alloys relative to the base alloy (Fig. 6.6b). This demonstrates that the fine size and high density of $Al_3(Sc,Zr)$ precipitates play a major role in strengthening the aluminum matrix at ambient temperature.

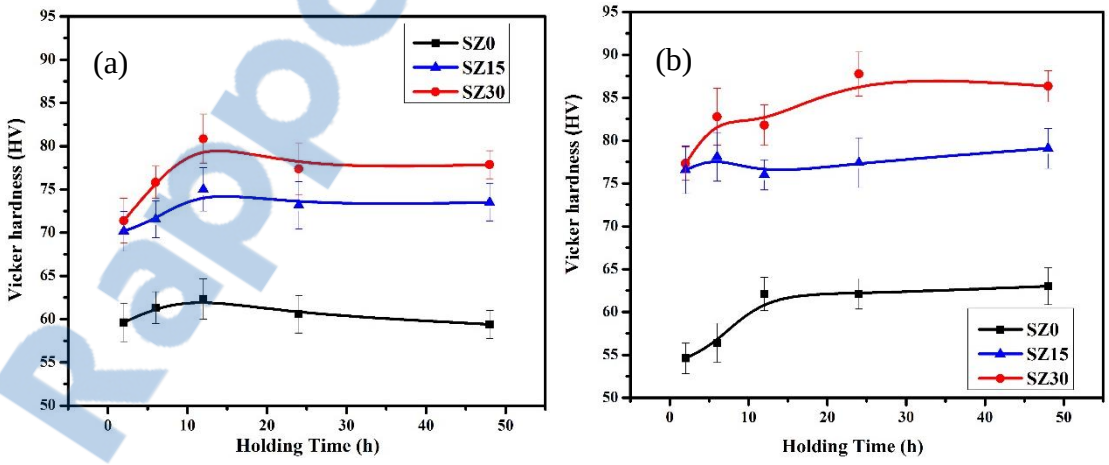

Fig. 6.11 Microhardness evolution of the three alloys as a function of holding time during heat treatment at (a) 300 °C and (b) 375 °C

6.3.3.2 Yield strength at ambient and elevated temperatures

The results of yield strength analysis at ambient and elevated temperatures after heat treating the three alloys at 300 °C and 375 °C are shown in Fig. 6.12. Regardless of the heat treatment temperature, the yield strength at ambient temperature increased greatly with increasing Sc and Zr content (Fig. 6.12a), which is consistent with the results of peak hardness. When the alloys treated at 300 °C without α-Al(Mn,Fe)Si precipitation, the yield strength increased from 88 MPa (base alloy) to 130 MPa (SZ15) and further to 135 MPa (SZ30). At a treatment temperature of 375 °C where combined precipitation of α-Al(MnFe)Si dispersoids and Al_3(Sc,Zr) precipitates occurs, the yield strength values of the three alloys are generally higher than that those treated at 300 °C; the yield strength increased from 98 MPa (base alloy) to 135 MPa (SZ15) and further to 154 MPa (SZ30). At both heat treatment conditions, at least more than 37 MPa increase in the yield strength could be achieved with the addition of Sc and Zr, illustrating the potent strengthening effect of Al_3(Sc,Zr) precipitates at the ambient temperature.

The yield strengths at 300 °C exhibit a somewhat different trend from those obtained at the ambient temperature. After heat treatment at 300 °C for 12 h, the yield strength at 300 °C is 62 MPa, 77 MPa and 78 MPa, respectively, for the SZ0, SZ15 and SZ30 alloys (Fig. 6.12b). They increased approximately by 15 MPa upon the addition of Sc and Zr, whereas the high Sc level in SZ30 showed almost no effect. The strengthening contribution of Al_3(Sc,Zr) precipitates on the yield strength at 300 °C could be clearly seen but it is far less than that at the ambient temperature. In the case of heat treatment at 375 °C for 24 h, the yield strengths of all the three alloys at 300 °C were found to be similar (around 80 MPa) and no remarkable change could be found despite the precipitation of the Al_3(Sc,Zr) in SZ15 and SZ30 alloys. It is noticed that a high density of Al_3(Sc,Zr) precipitated in Sc and Zr containing alloys (SZ15 and SZ30) but the amount of α-Al(Mn,Fe)Si dispersoids in both the alloys are dramatically lower than in the base alloy (see Fig. 6.6b). The complex effect of these two distinct populations of strengthening particles at ambient and elevated temperatures will be discussed later.

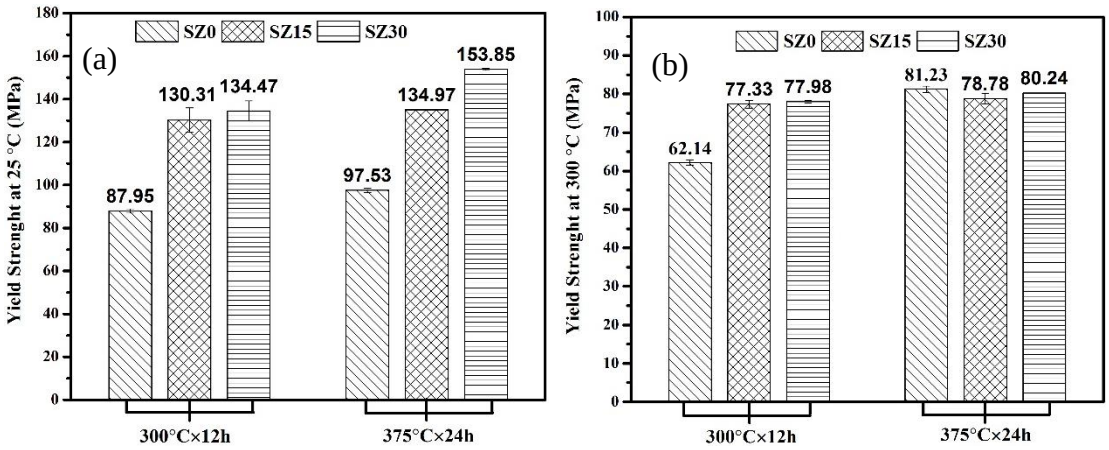

Fig. 6.12 Yield strengths (a) at 25°C and (b) at 300 °C for two heat treatment conditions

6.3.3.3 Creep resistance at 300 °C

Fig. 6.13 shows the typical compressive creep curves of the three alloys tested at 300 °C at a constant load of 58 MPa. It can be found that the total creep strain after 96 h decreased with an increase in the Sc and Zr content. At first, the total creep strain significantly decreased from 0.25 in the SZ0 alloy to 0.10 in the SZ15 alloy and then slightly reduced to 0.09 in the SZ30 alloy, indicating an improvement in the creep resistance by the addition of Sc and Zr. Moreover, the minimum creep rate, $\dot{\varepsilon}_m$, also decreased upon the addition of Sc and Zr. The minimum creep rate is calculated to be 7.58 x 10^{-7} s^{-1} for the base alloy (SZ0); it dropped to 1.69 x 10^{-7} s^{-1} in the SZ15 alloy and then slightly decreased to 1.67 x 10^{-7} s^{-1} in the SZ30 alloy. It is evident that with the addition 0.18%Sc and 0.18%Zr in SZ15, the creep resistance of the material can be significantly enhanced. However, at higher Sc level (0.29% in the SZ30 alloy), the creep resistance improved only slightly.

The creep behavior of dispersion-strengthened materials can generally be described by a modified power law equation [19, 20], in which a thermal threshold stress is assumed and the true stress exponent can be determined:

$$\dot{\varepsilon}_m = A_0\left(\frac{\sigma-\sigma_{th}}{G}\right)^{n_t}\exp\left(-\frac{Q}{RT}\right) \qquad \text{Eq. 6.2}$$

Where $\dot{\varepsilon}_m$ is the minimum creep rate, A_0 is constant, σ is the applied stress, σ_{th} is the threshold stress, G was the shear modulus, n_t is the true stress exponent, Q is the activation energy, R is the universal gas constant and T is the absolute temperature.

To better understand the creep behavior of Sc and Zr containing alloys, the creep tests at different loads were performed to determine two important creep parameters, namely the threshold stress (σ_{th}) and true stress exponent (n_t). The threshold stress σ_{th} is calculated as a stress value as the linear fitted curves corresponding to the minimum creep rates at different loads extrapolated to $1x10^{-10}$ s^{-1} (below which the creep is experimentally not measurable). The true stress exponent n_t is equivalent to the slope of $\ln\dot{\varepsilon}_m$ vs. $\ln(\sigma-\sigma_{th})$ curve. The calculated results are shown in Fig. 6.14. As shown in Fig. 6.14a, the minimum creep rates decreased with the addition of Sc and Zr in the SZ30 alloy at all applied loads; meanwhile the threshold stress σ_{th} increased from 29.1 MPa in the SZ0 alloy to 32.7 MPa in the SZ30 alloy, which is a significant improvement in the creep resistance at elevated temperature. It is reported that an increase of 3 MPa in the threshold stress translates into a decrease in the minimum creep rate by an order of magnitude [21]. Fig. 6.14b depicts the double logarithmic plots of the minimum creep rate as a function of the effective stress ($\sigma - \sigma_{th}$) along with the slopes of the plots, which yield the values of the true stress exponent. The true stress exponent values of the SZ0 and SZ30 alloys are 5.26 and 5.23, respectively, which suggests that creep is controlled by the high temperature dislocation climb mechanism [20, 22, 23].

Upon appropriate heat treatment (375 °C for 24 h), the precipitation of a number of α-Al(Mn,Fe)Si dispersoids in the 3004 alloy could greatly enhance its creep resistance compared to the conventional 3004 alloy without α-Al(Mn,Fe)Si dispersoids [3]. However, the precipitation of α-Al(Mn,Fe)Si dispersoids is centered in the dendrite cells and grains, leaving a relatively high volume fraction of DFZ in the interdendrite grain boundaries (Fig. 6.3). The DFZs are weak areas through which the dislocations can easily pass during creep deformation. In addition, a large DFZ in the vicinity of the grain boundary can promote grain boundary rotation and sliding due to the lack of a secondary strengthening phase, leading to a weak resistance to creep deformation. By the addition of Sc and Zr, finer Al_3(Sc,Zr) precipitates of

high density not only precipitated in the dendrite grains but also greatly extended to the dispersoid free zones, resulting in a much smaller particle free zone in the vicinity of the grain boundary (Fig. 6.10). Because the addition of Sc and Zr also causes a remarkable reduction in the volume fraction of α-Al(Mn,Fe)Si dispersoids (Fig. 6.6b), an increase in the creep resistance in the cores of the dendrite grains would be limited due to the presence of Al_3(Sc,Zr) precipitates. However, the precipitation of Al_3(Sc,Zr) precipitates in the dispersoid free zone can greatly inhibit dislocation movement as well as grain boundary rotation and sliding, which is considered to be the main factor behind the improved creep resistance of Sc and Zr containing alloys.

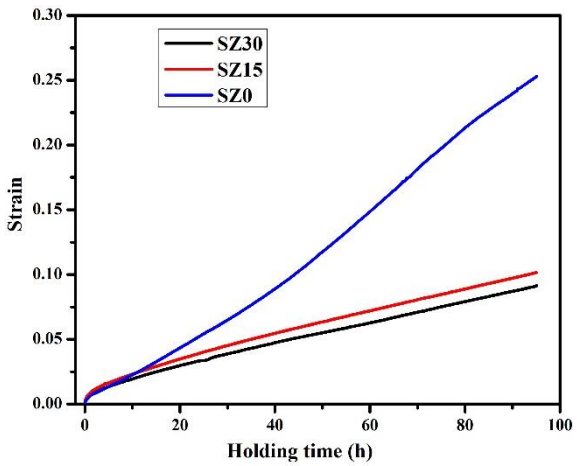

Fig. 6.13 Typical creep cures of SZ0, SZ15 and SZ30 alloys, conducted at 300 °C for 96 h with a load 58 MPa

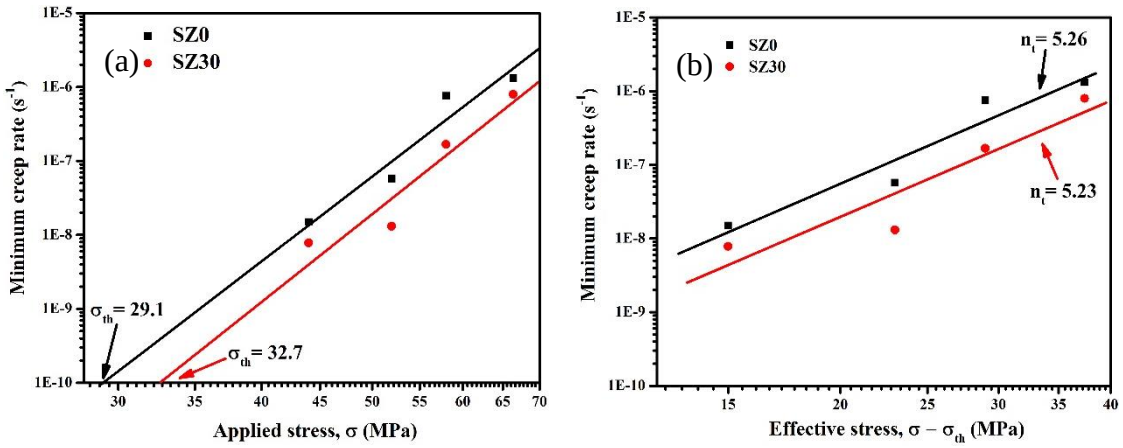

Fig. 6.14 Logarithmic plots of the minimum creep rate as a function of applied stress to determine the threshold stress σ_{th} (a) and logarithmic plots of the minimum creep rate as a function of effective stress to determine the true stress exponent n_t (b)

6.3.4 Quantitative analysis of yield strength at ambient and elevated temperatures

To understand the strengthening effect of two distinct populations of particles, α-Al(Mn,Fe)Si dispersoids and Al_3(Sc,Zr) precipitates, at ambient and elevated temperatures, the yield strengths of the experimental alloys were quantitatively analyzed at 25 °C and at 300 °C. The over yield strength could be considered from several parts, namely the aluminum matrix, solid solution of the alloying elements, α-Al(Mn,Fe)Si dispersoids and Al_3(Sc,Zr) precipitates, and it can be expressed as:

$$\sigma_y = \sigma_m + \Delta\sigma_{SS} + \Delta\sigma_{dispersoids} + \Delta\sigma_{precipitates} \quad \text{Eq. 6.3}$$

where σ_y is the yield strength, σ_m is the matrix strength, $\Delta\sigma_{SS}$ is the strengthening by solid solution, $\Delta\sigma_{dispersoids}$ is the strengthening by α-Al(MnFe)Si dispersoids and $\Delta\sigma_{precipitates}$ is the strengthening by Al_3(Sc,Zr) precipitates. Due to different strengthening mechanisms, the yield strengths at ambient and elevated temperatures are separately discussed.

6.3.4.1 Yield strength at ambient temperature

The matrix strength (σ_m) is considered to be 34 MPa at 25 °C according to the datasheet of a commercial pure 1100-O aluminum alloy [24]. The solid solution strengthening in the 3004 alloy contributes mainly through Mg and Mn elements and contributions by other elements are almost negligible due to their presence in extremely small quantities. After heat treatment at 375 °C for 24 h, all small Mg_2Si precipitates were assumed to dissolve in the aluminum matrix and the primary Mg_2Si intermetallic particles remained undissolved. At a given volume fraction of primary Mg_2Si intermetallic particles (Fig. 6.2), the concentrations of Mg in the solid solution of the experimental alloys could be calculated. In the case of Mn, both primary Mn-containing intermetallic particles and α-Al(Mn,Fe)Si dispersoids consumed Mn elements. Based on their volume fractions (Fig. 6.2 and Fig. 6.6b), the remaining concentration of Mn in the matrix could be calculated. The results are included in Table 6.2. The strengthening contribution of Mg and Mn at ambient temperature can be calculated according to Eq. 6.4 [25, 26]:

$$\Delta\sigma_{SS} = HC^{\alpha} \quad \text{Eq. 6.4}$$

where C was concentration of solute atoms, H_{Mg} = 13.8 MPa/wt%, $\alpha_{Mg} = 1$, H_{Mn} = 18.35 MPa/wt%, $\alpha_{Mn} = 0.9$ [25].

Table 6.2 Parameters used in the calculation

Alloys	Mg solute content (wt%)	Mn solute content (wt%)	α-Al(Mn,Fe)Si dispersoids		$Al_3(Sc,Zr)$ precipitates	
			Vol.%	Aver. radius (nm)	Vol.%	Aver. radius (nm)
SZ0	0.95	0.17	2.69	25.0	0	0
SZ15	0.84	0.27	1.24	33.2	0.24	4.4
SZ30	0.82	0.14	1.15	35.2	0.30	3.9

For precipitation-strengthened materials, the ambient-temperature strength can be generally explained and predicted using classical Orowan bypass mechanism when the radius of the strengthening particles is greater than 2 nm [27, 28]. In the present work, the radii of the α-Al(Mn,Fe)Si dispersoids and Al_3(Sc, Zr) precipitates are 25-35 nm and 3-4 nm, respectively, which are in the range of the Orowan bypass strengthening mechanism. Therefore, the contribution of both dispersoids and precipitates can be determined using Eq. 6.5 [2, 6]:

$$\Delta\sigma_{\text{Dispersoids}} \text{ or } \Delta\sigma_{\text{precipitates}} = \frac{0.84MGb}{2\pi(1-v)^{1/2}\lambda}\ln\frac{r}{b} \qquad \text{Eq. 6.5}$$

$$\lambda = r\left(\frac{2\pi}{3f}\right)^{1/2} \qquad \text{Eq. 6.6}$$

where M = 2 is the Taylor factor [6], G = 27.4 GPa is the shear modulus of Al matrix [6], b = 0.286 nm is the Burgers vector [6], v = 0.33 is the Poison ratio [6], λ is the inter-particle distance, r is the average radius of particles and f is the volume fraction of particles.

The solid solution strengthening of Mg and Mn can be calculated using Eq. 6.4. Using Eqs. 6.5 and 6.6, increments in the yield strength due to the presence of α-Al(Mn,Fe)Si dispersoids and Al_3(Sc,Zr) precipitates are calculated. The calculated results are shown in Table 6.3 and Fig. 6.15. It can be seen that solid solution strengthening due to Mg and Mn contributed a relatively small fraction to the strength increment. On the other hand, both α-Al(Mn,Fe)Si dispersoids and Al_3(Sc,Zr) precipitates contributed majorly to the increased strength. In the case of the SZ0 alloy, α-Al(Mn,Fe)Si dispersoids were the only strengthening particles, providing an increment of 52.1 MPa in the yield strength. In the cases of the alloys with Sc and Zr, two populations of particles existed, and the Al_3(Sc,Zr) precipitates contributed more to the increase in strength compared to the α-Al(Mn,Fe)Si dispersoids. Considering the SZ30 alloy for an example, α-Al(Mn,Fe)Si dispersoids and Al_3(Sc,Zr) precipitates led to 26 MPa and 64.9 MPa increments in strength, respectively. The volume fraction of the α-Al(Mn,Fe)Si dispersoids decreased from 2.69% (SZ0 alloy) to 1.15% (SZ30 alloy) due to the addition of Sc and Zr. Therefore, the yield strength contribution dropped from 52.1 MPa (SZ0 alloy) to 26

MPa (in SZ30 alloy). On the other hand, although the volume fraction of the $Al_3(Sc,Zr)$ precipitates was low, because of their small size and large number density, their strengthening effect was very strong at ambient temperature (64.9 MPa). This is the reason why the yield strength of Sc and Zr containing alloys are higher than that of the base alloy (SZ0). It is evident from Fig. 6.15 that a good agreement exists between the calculated and experimentally measured results, indicating that the above described analytical solution can be used to predict the yield strength of alloys containing two populations of strengthening phases.

Table 6.3 The yield strength contributions at 25 °C of each component (MPa)

	SZ0	SZ15	SZ30
Aluminum matrix	34	34	34
Mg solid solution	13.1	11.6	11.3
Mn solid solution	3.7	5.6	3.1
$Al_3(Sc,Zr)$	0	53.9	64.9
α-Al(Mn,Fe)Si	52.1	28.2	26.0
Total of calculated results	102.9	133.3	139.3
Experimental results	97.5	135.0	153.9

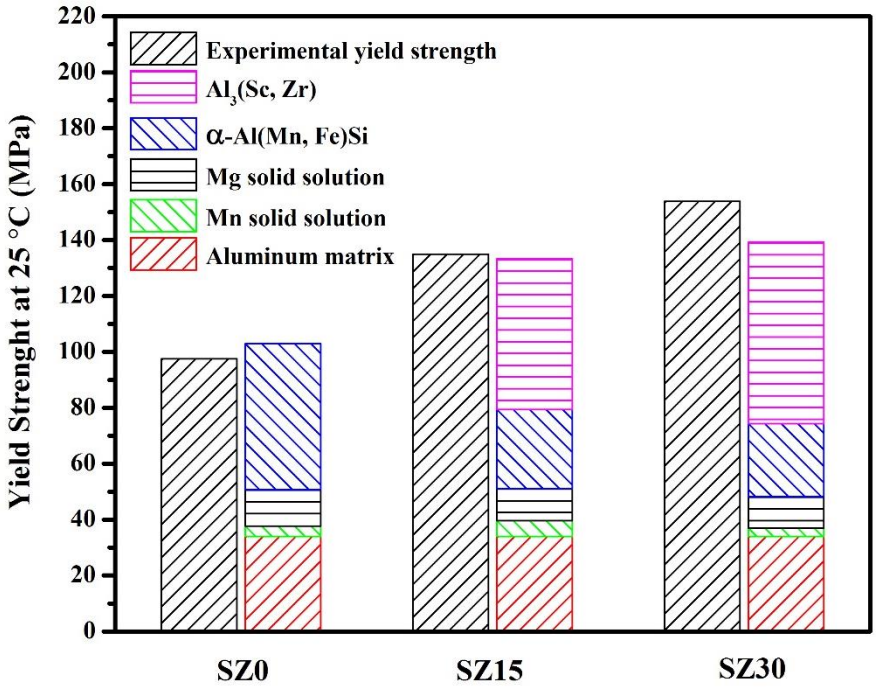

Fig. 6.15 The comparison between calculated and experimentally measured yield strengths at 25 °C.

6.3.4.2 Yield strength at 300 °C

It is difficult to estimate the contribution of solid solution strengthening due to Mg and Mn at 300 °C because of the lack of the necessary data on H and α at elevated temperatures in Eq. 6.4. To solve this problem, the available data on the yield strength of AA3004-O at 315 °C (41 MPa) [29] was used as a close approximation for both the matrix strength and the solid solution strengthening contribution of Mg and Mn at 300 °C.

In the case of the nanometer scale Al_3(Sc,Zr) precipitates, the elevated-temperature strength contribution is difficult to be explained by the classical Orowan bypass mechanism, which often overestimates the atual strength increment [28]. At elevated temperatures, there is sufficient thermal energy to allow dislocation to circumvent the precipitates by climbing over them. The dislocation climb mechanism becomes active when the alloys are deformed at elevated temperatures at low strain rates [30]. Because of the size range of the Al_3(Sc,Zr)

precipitates, the dislocation climb mechanism is invoked to better calculate the yield strength contribution of the coherent $Al_3(Sc,Zr)$ precipitates at 300 °C [28]. The increase in strength due to the dislocation climb ($\Delta\sigma_{Climb}$) consists of two parts, lattice mismatch strengthening ($\Delta\sigma_{LMC}$) and modulus mismatch strengthening ($\Delta\sigma_{MMC}$) which can calculated according to following equations [28, 30, 31]:

$$\Delta\sigma_{Climb} = \Delta\sigma_{LMC} + \Delta\sigma_{MMC} \quad \text{Eq. 6.7}$$

$$\Delta\sigma_{LMC} = \chi(\varepsilon G_m)^{\frac{3}{2}} M \sqrt{\frac{2fbr}{G_m b^2}} \quad \text{Eq. 6.8}$$

$$\Delta\sigma_{MMC} = \frac{F^{\frac{3}{2}} M}{\left(\frac{G_m b^2 2\pi}{3f}\right)^{\frac{1}{2}} br} \quad \text{Eq. 6.9}$$

where, χ = 2.6 was a constant [28, 31], ε was the constrained strain [28, 30], G_m = 21.1 GPa was the shear modulus of Al matrix [28], M = 3.06 was the mean matrix orientation factor [28], b = 0.288 nm was the Burgers vector [28], r was average radius of precipitates, f was volume fraction of precipitates, F was the force on the dislocations [28].

When the particle size of α-Al(Mn,Fe)Si dispersoids is large, the Orowan bypass strengthening mechanism is still valid at elevated temperatures [28]. Therefore, the yield strength contribution of α-Al(Mn,Fe) Si dispersoids at 300 °C can be calculated using Eqs. 6.5 and 6.6. The only different parameter is the shear modulus of the Al matrix, G_m, which changes from 27.4 GPa (at 25 °C) to 21.1 GPa (at 300 °C) [28]. Other constants remain unchanged with temperature. Because of the change in G_m, the increase in yield strength due to α-Al(Mn,Fe)Si dispersoids at 300 °C is lower than that at 25 °C for a given volume fraction.

The calculated results of each strengthening contribution are shown in Table 6.4 and Fig. 6.16. For the base alloy (SZ0), the strengthening contribution of α-Al(Mn,Fe)Si dispersoids decreased from 52.1 MPa (at 25 °C) to 40.1 MPa (at 300 °C). For the Sc and Zr containing alloys, the strength increments due to α-Al(Mn,Fe)Si dispersoids at 300 °C were 21.7 MPa (SZ15 alloy) and 20 MPa (SZ30 alloy) respectively, which were approximately 20 MPa less

than that of the SZ0 alloy due to the reduced volume fraction of the dispersoids. On the other hand, Al_3(Sc,Zr) precipitates led to an increase of 22 MPa in the SZ15 alloy and 23.4MPa in the SZ 30 alloys. These values are much lower than the strength contribution of Al_3(Sc,Zr) precipitates at the ambient temperature. At higher temperatures, atomic mobility and the number density of the vacancies are very high, and hence the dislocations can easily climb through the Al_3(Sc,Zr) precipitates, resulting in a small increase in the strength. The total strength contributions of α-Al(Mn,Fe)Si dispersoids and Al_3(Sc,Zr) precipitates are approximately 43 MPa in both SZ15 and SZ30 alloys, which is almost equivalent to the strength contribution of α-Al(Mn,Fe)Si dispersoids in the SZ0 alloy. As a result, the overall yield strengths at 300 °C of the base alloy and Sc and Zr containing alloys are almost similar, as shown in Fig. 6.16. It is evident that the calculated results agree well with the experimentally measured results.

Table 6.4 The yield strength contributions at 300 °C of each component (MPa)

	SZ0	SZ15	SZ30
Al matrix of AA3004-O	41	41	41
Al_3(Sc,Zr)	0	22.0	23.4
α-Al(Mn,Fe)Si	40.1	21.7	20.0
Total calculated results	81.1	84.7	84.4
Experimental results	81.2	78.8	80.2

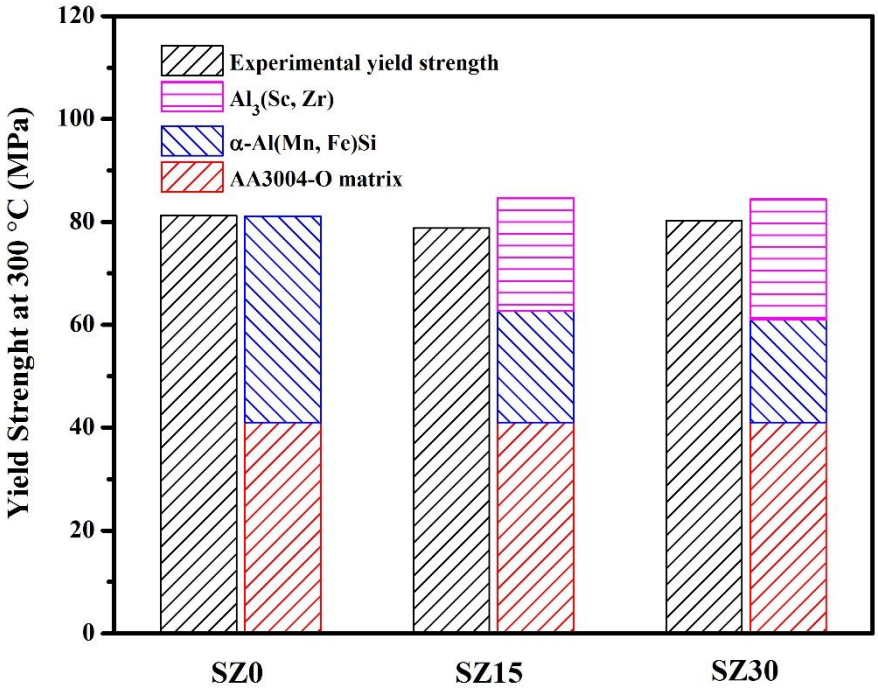

Fig. 6.16 The comparison between calculated and experimentally measured yield strengths at 300 °C.

6.3.5 Prospect for the synergetic strengthening effect of co-existing α-Al(Mn,Fe)Si dispersoids and Al_3(Sc,Zr) precipitates

The precipitation and subsequent strengthening mechanisms of α-Al(Mn,Fe)Si dispersoids and Al_3(Sc,Zr) precipitates in Al-Mn-Mg 3004 alloys are quite different due to their differences in morphology, size, volume fraction and distribution. However, for developing strong aluminum alloys with thermal stability for elevated temperature applications, the two strengthening populations can work in complementary manner in many aspects.

(a) Both α-Al(Mn,Fe)Si dispersoids and Al_3(Sc,Zr) precipitates in an aluminum matrix are thermally stable and coarsening resistant at 300-350 °C, which provides a common base for improving the strength and creep resistance at elevated temperatures, as they can effectively impede dislocation glide and climb at the intended service temperature. In addition, the precipitation temperature ranges of α-Al(Mn,Fe)Si dispersoids and Al3(Sc,Zr)

precipitates in Al-Mn-Mg 3004 alloys are quite similar. This makes the peak precipitation of both phases during heat treatment feasible.

(b) The amount of $Al_3(Sc,Zr)$ that can be precipitated is rather limited upon alloying with a small quantity of Sc (0.1-0.4%), which makes it suitable only to provide extra strength to the aluminum alloy. On the other hand, a relatively large amount of α-Al(Mn,Fe)Si dispersoids (~3 vol.%) can be precipitated in the conventional low cost Al-Mn-Mg 3004 alloys. Even though the strengthening due to α-Al(Mn,Fe)Si dispersoids is not very effective due to their large size in the submicron scale, their large volume fraction is very good for improving the strength and creep resistance at elevated temperatures [3, 5, 17]. If they can strengthen together in a complementary manner with fine nano-sized $Al_3(Sc,Zr)$, it would greatly reduce the inter-particle spacing and impede dislocation motion, resulting in a great improvement in the mechanical performance of the materials in both ambient and elevated temperatures.

(c) During the precipitation of α-Al(Mn,Fe)Si dispersoids, there is always a relatively large amount of an accompanying dispersoid free zone, which limits improvement in the strength and creep resistance. The uniform distribution of $Al_3(Sc,Zr)$ precipitates in the aluminum matrix, including in the dispersoid free zone, solves this problem perfectly, leading to further improvement in the strength and creep resistance of the material.

(d) In the present work, although the Sc content of the SZ30 alloy is 40% higher than that of the SZ15 alloy, the improvement margin in the yield strength and creep resistance of the high Sc alloy (SZ30) is much smaller than that of the low Sc alloy (SZ15) versus the Sc-free base alloy. Due to the high price of Sc, low Sc alloys (0.1-0.2%) are to be developed because of their cost effective nature; they exhibita synergetic strengthening effect owing to both α-Al(Mn,Fe)Si dispersoids and $Al_3(Sc,Zr)$ precipitates.

(e) In the present work, it is found that the addition of Sc and Zr considerably reduces the amount of α-Al(Mn,Fe)Si dispersoids precipitated in Al-Mn-Mg 3004 alloys. If this problem can be solved in the future, an excellent synergetic strengthening effect due to both phases can be expected.

6.4 Conclusions

The present work investigated the microstructure, mechanical properties and creep resistance of dispersion-strengthened Al-Mn-Mg 3004 alloy containing two populations of strengthening particles: 50-70 nm-sized α-Al(Mn,Fe)Si dispersoids and 6-8 nm-sized Al_3(Sc,Zr) precipitates. The following conclusions could be drawn.

1. With increasing Sc and Zr contents, the amount of Mn-containing intermetallics and primary Mg_2Si particles increased in the as-cast microstructure of the 3004 alloy.
2. With the addition of Sc and Zr, two populations of strengthening particles (α-Al(Mn,Fe)Si dispersoids and Al_3(Sc,Zr) precipitates) were formed in the 3004 alloy after heat treatment at 375 °C for 24 h. Both the populations contributed to the mechanical properties and creep resistance at ambient and elevated temperatures.
3. The volume fraction of the α-Al(Mn,Fe)Si dispersoids decreased while the volume fraction of the dispersoid free zone increased with increasing Sc and Zr content.
4. The microhardness and yield strength at the ambient temperature greatly increased while the yield strength at 300 °C did not vary even though the Sc and Zr content increased.
5. The addition of Sc and Zr significantly improved the creep resistance at 300 °C due to the precipitation of fine Al_3(Sc,Zr) and reduction of the particle free zone.
6. The combined effects of α-Al(Mn,Fe)Si dispersoids and Al_3(Sc,Zr) precipitates on the yield strengths at 25 °C and 300 °C were quantitatively analyzed based on the Orowan bypass and dislocation climb mechanisms. The analytically predicted yield strengths were in good agreement with the experimental observations.

References

1. Y. J. Li, L. Arnberg, Quantitative study on the precipitation behavior of dispersoids in DC-cast AA3003 alloy during heating and homogenization, Acta Materialia. 51 (2003) 3415-3428. Doi: http://dx.doi.org/10.1016/S1359-6454(03)00160-5.

2. A. M. F. Muggerud, E. A. Mørtsell, Y. Li, R. Holmestad, Dispersoid strengthening in AA3xxx alloys with varying Mn and Si content during annealing at low temperatures, Materials Science and Engineering: A. 567 (2013) 21-28. Doi: http://dx.doi.org/10.1016/j.msea.2013.01.004.

3. K. Liu, X. G. Chen, Development of Al–Mn–Mg 3004 alloy for applications at elevated temperature via dispersoid strengthening, Materials & Design. 84 (2015) 340-350. Doi: http://dx.doi.org/10.1016/j.matdes.2015.06.140.

4. Z. Li, Z. Zhang, X. G. Chen, Effect of magnesium on dispersoid strengthening of Al—Mn—Mg—Si (3xxx) alloys, Transactions of Nonferrous Metals Society of China. 26 (2016) 2793-2799. Doi: http://dx.doi.org/10.1016/S1003-6326(16)64407-2.

5. K. Liu, X.-G. Chen, Evolution of Intermetallics, Dispersoids, and Elevated Temperature Properties at Various Fe Contents in Al-Mn-Mg 3004 Alloys, Metallurgical and Materials Transactions B. 47 (2016) 3291-3300. Doi: http://dx.doi.org/10.1007/s11663-015-0564-y.

6. Y. J. Li, A. M. F. Muggerud, A. Olsen, T. Furu, Precipitation of partially coherent α-Al(Mn,Fe)Si dispersoids and their strengthening effect in AA 3003 alloy, Acta Materialia. 60 (2012) 1004-1014. Doi: http://dx.doi.org/10.1016/j.actamat.2011.11.003.

7. E. A. Marquis, D. N. Seidman, Coarsening kinetics of nanoscale Al3Sc precipitates in an Al–Mg–Sc alloy, Acta Materialia. 53 (2005) 4259-4268. Doi: https://doi.org/10.1016/j.actamat.2005.05.025.

8. E. A. Marquis, D. N. Seidman, Nanoscale structural evolution of Al3Sc precipitates in Al(Sc) alloys, Acta Materialia. 49 (2001) 1909-1919. Doi: https://doi.org/10.1016/S1359-6454(01)00116-1.

9. G. M. Novotny, A. J. Ardell, Precipitation of Al3Sc in binary Al–Sc alloys, Materials Science and Engineering: A. 318 (2001) 144-154. Doi: https://doi.org/10.1016/S0921-5093(01)01326-0.

10. C. Fuller, J. Murray, D. Seidman, Temporal evolution of the nanostructure of Al(Sc,Zr) alloys: Part I – Chemical compositions of Al(ScZr) precipitates, Acta Materialia. 53 (2005) 5401-5413. Doi: https://doi.org/10.1016/j.actamat.2005.08.016

11. J. Lai, Z. Zhang, X. G. Chen, The thermal stability of mechanical properties of Al–B4C composites alloyed with Sc and Zr at elevated temperatures, Materials Science and Engineering: A. 532 (2012) 462-470. Doi: https://doi.org/10.1016/j.msea.2011.11.013.

12. C. Fuller, D. Seidman, Temporal evolution of the nanostructure of Al(Sc,Zr) alloys: Part II-coarsening of Al(ScZr) precipitates, Acta Materialia. 53 (2005) 5415-5428. Doi: https://doi.org/10.1016/j.actamat.2005.08.015

13. P. Naga Raju, K. Srinivasa Rao, G. M. Reddy, M. Kamaraj, K. Prasad Rao, Microstructure and high temperature stability of age hardenable AA2219 aluminium alloy modified by Sc, Mg and Zr additions, Materials Science and Engineering: A. 464 (2007) 192-201. Doi: https://doi.org/10.1016/j.msea.2007.01.144.

14. P. Cavaliere, M. Cabibbo, Effect of Sc and Zr additions on the microstructure and fatigue properties of AA6106 produced by equal-channel-angular-pressing, Materials Characterization. 59 (2008) 197-203. Doi: https://doi.org/10.1016/j.matchar.2006.12.013.

15. Y. Deng, Z. Yin, K. Zhao, J. Duan, Z. He, Effects of Sc and Zr microalloying additions on the microstructure and mechanical properties of new Al–Zn–Mg alloys, Journal of Alloys and Compounds. 530 (2012) 71-80. Doi: https://doi.org/10.1016/j.jallcom.2012.03.108.

16. J. Lai, Z. Zhang, X. G. Chen, Precipitation strengthening of Al–B4C metal matrix composites alloyed with Sc and Zr, Journal of Alloys and Compounds. 552 (2013) 227-235. Doi: http://doi.org/10.1016/j.jallcom.2012.10.096.

17. Z. Li, Z. Zhang, X. G. Chen, Microstructure, elevated-temperature mechanical properties and creep resistance of dispersoid-strengthened Al-Mn-Mg 3xxx alloys with varying Mg and Si content, submitted to Materials Science and Engineering: A. (2017).

18. L. L. Rokhlin, N. R. Bochvar, I. E. Tarytina, N. P. Leonova, Phase composition and recrystallization of Al-based Al-Sc-Mn-Zr alloys, Russian Metallurgy (Metally). 2010 (2010) 241-247. Doi: http://dx.doi.org/10.1134/S0036029510030158.

19. R. A. Karnesky, L. Meng, D. C. Dunand, Strengthening mechanisms in aluminum containing coherent Al3Sc precipitates and incoherent Al2O3 dispersoids, Acta Materialia. 55 (2007) 1299-1308. Doi: http://dx.doi.org/10.1016/j.actamat.2006.10.004.

20. L. Pan, K. Liu, F. Breton, X. -Grant Chen, Effect of Fe on Microstructure and Properties of 8xxx Aluminum Conductor Alloys, Journal of Materials Engineering and Performance. 25 (2016) 5201-5208. Doi: http://dx.doi.org/10.1007/s11665-016-2373-0.

21. A. R. Farkoosh, X. Grant Chen, M. Pekguleryuz, Interaction between molybdenum and manganese to form effective dispersoids in an Al–Si–Cu–Mg alloy and their influence on creep resistance, Materials Science and Engineering: A. 627 (2015) 127-138. Doi: http://dx.doi.org/10.1016/j.msea.2014.12.115.

22. F. A. Mohamed, K.-T. Park, E. J. Lavernia, Creep behavior of discontinuous SiC Al composites, Materials Science and Engineering: A. 150 (1992) 21-35. Doi: http://dx.doi.org/10.1016/0921-5093(90)90004-M.

23. Y. Li, T. G. Langdon, An examination of a substructure-invariant model for the creep of metal matrix composites, Materials Science and Engineering: A. 265 (1999) 276-284. Doi: http://dx.doi.org/10.1016/S0921-5093(98)01131-9.

24. J. G. Kaufman, Properties of Aluminum Alloys: Tensile, Creep, and Fatigue Data at High and Low Temperatures. (ASM international, 1999), pp. 9.

25. E. L. Huskins, B. Cao, K. T. Ramesh, Strengthening mechanisms in an Al–Mg alloy, Materials Science and Engineering: A. 527 (2010) 1292-1298. Doi: http://dx.doi.org/10.1016/j.msea.2009.11.056.

26. Ø. Ryen, B. Holmedal, O. Nijs, E. Nes, E. Sjölander, H.-E. Ekström, Strengthening mechanisms in solid solution aluminum alloys, Metallurgical and Materials

Transactions A. 37 (2006) 1999-2006. Doi: http://dx.doi.org/10.1007/s11661-006-0142-7.

27. C. B. Fuller, D. N. Seidman, D. C. Dunand, Mechanical properties of Al(Sc,Zr) alloys at ambient and elevated temperatures, Acta Materialia. 51 (2003) 4803-4814. Doi: https://doi.org/10.1016/S1359-6454(03)00320-3.

28. J. Qin, Z. Zhang, X.-G. Chen, Mechanical Properties and Strengthening Mechanisms of Al-15 Pct B4C Composites with Sc and Zr at Elevated Temperatures, Metallurgical and Materials Transactions A. 47 (2016) 4694-4708. Doi: http://dx.doi.org/10.1007/s11661-016-3606-4.

29. J. G. Kaufman, Properties of Aluminum Alloys: Tensile, Creep, and Fatigue Data at High and Low Temperatures. (ASM international, 1999), pp. 102.

30. D. N. Seidman, E. A. Marquis, D. C. Dunand, Precipitation strengthening at ambient and elevated temperatures of heat-treatable Al(Sc) alloys, Acta Materialia. 50 (2002) 4021-4035. Doi: http://dx.doi.org/10.1016/S1359-6454(02)00201-X.

31. A. J. Ardell, Precipitation hardening, Metallurgical Transactions A. 16 (1985) 2131-2165. Doi: http://dx.doi.org/10.1007/BF02670416.

Chapter 7 The influence of Cu addition on dispersoid formation and mechanical properties of Al-Mn-Mg 3004 alloys

7.1 Introduction

Al-Mn-Mg AA3xxx alloys are widely used in automobile, packaging and architecture industries. Traditionally, AA3xxx alloys are strengthened by work hardening and classified as non-heat-treatable alloys. However, by applying appropriate heat treatment [1-4], a large number of α-Al(Mn,Fe)Si dispersoids could be precipitated in AA3xxx alloys. The α-Al(Mn,Fe)Si dispersoids are partially coherent with the aluminum matrix [1, 5]. Recently, the strengthening effect of α-Al(Mn,Fe)Si dispersoids at ambient and elevated temperatures are reported [1, 6-8]. Moreover, the α-Al(Mn,Fe)Si dispersoids have been proved to be thermally stable at 300 ºC [6], which is especially attractive to the materials for elevated temperature applications.

To improve the room- and elevated-temperature properties of AA3xxx alloys, a number of studies were conducted to investigate the influences of chemical compositions on precipitation behavior of α-Al(Mn,Fe)Si dispersoids in AA3xxx [8-13]. The Mn addition could enhance the precipitation of α-Al(Mn,Fe)Si dispersoids and improve the yield strength [8]. Fe decreased the solubility of Mn and accelerated the precipitation rate of α-Al(Mn,Fe)Si dispersoids [3]. The yield strength and creep resistance at elevated temperature could be improved with an optimized content of Fe [9]. In our previous work [13], the effects of Mg and Si on α-Al(MnFe)Si dispersoid precipitation, elevated-temperature strength and creep resistance in 3xxx alloys were systematically studied. The best combination of yield strength and creep resistance at 300 ºC was obtained by the alloy containing 1.0 wt.% Mg and 0.25 wt.% Si with the maximum volume fraction of dispersoids. It was found that Mg would affect the formation of α-Al(Mn,Fe)Si dispersoids by forming metastable Mg_2Si [7, 10, 11]. Metastable Mg_2Si precipitated during heating process and promoted the nucleation of α-Al(Mn,Fe)Si

dispersoids[14]. Si increased the volume fraction of α-Al(Mn,Fe)Si dispersoids [8] and decreased the size of α-Al(Mn,Fe)Si dispersoids [13]. With the addition of Mo, the size of dispersoids became finer and the volume fraction of dispersoids was increased [12]. Therefore, the yield strength and creep resistance at elevated temperature were remarkable improved by the Mo addition.

Cu is an important alloying element of AA7xxx alloys (Al-Zn-Mg) and AA6xxx alloys (Al-Mg-Si). By the addition of Cu and aging at 100 – 200 °C, nano-scale metastable $Mg(Zn,Al,Cu)_2$ in 7xxx alloys [15] and Q-AlCuMgSi (Q phase) in 6xxx alloys [16, 17] precipitated in the aluminum matrix. Metastable $Mg(Zn,Al,Cu)_2$ and Q-AlCuMgSi possessed a lower coarsening rate than metastable $MgZn_2$ and Mg_2Si [15, 18, 19]. However, the influence of Cu on the precipitation and coarsening behaviour of α-Al(Mn,Fe)Si dispersoids have never reported before. In addition, the effect of Cu on elevated-temperature properties of AA3xxx alloys is rarely found in the literature.

The aim of the present work is to investigate the effect of Cu on the precipitation and coarsening behavior of dispersoids as well as on the mechanical properties at ambient and elevated temperatures in Al-Mn-Mg 3004 alloy.

7.2 Experimental procedures

Four experimental alloys with different Cu content were designed in the present study. The base alloy contained 1.25 % Mn, 0.5% Fe, 1.0% Mg, 0.25% Si and without Cu. The other three alloys (DU35, DU75 and DU120) contained 0.37%, 0,72% and 1.23% Cu, respectively. The experimental alloys were prepared with commercially pure Al (99.7%), pure Mg (99.9%), and Al-25%Mn, Al-25%Fe, Al-50%Si and Al-50%Cu master alloys. The chemical compositions of experimental alloys analyzed by an optical emission spectrometer are listed in Table 7.1 (all of the alloy compositions are in wt.% in the present paper unless indicated otherwise). For each batch, approximately 3 kg of materials were melted in an electrical resistance furnace. The melt was maintained at 750 ºC for 30 min and degassed for 15 min. It

was then poured into a preheated steel permanent mold that was preheated at 250 ºC. The dimension of cast ingots was 30 mm × 40 mm × 80 mm.

Table 7.1 Chemical composition of experimental alloys (wt.%).

Alloy code	Cu	Si	Fe	Mn	Mg	Al
DU0 (base)	**0**	0.24	0.49	1.23	0.97	Bal
DU35	**0.37**	0.27	0.53	1.25	1.03	Bal
DU75	**0.72**	0.24	0.53	1.24	0.99	Bal
DU120	**1.23**	0.26	0.48	1.27	1.04	Bal

Two different heat treatments were used. For the precipitation of dispersoids, the samples were heated with a heating rate 5 ºC/min from room temperature to 375 ºC, 425 ºC and 475 ºC respectively, and then held at those temperature for 2 h to 48 h, followed by water quench to room temperature, as shown in Fig. 7.1(a). To study dispersoid nucleation process, the samples were heated from room temperature to 330 ºC, 425 ºC, or held at 425 ºC for 6 hours, followed by water quench to freeze the microstructure (Fig. 7.1(b)).

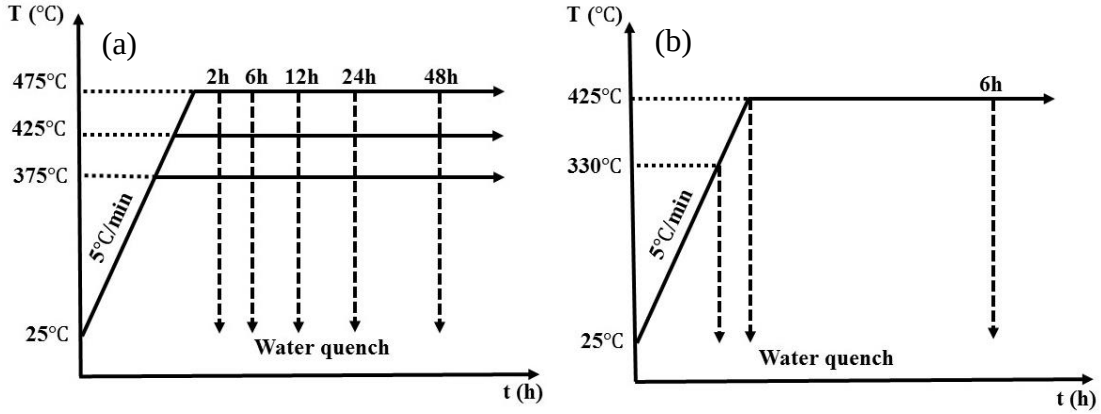

Fig. 7.1 The schematic diagram of two heat treatment conditions: (a) for the precipitation of dispersoids and (b) for the dispersoid nucleation.

The electrical conductivity was measured by Sigmascope SMP10 unit. 5 measurements were conducted for each sample. The Vicker hardness was evaluated by a NG-1000 CCD

microhardness test unit with a load of 200g and 20 second dwelling time. At least 10 measurements were performed to calculate the average value of each sample. Compression yield strength tests were conducted at 300 ºC with a strain rate 0.001 s^{-1} using a Gleeble 3800 thermomechanical testing unit. Cylinder samples with a 15 mm length and 10 mm diameter were used for the compression yield strength test. The results were obtained from the average value of three samples. Compression creep tests were conducted at 300 ºC for 96 h with a constant load of 58 MPa. The dimension of the creep test samples was the same as the Gleeble samples.

Optical microscope was used to observe the intermetallic particles and the distribution of dispersoids. The polished samples were etched by 0.5% HF for 20 seconds. Image analysis software (Clemex PE 4.0) was used to quantify the volume fractions of the dispersoid zone and the dispersoid free zone (DFZ). A transmission electron microscope (TEM, JEM-2100) equipped with an energy dispersive X-ray spectroscopy (EDS) was used to observe the dispersoids in details. TEM foils were prepared by twin-jet machine with a solution of 25% nitric acid in methanol at -20 to -30 ºC. Electron energy loss spectroscopy (EELS) attached to the TEM was used to measure the thickness of the TEM specimens. The TEM bright field images were recorded near <100> zone axis and {200} planes on two–beam diffraction conditions. The size and number density of dispersoids were quantified by image analysis on TEM images. The calculation of the dispersoid volume fraction was based on the published literature [3] using the following equation:

$$V_v = A_A \frac{K\bar{D}}{K\bar{D} + t}(1 - A_{DFZ}) \qquad \text{Eq. 7.1}$$

Where A_A is the volume fraction of dispersoids and $\bar{D}$ isthe average equivalent diameter of dispersoids in TEM images; A_{DFZ} is the volume fraction of dispersoid free zone; t is the TEM foil thickness; and K is the average shape factor of dispersoids.

7.3 Results and discussion

7.3.1 Influence of Cu on microstructure

7.3.1.1 Influence of Cu on intermetallic phases and dispersoid distribution

The typical as-cast microstructures of experimental alloys are shown in Fig. 7.2. In the base alloy (DU0, Cu-free), two types of intermetallic particles were observed (Fig. 7.2(a)). The grey particles were Al_6(Mn,Fe) intermetallic and the black ones are primary Mg_2Si; both intermetalllics distributed in aluminum dendrite boundaries. In the Cu containing alloys, the grey particles are Al_6(Mn,Fe) intermetallic, in which a small amount of Cu can be detected. The dark particles are primary Mg_2Si and Q-AlCuMgSi intermetallics. In additional, a small amount of light grey Al_2Cu phases is co-existed with Q-phase. The microstructure of the alloy containing 1.2% Cu is shown in Fig. 7.2(b). Using image analysis, the volume fractions of intermetallics as a function of Cu content were evaluated (Fig. 7.3). Most of the intermetallic phases in the experimental alloys are the Mn containing Al_6(Mn,Fe) particles (approximately 3.5-3.7 vol.%). Although the volume fractions of both Mg_2Si and Q-AlCuMgSi phases increase with increasing the Cu content, their amount is limited (0.1-0.3 vol.%) when compared to the Mn containing intermetallic phase. The total volume fractions of the intermetallic phases in all four alloys are very similar (3.8-3.9 vol.%), indicating that Cu addition does not significantly change the type and amount of intermetallic phases.

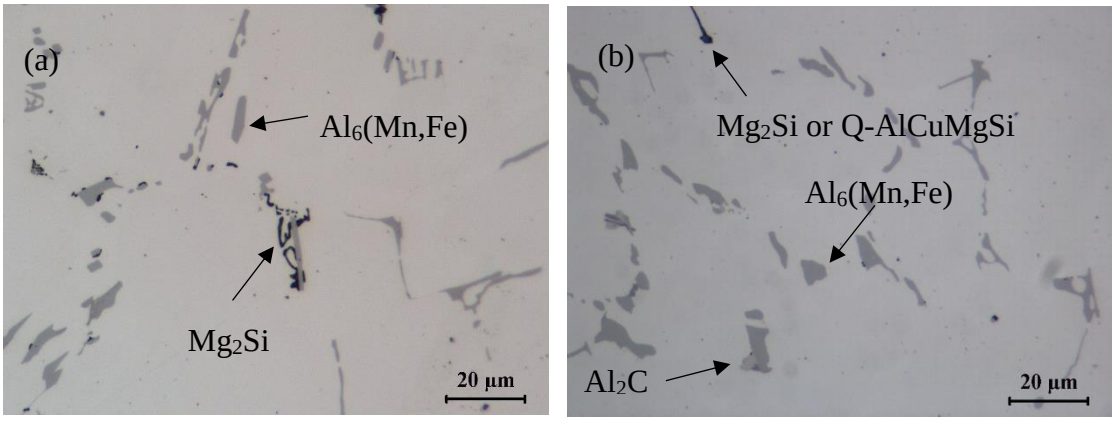

Fig. 7.2 Typical as-cast microstructures of (a) DU0 alloy and (b) DU120 alloy.

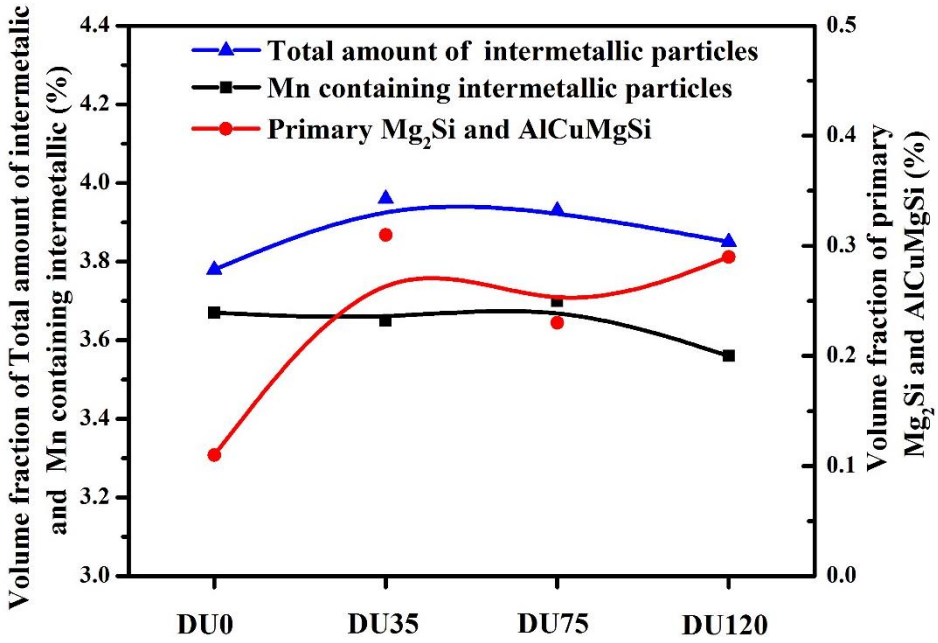

Fig. 7.3 The volume fractions of intermetallic particles in four experimental alloys.

α-Al(Mn,Fe)Si dispersoids can precipitate at approximately 400 ºC during heat treatment in 3xxx alloys [3, 6, 7]. Fig. 7.4 shows the optical images of DU0 and DU120 alloys after the heat treatment at 425 ºC for 6 h. The light yellow regions are the dispersoid zone where most dispersoids concentrated, and the white color regions are the dispersoid free zone (DFZ) where only few dispersoids appeared. The volume fractions of the dispersoid zone and DFZ are shown in Fig. 7.5. The volume fractions of the dispersoid zone are ~80% in all of the experimental alloys. The variation of the volume fractions of the dispersoid zone and DFZ between alloys is quite small, indicating the Cu has no significant influence on the dispersoid distribution.

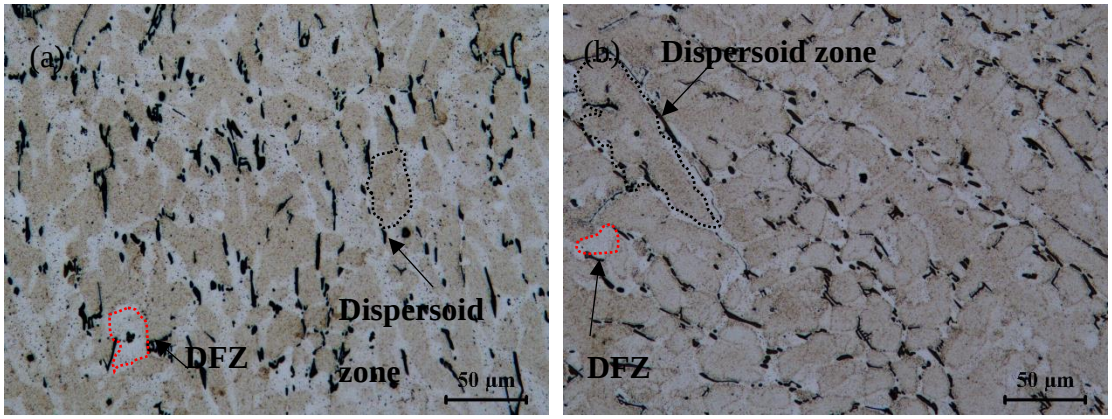

Fig. 7.4 Optical images of (a) DU0 alloy and (b) DU120 alloy after heat-treatment at 425 ºC for 6 h.

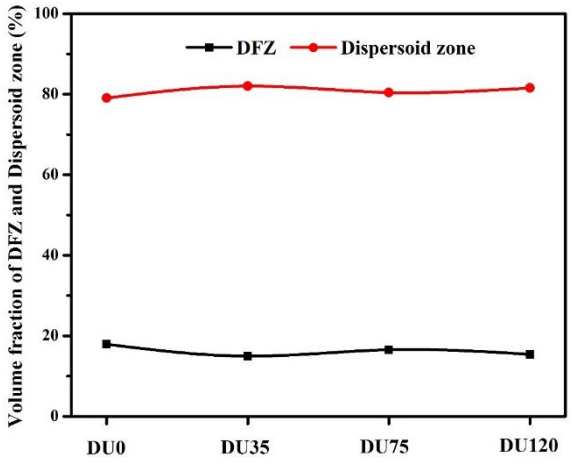

Fig. 7.5 The volume fractions of the dispersoid zone and dispersoid free zone (DFZ) in the experimental alloys.

7.3.1.2 The influence of Cu on dispersoid features and thermal stability

To reveal the influence of Cu on the precipitation behaviour of dispersoids, TEM observation was carried out. Fig. 7.6 is TEM bright field images showing the details of the dispersoids in the samples heat-treated at 425 ºC for 6 hours. The dispersoids in DU0 alloy (Fig. 7.6(a)) have rod-like or plate-like morphology. On the other hand, most of the dispersoids are cubic shape but a few of the dispersoids have rod-like or plate-like morphology in the Cu contained alloys (Figs. 7.6(b), (c) and (d)). A trace of Cu was detected in the dispersoids in the Cu contained alloys by TEM-EDS analysis. All dispersoids are identified as α-Al(Mn,Fe)Si

according to the results of TEM-EDS and literature [1-3, 5, 6]. The equivalent diameter of the dispersoids in the base alloy (DU0) is 47 nm, whereas the diameters of the dispersoids in the Cu containing alloys are between 32 and 37 nm (Fig. 7.7(a)), which is obviously smaller than that in the base alloy. In addition, the number density of dispersoids in the Cu containing alloys is higher than that in the base alloy. However, the volume fraction of dispersoids in the base alloy is slightly higher than that in the Cu contained alloys (Fig. 7.7(b)). Results indicate that the addition of Cu has strong effect on the size and number density of dispersoids.

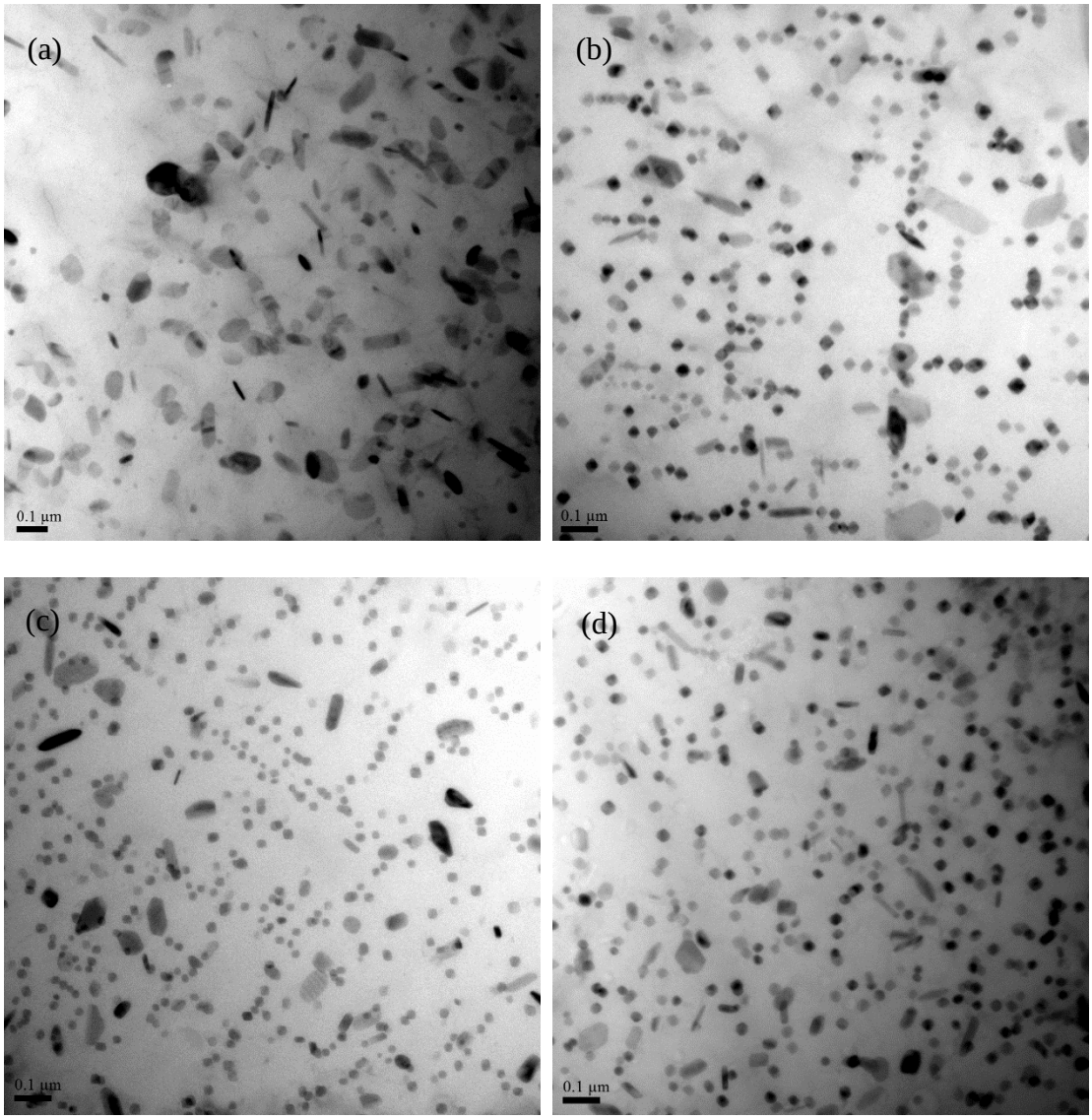

Fig. 7.6 TEM bright field images of dispersoids after heat-treated at 425 ºC for 6 h (a) DU0 alloy (0% Cu), (b) DU35 alloy (0.37% Cu), (c) DU75 alloy (0.72% Cu) and (d) DU120 alloy (1.23% Cu).

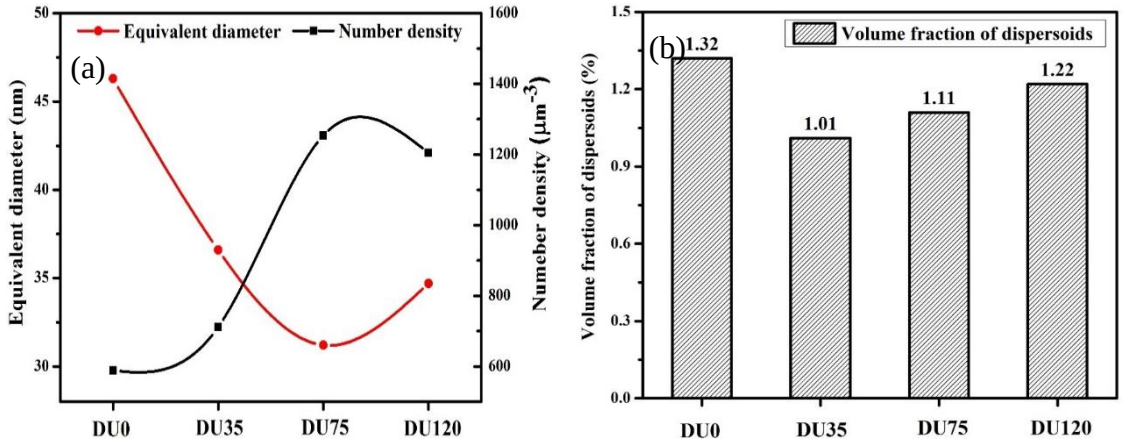

Fig. 7.7 (a) the equivalent diameter and number density of dispersoids and (b) the volume fraction of dispersoids in the experimental alloys.

The effect of Cu on dispersoid nucleation was studied using the quench technique and TEM observation. The typical TEM images of DU0 and DU120 alloys after heated at 330 ºC followed water quench are presented in Fig. 7.8. Lath-like and dark-dot precipitates appeared in DU0 alloy (Fig.7.8 (a)), which were metastable β'-Mg_2Si precipitates [20, 21]. The preferred precipitation directions of the β'-Mg_2Si are $<001>_{Al}$. In DU120 alloy, a large number of lath-like and dark-dot phase was also observed to be precipitated along $<001>_{Al}$ direction (Fig. 7.8(b)). Those precipitates were composed of Al, Mg, Si and Cu based on the TEM-EDS analysis (Fig. 7.9) and were identified as the metastable Q-AlCuMgSi phase [16, 17]. It is interesting to note that the number density of Q-phase in DU120 alloy is obviously higher than that of β'-Mg_2Si phase in DU0 alloy, which could be attributed to the presence of Cu [16].

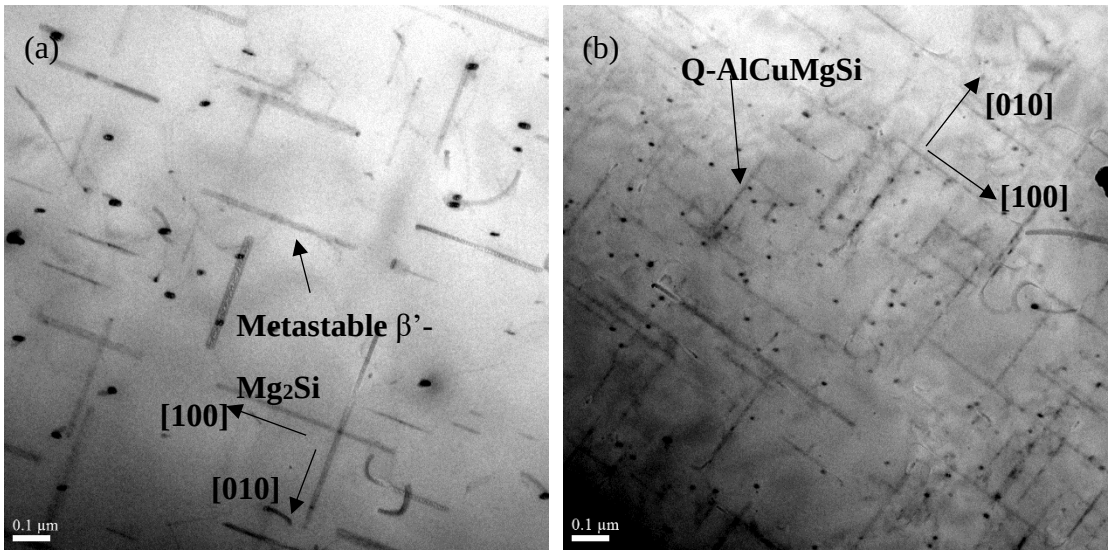

Fig. 7.8 TEM images of as-heated 330 ºC samples of (a) DU0 alloy and (b) DU120 alloy.

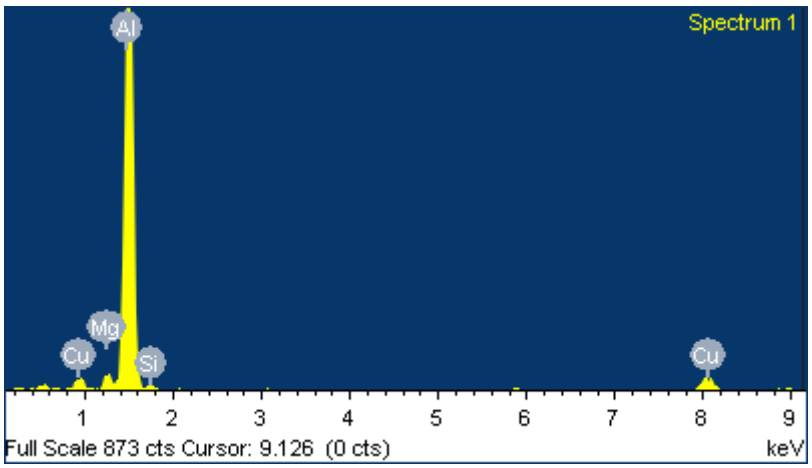

Fig. 7.9 The chemical composition of Q-phase in DU120 alloy.

During heating process from 330 ºC toward 425 ºC, both β'-Mg_2Si and Q-AlCuMgSi dissolved and disappeared in DU0 and DU120 samples. After heated at 425 ºC, a large number of small dispersoids precipitated in the aluminum matrix (Fig. 7.10). Interestingly, all of dispersoids in DU0 and DU120 alloys precipitated along $<001>_{Al}$ directions, which were the preferred precipitation orientation of previous β'-Mg_2Si and Q-AlCuMgSi phases (Fig. 7.8). In our previous work, it was found [14] that without pre-existing β'-Mg_2Si in Al-Mn-Mg 3xxx alloys, α-Al(Mn,Fe)Si dispersoids could hardly form. The pre-existing β'-Mg_2Si promoted the nucleation of α-Al(Mn,Fe)Si dispersoids as the local Si-rich areas on the previously dissolved

β'-Mg_2Si provided favorable nucleation sites for α-Al(MnFe)Si dispersoids. But the effect of the Q-AlCuMgSi phase on dispersoid nucleation has not been reported yet. In the present work, it is confirmed that the pre-existing Q-AlCuMgSi can also promote the α-Al(Mn,Fe)Si dispersoid nucleation in the Cu containing 3004 alloys. In fact, the number density of dispersoids in DU120 alloy is higher than that in DU0 alloy (Fig. 7.10), suggesting that pre-existing Q-AlCuMgSi precipitates seem to be more effective to promote the dispersoid nucleation than pre-existing β'-Mg_2Si precipitates.

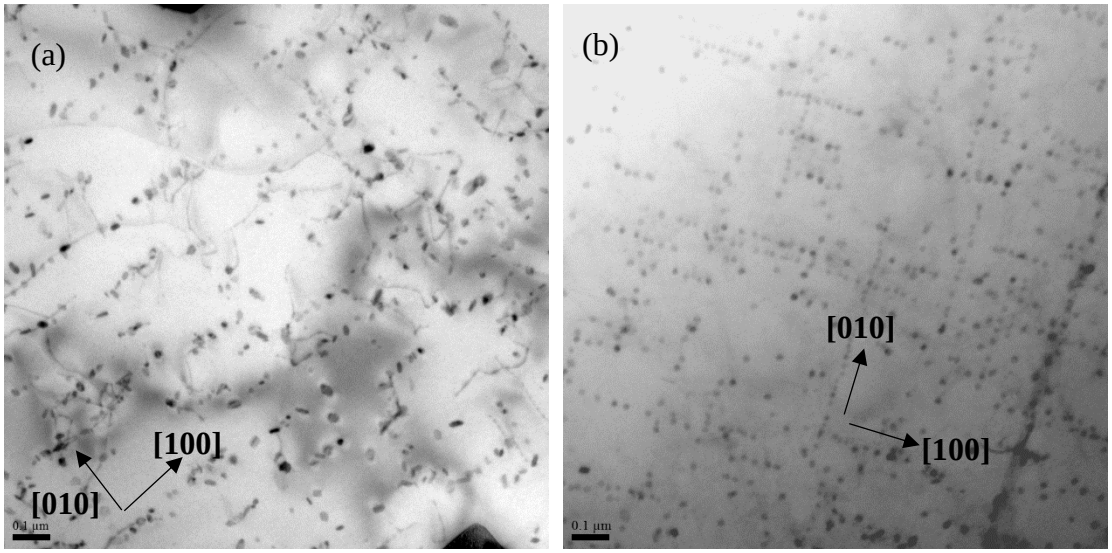

Fig. 7.10 TEM images of as-heated 425 ℃ samples of (a) DU0 and (b) DU120 alloys.

When the samples were further held for 6 hours at 425 ºC, the dispersoids in both alloys grew and their size increased (Fig. 7.10 vs. Fig. 7.6). To examine the thermal stability of dispersoids in the experimental alloys, the samples after treated at 425ºC/6h were held for a prolonged period of 500 hours at 350 ºC. The typical TEM images after a long-term thermal holding are shown in Fig. 7.11. The dispersoids in DU0 alloy after 350ºC/500h are much larger than those in DU120 alloys (Fig. 7.11). The equivalent diameter of dispersoids in DU0 alloy increases from initial 46.3 nm to 59.2 nm after 350ºC/500h (Fig. 7.12). The size of disoersoids increases by 28% after a long-term thermal holding, indicating a significant coarsening process during prolonged exposure at 350 ºC. On the other hand, the equivalent diameter of dispersoids in the Cu containing DU120 alloy increases from initial 33.6 nm to 37.1 nm after the long-term

thermal holding (Fig. 7.12), which represents a 10% of the size increase. It demonstrates that the coarsening of dispersoids in the Cu containing alloys is remarkably slower than that in the Cu-free base alloy. Therefore, the Cu addition results in an improvement of the thermal stability of dispersoids, which can be benefit to the elevated-temperature properties of materials during long exposure at high service temperature. The mechanism of the Cu addition on the improvement of the thermal stability of dispersoids is not clear yet.

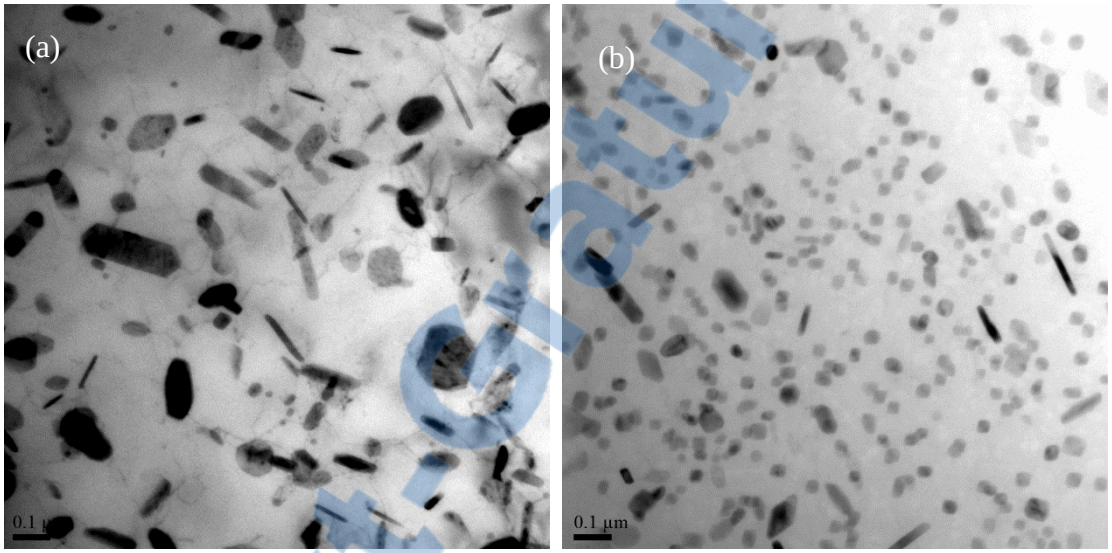

Fig. 7.11 TEM images of dispersoids after holding at 350 ºC for 500 h in (a) DU0 alloy and (b) DU120 alloy.

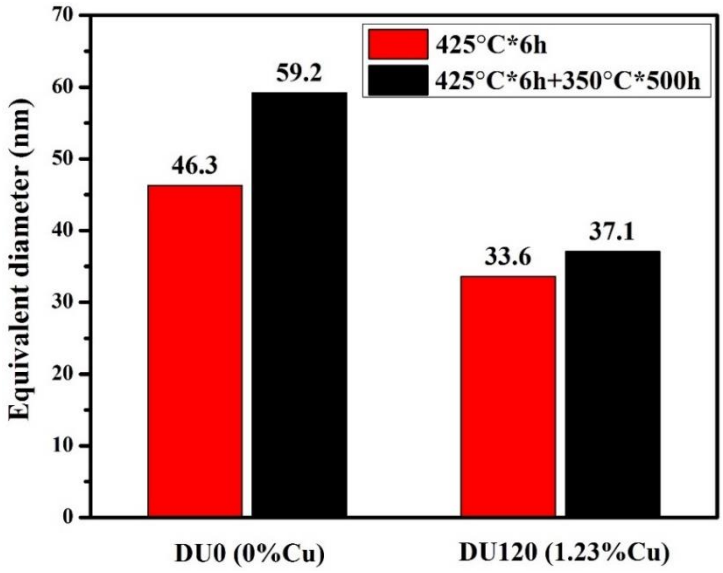

Fig. 7.12 The comparison of the dispersoid size before and after a long-term thermal holding at 350ºC/500h.

7.3.2 Influence of Cu on mechanical properties

7.3.2.1 Influence of Cu on microhardness at ambient temperature

Fig. 7.13 shows the microhardness evolution of experimental alloys at three treatment temperatures as a function of holding time. When the samples treated at 375 ºC, the peak hardness arrived in different holding times for four alloys. For example, the peak hardness of DU0 alloy (65 HV) was achieved after 36 h while it arrived in 12 h (73 HV) for DU120 alloy. The peak values of microhardness and their corresponding times of all alloys are listed in Table 7.3. When treated at 425 ºC (Fig. 7.13(b)), the peak hardness of DU0, DU35 and DU75 alloys was reached after holding for 6 hours. For DU120 alloy, the peak value is 80 HV at 425ºC/2h, which is slightly higher than the value of 77 HV after 425ºC/6h. When treated at 475 ºC (Fig. 7.13(c)), the peak hardness of all four alloys was reached after 2 hours. After holding more than 2 hours, the hardness of all four alloys decreased with the increase of the holding time. Based on the above observation, the heat treatment condition, 425 ºC for 6 hours, is used to study the effect of the Cu addition on mechanical properties and creep resistance.

In general, the microhardness of all the Cu containing alloys is higher than that of the Cu-free base alloy at any given temperature and holding time. Moreover, the microhardness increases with the increase of the Cu content (Fig. 7.13). It is worthy to mention that the dispersoid precipitation was observed in all of experimental alloys at three heat treatment temperatures. The microhardness evolution involved the dispersoid strengthening and solid solution strengthening during heat treatment. The finer size and higher number density of dispersoids in the Cu containing alloys (Fig. 7.7(a)) promotes the dispersoid strengthening. On the other hand, to evaluate the solute solution strengthening, the amount of solute atoms in aluminum matrix was evaluated by electrical conductivity. The values of electrical conductivity corresponding to the peak hardness are also listed in Table 7.3. The electrical conductivity of the Cu containing alloys is generally lower than that of the base alloy, and the values decrease with the increase of the Cu content. It indicates that more Cu solute atoms contain in the high Cu containing alloys, which are benefit to the microhadness due to solid solution strengthening.

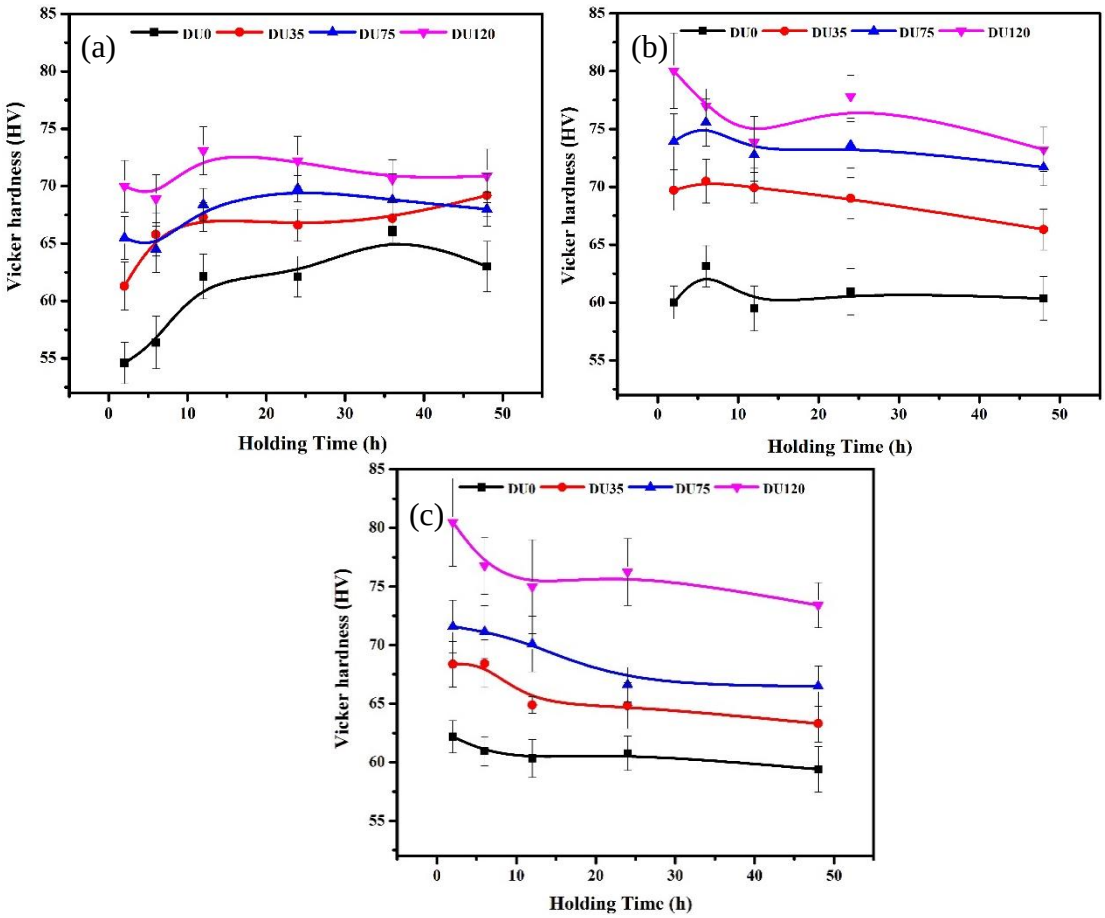

Fig. 7.13 Microhardness of experimental alloys as a function of holding time at (a) 375 ºC, (b) 425 ºC and (c) 475 ºC.

Table 7.3 Peak hardness values and their corresponding times and electrical conductivity

Treatment temperature (ºC)	Properties	DU0	DU35	DU75	DU120
375	Peak hardness	65HV/36h	68HV/48h	70HV/24h	73HV/12h
	EC (MS/m)	23.0	22.8	22.0	21.0
425	Peak hardness	62HV/6h	70HV/6h	75HV/6h	80HV/2h
	EC (MS/m)	22.5	22.2	21.6	20.5
475	Peak hardness	62HV/2h	68HV/2h	72HV/2h	80HV/2h
	EC (MS/m)	21.8	21.5	21.2	20.2

7.3.2.2 Influence of Cu on yield strength at 300 ºC

The yield strengths of four experimental alloys at 300 ºC are shown in Fig. 7.14. Generally, the yield strengths of the Cu containing alloys are higher than that of the Cu-free base alloy. Moreover, the yield strength increases with the increase of Cu content. Among all experimental alloys, the maximum yield strength is 87.4 MPa in DU120 alloys, which is 14% higher than that in DU0 alloy (76.7 MPa). It is apparent that the Cu addition improves the yield strength at elevated temperature, which is likely attributed to the dispersoid strengthening and solid solution strengthening.

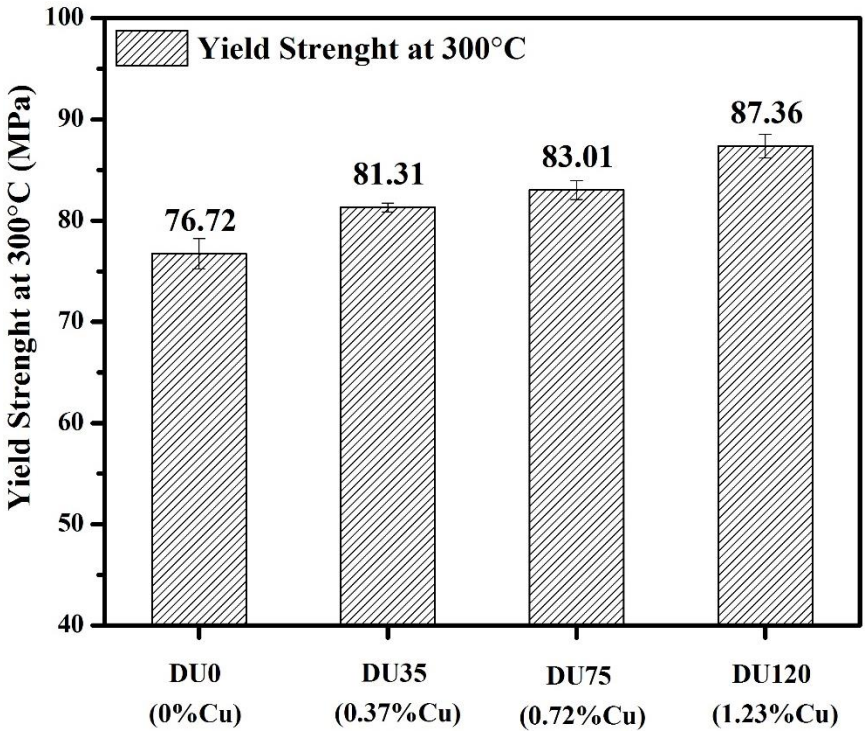

Fig. 7.14 Yield strength at 300 ºC of experimental alloys after heat treatment at 425ºC/6h.

To clarify the strength contributions, the yield strength at 300 ºC is assessed based on the assumption that the contribution of the yield strength is composed of: (1) dispersoid strengthening; (2) Cu solid solution strengthening and (3) aluminum matrix contribution (including contributions of aluminum grains, intermetallic particles and other solute atoms):

$$\sigma_y = \sigma_m + \Delta\sigma_{SS} + \Delta\sigma_{dispersoids} \quad \text{Eq. 7.2}$$

where σ_y is the yield strength, σ_m is the matrix strength, $\Delta\sigma_{SS}$ is the strengthening by solid solution, $\Delta\sigma_{dispersoids}$ is the strengthening by α-Al(Mn,Fe)Si dispersoids.

For the dispersoid strengthening, Orowan bypassing mechanism can be used to calculate the dispersoid strengthening contribution ($\Delta\sigma_{Dispersoids}$) using the Eq. 7.3 [1, 8]:

$$\Delta\sigma_{Dispersoids} = \frac{0.84MGb}{2\pi(1-v)^{1/2}\lambda}\ln\frac{r}{b} \quad \text{Eq. 7.3}$$

$$\lambda = r\left(\frac{2\pi}{3f}\right)^{1/2} \quad \text{Eq. 7.4}$$

Where M is the Taylor factor for aluminum, which is equal to 2 [1]; G is the shear modulus, G=21.1GPa for Al matrix at 300 ºC [22]; b is the burgers vector, for aluminum b=2.86 nm [1]; v is the Poison ratio, which is equal to 0.33 for aluminum [1]; λ is the inter-particle spacing of dispersoids; r is the average radius and f is the volume fraction of dispersoids.

Using the dispersoid data in Fig. 7.7, the calculated results are presented in Table 7.4. The dispersoid strength contribution is 30.1 MPa, 31.5 MPa, 37.3 MPa and 36.2 MPa for DU0, DU35, DU75 and DU120 alloys, respectively.

On the other hand, solute Cu atoms in the matrix can have contribution to the yield strength. The yield strength contribution ($\Delta\sigma_{SS}$) of solute atoms can be estimated according to Eq. 7.5 [23, 24]:

$$\Delta\sigma_{SS} = HC^{\alpha} \quad \text{Eq. 7.5}$$

Where C is the concentration of solute atoms, H was the yield strength increment provided by solute atoms per weight percentage, α is a constant and α=1.

Here, most of the Cu content in the experimental alloys are assumed in the solid solution because that the amount of Cu detected in intermetallic particles and dispersoids is very limited. However, there is no published data on H available for Cu at elevated temperature. Based on the yield strength difference between the AA1100-O alloy and AA2024-O alloy (4.5%Cu) measured at 315 ºC [25, 26], it was calculated that 1% Cu could contribute 6 MPa yield strength increment, which was used a close approximation of H for Cu solute atoms at 300 ºC. Based

on Eq. 7.5, the strength contributions of Cu solute atoms are 2.1 MPa, 4.5 MPa and 7.2 MPa for DU35, DU75 and DU120 alloys, respectively (Table 7.4).

To estimate the yield strength contribution of the aluminum matrix, the yield strength of AA3004-O alloy at 315 ºC (41 MPa) [27] was used as a reasonable approximation, because the chemical compositions of all experimental alloys are similar to AA3004 alloy except the Cu content.

The contribution of different strengthening components is listed in Table 7.4. The overall calculated results of the yield strength at 300 ºC are compared with the experimentally measured ones (Fig. 7.15). The calculated results agree well with experimentally measured strengths in all four alloys.

It can be seen that the dispersoid strengthening contributes approximately 40% of the total yield strength, indicating that it is the main strengthening mechanism at elevated temperature in the experimental alloys. Among all of four alloys, the dispersoid strengthening contribution of DU0 alloy is the lowest due to large dispersoid size and low number density (Fig. 7.7(a)). As the Cu content increases, the dispersoid strengthening becomes stronger. The high number density and small size of dispersoids in DU35, DU75 and DU120 alloys are apparently benefit to the positive effect of the dispersoid strengthening. The calculated results of the Cu solute atoms show that the solid solution strengthening increases with increasing Cu content and it reaches the maximum of 7.2 MPa in DU120 alloy. In brief, the addition of Cu improves the dispersoid strengthening by increasing the dispersoid number density and decreasing of the dispersoid size. In addition, the Cu solute atoms in the matrix provide the solid solution strengthening for the Cu containing alloys.

Table 7.4 The contribution of yield strength at 300 ºC by different strengthening components

Strength contribution	DU0	DU35	DU75	DU120
AA3004-O matrix (MPa)	41	41	41	41
Dispersoids (MPa)	30.1	31.5	37.3	36.2
Cu solid solution (MPa)	0	2.1	4.5	7.2
The total calculated results (MPa)	71.1	74.6	82.8	84.4
The experimental results (MPa)	76.7	81.3	83.0	87.4

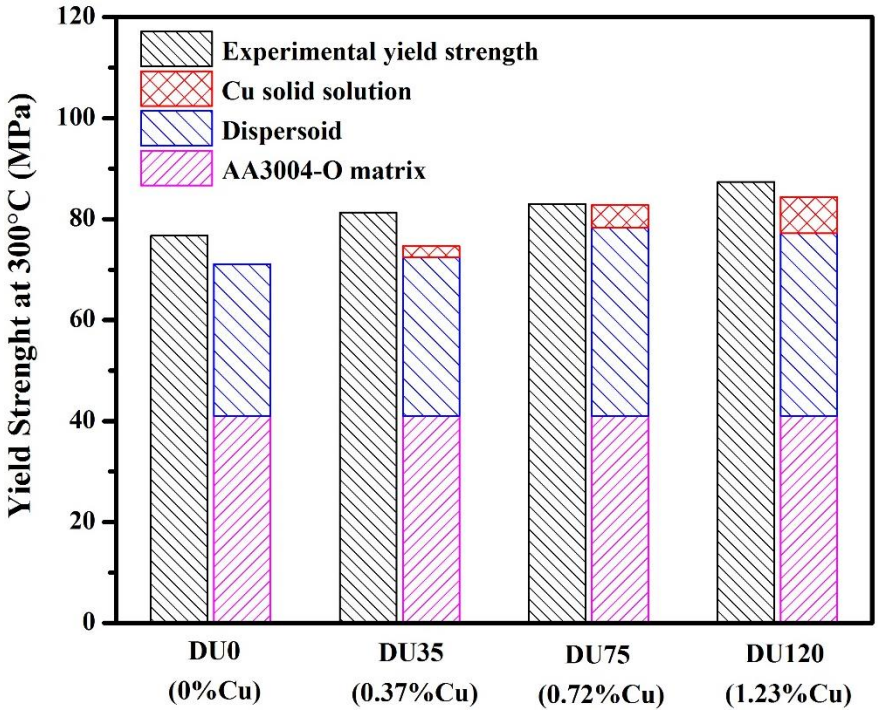

Fig. 7.15 The comparison of the yield strength at 300 ºC between calculated and experimentally measured ones

7.3.2.3 Influence of Cu on creep resistance

Creep resistance is an important property for the materials working at elevated temperature. Fig. 7.16 shows the typical creep curves of all four alloys at 300 ºC with a constant load of 58 MPa. The total creep stains are 0.27, 0.22, 0.14 and 0.035 for DU0, DU35, DU75 and DU120 alloys, respectively. It is evident that the total creep strain significantly decreases with increasing the Cu content, indicating a remarkable improvement of creep resistance with the increase of the Cu content at elevated temperature. Moreover, the minimum creep rate is calculated to be $7.8*10^{-7}$ s^{-1}, $5.8*10^{-7}$ s^{-1}, $4.1*10^{-7}$ s^{-1} and $1.2*10^{-7}$ s^{-1} for DU0, DU35, DU75 and DU120 alloys, respectively. Similar as the trend of the total creep stain, the minimum creep rate also significantly decreases with increasing the Cu content.

According to the microstructure observation in the section 3.1, the addition of Cu increased the dispersoid number density and decreased the dispersoid size (Fig. 7.7 (a)). Dispersoids

generally act as obstacles to inhibit the movement of dislocations. Obviously, higher the number density and finer size of dispersoid, higher the creep resistance is due to inhibiting the dislocation migration during creep deformation. On the other hand, the solute atoms in the aluminum matrix also play an important role on creep resistance because the interactions between solute atoms and dislocations retard the movement of dislocations. Therefore, a better creep resistance can be expected with the increase of Cu solute atoms in the Cu containing alloys.

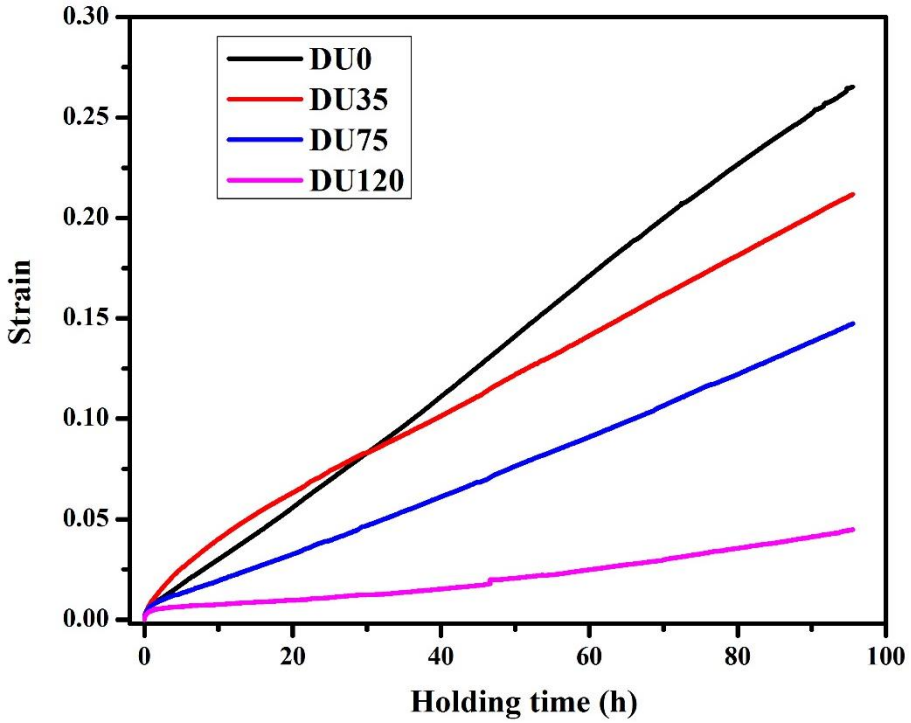

Fig. 7.16 Typical creep curves of four experimental alloys

7.4 Conclusions

1) The addition of Cu in Al-Mn-Mg 3004 alloy promotes the α-Al(Mn,Fe)Si dispersoid precipitation by increasing the number density of dispersoids and decreasing the size of dispersoids.
2) β'-Mg_2Si precipitation in the Cu-free base alloy and Q-AlCuMgSi precipitation in the Cu containing alloys were observed during heating process of the heat treatment. Although

dissolved in the further heating process, both pre-existing β'-Mg_2Si and Q-AlCuMgSi precipitates can provide favorable nucleation sites for dispersoid precipitation.

3) The coarsening resistance of α-Al(Mn,Fe)Si dispersoids in the 1.2% Cu containing alloy is significantly higher than that in the Cu-free base alloy under a prolonged thermal holding at 350 ºC for 500 h.

4) The addition of Cu improves the microhardness at ambient temperature as well as the yield strength and creep resistance at 300 ºC. Higher Cu contents in the alloys, higher strength and creep resistance of the alloys have. It is mainly attributed to the dispersoid strengthening and Cu solid solution strengthening.

5. The yield strength contribution at 300 ºC is quantitatively evaluated based on the dispersoid, solid solution and matrix contributions. It is confirmed that the dispersoid strengthening is the main strengthening mechanism at elevated temperature in the experimental alloys. The predicted yield strengths at 300 ºC are in good agreement with experimental data.

References

1. Y. J. Li, A. M. F. Muggerud, A. Olsen, T. Furu, Precipitation of partially coherent α-Al(Mn,Fe)Si dispersoids and their strengthening effect in AA 3003 alloy, Acta Materialia. 60 (2012) 1004-1014. Doi: http://dx.doi.org/10.1016/j.actamat.2011.11.003.
2. M. Dehmas, E. Aeby-Gautier, P. Archambault, M. Serrière, Interaction Between Eutectic Intermetallic Particles and Dispersoids in the 3003 Aluminum Alloy During Homogenization Treatments, Metallurgical and Materials Transactions A. 44 (2013) 1059-1073. Doi: http://dx.doi.org/10.1007/s11661-012-1473-1.
3. Y. J. Li, L. Arnberg, Quantitative study on the precipitation behavior of dispersoids in DC-cast AA3003 alloy during heating and homogenization, Acta Materialia. 51 (2003) 3415-3428. Doi: http://dx.doi.org/10.1016/S1359-6454(03)00160-5.
4. H.-W. Huang, B.-L. Ou, Evolution of precipitation during different homogenization treatments in a 3003 aluminum alloy, Materials & Design. 30 (2009) 2685-2692. Doi: http://dx.doi.org/10.1016/j.matdes.2008.10.012.

5. A. M. F. Muggerud, J. C. Walmsley, R. Holmestad, Y. Li, Combining HAADF STEM tomography and electron diffraction for studies of α-Al(Fe,Mn)Si dispersoids in 3xxx aluminium alloys, Philosophical Magazine. 95 (2015) 744-758. Doi: http://dx.doi.org/10.1080/14786435.2015.1006294.

6. K. Liu, X. G. Chen, Development of Al–Mn–Mg 3004 alloy for applications at elevated temperature via dispersoid strengthening, Materials & Design. 84 (2015) 340-350. Doi: http://dx.doi.org/10.1016/j.matdes.2015.06.140.

7. Z. Li, Z. Zhang, X. G. Chen, Effect of magnesium on dispersoid strengthening of Al—Mn—Mg—Si (3xxx) alloys, Transactions of Nonferrous Metals Society of China. 26 (2016) 2793-2799. Doi: http://dx.doi.org/10.1016/S1003-6326(16)64407-2.

8. A. M. F. Muggerud, E. A. Mørtsell, Y. Li, R. Holmestad, Dispersoid strengthening in AA3xxx alloys with varying Mn and Si content during annealing at low temperatures, Materials Science and Engineering: A. 567 (2013) 21-28. Doi: http://dx.doi.org/10.1016/j.msea.2013.01.004.

9. K. Liu, X.-G. Chen, Evolution of Intermetallics, Dispersoids, and Elevated Temperature Properties at Various Fe Contents in Al-Mn-Mg 3004 Alloys, Metallurgical and Materials Transactions B. 47 (2016) 3291-3300. Doi: http://dx.doi.org/10.1007/s11663-015-0564-y.

10. L. Lodgaard, N. Ryum, Precipitation of dispersoids containing Mn and/or Cr in Al–Mg–Si alloys, Materials Science and Engineering: A. 283 (2000) 144-152. Doi: http://dx.doi.org/10.1016/S0921-5093(00)00734-6.

11. H. Hirasawa, Precipitation process of Al-Mn and Al-Cr supersaturated solid solution in presence of age hardening phases, Scripta Metallurgica. 9 (1975) 955-958. Doi: http://dx.doi.org/10.1016/0036-9748(75)90551-7.

12. K. Liu, H. Ma, X. G. Chen, Enhanced elevated-temperature properties via Mo addition in Al-Mn-Mg 3004 alloy, Journal of Alloys and Compounds. 694 (2017) 354-365. Doi: http://dx.doi.org/10.1016/j.jallcom.2016.10.005.

13. Z. Li, Z. Zhang, X. G. Chen, Microstructure, elevated-temperature mechanical properties and creep resistance of dispersoid-strengthened Al-Mn-Mg 3xxx alloys with

varying Mg and Si contents, Materials Science and Engineering: A. 708 (2017) 383-394. Doi: https://doi.org/10.1016/j.msea.2017.10.013.

14. Z. Li, Z. Zhang, X. G. Chen, Effect of metastable Mg_2Si and dislocations on α-Al(MnFe)Si dispersoid formation in Al-Mn-Mg 3xxx alloys, Submitted to Materials Characterization. (2017).

15. T. Marlaud, A. Deschamps, F. Bley, W. Lefebvre, B. Baroux, Influence of alloy composition and heat treatment on precipitate composition in Al–Zn–Mg–Cu alloys, Acta Materialia. 58 (2010) 248-260. Doi: http://dx.doi.org/10.1016/j.actamat.2009.09.003.

16. C. Marioara, S. Andersen, T. Stene, H. Hasting, J. Walmsley, A. Van Helvoort, R. Holmestad, The effect of Cu on precipitation in Al–Mg–Si alloys, Philosophical Magazine. 87 (2007) 3385-3413. Doi: http://dx.doi.org/10.1080/14786430701287377.

17. X. Wang, S. Esmaeili, D. J. Lloyd, The sequence of precipitation in the Al-Mg-Si-Cu alloy AA6111, Metallurgical and Materials Transactions A. 37 (2006) 2691-2699. Doi: http://dx.doi.org/10.1007/BF02586103.

18. C. D. Marioara, S. J. Andersen, J. Røyset, O. Reiso, S. Gulbrandsen-Dahl, T.-E. Nicolaisen, I.-E. Opheim, J. F. Helgaker, R. Holmestad, Improving Thermal Stability in Cu-Containing Al-Mg-Si Alloys by Precipitate Optimization, Metallurgical and Materials Transactions A. 45 (2014) 2938-2949. Doi: http://dx.doi.org/10.1007/s11661-014-2250-0.

19. J. Man, L. Jing, S. G. Jie, The effects of Cu addition on the microstructure and thermal stability of an Al–Mg–Si alloy, Journal of Alloys and Compounds. 437 (2007) 146-150. Doi: http://doi.org/10.1016/j.jallcom.2006.07.113.

20. G. A. Edwards, K. Stiller, G. L. Dunlop, M. J. Couper, The precipitation sequence in Al–Mg–Si alloys, Acta Materialia. 46 (1998) 3893-3904. Doi: http://dx.doi.org/10.1016/S1359-6454(98)00059-7.

21. R. Vissers, M. A. van Huis, J. Jansen, H. W. Zandbergen, C. D. Marioara, S. J. Andersen, The crystal structure of the β′ phase in Al–Mg–Si alloys, Acta Materialia. 55 (2007) 3815-3823. Doi: http://dx.doi.org/10.1016/j.actamat.2007.02.032.

22. J. Qin, Z. Zhang, X.-G. Chen, Mechanical Properties and Strengthening Mechanisms of Al-15 Pct B4C Composites with Sc and Zr at Elevated Temperatures, Metallurgical and Materials Transactions A. 47 (2016) 4694-4708. Doi: http://dx.doi.org/10.1007/s11661-016-3606-4.

23. E. L. Huskins, B. Cao, K. T. Ramesh, Strengthening mechanisms in an Al–Mg alloy, Materials Science and Engineering: A. 527 (2010) 1292-1298. Doi: http://dx.doi.org/10.1016/j.msea.2009.11.056.

24. Ø. Ryen, B. Holmedal, O. Nijs, E. Nes, E. Sjölander, H.-E. Ekström, Strengthening mechanisms in solid solution aluminum alloys, Metallurgical and Materials Transactions A. 37 (2006) 1999-2006. Doi: http://dx.doi.org/10.1007/s11661-006-0142-7.

25. J. G. Kaufman, Properties of Aluminum Alloys: Tensile, Creep, and Fatigue Data at High and Low Temperatures. (ASM international, 1999), pp. 9.

26. J. G. Kaufman, Properties of Aluminum Alloys: Tensile, Creep, and Fatigue Data at High and Low Temperatures. (ASM international, 1999), pp. 41.

27. J. G. Kaufman, Properties of Aluminum Alloys: Tensile, Creep, and Fatigue Data at High and Low Temperatures. (ASM international, 1999), pp. 102.

Chapter 8 Conclusions and Recommendations

8.1 Conclusions

In this Ph.D. project, the influences of Mg, Si, Sc, Zr and Cu elements on the microstructure and mechanical properties at both ambient and elevated temperatures were investigated. Moreover, the nucleation mechanisms of α-Al(MnFe)Si dispersoids that was the main strengthening phase were studied. From the experimental results obtained and their analyses, the following conclusions can be drawn, which categorized in four parts corresponding to the different aspects that were studied.

Part I: Microstructure, elevated-temperature mechanical properties and creep resistance of dispersoid-strengthened Al-Mn-Mg 3xxx alloys with varying Mg and Si content

1. Mg and Si have a significant influence on the distribution and volume fraction of dispersoids in Al-Mn-Mg 3xxx alloys. Without Mg or Si addition, α-Al(MnFe)Si dispersoids could hardly form during the precipitation heat treatment.
2. Mg and Si strongly promote the formation of α-Al(MnFe)Si dispersoids during precipitation heat treatment at 375 ^{o}C. With 1% Mg and 0.25% Si, the alloy obtained the maximum volume fraction of dispersoids and the minimum volume fraction of the dispersoid-free zone. Further increase of Mg and Si content resulted in a reduced volume fraction of dispersoids.
3. The base alloy free of Mg or Si possessed low yield strength and creep resistance at elevated temperature due to the lack of the strengthening phases. The alloy containing 1.0% Mg and 0.25% Si demonstrated the best overall performance in terms of the distribution and volume fraction of dispersoids, elevated-temperature yield strength and creep resistance.

Part II: Effect of metastable Mg_2Si and dislocations on α-Al(MnFe)Si dispersoid formation in Al-Mn-Mg 3xxx alloys

4. In Al-Mn-Mg 3xxx alloys, Mg plays an important role in promoting the formation of α-Al(Mn,Fe)Si dispersoids. Without Mg addition, the precipitation of α-Al(Mn,Fe)Si dispersoids was so difficult that only an insufficient number of dispersoids could obtain. The number density and volume fraction of dispersoids in the Mg containing alloy are much higher than that in the base alloy without Mg, resulting in a strong dispersoid strengthening effect.
5. During heating process of the heat treatment in the Mg containing alloy, metastable Mg_2Si precipitated and dissolved, leaving local Si-rich areas of pervious metastable Mg_2Si, which provide favourable nucleation sites for α-Al(Mn,Fe)Si dispersoids. Both metastable β'-Mg_2Si precipitates are more effective than β''-Mg_2Si on the promotion of the dispersoid nucleation.
6. In the deformed sample, the dislocations become the preferable sites for the α-Al(Mn,Fe)Si dispersoid nucleation. Due to the presence of a great number of dislocations, α-Al(Mn,Fe)Si dispersoids can nuclear and grow in the Mn depleted zone (formerly DFZ) close to intermetallic particles and grain boundaries, resulting in a more uniform despersoid distribution compared to the non-deformed sample.

Part III: Improvement of mechanical properties and creep resistance in Al-Mn-Mg 3004 alloy with Sc and Zr addition

7. With the addition of Sc and Zr, the amount of Mn-containing intermetallics and primary Mg_2Si particles increased in the as-cast microstructure of 3004 alloy. Moreover, two populations of strengthening particles (α-Al(Mn,Fe)Si dispersoids and $Al_3(Sc,Zr)$ precipitates) were formed after heat treatment at 375 ℃ for 24h. Both populations of particles contributed to the mechanical properties and creep resistance at ambient and elevated temperatures

8. The microhardness and yield strength at room temperature greatly increased while the yield strength at 300 ℃ did not change with increasing Sc and Zr contents. The addition of Sc and Zr significantly improved the creep resistance at 300 ℃ due to the precipitation of fine Al_3(Sc,Zr) and the reduction of the particle free zone.
9. The combined effects of α-Al(Mn,Fe)Si dispersoids and Al_3(Sc,Zr) precipitates on the yield strengths at 25 ℃ and 300 ℃ were quantitatively analyzed based on the Orowan bypass mechanism and the dislocation climb mechanism. The predicted yield strengths by the analytical solution were in good agreement with experimental data.

Part IV: The influence of Cu addition on dispersoid formation and mechanical properties of Al-Mn-Mg 3004 alloys

10. Cu addition promotes the dispersoid precipitation. The number density of the dispersoids in the Cu containing alloys is significantly higher than that in the Cu-free base alloy, and the size of dispersoids in the former is smaller than that of the latter.
11. Metastable Q-AlCuMgSi precipitates in the Cu containing alloys and metastable β'-Mg_2Si precipitates in the Cu-free base alloy were observed during heating process of the heat treatment. Although dissolved in the further heating process, both metastable precipitates promote the dispersoid nucleation.
12. Cu addition improves the hardness at ambient temperature, the yield strength and creep resistance at 300 ºC, which is mainly attributed to the dispersoid strengthening and Cu solid solution strengthening. The yield strength contribution at 300 ºC is quantitatively evaluated based on the analytical solution. The predicted yield strengths were in good agreement with experimental data.

8.2 Recommendations

The effect of Mg, Si, Sc, Zr and Cu elements on the microstructure and elevated temperature mechanical properties of Al-Mn-Mg-Si alloys (AA3xxx) were systematically

investigated. Based on the present study, following recommendations can be given for future work in this field.

1. According to the present study, Cu could slow down the coarsening process of dispersoids. The mechanism of this phenomenon is worth for further investigating. High resolution TEM or Atom Probe Tomography are recommended to analyze the segregation of Cu atoms in the dispersoids.

2. In the present study, the temperature of heat treatment for dispersoids precipitation is around 375-400°C. However, once high temperature homogenization and solution treatment were applied before the precipitation treatment, a large size and low density of dispersoids occurred, which caused the remarkably decrease of mechanical properties in AA3xxx alloys. The mechanism of this phenomenon is advised to study.

3. With the addition of Sc and Zr, the room-temperature mechanical properties of AA3xxx alloys increased. However, the elevated-temperature strength remained unchanged due to a significant decrease of the dispersoid volume fraction. Solving this problem would be an interesting project for further improving elevated-temperature properties through the best use of two different populations of strengthening particles.

4. Due to the possibility of the precipitation of thermally stable dispersoids by Cr or V elements in AA3xxx alloys, the influences of Cr and V on the microstructure and elevated-temperature properties of AA3xxx alloys are suggested to investigate.

5. The elevated-temperature properties of final deformed AA3xxx alloys, namely of the final products after extrusion, rolling and forging, need to be confirmed under various process and thermomechanical conditions.